Numerical simulation of a cavitating line vortex in a converging-diverging nozzle

using RANS and SRS methods

Maurits Willem van den Boogaard
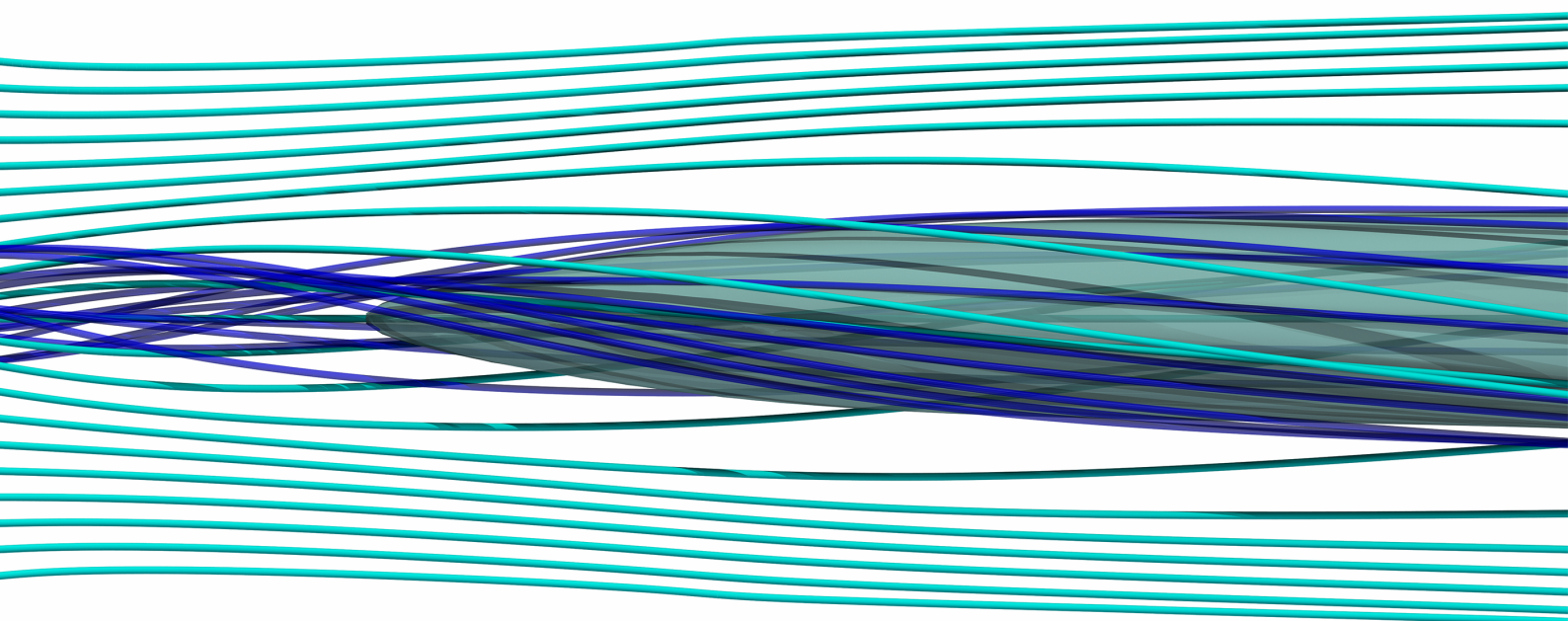
Faculty of Mechanical, Maritime and Materials Engineering, 3mE
Delft University of Technology
Netherlands

Numerical simulation of a cavitating line vortex in a converging-diverging nozzle

using RANS and SRS methods

by

Maurits Willem van den Boogaard

to obtain the degree of Master of Science in Marine Technology
at the Delft University of Technology,
to be defended publicly on Friday September 27, 2019 at 02:00 PM.

Cover image is a render of vortex cavity and streamlines in the Venturi throat. Document typeset in LaTeX. References, abbreviations, figures and tables use hypertext.

Abstract

Tip vortex cavitation was previously identified as a source of the broadband noise emitted by ships underwater. This leads to unwanted noise and vibrations on board, which reduces passenger comfort, and increases the underwater signature of naval ships. The influence of different cavitation regimes on propellers and boundary layer transition on wings, has led to studies that isolate the cavitating tip vortex. This is done by using a converging-diverging nozzle (Venturi tube) geometry, combined with a suitable inflow condition to simulate a cavitating line vortex. The currently available computational power allowed for a comparative study of Scale-Resolving Simulation (SRS) methods (i.e. the Improved Delayed Detached-Eddy Simulation (IDDES) model) and Reynolds-Averaged Navier-Stokes (RANS) models (i.e. the $k - \omega$ Shear Stress Transport (SST) and Explicit Algebraic Reynolds Stress Model (EARSM)) in wetted and cavitating vortex conditions. Both the general flow field, as well as the dynamics of the cavity deformations in the vortex were analyzed in this thesis.

The geometry was selected based on the available experimental validation data for the wetted flow case, whereby preliminary studies determined the inflow and outflow lengths of the domain. A Lamb-Oseen tangential velocity profile was specified at the inlet. The vortex strength and viscous core size were tuned to obtain similar inflow conditions as in the experimental measurements, which used a fixed-blade swirl generator to generate the line vortex.

The flow field in the wetted vortex case demonstrated an excessive amount of viscous diffusion of the vortex for both RANS models. As in previous research regarding RANS modeling of vortices, this was caused by the overproduction of modeled turbulent kinetic energy at the viscous core edge. EARSM resuls were verified in a grid- and time step refinement study, however the large modeling error in the viscous core prevented the validation of the results. The IDDES model results were closer to the experimental reference, but were obtained with an almost laminar flow field. Modeled turbulence was mostly dissipated and no resolved velocity fluctuations were present in the flow at the measurement section.

The increased numerical diffusion of the EARSM led to a more diffuse vapor core interface and a more downstream development of the vortex cavity compared to IDDES. The IDDES flow field remained predominantly laminar at the measurement section. Both EARSM and IDDES predicted a solid-body rotation of the vapor core, combined with an increase of radial velocity towards the vapor core edge. The non-negligible radial velocity resulted in a conical cavity shape. The velocity profile of the simulated line vortex therefore did not correspond to that of a cavitating Lamb-Oseen vortex (which assumes no radial velocity components), such that the simulated line vortex was not representative of a cavitating tip vortex.

  The sheet cavities originating from sharp edges at the front and end of the Venturi throat strongly influenced the flow field and cavity dynamics. The developed front sheet cavity determined the streamwise inception of the vapor core of the vortex. Periodic shedding and collapse of the irregular downstream sheet cavity caused axial and radial contractions of the vapor core as well as a noncircular deformation of the cavity cross-section. No traveling or standing Kelvin waves could be identified on the cavity interface using the developed post-processing and spectral analysis tool. The identified cross-sectional deformation did not correspond to cavity deformation modes defined in previous research and none of the other deformation modes were found to occur. Grid-dependent solutions, numerical noise and large wavenumber resolution indicated that a finer grid is required and that the analyzed length of the cavity should increase to improve the quality of numerical analyses of simulated cavity dynamics.

Acknowledgments

Contents

Nomenclature

The following list of symbols contains entries that are used across multiple sections in this thesis. If any symbol takes on another meaning, this is stated in the text. Einstein notation is generally used, however vector notation is sometimes used for sake of brevity.

List of symbols

Latin symbols

a_{ij}	Reynolds Stress anisotropy tensor
c	Speed of sound
f_i	Body force term
I	Turbulence intensity
k	Turbulent kinetic energy
L_∞	Normalized global residual
l	Length scale
L_2	Normalized root-mean-square residual
$\dot{m}$	Mass transfer rate
p	Pressure
$\dot{Q}$	Volumetric flow rate
r	Diameter
r	Radius
S_{ij}	Strain-rate tensor
$S_{\mathbf{vap}}$	Cavitation source term
T	Period
t	Time
T_ω	Surface tension
$U_{\mathbf{disc}}$	Discretization uncertainty
u_i	Velocity component in i-direction
$U_{\mathbf{stat}}$	Statistical uncertainty

Greek symbols

Γ	Circulation
Δl	Grid spacing
Δt	Timestep
Ω_{ij}	Vorticity tensor
α	Volume fraction
β	Angle of the velocity vector
δ_{ij}	Kronecker delta
ε	Turbulence dissipation
κ	Nondimensional wavenumber
μ	Dynamic viscosity
ν	Kinematic viscosity
ν_t	Eddy viscosity
ρ	Density
σ	Cavitation number
τ	Time scale
τ_{ij}	Reynolds stress tensor
ω	Specific dissipation rate
$\tilde{\omega}$	Dimensionless frequency
ϕ	Arbitrary flow quantity

Super- and subscripts

∞	(Far field) reference value
$+$	Nondimensional wall distance
0	Initial value
c	Cavity
l	Liquid
r	Radial
v	Viscous
vap	Vapor
x	Axial
θ	Tangential
$\bar{\phi}$	Time-averaged quantity
ϕ'	Turbulent fluctuation
ϕ^*	Non-dimensional quantity
$\boldsymbol{\phi}$	Vector quantity

Dimensionless numbers

Co	Courant number
Ma	Mach number
Re	Reynolds number
Sn	Swirl number
We	Weber number

Operators

$\nabla \times \boldsymbol{\phi}$	Curl operator
$\nabla \cdot \boldsymbol{\phi}$	Divergence operator
$\nabla \boldsymbol{\phi}$	Gradient operator

List of abbreviations and acronyms

ARSM	Algebraic Reynolds Stress Model
CFD	Computational Fluid Dynamics
CPSD	Cross-power Spectral Density
DDES	Delayed Detached-Eddy Simulation
DES	Detached-Eddy Simulation
DNS	Direct Numerical Simulation
EARSM	Explicit Algebraic Reynolds Stress Model
EFD	Experimental Fluid Dynamics
EVM	Eddy Viscosity Model
FFT	Fast Fourier Transform
FRESCO	Fast RANS Equations solver for Ships and Constructions Offshore
IDDES	Improved Delayed Detached-Eddy Simulation
LDV	Laser-Doppler Velocimetry
LES	Large Eddy Simulation
LLM	Log-Layer Mismatch
LRR	Launder-Reece-Rodi (Reynolds Stress model)
MSD	Modeled Stress Depletion
PSD	Power Spectral Density
PVC	Precessing Vortex Core

QUICK   Quadratic Upwind Interpolation for Convective Kinematics

RANS   Reynolds-Averaged Navier-Stokes
RHS   Right-Hand Side
RSM   Reynolds Stress Model

SGS   Subgrid-Scale
SIDR   Swirl Intensity Decay Rate
SIMPLE   Semi-Implicit Method for Pressure Linked Equations
SRS   Scale-Resolving Simulation
SST   Shear Stress Transport

TST   Transient Scanning Technique

V&V   Verification and Validation
VOF   Volume-of-Fluid

WMLES   Wall-modeled Large Eddy Simulation

Introduction

The advent of affordable numerical simulations of the flow around ships, using potential and Computational Fluid Dynamics (CFD) codes, has drastically increased the possibilities for producing efficient new designs and improving already built vessels (e.g. using add-on energy-saving devices) in order to reduce costs, fuel consumption and emissions. Since the hull of the vessel is constrained due to cargo requirements, a significant increase in efficiency can be found by reducing losses from the propeller. As propeller research allows for ever more efficient designs, the risk of unacceptable cavitation nuisance increases. Cavitation is defined as the phase change from liquid to vapor caused by a change in pressure, as opposed to temperature (boiling). The locally high flow velocities around the propeller blade induce very low pressure regions, that might lead to cavitation. Cavitating vortices, originating from the tip of the propeller blade, generate pressure pulses on e.g. the rudder or hull and radiate broadband noise into the environment [1]. The emitted frequency is usually between 30-100 Hz when measured on the hull above the propeller [2]. The prediction and quantification of these vibrations and the emitted noise are of great interest for designers of passenger and navy vessels to respectively increase the comfort on board and reduce the underwater signature of vessels. Noise radiated from ships also has a negative impact on marine life and it is therefore of general interest to design propellers such that the noise emission is limited.

The numerical modeling of a tip vortex is challenging due to the interaction of turbulence and cavitation, each requiring their own model as well as the complex dynamics involved. The accuracy required for an acoustic calculation requires a careful selection of these models, for which there is still a lack of industry guidelines. While there has been extensive research into the modeling of sheet and bubble cavitation, it is difficult to study the tip vortex as an isolated phenomenon on propellers owing to the interaction with e.g. sheet cavities. Furthermore, using a fully rotating propeller geometry in the domain is computationally very expensive, leading to simplifications that try to maintain as much of the dynamics of generating the tip vortex, but simplify the geometry and try to isolate the vortex. Various types of wings were developed as test cases, and the Arndt wing [3, 4] is an often used reference case in literature. An important issue with using a wing-shaped blade is the transition of flow from laminar to turbulent along the blade surface. The difficulty of the exact determination of the transition location and the limited applicability of transition models [5] make it interesting to try and eliminate the blade geometry to isolate the tip vortex even further. Previous research of isolated tip vortices [2, 6] has focused on the development of semi-analytical relations to predict the dynamics and noise emission from a cavitating tip vortex. For the present numerical simulation, the tip vortex is generated using a boundary condition at the inlet of the domain. As such, it is more correct to use the term 'line vortex' for such cases. A Venturi tube - a circular domain consisting of a contraction followed by a parallel section and an expansion - was previously used as a computational domain for such simulations [6, 7]. The contraction causes the flow to accelerate, leading to a sufficiently low pressure for the vortex to start cavitating. The simple geometry should allow for the generation of a high-quality grid with a limited number of cells so that extensive Verification and Validation (V&V) studies can be performed at reasonable computational cost.

1.1. Research objectives

Janssen [6] and de Montgolfier [7] performed numerical computations of a cavitating line vortex in a Venturi. Both studies were made without experimental validation and coarse grids were used, especially given today's computing power. Finer grids need to be generated using a geometry for which experimental validation material is available. The experimental study of a wetted and cavitating line vortex by Rudolf et al. [8] is used in the present study as a validation base for the wetted flow vortex.

The preceding considerations allow the formulation of the following research question:

Which turbulence model is most suitable to be used for the accurate simulation of the flow field inside an isolated cavitating line vortex and its dynamics in a converging-diverging nozzle?

With the subquestions:

i) What are suitable inflow conditions to obtain a realistic vortex at the inlet of the converging nozzle?

ii) To what extent do SRS and higher-order turbulence models perform superiorly to standard two-equation RANS models in the context of predicting the flow variables in the vortex core for a wetted line vortex?

iii) How do different turbulence models influence the structure of the vortex core of a cavitating tip vortex?

iv) What influence do different turbulence models have on the cavity dynamics of the cavitating line vortex inside the Venturi throat?

Given these research questions, the following approach was taken to provide the answers. The experimental flow field measurements by Rudolf et al. [8] were obtained using Laser-Doppler Velocimetry (LDV). The vapor core inside the vortex core reflects the laser beams, such that no reliable measurements within the vapor core could be made. Therefore, only the wetted vortex can validated using these experimental results. The specification of a suitable boundary condition can be based on [6, 7] to a certain extent but requires tuning based on the experimentally generated vortex in [8]. Rudolf et al. reported the measured velocity angles [9] which serve as a way to tune the inflow condition such that a realistic flow field is obtained at the inlet of the converging nozzle. The currently available computational power permits the use of turbulence models such as the IDDES model and the EARSM that should lead to improved results compared to the common $k - \omega$ SST approaches used in the past [6, 7]. This can be reasonably expected based on results by Rudolf et al. [9] and Pereira [10].

The recent application of semi-analytical cavitating vortex model predictions to empirical measurements, including a detailed spectral analysis of the cavity dynamics by Bosschers [2] is a promising step towards predicting the acoustic signature of a tip vortex. The present work will make an attempt to apply the same analysis to numerical results, hoping to identify deformation modes of the cavitating line vortex.

An answer also needs to be provided to the question whether the Venturi tube is a suitable candidate to simulate isolated tip vortices. It is of interest to evaluate, taking into account results by Liebrand [11] obtained for the elliptical Arndt foil, to what extent the findings for the current test case can be extended towards a tip vortex originating from a wing.

1.2. Thesis structure

This work begins with a thorough introduction in Chapter 2 of the different physical phenomena present in cavitating tip vortices and the numerical techniques that are used to model these physics. The flow inside the Venturi tube is considered to be fully turbulent and turbulent effects are expected to significantly affect the prediction of the vortex. Turbulence is therefore discussed first. The dynamics and description of vortices is touched upon afterwards, introducing the boundary condition that is used to simplify a tip vortex into the line vortex simulated in this thesis. The dynamics and numerical modeling of cavitation is treated subsequently, followed by the dynamics of cavitating vortices. The previously mentioned noise emission from cavitating tip vortices was traced back to small-scale oscillations of the cavity [12], which can be studied in the spectral domain to identify deformation modes of the cavitating vortex core [2, 13]. The method used by Bosschers [2] for this analysis is presented in the fourth section of this chapter. Afterwards, the V&V procedure is discussed, followed finally by the discretization procedures applied in the CFD code REFRESCO that was used for this work.

The third chapter considers the numerical set-up of the simulation, comprising the domain discretization, applied boundary conditions, the measurement locations and the normalization procedure. Preliminary simulations were carried out in order to determine the required domain length and the tuning parameters for the specification of the vortex at the inflow boundary. These studies are discussed at the end of Chapter 3.

Next, in Chapter 4, the flow field in a wetted vortex is analyzed and discussed, whereby the coarse grid performance of the different turbulence models is compared first. This is followed by the grid- and time step convergence study.

Cavitating vortex results can be found in Chapter 5 of which the first section contains an analysis of the flow field as in the previous chapter. The second section is dedicated to the discussion of the cavity dynamics in the spectral domain.

Final conclusions and recommendations can be found in Chapter 6 at the end of this work.

$$2$$

Theoretical and numerical concepts

This chapter provides an overview of the theoretical knowledge that was gathered to understand and critically judge the obtained results in Chapter 4 and Chapter 5. This thesis combines three major areas of research within the Computational Fluid Dynamics (CFD) community: turbulence, vortex dynamics and cavitation. These three topics form the first three sections of this chapter. Fourth, the dynamics of cavitating vortices are discussed from the angle of the previous work by Bosschers [14] and Pennings et al. [15], who observed the cavity deformations in the spectral domain. Next, the quantification of numerical uncertainties and validation procedure is discussed, followed by the characteristics of the REFRESCO CFD code used in this work.

2.1. Turbulence

Turbulent flows can be found everywhere in our daily lives: in the rivers flowing through the landscape, in the smoke rising from a cigar and in the strong wind blowing into the sails of a sailing boat. If one pays attention, these flows seem chaotic, irregular and even random and are very unsteady. Pope [16] remarks that the velocity field is a function of both space and time $u(\mathbf{x}, t)$ and varies significantly and irregularly in these four dimensions. Due to the characteristics of turbulent flows (i.a. improved mixing) and the prevalence of turbulent flow in engineering applications (i.a. airplanes, cars and ships) a lot of research has been dedicated to try to understand the guiding physical processes. The Navier-Stokes equations that govern the flow of incompressible and viscous fluids also apply to turbulent flows and the mass and momentum conservation equations are given in respectively Equations (2.1) and (2.2) in the incompressible, single-phase formulation:

$$\frac{\partial u_i}{\partial x_i} = 0, \tag{2.1}$$

$$\frac{\partial u_i}{\partial t} + u_j \frac{\partial u_i}{\partial x_j} = -\frac{1}{\rho} \frac{\partial p}{\partial x_i} + \frac{\partial}{\partial x_j} \left(\nu \frac{\partial u_i}{\partial x_j} \right) + f_i, \tag{2.2}$$

where f_i is an external force applying to the bulk of the fluid (i.e. a body force). Arguably one of the more important characteristics of a turbulent flow is the presence of a (large) spectrum of different scales. The higher the Reynolds number, the larger the separation between these scales [16]. The Reynolds number defines the ratio of inertial to viscous forces: $Re = u_\infty l_\infty / \nu$, where u_∞ and l_∞ are the reference velocity and length scale and ν is the kinematic viscosity. The different ways in which turbulent flows are simulated, then, can be categorized based on the amount of scales they resolve. Direct Numerical Simulation (DNS) resolves all turbulent scales, but is limited to lower Reynolds numbers and not commonly applied outside a fundamental research context due to the computational cost (the number of grid cells scales with $Re^{9/4}$). The Reynolds-Averaged Navier-Stokes (RANS) method on the other hand, models all turbulent scales and is discussed in the next section.

2.1.1. Reynolds-Averaged Navier-Stokes (RANS) modeling

RANS modeling is arguably the most commonly used approach when dealing with turbulent flows in industrial applications and at high Reynolds numbers. For most common engineering flows, two-equation RANS models (e.g. $k-\omega$, $k-\varepsilon$) manage to deliver results with sufficient accuracy despite their relatively moderate computational cost. RANS takes a statistical approach to turbulence, which requires a separation between the large scales of motion and the irregular smaller scales. The large scales have the largest velocity and timescales, and the timescales are used to achieve the separation between the unsteadiness of the mean field $\bar{f}$ (caused by the large scales) and turbulent fluctuations (of the small scales) through a form of filtering called Reynolds averaging [17], defining the resolved field $\bar{f}(t)$ as:

$$\bar{f}(t) = \frac{1}{T} \int_{t-T}^{t} f(s) \mathrm{d}s \qquad \text{with } T \gg \tau, \tag{2.3}$$

where τ is the characteristic timescale of turbulence, T is the averaging period and $\tau \ll T \ll \theta$, where θ is the characteristic period for the temporal evolution of the mean properties.

To achieve this separation using the Navier-Stokes equations, Reynolds put forward the idea of splitting the local velocity

field u_i in a mean $\overline{u}_i$ and a fluctuating u_i' part [18]. The same rationale applies to the pressure. Reynolds based the flow field decomposition on the assumption that the flow and the turbulence is steady from a statistical perspective, i.e. time-derivative terms are zero, but the decomposition itself remains valid for some unsteady flows as well. Some flow problems are characterized by a slow periodic motion without relation to turbulence (e.g. the flow over a helicopter blade) and therefore still demonstrate a scale separation between the unsteadiness of the mean flow field and turbulence. These flow problems can be still solved quite accurately using the rationale of unsteady RANS modeling, which includes the time derivative in the momentum equation. The flow variables could then be split in a time-averaged part $\bar{\phi}$, coherent fluctuating part $\tilde{\phi}$ and a chaotic (turbulent) fluctuation ϕ' [17]:

$$\phi = \bar{\phi} + \tilde{\phi} + \phi'. \tag{2.4}$$

The Reynolds average of a quantity ϕ has the following properties:

$$\overline{\overline{\phi}_i} = \overline{\phi}_i, \tag{2.5}$$

$$\overline{\phi}_i \overline{\phi}_j = \overline{\phi_i \phi_j}, \tag{2.6}$$

$$\overline{\phi_i'} = 0. \tag{2.7}$$

The last identity follows from applying the Reynolds average to the continuity equation. The Reynolds-averaged form of the incompressible, single-phase Navier-Stokes equations is given by:

$$\frac{\partial \overline{u}_i}{\partial x_i} = 0, \tag{2.8}$$

$$\frac{\partial \overline{u}_i}{\partial t} + \overline{u_j \frac{\partial u_i}{\partial x_j}} = -\frac{1}{\rho}\frac{\partial \bar{p}}{\partial x_i} + \frac{\partial}{\partial x_j}\left(\nu \frac{\partial \overline{u}_i}{\partial x_j}\right) - \frac{\partial \overline{u_j' u_i'}}{\partial x_j}. \tag{2.9}$$

The last term in Equation (2.9) contains the turbulent stresses that make up the Reynolds stress tensor τ_{ij}. Since there is no complete information available in the flow to calculate $-\overline{u_i' u_j'}$ exactly, a certain degree of modeling is required to close the system of equations.

2.1.2. The eddy viscosity hypothesis

The most straightforward method of closing the system of equations, employed by the majority of the turbulence models (i.a. $k-\omega$, $k-\varepsilon$) used nowadays, uses the Boussinesq hypothesis to model all components of the symmetric Reynolds stress tensor. In this way, no separate transport equation needs to be solved for each of its six components. An explicit constitutive relation is used instead to compute the Reynolds stress tensor, using transport equations for turbulent variables. Without resolving the turbulent stresses, the turbulent stress tensor is then merely a function of the mean velocity gradient and the turbulent length and velocity scales [19]. In fact, the main idea brought forward by Boussinesq was that the principal axes of the Reynolds stress tensor τ_{ij} align with the rate-of strain tensor S_{ij}, with the eddy viscosity ν_t as the proportionality constant of choice [20]. This idea was originally introduced by Boussinesq in 1877, even before the formal definition of the Reynolds stress tensor (which was in 1895) [21]. The introduction of the eddy viscosity ν_t into the linear relation between the rate-of-strain and Reynolds stress tensor in Equation (2.10) gives name to the models that use this approximation: linear Eddy Viscosity Models (EVMs). The eddy viscosity can be computed in different ways, but the most popular models use two transport equations to calculate the eddy viscosity based on the turbulent kinetic energy k. The $k-\omega$ Shear Stress Transport (SST) model, perhaps the most used two-equation model nowadays, is discussed next.

$$\frac{\tau_{ij}}{\rho} = -2\nu_t S_{ij} - \frac{2}{3}k\delta_{ij}, \tag{2.10}$$

where k is the turbulent kinetic energy and δ_{ij} is the Kronecker delta:

$$\delta_{ij} = \begin{cases} 0 & \text{if } i \neq j, \\ 1 & \text{if } i = j. \end{cases} \tag{2.11}$$

The strain-rate tensor S_{ij} is defined as:

$$S_{ij} = \frac{1}{2}\left(\frac{\partial \overline{u}_i}{\partial x_j} + \frac{\partial \overline{u}_j}{\partial x_i}\right). \tag{2.12}$$

2.1.3. $k-\omega$ Shear-Stress Transfer (SST) model

The $k-\omega$ SST model solves transport equations for the turbulence kinetic energy k and the specific turbulence dissipation rate ω. Menter developed the original version of the model in 1994 [22] and a revision of the model took place in 2003

by Menter et al. [23]. Menter's aim was to combine the strong points of the $k - \varepsilon$ and $k - \omega$ models into a single set of equations. The SST model blends between the formulations of the $k - \omega$ and $k - \varepsilon$ models, using the $k - \omega$ formulation close to a non-slip boundary (in the viscous sublayer) and blending to the $k - \varepsilon$ model in the free-stream. This is accomplished by an additional cross-diffusion term in the ω transport equation that contains a blending function $(1 - F_1)$, where $F_1 = 1$ in the viscous sublayer and logarithmic layer and gradually switches to zero in the wake region [23]. The modifications that were applied to the original SST model in 2003 comprise i) the use of the rate-of-strain tensor **S** in the definition of the eddy viscosity v_t and ii) a factor 10 instead 20 in the production term limiter. The $k - \omega$ SST transport equations are given in Equations (2.13) and (2.14) using the modifications described in [23]. The derivations, constants and definitions of relevant functions are provided in Appendix A.1.

$$\frac{\partial(\rho k)}{\partial t} + \frac{\partial(\rho \bar{u}_i k)}{\partial x_i} = \tilde{\mathcal{P}}_k - \beta^* \rho k \omega + \frac{\partial}{\partial x_i} \left[(\mu + \sigma_k \mu_t) \frac{\partial k}{\partial x_i} \right], \tag{2.13}$$

$$\frac{\partial(\rho \omega)}{\partial t} + \frac{\partial(\rho \bar{u}_i \omega)}{\partial x_i} = \alpha \rho S^2 - \beta \rho \omega^2 + \frac{\partial}{\partial x_i} \left[(\mu + \sigma_\omega \mu_t) \frac{\partial \omega}{\partial x_i} \right] + 2(1 - F_1) \rho \sigma_{w2} \frac{1}{\omega} \frac{\partial k}{\partial x_i} \frac{\partial \omega}{\partial x_i}. \tag{2.14}$$

The eddy viscosity is determined using Equation (2.15)

$$v_t = \frac{a_1 k}{\max(a_1 \omega, SF_2)}, \tag{2.15}$$

where S is the invariant measure of the strain rate:

$$S = \sqrt{2 S_{ij} S_{ij}} = \sqrt{2} |S_{ij}|, \tag{2.16}$$

and F_2 is a second blending function. The definition of the production term $\mathcal{P}_k$ is derived from the Boussinesq hypothesis. The quadratic dependence on the strain rate in the kinetic energy production term $\mathcal{P}_k$ leads to a build up of turbulence in stagnation regions, which is solved by adding a production limiter $\tilde{\mathcal{P}}_k$:

$$\mathcal{P}_k = \mu_t \frac{\partial \bar{u}_i}{\partial x_j} \left(\frac{\partial \bar{u}_i}{\partial x_j} + \frac{\partial \bar{u}_j}{\partial x_i} \right) \rightarrow \tilde{\mathcal{P}}_k = \min(\mathcal{P}_k, 10\beta^* \rho k \omega). \tag{2.17}$$

Streamline curvature- and flow rotation corrections
Linear EVM models (i.a. the $k - \omega$ SST model) cannot correctly predict the effects of streamline curvature [20]. The effects of curvature are contained in the production term of the turbulent kinetic energy k, more specifically the strain-rate tensor. Considering the linear relation between the Reynolds stresses and the magnitude S of the strain-rate tensor, more modeled turbulent kinetic energy is produced as S increases. This is not a physical increase of turbulence, which led to the development of correction methods to reduce the amount of turbulent kinetic energy in such cases. Effects of curvature are usually negligible since the flow generally varies much faster in cross-stream direction than the ratio of the mean (axial) velocity and the streamline curvature radius $\mathcal{R}$; i.e. $\partial u_x / \partial y \gg u_x / \mathcal{R}$ [20]. The curvature correction terms that can be added to the transport equation do improve the accuracy of some simulations when significant streamline curvature is present. They are still ad hoc modifications however, which cannot be generalized for arbitrary flows. Additionally, the linear EVMs are not able to correctly predict prominent features of rotating (and stratified) flows unless these ad hoc corrections are added to the transport equations [20].
The Spalart-Shur correction is the most common of these modifications and applicable to the SST model. The derivation and application are discussed by Smirnov & Menter [24]. A simpler correction is applied by Dacles-Mariani [25] which just takes into account the incorrect turbulence prediction in locations of pure (solid-body) rotation such as inside the core of a vortex. The eddy viscosity is reduced artificially in regions where vorticity is dominant over strain rate, slightly improving results in some cases.

Studies comparing standard SST & Spalart-Allmaras one-equation models and the rotation and/ or curvature correction versions show that a moderate improvement can be achieved regarding pressure and (tangential) velocity prediction inside the viscous core [26–29]. The curvature correction mainly improves the prediction of the sharp velocity gradients inside the vortex core [29]. Results obtained by Cheng et al. [30], studying the tip leakage of a hydrofoil, still demonstrate the deficiency of eddy viscosity models in predicting the correct axial velocity, pressure and turbulence quantities inside the vortex core. This is due to their assumption of homogeneous isotropic turbulence, which inside the strongly swirling flow in a (tip) vortex is no longer valid [29]. One of the goals of this research is to present a comparison of results obtained with more advanced models (the Explicit Algebraic Reynolds Stress Model (EARSM) and Improved Delayed Detached-Eddy Simulation (IDDES) model) which do not require additional curvature-correction terms. This, combined with the ad hoc nature of the correction anyway, forms the basis for the decision to *not* apply curvature or rotation corrections to the SST model for the present research.

2.1.4. Reynolds Stress Modeling (RSM)

Although the models involving the Boussinesq approximation generally perform quite well, the previous paragraph demonstrated that there are applications where they do run into trouble and experimental and numerical measurements differ greatly. As mentioned previously, problems arise for flows with sudden changes in the strain-rate, as the way in which Reynolds stresses adjust to them is not related to processes or timescales in the mean flow, as assumed in Boussinesq's hypothesis. Despite the large amount of flows for which Boussinesq-based models should theoretically not be used, they are still the most commonly used models due to the large gap in computational expense with alternative models and in some cases still sufficiently accurate results. A more complex closure approach for the Reynolds stresses $-\rho \overline{u_i' u_j'}$, relying on a non-linear relation with the eddy viscosity and involving more than just the strain-rate tensor, is provided by Reynolds Stress Models (RSMs) and will be discussed on the next pages.

Analytical expression for the transport equation

Unless indicated otherwise, the discussion follows the discourse of Hellsten [19]. As a first step in deriving a model for the Reynolds stresses, the transport equation for the Reynolds stress tensor τ_{ij} can be derived by:

  i) rewriting Equation (2.9) for the velocity component u_i',

 ii) subtracting said expression from Equation (2.9),

iii) multiplying it by u_j',

 iv) Reynolds-averaging this expression and

  v) applying the same procedure for u_j' and adding both expressions together to obtain [19, 31]:

$$\frac{\partial \tau_{ij}}{\partial t} + \overline{u_k}\frac{\partial \tau_{ij}}{\partial x_k} = \underbrace{-\tau_{ik}\frac{\partial \overline{u_j}}{\partial x_k} - \tau_{jk}\frac{\partial \overline{u_i}}{\partial x_k}}_{\text{production}} - \underbrace{\varepsilon_{ij}}_{\text{dissipation}} - \underbrace{\Phi_{ij}}_{\text{redistribution}} + \underbrace{\frac{\partial}{\partial x_k}\left[\nu\frac{\partial \tau_{ij}}{\partial x_k} + T_{ijk}\right]}_{\text{diffusion}}, \qquad (2.18)$$

where:

$$\Phi_{ij} = \overline{\frac{p'}{\rho}\left(\frac{\partial u_i'}{\partial x_j} + \frac{\partial u_j'}{\partial x_i}\right)}, \qquad (2.19)$$

$$\varepsilon_{ij} = 2\nu\overline{\frac{\partial u_i'}{\partial x_k}\frac{\partial u_j'}{\partial x_k}} \qquad \text{and} \qquad (2.20)$$

$$T_{ijk} = -\overline{u_i' u_j' u_k'} - \frac{1}{\rho}\left(\overline{p' u_i'}\delta_{jk} - \overline{p' u_j'}\delta_{ik}\right). \qquad (2.21)$$

The diffusion term contains the turbulent fluxes term T_{ijk}, responsible for the transport of the Reynolds stress by turbulence. The trace of the dissipation tensor ε_{ij} reduces to twice the dissipation rate ε of k in homogeneous isotropic turbulence. The goal of deriving a transport equation of the Reynolds stress is to be able to solve a transport equation for each of the components of the Reynolds stress tensor and k. Neither the production term nor the convection by the mean flow in Equation (2.18) require modeling, which explains the interest in the RSM approach. The other terms, however, do require modeling, often involving strong assumptions. The tensor functions that make up the models in RSM assume isotropy to ensure that their application does not depend on the rotation of the reference frame. Scalar invariants (recognizable by the Roman numerals in the model equations) are introduced to simplify higher-order tensor products based on the Cayley-Hamilton theorem. The modeling of the different terms can be found in Appendix A.2.1.

Algebraic Reynolds Stress modeling

The Algebraic Reynolds Stress Model (ARSM) approach significantly simplifies the solution procedure compared to a full RSM, but inherently also cannot represent transport effects as well as the latter [32]. Algebraic models neglect the convection and diffusion (i.e. transport) terms of the anisotropy tensor a_{ij}, Equation (2.22). The anisotropy tensor redistributes the energy to the different Reynolds stress components. The algebraic modeling approach also links the transport of the turbulent fluctuations directly to the transport of kinetic energy ($\mathfrak{D}(k) = \mathcal{P} - \varepsilon$), $\mathfrak{D}$ being a transport operator defined by Equation (2.23) [19].

$$a_{ij} = \frac{\overline{u_i' u_j'}}{k} - \frac{2}{3}\delta_{ij} \qquad (2.22)$$

$$\mathfrak{D}\left(\overline{u_i' u_j'}\right) \approx \left(a_{ij} + \frac{2}{3}\delta_{ij}\right)(\mathcal{P} - \varepsilon) \qquad (2.23)$$

The weak-equilibrium limit is used to express the traceless anisotropy tensor a_{ij} as a (tensor) function of two second-order tensors; the strain-rate S_{ij} and vorticity tensor Ω_{ij}:

$$a_{ij} = f(S_{ij}, \Omega_{ij}). \tag{2.24}$$

In the weak-equilibrium limit, the assumption is made that the anisotropy only depends on the mean-velocity gradients and the timescale τ. This assumption allows the expression of a_{ij} as its *integrity basis* (i.e. the most general representation invariant under transformations) as a polynomial with 10 independent terms, see Appendix A.2.2. The global system of equations is not closed yet as there is still a scalar unknown: $\mathcal{P}/\varepsilon = -a_{ij}S_{ji}$. EARSM models calculate the ratio $\mathcal{P}/\varepsilon$ explicitly using a cubic approximation of a sixth-order equation. The final expression of the Reynolds stress term is:

$$-\rho \overline{u_i' u_j'} = -\rho k \left(\frac{2}{3} \delta_{ij} + a_{ij} \right). \tag{2.25}$$

2.1.5. Hellsten's Explicit Algebraic Reynolds Stress Model (EARSM)

The EARSM by Hellsten can be split into two parts: a constitutive and a scale-determining model. Both parts are elaborated upon in the following two sections. Unless stated otherwise, the formulation of the model as outlined below is adapted from the PhD thesis of Hellsten [19].

Constitutive model

The Hellsten model uses the EARSM framework developed by Wallin and Johansson [32] as a constitutive model. The C coefficients are chosen from the Launder-Reece-Rodi (Reynolds Stress model) (LRR), with a modification for C_2 so that $A_2 = 0$ to simplify the solution process. The version of the model implemented in REFRESCO contains a curvature correction with a recalibrated A_0 coefficient, leading to modified values for all C coefficients except C_2. All coefficients for the model are provided in Appendix A.3.

The explicit expression for the Reynolds stress anisotropy tensor in the Wallin & Johansson constitutive model is given by:

$$\begin{aligned}
a_{ij} = {}& \beta_1 S_{ij} \\
& + \beta_3 \left(\Omega_{ij}^* \Omega_{kj}^* - \frac{1}{3} \mathrm{II}_\Omega \delta_{ij} \right) + \beta_4 \left(S_{ij} \Omega_{kj}^* - \Omega_{ik}^* S_{kj} \right) \\
& + \beta_6 \left(S_{ik} \Omega_{kl}^* \Omega_{kl}^* S_{lj} - \Omega_{ik}^* \Omega_{kl}^* S_{lj} - \frac{2}{3} \mathrm{IV} \delta_{ij} \right) \\
& + \beta_9 \left(\Omega_{ik}^* S_{kl} \Omega_{lm}^* \Omega_{mj}^* - \Omega_{ik}^* \Omega_{kl}^* S_{lm} \Omega_{mj}^* \right),
\end{aligned} \tag{2.26}$$

where the nondimensional vorticity Ω^* includes an optional rotation modification to improve the behavior of the model in flows with strong streamline curvature, see Equation (A.24) in Appendix A.3.1. For a background on this term, the reader is advised to consult [33]. The timescale τ used to nondimensionalize the vorticity and strain-rate tensors is now redefined as the maximum of the turbulent and viscous timescales:

$$\tau = \max \left(\frac{1}{\beta^* \omega}; \; C_\tau \sqrt{\frac{\nu}{\beta^* k \omega}} \right), \tag{2.27}$$

using the coefficient values of $C_\tau = 6.0$ and $\beta^* = 0.09$. The β functions in the solution of Equation (2.26) depend on the invariants of the strain and vorticity tensors. The β functions and invariants are given in Appendix A.3.1.

For an easier implementation in codes already containing the eddy viscosity models, the Reynolds stress term is slightly altered in the EARSM. The eddy viscosity is replaced by an effective eddy viscosity, Equation (2.29), which is balanced by adding a corrective additional anisotropy term $a_{ij}^{(ex)}$, see Equation (2.30) [19]:

$$\frac{\tau_{ij}(u_i, u_j)}{\rho} = 2\nu_t |S_{ij}| - \frac{2}{3} k \delta_{ij} - a_{ij}^{(ex)}. \tag{2.28}$$

$$\nu_t = C_\mu k \tau, \qquad \text{with} \qquad C_\mu = -\frac{1}{2} (\beta_1 + \mathrm{II}_\Omega \beta_6), \text{ so that:} \tag{2.29}$$

$$a_{ij}^{(ex)} = a_{ij} - (\beta_1 + \text{II}_\Omega \beta_6)$$

$$= \beta_3 \left(\Omega_{ij}^* \Omega_{kj}^* - \frac{1}{3} \text{II}_\Omega \delta_{ij} \right) + \beta_4 \left(S_{ij} \Omega_{kj}^* - \Omega_{ik}^* S_{kj} \right)$$

$$+ \beta_6 \left(S_{ik} \Omega_{kl}^* \Omega_{kl}^* S_{lj} - \Omega_{ik}^* \Omega_{kl}^* S_{lj} - \text{II}_\Omega S_{ij} - \frac{2}{3} \text{IV} \delta_{ij} \right)$$

$$+ \beta_9 \left(\Omega_{ik}^* S_{kl} \Omega_{lm}^* \Omega_{mj}^* - \Omega_{ik}^* \Omega_{kl}^* S_{lm} \Omega_{mj}^* \right). \tag{2.30}$$

Scale-determining model

The Hellsten model is based on the $k - \omega$ SST model, but uses space-dependent coefficients. The transport equations for k and ω in the formulation of [19] are given by:

$$\frac{\mathrm{D}k}{\mathrm{D}t} = \mathcal{P} - \beta^* k\omega + \frac{\partial}{\partial x_j} \left[(\nu + \sigma_k \nu_t) \frac{\partial k}{\partial x_j} \right], \tag{2.31}$$

$$\frac{\mathrm{D}\omega}{\mathrm{D}t} = \gamma \frac{\omega}{k} \mathcal{P} - \beta \omega^2 + \frac{\partial}{\partial x_j} \left[(\nu + \sigma_\omega \nu_t) \frac{\partial \omega}{\partial x_j} \right] + \frac{\sigma_d}{\omega} \max \left(\frac{\partial k}{\partial x_j} \frac{\partial \omega}{\partial x_j}, 0 \right). \tag{2.32}$$

The variation of the coefficients in space is governed by a new blending function f_{mix} that replaces the original blending function F_1. Even though the blending function f_{mix} is defined in a different way than Menter's F_1, the idea is more or less the same. As the F_1 function, $f_{\text{mix}} \to 1$ almost up to the boundary layer edge and is zero in free turbulent flows.

2.1.6. Hybrid RANS-LES models

The moderate cost of unsteady RANS approaches and their decent performance for most flows reflects itself in the popularity of models such as the $k - \omega$ (SST) and $k - \varepsilon$ models and to a smaller extent the more complicated EARSM and general RSM. Despite this success, the interest in accurately resolving smaller turbulent scales occurring in massively separating flows, present in many fluid dynamics applications, has led to a shift towards Large Eddy Simulation (LES) modeling. RANS models fall short when large scale unsteadiness dominates time-averaged solutions and wake turbulence is more important than the turbulence generated from upstream boundary layers [17]. As LES resolves all but the smallest turbulent scales, the computational requirements at high Reynolds numbers are significantly larger than for RANS but still lower than for DNS. This has led to the development of hybrid schemes of which the hybrid RANS-LES,Detached-Eddy Simulation (DES), Delayed Detached-Eddy Simulation (DDES) and IDDES models are the most widely used. Following the classification of Sagaut et al. [17], these models fall in the category of "global hybrid RANS-LES" models[1] and have the following characteristics:

  i) a weak coupling between RANS and LES zone: modeled turbulence is not converted into resolved turbulence,

 ii) a single set of equations is used in the domain,

iii) the RANS-LES interface is continuous and

 iv) eddies can develop rapidly due to the decrease of eddy viscosity away from solid walls, but there is no reconstruction of (resolved) velocity fluctuations at the interface.

The DES and DDES methods are briefly introduced below, followed by a more detailed description of the IDDES model which was chosen for this work as it is the most recent development of this series of hybrid RANS-LES models implemented in REFRESCO.

Detached-eddy simulation (DES)

The aim of the development of the DES model by Spalart [34] in 1997 was to combine the relative affordability of RANS simulations with the accuracy obtainable by LES simulations. Based on the local grid conditions, DES solves the Navier-Stokes equations using RANS or LES length scales to model or resolve part of the flow. A smooth transition is maintained between the regions where the LES and RANS length scales are used. Attached boundary layers are home to the smallest of eddies, which are often prohibitively expensive to solve using LES, so that RANS is used in these regions. Larger (i.e. detached) eddies in the free-stream and separation and wake regions are resolved by the LES model up to the filter size. The RANS model functions as a sort of Subgrid-Scale (SGS) model in the LES region [35]. In between these two regions there is a transition region called "gray area" where both models are active. The physics in this area are unclear as the model transitions to fully modeled turbulence in the attached boundary layer to mostly resolved turbulence in the free stream. This may lead to grid-induced separation, see Section 2.1.6 and is a necessary but unwanted characteristic of global hybrid RANS-LES models [17]. The regions in DES simulations are sketched in Figure 2.1.
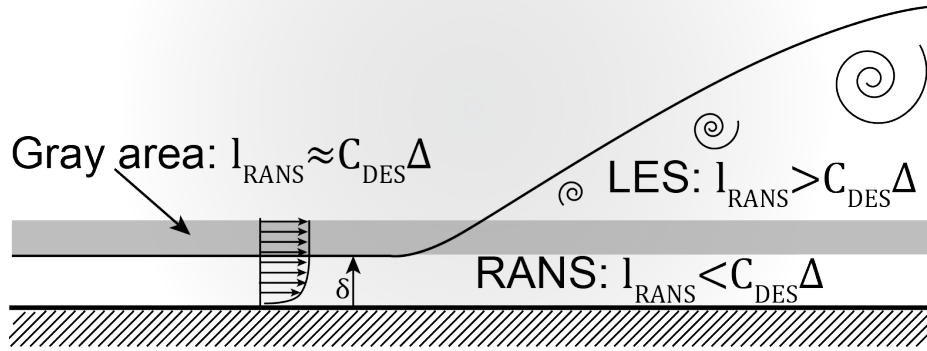
Figure 2.1: Illustration of RANS and LES regions in the DES simulation of a flat plate. Image adapted from [17].

The mathematical definitions of the model as implemented in REFRESCO are adapted from the work by Strelets [36] using the SST model as the background RANS model with corresponding turbulent length length scale $l_{k-\omega}$:

$$l_{k-\omega} = \frac{k^{1/2}}{\beta^* \omega}. \tag{2.33}$$

The length scale is incorporated into the dissipation term $\mathcal{D}_{SST}^k$ of the transport equation for the turbulent kinetic energy k.

$$\mathcal{D}_{SST}^k = \rho \beta^* k \omega = \rho \frac{k^{3/2}}{l_{k-\omega}}. \tag{2.34}$$

DES uses a modified length scale $\tilde{l}$ depending also on the local grid spacing, which is substituted for $l_{k-\omega}$ in Equation (2.34).

$$\tilde{l} = \min\left\{ l_{k-\omega}, \underbrace{C_{DES}\Delta l}_{l_{LES}} \right\}, \tag{2.35}$$

where $\Delta l = \max\{h_x, h_y, h_z\}$ is the grid spacing. The SST model blends between $k - \varepsilon$ and $k - \omega$ formulations using the F_1 function built into the model.

Delayed detached-eddy simulation (DDES)
DDES was introduced eight years after the original formulation to combat the issue of Modeled Stress Depletion (MSD). MSD occurs when the DES model switches to a LES formulation in a region where it is not supposed to (e.g. an attached boundary layer) due to the local value of the DES limiter switching to LES mode. The grid is too coarse to fully resolve the velocity fluctuations in LES mode, but reduces the eddy viscosity nonetheless. This also decreases the modeled Reynolds stress, but, since the grid is too coarse, there is no increase in the resolved Reynolds stress to restore the balance - hence the name of modeled stress depletion [37]. This is prevented in DDES by a shielding function f_d active in attached boundary layers, incorporated in the modified definition of the DES length scale and defined as [38]:

$$l_{DDES} = l_{RANS} - f_d \max(0, \ l_{RANS} - l_{LES}), \tag{2.36}$$
$$f_d = 1 - \tanh\left[(C_{d1} r_d)^{C_{d2}}\right], \tag{2.37}$$

where l_{RANS} in this case is the $k - \omega$ length scale defined above, and r_d is a function used to detect attached shear layers. The corresponding definitions are provided in Appendix A.5.

Improved Delayed Detached-Eddy Simulation (IDDES)
IDDES was developed to solve the problem of Log-Layer Mismatch (LLM) that arose when DES or DDES was applied to higher quality ("LES") grids leading to large errors in the predicted skin friction. IDDES additionally consists of a single set of functions that allow it to resolve attached boundary layers in WMLES mode if velocity fluctuations (i.e. turbulent content)

---

[1]The IDDES model with specified turbulent content operates in Wall-modeled Large Eddy Simulation (WMLES) mode, making it a "zonal hybrid RANS-LES" model according to Sagaut's definition [17], and therefore has the opposite characteristics

is present in the local flow field and if the grid is fine enough [39]. WMLES models were developed to weaken the strong dependency of LES on the Reynolds number for wall-bounded flows. The dependence is weakened by resolving most of the turbulence in boundary layer by LES and only a small region close to the wall in RANS mode. The modeling of all dynamics in the inner layer (i.e. viscous sublayer and log-layer) removes the production of turbulence in this region. The resolved turbulence in the flow is therefore only produced and dissipated in the outer layer (which is solved in LES mode) [40]. The computational effort of WMLES is 10-100 times higher than for DES due to the more stringent resolution requirements in the inner layer to resolve the smaller turbulent structures [38, 40].

Despite significant theoretical differences compared to DES and DDES - elaborated upon in the following paragraphs - there are no large differences in the implementation of IDDES [39]. Since IDDES no longer simply bans the use of LES in boundary regions, but is a more all-encompassing approach which switches between wall-modeled LES and RANS based on the specification of turbulent fluctuations, it is convenient to define the DDES and WMLES branches for IDDES which are briefly discussed subsequently. The formulation discussed below is based on the work presented in [39].

Modified sub-grid length scale

The sub-grid length scale of the LES model was modified from the DDES length scale to maintain a single definition for wall-bounded and free turbulent flows. Its derivation can be found in Appendix A.6. The new length scale is defined as:

$$\Delta l = \min\{\max[C_w d_w, C_w h_{\max}, h_{wn}], h_{\max}\}, \tag{2.38}$$

where h_{wn} is the grid step in wall-normal direction and $C_w = 0.15$ is an empirical constant independent of the specific SGS model.

DDES BRANCH OF IDDES

The DDES branch of IDDES activates if there is no turbulent content specified at the inflow. The DDES definitions are the same as the ones provided in Appendix A.5 according to [39], however there is some debate regarding the differences in results between DDES and IDDES on the same grid. Pereira notes in [10] that the SST IDDES model, contrary to its DDES counterpart, does not fall back into full RANS mode if the grid is too coarse to support an LES. This hypothesis is not backed up by the work of Saini et al. [41], which demonstrated that on coarse meshes the SST-based IDDES successfully identifies the region as too coarse to perform LES calculations, contrary to the Spalart-Allmaras IDDES implementation. The simulations performed by Shur et al. [39] also show that the IDDES model falls back into DDES mode when no turbulent content is specified. However, differences between DDES and IDDES model results were also reported in [5], which indicates that a certain caution should be used when selecting the IDDES model.

WMLES BRANCH OF IDDES

The WMLES branch is activated when an unsteadiness or turbulent content is present at the inflow or existent in the initial conditions, if the grid is fine enough to resolve dominant eddies in the boundary layer. Also for this branch an empirical function is used to blend between RANS and LES length scales to obtain a new length scale $\tilde{l}_{\text{WMLES}}$:

$$\tilde{l}_{\text{WMLES}} = f_{\text{B}}(1 + f_e)\tilde{l}_{\text{RANS}} + (1 - f_{\text{B}})\tilde{l}_{\text{LES}}, \tag{2.39}$$

where $\tilde{l}_{\text{RANS}}$ and $\tilde{l}_{\text{LES}}$ are the RANS and LES length scales. The f_{B} function is responsible for the rapid switching from RANS (where $f_{\text{B}} = 1$) to LES mode (in which case $f_{\text{B}} = 0$) within the wall-distance range $0.5h_{\max} \leq d_w \leq h_{\max}$ so that dynamics of the flow don't linger between both modes:

$$f_{\text{B}} = \min\{2\exp[-9\alpha^2], 1.0\}, \qquad \alpha = 0.25 - \frac{d_w}{h_{\max}}. \tag{2.40}$$

The elevating function f_e is responsible for combating the mismatch in the log-layer. This is done by preventing an excessive reduction of the Reynolds stresses modeled by the RANS model, which was observed to happen in the interfacial region between LES and RANS. In two cases the function should be almost zero:

1. when the grid is fine enough to do a wall-resolved LES (negligible modeled Reynolds stress near the interface)

2. when the final IDDES performs as the base RANS model (the SST model in the present case)

The final function is defined as [38, 39]:

$$f_e = f_{e2} \max\{(f_{e1} - 1),\, 0\}, \tag{2.41}$$

where:

$$f_{e1} = \begin{cases} 2\exp\left[-11.09\alpha^2\right] & \text{for } \alpha \geq 0 \\ 2\exp\left[-9.0\alpha^2\right] & \text{for } \alpha < 0 \end{cases}, \tag{2.42}$$

$$f_{e2} = 1.0 - \max\{f_t, f_l\}, \tag{2.43}$$

$$f_t = \tanh\left[(C_t^2 r_{\mathrm{dt}})^3\right], \tag{2.44}$$

$$f_l = \tanh\left[(C_l^2 r_{\mathrm{dl}})^{10}\right]. \tag{2.45}$$

The quantities r_{dt} and r_{dl} are the turbulent and laminar analogues of r_d (which identifies the wall region), defined by:

$$r_{\mathrm{dt}} = \frac{\nu_t}{\kappa^2 d_w^2 \sqrt{0.5 \cdot (S^2 + \Omega^2)}}, \tag{2.46}$$

$$r_{\mathrm{dl}} = \frac{\nu}{\kappa^2 d_w^2 \sqrt{0.5 \cdot (S^2 + \Omega^2)}}. \tag{2.47}$$

The values of the additional model constants are provided in Appendix A.6 and were obtained from [38].

BLENDING OF DDES AND WMLES BRANCHES

A slight modification needs to be made to the DDES length scale definition to obtain a model which automatically selects between both branches. The new definition becomes [38]:

$$\tilde{l}_{\mathrm{DDES}} = \tilde{f}_d\, l_{\mathrm{RANS}} + (1 - \tilde{f}_d)\, l_{\mathrm{LES}}, \tag{2.48}$$

in which new the shielding functions $\tilde{f}_d$ is defined as [38, 39]:

$$\tilde{f}_d = \max\{(1 - f_{dt}),\, f_{\mathrm{B}}\}, \tag{2.49}$$

$$f_{dt} = 1 - \tanh\left[(C_{dt1} r_{dt})^{C_{dt2}}\right]. \tag{2.50}$$

The final IDDES length scale, combining both DDES and WMLES, is then implemented as:

$$l_{\mathrm{hyb}} = \tilde{f}_d (1 + f_e)\, l_{\mathrm{RANS}} + (1 - \tilde{f}_d)\, l_{\mathrm{LES}}. \tag{2.51}$$

For inflow or initial conditions that include fluctuations, $r_{dt} \approx 0$, $f_{dt} \approx 1$ and $f_d \approx f_b$, so that l_{hyb} reduces to l_{WMLES}. Without turbulence, the elevation function $f_e = 0$ and DDES behavior is theoretically recovered.

Apart from being the most recently developed model, the IDDES model was used for the simulations in this thesis considering its capability of dealing with turbulent inflow conditions and locally switching to WMLES mode. This is considered to be out of the scope of this work, as the method to generate the turbulent information is being extensively tested in REFRESCO by Klapwijk and described in [42]. This could allow for a comparison of the model with and without turbulent inflow conditions on the same mesh and with simmilar numerical settings.

FURTHER CONSIDERATIONS

The main issue of global hybrid RANS-LES models is the presence of a gray area where $C_{\mathrm{DES}}\Delta l$ is of same order as l_{RANS}. In this region, the detached shear layer is supposed to grow free shear eddies, but does not receive information on the small boundary layer eddies as they are suppressed by the RANS model [34]. The flow physics in this area are unclear and possibly unphysical, so that the goal is generally to have the gray area as thin as possible. The channel flow simulations by Saini et al. [41] highlighted the significant size of this gray zone, where both RANS and LES models are active, but turbulent information is not transferred between them. In the same study the gray area seems to be larger for the SST based model than for the Spalart-Allmaras formulation, but no clear cause was identified.

2.2. Wetted vortex dynamics

This section starts of by introducing the physical concept of a vortex and how vortices are generated and collapse. Secondly, the most commonly used vortex models are discussed as they form the basis for interpreting the results for the tangential velocity and pressure distribution inside the vortex core.

2.2.1. Vortex generation

A vortical structure is defined as a circulating flow in a certain plane in a fluid, meaning that the streamlines are closed and contain only fluid. A vortex can also be defined as a concentration of vorticity in a single direction. Vorticity can only be generated as a result of shear forces in the fluid; meaning that the fluid element deforms, but does not rotate [43]. The vortical structure has a strength Γ, called the circulation. The circulation around any closed curve s is invariant with time (Kelvin's theorem) [44]. The contour integral of the velocity $\mathbf{u}$ along a streamline s can be rewritten as the integral of vorticity $\mathbf{\Omega} = \nabla \times \mathbf{u}$ in an area $\mathrm{d}A$ enclosed by that streamline using the Stokes theorem:

$$\Gamma = \oint_s \mathbf{u} \mathrm{d}s = \iint_A \mathbf{\Omega} \mathrm{d}A. \tag{2.52}$$

In wall-bounded flows (no-slip) boundaries will generate vorticity, whereas in free flows a vortex can only be generated as a result of separation. When a vortex is formed, it tends to roll up into an approximately cylindrical shape [43]. An example of the roll-up mechanic is given in Figure 2.2a. The 'coherent structures' often discussed in literature are based on the definition of vortex tubes, which are the surfaces consisting of all vortex lines passing through the surface bounded by s. Vortex lines are defined as lines that are tangent to the vorticity vector. By the Helmholtz theorem, vortex lines and tubes are considered material lines and surfaces respectively, meaning that they consist of the same material elements and move with the fluid flow [45]. Also according to the Helmholtz theorem, the ratio of vorticity Ω and length of a vortex tube δl is constant; i.e. as a vortex is stretched, its cross-sectional area δs decreases and the vorticity per cross-section increases accordingly [44]. This can be interpreted as a faster rotating vortex tube, visualized in Figure 2.2b where $\Omega_2 > \Omega_1$. The independence of the circulation on the cross-section of a vortex tube implies that the circulation Γ is constant and that a vortex tube never ends inside the fluid [44].

(a) Vortex roll-up behind a wing. Image adapted from [43].   (b) Vortex stretching of an ideal vortex.
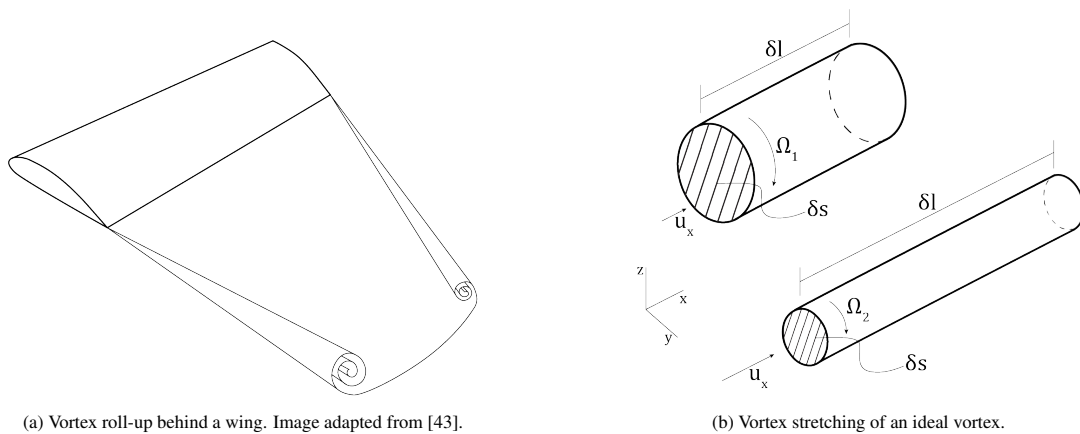
Figure 2.2: Illustration of Vortex roll-up and vortex stretching.

The above theorems are derived assuming inviscid flow (around the vortex contour), barotropic flow (i.e. density is only a function of local pressure) and that conservative body forces (like gravity) act through the center of mass of each particle (i.e. don't rotate the particle). The first assumption is violated in the presence of viscous effects along the path of the contour, which can occur due to viscosity in boundary layers and more importantly turbulence. These viscous effects lead to the diffusion of vorticity outward from the vortex core and subsequently reduce the circulation Γ [45].

A vortex is characterized by two zones: a vortex core with constant vorticity and dominant viscous effects and an outer region which is mainly irrotational and where the fluid can be assumed to be inviscid [44]. This does not mean that there are no viscous stresses in the fluid, but rather that the net viscous force on each fluid particle is zero [45]. The irrotational outer flow follows from the assumption that all the vorticity is fully contained inside the vortex core. The vortex core consists of a viscous core which rotates like a solid body, surrounded by a thin layer where viscosity leads to viscous dissipation of the vorticity outwards from the viscous core.

2.2.2. Vortex breakdown

A vortex breakdown phenomenon is defined in [46] as an abrupt structural change, occurring for swirling flows along the swirl axis. In that context, vortex breakdown implies the formation of a free stagnation point or a recirculation zone on this axis for flows with a significant vorticity in streamwise direction. A first breakdown method consists of the formation of an almost axisymmetric bubble-like structure and is called axisymmetric breakdown. Another way in which vortices break down is characterized by the spiraling of the vortex without a growth in core size [47]. This mode is called the spiral mode, and can lead to the formation of a double helix depending on the swirl number [48]. The spiral mode is more frequently observed for delta wings at high angles of attack and the axisymmetric breakdown appears in an axisymmetric swirling flow [49].
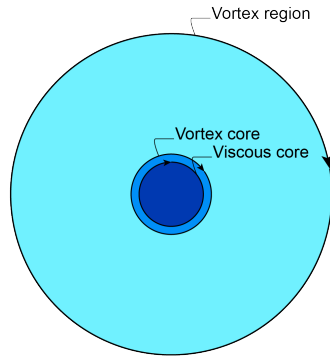
Figure 2.3: Sketch of the different regions of a wetted vortex.

2.2.3. Analytical vortex models

An ideal vortex following the Kelvin and Helmholtz theorems is represented as two-dimensional, even though the vortex roll-up clearly demonstrates its three-dimensional nature. For most practical flow cases, the two-dimensional vortex is a good assumption and can be extended into the third dimension invoking self-similarity. To simplify matters further, the vortex is often also assumed to be axisymmetric. For a tip vortex originating from a wing, this approximation was validated i.a. by Fruman et al. [50], albeit only after a certain distance (two chord lengths) behind the wing in his case.

It was also shown that the pressure is proportional to the square of the ratio between the maximum of tangential velocity and free-stream velocity, no matter the shape of $u_\theta(r)$ [50]:

$$C_p(x) = -2 \int_0^\infty \frac{u_\theta^2(x,r)}{u_\infty^2} \frac{\mathrm{d}r}{r} \approx -k \left[\frac{u_{\theta,\max}}{u_\infty} \right]^2, \tag{2.53}$$

where C_p is the pressure coefficient, u_θ is the free stream velocity, $u_{\theta,\max}$ is the maximal tangential velocity and k is a proportionality constant depending on the shape of the tangential velocity profile.

This section first discusses two frequently used two-dimensional base models called the Rankine and Lamb-Oseen vortex models. The Rankine vortex is discussed first since it is based on the ideal case of an inviscid vortex. Second, the Lamb-Oseen vortex model is discussed as it was shown to fit the experimentally measured flow field [8] that was used for the validation of the numerical data presented in this thesis. Previous studies of a cavitating line vortex in a Venturi by Janssen [6] and de Montgolfier [7] also applied the Lamb-Oseen vortex as an inflow condition.

Rankine vortex

The definition of an ideal Rankine vortex, is a vortex where all the vorticity is assumed to be concentrated in an infinitely small circle in a plane perpendicular to the vortex. The strength of the vortex is defined by the circulation Γ and is maintained as the radius of the core becomes infinitesimally small. This leads to a singular situation with infinite velocity at $r = 0$. The resulting velocity field is called the Rankine vortex, and the flow field around it is only determined by Γ:

$$u_\theta(r) = \frac{\Gamma}{2\pi r}. \tag{2.54}$$

The axial velocity gradient in radial direction $\partial u_x/\partial r$ is relatively moderate away from the center, so that viscosity can be neglected. Additionally there is assumed to be no vorticity in the outer flow of a vortex (i.e. potential flow). The outer flow field can then be described by adding and distributing several Rankine vortices. It is obvious that this representation is not realistic due to the singularity at the vortex axis. In reality, the tangential velocity at the center needs to be 0 to satisfy the symmetry condition. The strength of the vortex is measured by the circulation at the vortex core radius, where the velocity gradient in radial direction becomes very large. The strong velocity gradients increase the importance of viscosity, which reduces the tangential velocities. A certain vorticity distribution is created, reaching its maximum value at the vortex axis. The circulation Γ decreases inward from the vortex core radius due to the vorticity, governed by the decreasing area in Equation (2.52) and leads to a deviation from the ideal Rankine distribution (Equation (2.54)). The tangential velocity is subsequently zero at the vortex center and the maximum tangential velocity is reached at $r = \sqrt{\alpha}\sqrt{4\nu t}$. This is the viscous core radius r_v, which is used as definition of the core radius since it can be determined directly from the velocity field. If it is assumed that all vorticity is contained within this radius, the viscous core radius and the vortex core radius coincide. The vorticity and tangential velocity then follow a linear distribution and the core rotates like a solid body.

Assuming a solid body rotation of the viscous core and no vorticity outside the viscous core, the velocity distribution for a

(non-ideal) Rankine vortex is given by:

$$u_\theta(r) = \begin{cases} \dfrac{\Gamma r}{2\pi r_v^2} & \text{for } 0 \leq r < r_v, \\[2mm] \dfrac{\Gamma}{2\pi r} & \text{for } r_v \leq r < R. \end{cases} \quad (2.55)$$
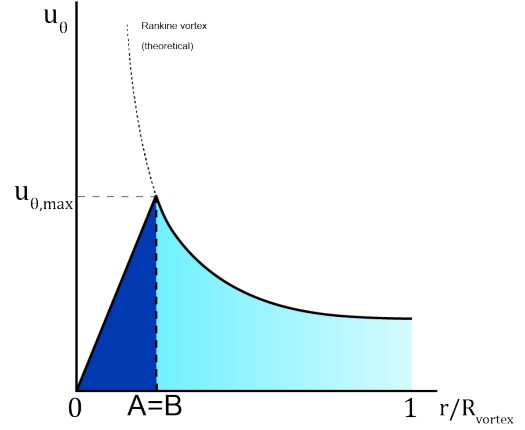
Figure 2.4: Tangential velocity distribution of the Rankine vortex.

The pressure is lower in a vortex than in the surrounding fluid due to centrifugal effects, where for a Rankine vortex:

$$\frac{\partial p}{\partial r} = \rho \frac{u_\theta^2(r)}{r},$$
$$p_\infty - p(r_v) = \rho \frac{\Gamma^2}{4\pi^2 r_v^2}. \quad (2.56)$$

The pressure drop inside the core is independent of the viscous core radius (r_v) and defined as:

$$p_{\min} - p(r_v) = \rho \frac{\Gamma^2}{4\pi}. \quad (2.57)$$

The minimum pressure is then given by:

$$p_\infty - p_{\min} = \rho \frac{\Gamma^2}{4\pi^2 r_v^2}. \quad (2.58)$$

Lamb-Oseen vortex

A more realistic velocity distribution can be found when using the Lamb-Oseen vortex, which is an exact solution of the laminar Navier-Stokes equations and is based on the (singular) Rankine vortex. The velocity gradients are very large in the viscous core and viscosity will create an outward dissipation of vorticity. The velocity has an asymptotic behavior in radial direction and approximately follows the Rankine distribution outside of the vortex core radius $r_v(t) = 2\sqrt{vt}$. This implies that potential flow is assumed outside the vortex core. The maximum tangential velocity $u_{\theta,\max}$ is reached at the radius $r_{\max} = \sqrt{\alpha} r_v(t)$, where $\alpha = 1.25643$ [51]. The tangential velocity distribution for the Lamb-Oseen vortex at a time t is given by:

$$u_\theta(r) = \frac{\Gamma}{2\pi r} \left[1 - e^{-r^2/r_v^2} \right]. \quad (2.59)$$
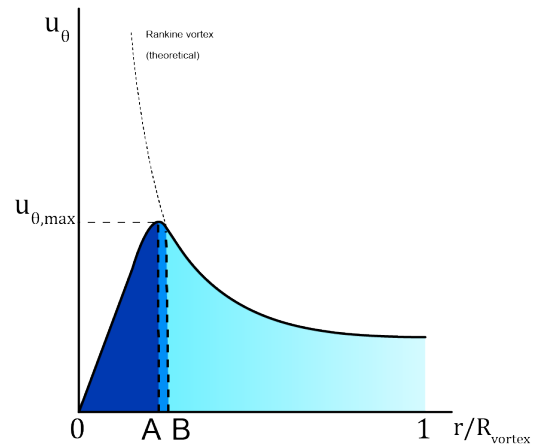
Figure 2.5: Tangential velocity distribution of the Lamb-Oseen vortex.

The minimum pressure for the Lamb-Oseen vortex is given by:

$$p_\infty - p_{\min} = \rho \frac{\Gamma^2}{4\pi^2} \frac{\ln(2)}{4vt}. \quad (2.60)$$

This means that there is only a difference of factor ln(2) between the Rankine and Lamb-Oseen vortex models in the minimum pressure for equal max. velocities $u_{\theta,\max}$, as visualized in Figure 2.6b.

(a) Velocity distribution   (b) Pressure distribution
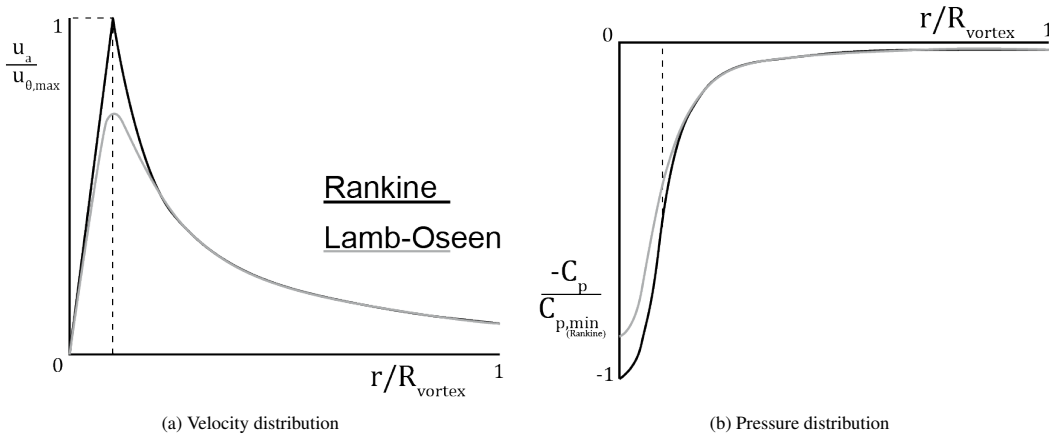
Figure 2.6: Comparison of tangential and pressure profiles of Rankine and Lamb-Oseen vortex definitions.

2.2.4. Vortex detection

There are various methods to visualize vortices present in a flow. The first method is based on intuition and is based around using regions of low pressure for vortex detection. As proposed by Robinson et al. [52], low pressure regions in incompressible turbulent flows almost always indicate vortex cores. When two vortices merge, the isobaric surfaces become indistinctive, however, and the criterion can no longer be used to identify individual vortices [53]. A second possibility is to detect vortices based on the analysis of the velocity gradient tensor $\mathbf{D} = \nabla \mathbf{u}$. The velocity gradient tensor $\mathbf{D}$ is defined as :

$$D_{ij} = \frac{\partial u_i}{\partial x_j}, \tag{2.61}$$

which is a second-order tensor, allowing it to be decomposed into a symmetric and skew-symmetric part; respectively the strain-rate S_{ij} and vorticity Ω_{ij} tensors:

$$D_{ij} = S_{ij} + \Omega_{ij}, \tag{2.62}$$

$$\text{where } S_{ij} = \frac{1}{2}\left(\frac{\partial u_i}{\partial x_j} + \frac{\partial u_j}{\partial x_i}\right), \tag{2.63}$$

$$\text{and } \Omega_{ij} = \frac{1}{2}\left(\frac{\partial u_i}{\partial x_j} - \frac{\partial u_j}{\partial x_i}\right). \tag{2.64}$$

The characteristic equation for $\nabla \mathbf{u}$ is given by:

$$\lambda^3 + P\lambda^2 + Q\lambda + R = 0, \tag{2.65}$$

where P, Q and R are the three invariants of the velocity gradient tensor and λ its eigenvalues. From decomposing these invariants into their symmetric and skew-symmetric parts follows that [54]:

$$P = -\text{tr}(D_{ij}), \tag{2.66}$$

$$Q = \frac{1}{2}\left(\text{tr}(D_{ij})^2 - \text{tr}(D_{ij}^2)\right) = \frac{1}{2}\left(||\Omega_{ij}||^2 - ||S_{ij}||^2\right), \tag{2.67}$$

$$R = -\det(D_{ij}). \tag{2.68}$$

This forms the basis for the common different vortex detection methods (Q, λ_2 and Δ), of which the Q-criterion was chosen as it is easily obtained using REFRESCO.

Q-criterion

This method was developed by Hunt, 1988 (as cited in [53]). When using the Q-criterion, the vortex is defined as the spatial region in which the second invariant $Q > 0$, see Equation (2.67). In other words, the vortex is defined as the connected region where the magnitude of vorticity is greater than the strain-rate [54]. The Q-criterion is also widely used in similar research for visualization of the vortex.

Due to the simplicity of the single vortex in this research, the Q-criterion is expected to be sufficient for visualization purposes of the vortex. The size of the vortex core can be easily identified by determining the location at which the highest tangential velocity is attained. The Q-criterion is also widely used in literature to identify the vortex, where the value of Q is often chosen by the authors based on the size of the turbulent structures to be identified.

2.3. Cavitation

Cavitation is generally defined as the phenomenon where a phase change takes place from liquid to vapor due to a decrease in pressure instead of an increase in temperature (which would be boiling). Even though water is often assumed to be incompressible, the water molecules can be torn apart (i.e. the molecular distance increases without breaking the hydrogen bonds) to create vapor cavities. This rupture occurs when the tension exerted on the liquid exceeds the tensile strength of the liquid. The tension is defined by the difference between the local pressure p and the vapor pressure p_{vap}: $(p_{vap} - p)$. The tensile strength is defined as

$$\Delta p = \frac{2T_\omega}{R_{crit}},\tag{2.69}$$

where T_ω is the surface tension and R_{crit} is a critical bubble radius, comparable to the intermolecular distance. Both parameters are temperature dependent [55]. Early experiments by Briggs [56] pointed out that although the tensile strength of water is generally high, it can quickly drop by an order of magnitude and the purity of the water has an important impact. Cavitation generally initiates at a so called cavitation nucleus, which may be a gas bubble, solid particle or surface imperfection [15]. Water which has not been filtered or degassed contains plenty of cavitation nuclei, which considerably lowers the tensile strength of the water and leads to cavitation close to the vapor pressure [57].

Cavitation occurs in two phases: i) cavitation inception, which is the limiting regime between non-cavitating and cavitating flow and ii) developed cavitation, which implies a certain permanency and extent of the cavitating flow. Additionally, cavitation inception and collapse happens on a small timescale; the duration of the final stage of bubble/ cavitating vortex collapse is in the order of 1×10^{-6} second [44]. The pressure coefficient C_p and the cavitation number σ are useful dimensionless quantities to quantitatively assess cavitation phenomena:

$$C_p = \frac{p}{1/2\rho_l u_\infty^2},\tag{2.70}$$

$$\sigma = \frac{p_\infty - p_{vap}}{1/2\rho_l u_\infty^2},\tag{2.71}$$

where ρ_l is the liquid density, u_∞ and p_∞ are the reference (free stream) flow velocity and pressure respectively. Vaporization and condensation are two terms that are used throughout literature and in the remainder of this work to denote the phase change from liquid to vapor and vapor to liquid respectively. The inception of cavitation may be difficult to define as the relationship between the vapor pressure is altered by i.a. the surface tension delaying bubble growth, the time required for nuclei to become observable and turbulent fluctuations of the pressure [58]. It is nonetheless commonly accepted to postulate that cavitation will occur when reaching the vapor pressure in numerical simulations, as the cavitation models only depend on the difference between the local and the vapor pressure to determine the source term that determines the creation/ destruction of vapor.

In the next section, the theoretical description of the physical process governing bubble growth and collapse is introduced. This is followed by the description of the Schnerr-Sauer model which was chosen for the cavitating vortex simulations.

2.3.1. Bubble growth and collapse dynamics

Unless stated otherwise, this section was based on the work by Brennen [58]. Figure 2.7 provides an illustration of a bubble, indicating the different terms used in the equations.

Bubble growth is governed by the Rayleigh-Plesset equation:

$$\frac{p_B(t) - p_\infty(t)}{\rho_l} = R\frac{d^2R}{dt^2} + \frac{3}{2}\left(\frac{dR}{dt}\right)^2 + \frac{4\nu_l}{R}\frac{dR}{dt} + \frac{2T_\omega}{\rho_l R},\tag{2.72}$$

whereby the pressure inside the bubble is defined as

$$p_B(t) = p_{vap}(T_B)p_{G0}\left(\frac{T_B}{T_\infty}\right)\left(\frac{R_0}{R}\right)^3,\tag{2.73}$$

with p_{G0} the initial pressure at (t_∞, R_0), T_∞ the reference temperature, R_0 the initial bubble size and T_ω the surface tension. The expression for p_B can now be substituted in the generalized Rayleigh-Plesset equation Equation (2.72) to account for the
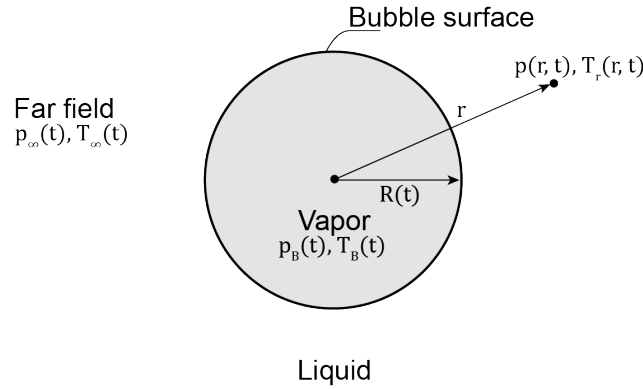
Figure 2.7: Image of a bubble indicating variables used in the Rayleigh-Plesset equation. Image was adapted from [58].

bubble contents:

$$\underbrace{\frac{p_{\text{vap}}(T_\infty) - p_\infty(t)}{\rho_l}}_{\text{driving term}} + \underbrace{\frac{p_{\text{vap}}(T_B) - p_{\text{vap}}(T_\infty)}{\rho_l}}_{\text{thermal term}} + \frac{p_{G0}}{\rho_l}\left(\frac{T_B}{T_\infty}\right)\left(\frac{R_0}{R}\right)^3 \tag{2.74}$$

$$= R\frac{\mathrm{d}^2 R}{\mathrm{d}t^2} + \frac{3}{2}\left(\frac{\mathrm{d}R}{\mathrm{d}t}\right)^2 + \frac{4\nu_l}{R}\frac{\mathrm{d}R}{\mathrm{d}t} + \frac{2T_\omega}{\rho_l R}.$$

The first term of this equation represents the instantaneous surface tension determined by the far-field conditions. The second term is the thermal term, which has a significant influence on bubble dynamics. If one assumes inertially controlled growth, thermal effects do not influence bubble growth and the temperature is constant and uniform, so that the thermal term drops out of the Rayleigh-Plesset equation:

$$\frac{p_{\text{vap}}(T_B) - p_{\text{vap}}(T_\infty)}{\rho_L} = 0. \tag{2.75}$$

Neglecting the effects of temperature is quite practical in describing the bubble growth process, but misleading for the dynamics of bubble collapse. During collapse, various (inertial) assumptions are violated; thermal effects are important, the liquid does not behave as incompressible at high velocities and pressures and spherical symmetry is lost during collapse. Nevertheless, compressible and thermal effects are neglected for most practical fluid dynamics computations as the added complexity requires substantial computational effort which might not always be necessary.

2.3.2. Numerical modeling

The large amount of processes in different industries (hydraulics in particular) that are plagued by cavitation, has led to the development of a variety of different models. Cavitation entails the existence of two-phases in the flow and the transition between these phases. The interface between the vapor and liquid phase constitutes a jump in density from pure liquid to pure vapor. Numerical treatments were developed to smoothen the density distribution at this interface. The first method is to track the interface of every vapor bubble, which for the large amount of cavitation nuclei is too expensive [59]. The second way captures the interface between both phases, by determining the relative volume of a cell that is filled by either liquid of vapor. The dynamics of bubble growth and collapse are then modeled by a mass transport equation between the species. The interface is therefore relatively coarse, but low storage requirements are a great benefit of this method [60]. The Volume-of-Fluid (VOF) method, developed by Hirt & Nichols [60], is a common interface-capturing model and is also used in REFRESCO. Cavitation models which use the VOF method to capture the bubble interface generally also assume the fluid to be a homogeneous mixture of dispersed vapor bubbles. The phases in this mixture are assumed to be in kinematic, mechanical and thermal equilibrium so that phases locally have the same velocity, pressure and temperature. This type of cavitation models, called 'mixture models', can be subdivided based on the origin of their mathematical description of the phase transition and accompanying mass transport. They either stem from the (simplified) Rayleigh-Plesset equation (bubble dynamics models), or they solve a continuum formulation for the transport of the vapor phase (vaporization-condensation models). Assuming an homogeneous mixture for practical cavitation problems is generally accepted due to the lack of reliable physical models that would model the mass transfer in a two-fluid formulation. The simplification of assuming no slip between vapor and liquid phases is warranted for most cases, since the low-pressure regions normally coincide with regions of high velocity in which the slip is in fact rather small [61]. The following derivation is adapted from the work by Schnerr & Sauer [59].

The introduction of a second phase requires solving an additional transport equation for the vapor volume fraction of a

cell α_{vap}:

$$\frac{\mathrm{D}\alpha_{\mathrm{vap}}}{\mathrm{D}t} = \frac{\partial \alpha_{\mathrm{vap}}}{\partial t} + \frac{\partial \alpha_{\mathrm{vap}} u_i}{\partial x_i} = 0. \tag{2.76}$$

The continuity equation in derivative form is given below, where for incompressible flow without phase transition the right-hand side becomes zero;

$$\frac{\partial u_i}{\partial x_i} = -\frac{1}{\rho}\frac{\mathrm{d}\rho}{\mathrm{d}t}. \tag{2.77}$$

When assuming that the fluid is actually a mixture, the mixture density ρ and the mixture viscosity μ are defined as follows:

$$\rho = \alpha_{\mathrm{vap}}\rho_{\mathrm{vap}} + (1 - \alpha_{\mathrm{vap}})\rho_l, \tag{2.78}$$

$$\mu = \alpha_{\mathrm{vap}}\mu_{\mathrm{vap}} + (1 - \alpha_{\mathrm{vap}})\mu_l. \tag{2.79}$$

Using these definitions, the derivative of the mixture density $\mathrm{d}\rho/\mathrm{d}t$ becomes:

$$\frac{1}{\rho}\frac{\mathrm{d}\rho}{\mathrm{d}t} = \frac{1}{\alpha_{\mathrm{vap}}\rho_{\mathrm{vap}} + (1 - \alpha_{\mathrm{vap}})\rho_l} \frac{\mathrm{d}\big(\alpha_{\mathrm{vap}}(\rho_{\mathrm{vap}} - \rho_l)\big)}{\mathrm{d}t}. \tag{2.80}$$

The velocity field is no longer divergence free, i.e.:

$$\frac{\partial u_i}{\partial x_i} = -\frac{\rho_{\mathrm{vap}} - \rho_l}{\alpha_{\mathrm{vap}}\rho_{\mathrm{vap}} + (1 - \alpha_{\mathrm{vap}})\rho_l} \frac{\mathrm{d}\alpha_{\mathrm{vap}}}{\mathrm{d}t}, \tag{2.81}$$

and a source term S_{vap} has to be added to the vapor transport equation Equation (2.76):

$$\frac{\partial \alpha_{\mathrm{vap}}}{\partial t} + \frac{\partial \alpha_{\mathrm{vap}} u_i}{\partial x_i} = \frac{S_{\mathrm{vap}}}{\rho_{\mathrm{vap}}}. \tag{2.82}$$

Assuming that $\rho_l \gg \rho_{\mathrm{vap}}$ The continuity equation for the mixture can then be written as:

$$\frac{\partial u_i}{\partial x_i} = \left(\frac{1}{\rho_{\mathrm{vap}}} - \frac{1}{\rho_l}\right) S_{\mathrm{vap}}. \tag{2.83}$$

The source term is also incorporated into the conservation equation of linear momentum as an additional force. The force slows down the flow during evaporation ($S_{\mathrm{vap}}/\rho_{\mathrm{vap}} > 0$) and accelerates it during condensation ($S/\rho_{\mathrm{vap}} < 0$):

$$\frac{\mathrm{D}\rho u_i}{\mathrm{D}t} = f_i - \rho u_i\left(\frac{\partial u_i}{\partial x_i}\right) = f_i - \rho u_i\left(\frac{S_{\mathrm{vap}}}{\rho_{\mathrm{vap}}}\right), \tag{2.84}$$

for the ith component of the velocity vector $\mathbf{u}$ and where pressure and viscous forces are contained in the f_i term. An equivalent notation sometimes used in literature splits the source term into a positive (vapor production) and negative (vapor destruction) mass transfer rate, $\dot{m}^+$ and $\dot{m}^-$ respectively:

$$\frac{\partial \alpha_{\mathrm{vap}}}{\partial t} + \frac{\partial \alpha_{\mathrm{vap}} u_i}{\partial x_i} = \frac{1}{\rho}\left(\dot{m}^+ + \dot{m}^-\right). \tag{2.85}$$

Bubble dynamics models: The Schnerr-Sauer model

The first class of models is based on the description of bubble dynamics by the Rayleigh-Plesset equation. A simplified form of this equation is used, neglecting the second-order time derivative of the bubble radius and the effect of non-condensible gases. Empirical constants are then used to make up for this simplification, but require tuning for different types of simulations [62]. In bubble dynamics models, every vapor bubble originates from a cavitation nucleus. The increase of the vapor volume fraction due the growth of the nuclei is compensated by loss of vapor fraction due to bubbles that are displaced out of a cell [59]. The Schnerr-Sauer model was chosen for the cavitating flow simulations in this thesis, since it is the most commonly used model for cavitating simulations in REFRESCO. Other types of bubble dynamics models exist, most notably the Singhal and Zwart models.

The Schnerr-Sauer Model, introduced in 2001 by Schnerr and Sauer [59], assumes that bubble-bubble interactions and the coalescence (merging) of bubbles can be neglected. Bubbles are also assumed to remain spherical throughout their growth and collapse process. The bubble growth process is governed by the simplified Rayleigh-Plesset equation:

$$\frac{p_{\mathrm{vap}} - p}{\rho_L} - \frac{4\nu_L}{R}\frac{\mathrm{d}R}{\mathrm{d}t} - \frac{2T_\omega}{\rho_L R} = R\frac{\mathrm{d}^2 R}{\mathrm{d}t^2} + \frac{3}{2}\left(\frac{\mathrm{d}R}{\mathrm{d}t}\right)^2. \tag{2.86}$$

Inertially controlled bubble growth is assumed, so that bubble growth is modeled by the Rayleigh relation:

$$\frac{DR}{Dt} = \sqrt{\frac{2}{3}\frac{p_{vap}-p}{\rho_l}}. \tag{2.87}$$

The increase of the vapor fraction inside a cell now depends on the amount of bubbles in each cell and how the volume of a single bubble changes, as well as on the convection of bubbles downstream. The vapor fraction α_{vap} can be expressed as a function of the initial amount of nuclei n_0:

$$\alpha_{vap} = \frac{V_c}{V_{cell}} = \frac{N_{bubbles} \cdot 4/3\pi R^3}{V_{vap} + V_l} = \frac{n_0 V_l 4/3\pi R^3}{n_0 V_l 4/3\pi R^3 + V_l} = \frac{n_0 \cdot 4/3}{1 + n_0 \cdot 4/3\pi R^3}, \tag{2.88}$$

so that:

$$\frac{4}{3}R^3 n_0 = \frac{\alpha_{vap}}{1-\alpha_{vap}}. \tag{2.89}$$

The number of nuclei $N_{bubbles}$ is explicitly linked to the volume of water in a cell V_l, allowing the number of bubbles to be conserved. This is visualized in Figure 2.8.
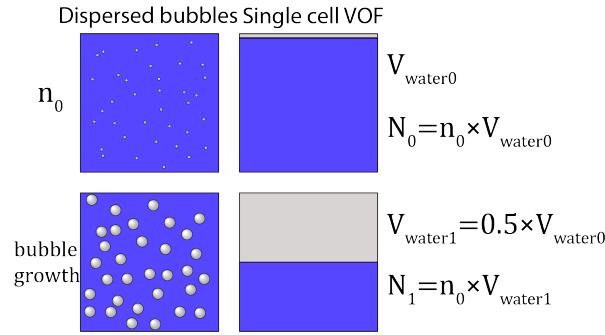
Figure 2.8: Relation between the size and amount of dispersed bubbles and the vapor fraction in the VOF method. Image was adapted from [59].

Combining the expressions in Equation (2.81) and Equation (2.88), defines the source term S_{vap}/ρ_{vap} as:

$$\frac{S_{vap}}{\rho} = \left(\frac{n_0}{1 + n_0 \cdot 4/3\pi R^3}\right)\frac{d}{dt}\left(\frac{4}{3}\pi R^3\right). \tag{2.90}$$

This equation can be rewritten using the relation in Equation (2.89) into the formulations used in REFRESCO for evaporation and condensation respectively: Equations (2.91) and (2.92).

$$\dot{m}^+ = 3\left(\frac{4}{3}\pi R^3 n_0\right)\frac{1-\alpha_{vap}}{R}\frac{DR}{Dt}, \tag{2.91}$$

$$\dot{m}^- = 3\frac{\alpha_{vap}}{R}\frac{DR}{Dt}. \tag{2.92}$$

The bubble radius R is defined in REFRESCO as [63]:

$$R = \min\left\{\max\left[3\times10^{-5}, \left(\frac{3\alpha_{vap}}{4\pi n_0(1-\alpha_{vap})}\right)^{1/3}\right], 10^{-2}\right\}. \tag{2.93}$$

The initial amount of nuclei n_0, the bubble size limits 3×10^{-5} and 1×10^{-2} can be set by the user. The initial amount of nuclei was set to $n_0 = 10^9$ as this improved stability. The limiters were left at the default values for the simulations presented in this thesis.

Considerations regarding compressibility

The $\mathcal{O}(10^4)$ difference in density of vapor and liquid leads to large variations in the local mixture density. The local Mach number $Ma = u/c$ also varies greatly due to the much lower speed of sound in mixtures of air and water than in air [58, 64]. Compressible effects become important when $Ma > 0.3$ [45], which can be attained within cavitating flow cases due to the lower speed of sound in mixtures. REFRESCO is an incompressible solver and compressible simulations therefore lie outside the scope of this work. That does not take away that it is useful to mention ways to deal with compressible effects in incompressible flows and determine the actual necessity of applying compressibility corrections in similar flow cases.

As mentioned in the previous paragraph, compressible effects are present in the mixture of vapor and liquid that is cavitation. The question is whether it is necessary to incur additional computational cost by running the simulations using a compressible solver instead of an incompressible one. Studies by Coutier-Delgosha et al. [65] showed that the unsteady dynamics of the cavity are better captured using a compressible approach. They incorporated the turbulent Mach number into the β and β^* parameters in the k and ω transport equation respectively for the $k - \omega$ model. These modifications (called the *Sarkar-Zeman-Wilcox compressibility corrections*) were proposed by Wilcox in [20] and aimed to correct the deficiency of the k-equation in correctly predicting the compressible mixing layer. The mixing layer grows as the Mach number increases, which is not likely the result of a change in density across the layer.

Based on the comparison between incompressible and compressible solution methods by Goncalvés da Silva et al. [66] and the lack of similar studies for vortex cavitation, this seems to be more of an issue for sheet cavitation and the prediction of the re-entrant jet formation than for vortex cavitation. Regardless of the limitations of assuming incompressibility, it is still a commonplace decision to use incompressible solvers, due to their relative computational simplicity, for the re-entrant jet prediction e.g. [67–69] with reasonable results.

Influence of eddy viscosity on cavity dynamics

The introduction of a second phase with a density that differs considerably from the primary (liquid) phase has an effect on the turbulent eddies inside the flow. The effect of compressibility on turbulence was assessed in a series of computations in [65]. The main takeaway from this work is that, for RANS models relying on the Boussinesq hypothesis, eddy viscosity is generally too high in the two-phase flow area. This is not an issue for Scale-Resolving Simulation (SRS) methods. This excessive value of the eddy viscosity can be countered by modifying the turbulence models. The modification is based around the incorporation of compressibility effects due to the considerably lower speed of sound in a liquid-vapor mixture. The disproportionate amount of eddy viscosity was shown to lead to entirely different flow patterns by Egorov, 2004 (as cited in [28]) with and without inclusion of a turbulence damping term.

The application of a dilatation correction (i.e. the Sakar model), solved the problem of non-shedding sheet cavitation in [65]. Another correction, which appears more frequently in literature, is the Reboud correction, first brought forward in [70] and implemented in [65]. This correction was developed (like the Sakar model) to reproduce sheet cavity shedding that was not reproduced without corrections [28, 70]. Again, the focus was on the shedding of sheet cavities, where excessive eddy viscosity prevented the formation of a re-entrant jet [70]. Apart from the too high eddy viscosity, Coutier-Delgosha, Fortes-Patella & Reboud [71] noticed that the self-oscillatory behavior of the cavity (see Section 2.4.1) could not be recovered without modifying the incompressible RNG $k - \varepsilon$ model. The modification outlined below, which is the form implemented in REFRESCO [72], therefore increases the damping of v_t:

$$v_{t,\text{cav}} = v_t \left[\frac{\rho_{\text{vap}} + (1 - \alpha_{\text{vap}})^n (\rho_l - \rho_{\text{vap}})}{\rho_{\text{vap}} + (1 - \alpha_{\text{vap}})(\rho_l - \rho_{\text{vap}})} \right], \tag{2.94}$$

where the exponent $n \approx 10$.

The concluding remarks by Schot in [28] highlight the significant smearing of the cavity interface by using the VOF method. This might have a much larger impact than an ad hoc reduction of the eddy viscosity by any of the commonly used corrections. Since no additional cost has to be paid to incorporate the Reboud correction, and recognizing the importance of the self-oscillatory behavior of the cavity as discussed in [65], the Reboud correction was applied to the EARSM simulations.

2.4. Dynamics of cavitating vortices

This section builds on the vortex dynamics discussed in Section 2.2 and starts off by introducing the concept of cavitating vortices and their sensitivity to the surrounding flow. This is followed by a short summary of the work by Bosschers [14] and Pennings et al. [13] regarding spectral analysis of cavitating vortex dynamics. The methodology described in this section is applied to the cavitating flow simulations in this thesis.

2.4.1. Cavitating vortices

Unless stated otherwise, the following section is based on the work of Franc & Michel [44]. Vortex cavitation is the latest form of cavitation to be studied, in particular by Genoux & Chahine in 1983 [73], and by Ligneul in 1989 [74]. The cavitation number at inception σ_i for tip vortex flows can be calculated using two estimators: the circulation Γ around the vortex and the size of the viscous core. Cavitation inception strongly modifies the flow geometry close to the vortex axis. The change of vortex diameter due to cavitation is governed by [44]:

$$\frac{d_l}{d_c} = \sqrt{\frac{\rho_{\text{vap}}}{\rho_l}}, \tag{2.95}$$

with d_l the diameter of the cylindrical volume of liquid before phase change, d_c the cylindrical vapor core diameter and ρ_l and ρ_{vap} respectively the liquid and vapor density. The evolution of a cavitating vortex depends on the external pressure and the induced pressure drop due to the velocity and gradients inside the vortex core. A sketch of the different parts of a cavitating Lamb-Oseen vortex, including the radial distribution of tangential velocity is provided in Figure 2.9. The tangential velocity inside the vapor core increases linearly towards the edge of the vapor core as the vapor rotates as a solid body. The Lamb-Oseen profile describes the tangential velocity outside of the vapor core. Bosschers [2] derived an analytical expression for the tangential velocity profile of a cavitating Lamb-Oseen vortex, using that the viscous core size $r_v(t) = \sqrt{4\nu\alpha_R t}$:

$$u_\theta(r) = \frac{\Gamma}{2\pi r}\left[1 - \beta_R \exp\left(-\alpha_R \frac{r^2}{r_v^2}\right)\right]. \tag{2.96}$$

The β_R parameter is given by

$$\beta_R = \frac{r_v^2}{r_v^2 + \alpha_R r_c^2} \exp\left(\alpha_R \frac{r_c^2}{r_v^2}\right), \tag{2.97}$$

where r_c is the cavitating core radius. This profile can be used to compare the obtained solutions in the cavitating vortex simulations to the theory. When the vortex core fills with vapor, the size of the vortex becomes dependent on the pressure field.
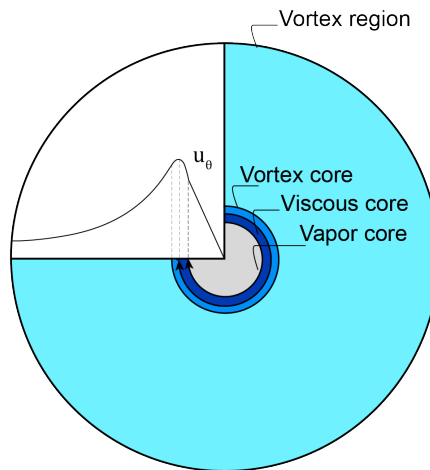
Figure 2.9: Structure of and tangential velocity profile inside a cavitating Lamb-Oseen vortex.

This dependency breaks the link between the elongation rate δl of a rotating filament and its vorticity: $\Omega/\delta l \neq textconst$. For a constant ambient pressure, vortex stretching will increase the rotation rate and the vapor core radius. For constant vortex length, the increase of ambient pressure leads to two opposing effects. The increasing ambient pressure will reduce the size of the vapor core and therefore the vortex core size. At the same time it increases the rate of rotation which increases the centrifugal force and subsequently enlarges the vapor core. This antagonistic behavior can lead to oscillatory cavity behavior for isolated vortices, called self-oscillatory behavior. The volume variations affect the translation velocity of the vortex as the

added mass (half of the mass of the displaced fluid) governs the resistance experienced by the cavitating vortex core. When the vortex cavity finally collapses, it will do so either in an axial or radial mode. The former happens for vortices ending on solid walls. The radial collapse mode requires the presence of (viscous) dissipation. The stability of a vortex is promoted by large surface tension (an effect generally neglected in the numerics) and small circulation (i.e. low vortex strength).

Vortex cavitation is most often studied in the context of tip vortex cavitation, where a cavity originates from a propeller or a foil due to the boundary-layer roll-up and subsequent formation of a tip vortex with a sufficiently low pressure on the vortex axis. The sensitivity of the cavity is discussed below in the context of tip vortex cavitation contrary to the isolated line vortex studied in this work. The main difference is the confinement of the vortex due to the venturi, and the absence of a vortex trajectory. The length of the cavitating part of the vortex is - in this study - also dependent on the domain, whereas for tip vortices a large influence is noticeable between different turbulence models when comparing the streamwise extent of the cavity in [5].

Sensitivity to flow velocity

For (tip) vortices originating from wings, the influence of the Reynolds number can be found mainly in the thickness of the boundary layer. The boundary layer becomes thinner as Reynolds number increases, which influences the viscous core size and the pressure drop in the vortex core [11]. The relation between the tip vortex core radius and the boundary layer thickness was first assessed by McCormick, 1962 (as cited in [44]). The dependence of cavitation inception at σ_i on the lift coefficient C_l was confirmed by the experiments conducted by Maines & Arndt [3], who fitted the scaling law in Equation (2.98) to experimental observations. This scaling law was in first instance derived by McCormick, relating the tip vortex core radius and the boundary layer thickness. Experimental results by Arndt & Dugue, 1992 (as cited in [3]) as well as Fruman, 1994 (as cited in [3]) confirmed its validity and determined the value of 0.4 as the exponent for the Reynolds number.

$$\sigma_i = K C_l^2 Re^{0.4}, \tag{2.98}$$

where $0.045 \le K \le 0.073$ is a proportionality constant depending on the boundary layer thickness [3]. Despite this proven correlation, there is no direct link between the boundary layer thickness and the core radius. Furthermore, the original hypothesis stated by McCormick implies a transitional boundary layer, whereas some authors of the experimental results assume a fully turbulent boundary layer on the wing. The boundary layer thickness scales with power 0.4 for the former, but power 0.2 for the latter, so that the power of the Reynolds number in Equation (2.98) should theoretically vary based on the exact state of the boundary layer on the foil, which is contradicted the experiments [4]. Further research on this relation and the effects of the boundary layer thickness on the tip vortex cavity has been conducted by Liebrand [5]. As there is no boundary layer roll-up for the case studied in this thesis, the Reynolds number should not influence the size of the cavity for the same circulation Γ.

Sensitivity to turbulence

In turbulent flows, both the flow velocity and the pressure consist of mean ($\bar{\phi}$) and fluctuating (ϕ') parts. The pressure fluctuations contribute to the cavitation inception criterion insofar that they are able to locally (and during small timescales) decrease the pressure leading to cavitation inception. This is demonstrated by Franc & Michel [44] for the inception of jet cavitation, defining the inception criterion:

$$\sigma_i < -C_{\bar{p}} - \underbrace{\frac{p_{\text{vap}} - p_{\text{crit}}}{1/2 \rho u_\infty^2}}_{\approx 0} + \frac{p'}{1/2 \rho u_\infty^2}. \tag{2.99}$$

The first term on the right hand side takes into account the mean pressure field of the turbulent flow. The second term expresses the static delay in cavitation inception due to the difference between vapor pressure and the actual critical pressure of the nuclei. It is usually negligible for industrial flows. The third term expresses the advance to cavitation inception due to the pressure fluctuations and is the hardest to model. Statistically speaking, pressure fluctuations are proportional to turbulent stress $-\rho \overline{u_i' u_j'}$. The pressure fluctuation term can be determined by assuming that the root-mean-square value of the fluctuation p' is correlated with the turbulent kinetic energy k [44]:

$$k = \frac{1}{2} \left(\overline{u'^2} + \overline{v'^2} + \overline{w'^2} \right), \tag{2.100}$$

$$\sqrt{\overline{p'2}} = C \frac{2}{3} k = C \rho \overline{u_i'^2}, \qquad \text{where } C \approx 0.7. \tag{2.101}$$

Apart from these observations, there is a general lack of understanding regarding the interplay of turbulence (models) and cavitation (models) [75]. The interplay of turbulence models and cavitation is something that this thesis aims to improve upon.

2.4.2. Spectral assessment of cavity dynamics

The ultimate goal of this project is to predict acoustic emissions from an oscillating cavity. The dynamic behavior of a vortex cavity results in broadband hull-pressure fluctuations and underwater radiated noise. The extrapolation from cavity oscillation to radiated noise is described in detail in the work of Bosschers [2, 76]. The center frequency of the broadband hump was linked to tip vortex cavity resonance by Ræstad, 1996 (as cited in [13]) and Bosschers [1]. Previous analyses of the dynamic cavity behavior were presented in the research by Bosschers [2, 12, 14] and Pennings et al. [13].

Analytical dispersion relation

The different modes in which the cavity deforms each have a distinct dispersion relation between frequency and wave number [13] that allows them to be identified in spectral space. This section only contains the equations that determine the lines in wavenumber-frequency space, the derivation of the dispersion relation can be found in Appendix B.1.

Three different modes can be distinguished by their shape: mode $n = 0$ (*breathing mode*) shows a volume variation, whereas mode $n = 1$ (*helical mode*) shows a displacement of the vortex centerline. Mode $n = 2$ (*double helix mode*) has an elliptical vortex core shape. The shape of the three modes is presented in Figure 2.10. The distortions of the vortex core are propagating inertial waves, often referred to as Kelvin waves [13] as they were first studied by Lord Kelvin.
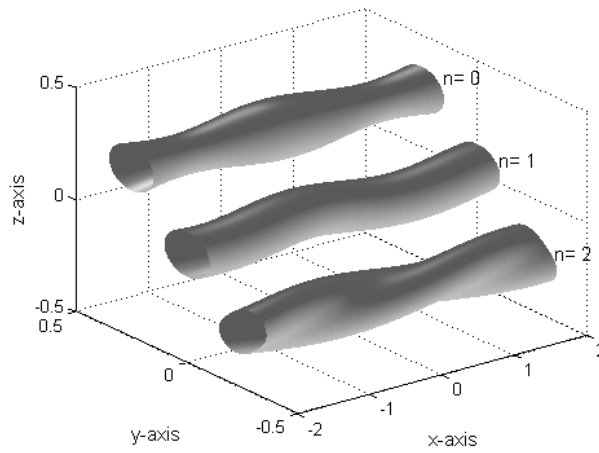
Figure 2.10: Deformation modes $n = 0$, 1 and 2, reproduced with permission from [12].

The non-dimensional dispersion relation is given by:

$$\tilde{\omega}^{\pm}(\kappa, n) = \frac{\omega^{\pm} r_c}{u_{\infty}} = \tilde{u}_{x,c} k_z r_c + \tilde{u}_{\theta,c} n \pm \sqrt{K_{\sigma}} \sqrt{\frac{-\kappa H_n^{(1)'}(\kappa)}{H_n^{(1)}(\kappa)}} T_{\omega}, \tag{2.102}$$

where $\kappa = k_r r_c$ is the non-dimensional radial wavenumber, r_c is the average cavity radius and $\tilde{u}_{x,c} = u_{x,c}/u_{\infty}$, $\tilde{u}_{\theta,c} = u_{\theta,c}/u_{\infty}$ are the non-dimensional forms of respectively axial and azimuthal velocity at the cavity interface. The T_{ω} parameter represents the surface tension:

$$T_{\omega}(k_z, n) = \sqrt{1 + \frac{1}{K_{\sigma} We}(n^2 + k_z^2 r_c^2 + 1)}, \tag{2.103}$$

with the Weber number We:

$$We = \frac{\rho u_{\infty}^2 r_c}{T_{\omega}}. \tag{2.104}$$

The K_{σ} in Equation (2.105) represents a stiffness in the equation of motion of the cavity perturbation, see Chapter 4 of [2] for more background on this term. The stiffness coefficient K_{σ} is defined as:

$$K_{\sigma} = \sigma \frac{r_c^2}{r_v^2 + r_c^2}, \tag{2.105}$$

where σ is the cavitation number. The velocities at the cavity interface, as well as the contribution of the surface tension need to be tuned using experimental or numerical solutions to determine the dispersion relation for the dynamics of a particular cavitating line vortex. The dispersion lines were drawn using the above definitions for a cavitating ideal line vortex similar to a simulated one in this thesis and are presented in Figure 2.11.
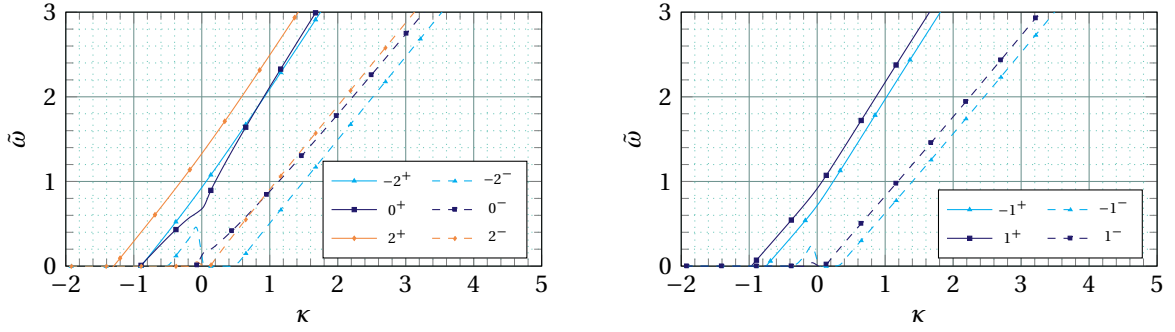
Figure 2.11: Analytical dispersion lines for a vortex similar to the one simulated (M$_4$ IDDES SS): $r_c = 0.006$ m, $r_v = 1.41\, r_c$, $u_\infty = 14.147$ ms^{-1}, $u_{x,c} = 1.1\, u_\infty$, $u_{\theta,c} = 0.2\, u_\infty$, $\sigma = 0.65$. Numbers indicate deformation modes.

Application to experimental results

Pennings et al. [13] performed experimental measurements of cavity deformation of a cavitating tip vortex generated by the Arndt foil, which is an elliptical wing used previously in experiments by Arndt [3, 4]. High-speed video shadowgraphy was used in two orthogonal planes (xy, xz), along with force and sound measurements. The frame rate of the cameras was 5000 frames per second, with a resolution of 1920×1080 pixels. The phase difference between images recorded by both cameras helps distinguishing the different modes. The evolution of the cavity diameter was subsequently studied seperately in the time- and spatial domain, followed by a spectral study using a two-dimensional Fourier transform.

Two different flow cases from the experiments carried out by Pennings [13, 15] were analyzed by Bosschers in [2] to establish the differences in their respective cavity dynamics. The frequency spectrum of both experimental cases was also assessed by Bosschers [2], with the difference that Pennings et al. [13] considered positive wavenumbers and positive and negative frequencies and Bosschers positive frequencies and positive and negative wavenumbers. A one-dimensional Fast Fourier Transform (FFT) was used to determine the Power Spectral Density (PSD) of the spatially averaged and time-averaged diameter separately. This was done to highlight tonal frequencies from the cavitation tunnel used by Pennings et al. [13] and to obtain a first indication of the cavity shape. The broadband noise that is commonly emitted by tip vortex cavities could also be identified for one of the cases. Bosschers [2] applied the analytically-derived dispersion relation to identify the different modes in the experimental results in [13, 15] and the spectrum of the time-averaged diameter allowed for a first estimate of the non-dimensional wavenumber κ.

The more rigorous analysis and the comparison between the analytical and experimental dispersion relation, also described in [2], requires a two-dimensional FFT of the diameter fluctuations for modes $n = 0$, 2, and the fluctuations of the centerline location for mode $n = 1$. The analysis in the wavenumber-frequency domain allows an even clearer distinction between modes and allows for the validation of the derived dispersion relation for a three-dimensional vortex by Bosschers [2]. The dominant feature in wavenumber-frequency plots is a straight line of which the slope $\partial\omega/\partial k_x$ equals the group velocity. These plots also allow identifying harmonics of the group velocity, which are small perturbations on the cavity interface that are linked to disturbances in the free stream. A stationary wave can be identified by the zero-crossing wave-number of the group velocity line. The identification of the modes depends on the group velocity and the related amount of energy transfer with other modes [13]. An example of a wavenumber-frequency plot is given in Figure 2.12.
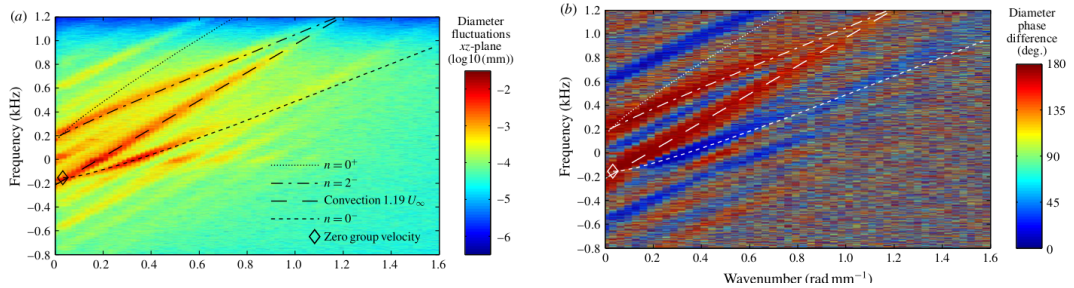
Figure 2.12: Wavenumberfrequency amplitude (left) and phase spectrum (right). Included are the lines for the breathing $n = 0^\pm$ and helical $n = 2^-$ modes and a line for constant group velocity that is 19 % larger than the tunnel free stream velocity, reproduced with permission from [13].

The frequency and wave number where the group velocity becomes zero is defined by a local minimum/maximum of the

mode $n = 0^-$ line [14], since the axial group velocity is defined by Bosschers in [76] as:

$$\bar{c}_{g_{1,2}} = \frac{c_{g_{1,2}}}{u_x} = \frac{\partial \omega_{1,2}/\partial k_z}{u_x}. \tag{2.106}$$

The analytical dispersion (prediction) curves in the frequency-wavenumber domain were obtained by tuning the characteristic cavity dynamics parameters $\tilde{u}_{x,c}$, $\tilde{u}_{\theta,c}$ and K_σ to the experimental spectrum from [77]. The stiffness coefficient K_σ was determined using the slope and wave number at $\tilde{\omega} = 0$ for the mode $n = 0^-$. The axial and tangential velocities at the interface $\tilde{u}_{x,c}$ and $\tilde{u}_{\theta,c}$ were derived by matching the curves for $n = 1^+$ and $n = 1^-$ to the experimental curves obtained in [77] and [15]. The effect of surface tension (taken into account in the analytical formulation) was shown to be very small $T_\omega = 1.026$ for mode $n = 2$.

Bosschers [2] argued that the agreement between the fitted prediction curves and the dispersion curves from the experiments was relatively good for the experimental case studied in [15], where the helical mode ($n = 2$) was absent. Larger discrepancies existed for the case with more developed cavitation studied in [13], although the twisting characteristic of the cavity was easily distinguishable. The differences concerned mostly the appearance of possible harmonics in the experimental spectrum which could not be directly attributed to a mode. Significant differences were noted by Bosschers [2] between the matched and experimental tangential velocity at the cavity interface for both experimental cases, whereas the axial velocity was approximately equal. Bosschers [2] did conclude that the stiffness coefficient could be calculated using the square of the tangential velocity at the interface.

The spectra obtained using the centerline variations and the prediction curves for mode $n = 1$) are demonstrated by Bosschers [2] to agree quite well for the case without the helical mode, however the phase angles differed from the expected 90 degrees. The case with more developed cavitation and a helical deformation of the tip vortex showed the opposite behavior, with poor correlation between prediction and experiment, but a correct phase angle.

2.5. Quantification of numerical uncertainties

It is important to verify the independence of the solution from the grid size and the time step used to justify that the obtained answer was not just obtained by chance. This is part of what is called Verification and Validation (V&V) of CFD studies. The difference between verification and validation is nicely illustrated by the following definition by Roach from 1984 as cited in [78]: verification checks whether the equations are solved right, whereas validation has to show if the right equations are solved. Validation requires the input of numerical uncertainties, which are calculated during the verification stage. The verification procedure is addressed first, followed by the validation procedure.

2.5.1. Verification and numerical uncertainty

This paragraph is based on the procedure by Eça & Hoekstra [78] and Rosetti et al. [79] for the assessment of the discretization uncertainty for unsteady problems. Verification can be split into code verification and solution verification. Code verification has to demonstrate that the equations of a certain model are solved correctly. Solution verification estimates the error or uncertainty of a calculation without knowledge of the exact solution. An error requires knowing the exact solution and has a plus or a minus sign, whereas an uncertainty is an interval which contains the 'truth' or exact solution with a certain degree of confidence and has a $\pm$ sign. The uncertainty U_ϕ is defined as the absolute value of the error estimate ε_ϕ times a safety factor F_s in the procedure laid out in [78].

Five types of numerical errors can be distinguished: i) round-off error, ii) iterative error, iii) discretization error, iv) input error and v) statistical error. The round-off error is in the order of machine precision and sufficiently low if double precision is used. The iterative error is a result of the non-linearity of the Navier-Stokes equation and is the most common error that is referred to in literature when the simulation is said to be converged. For the simulations presented in this thesis, it was the goal to obtain local L_∞ residuals (which can be seen as normalized values of the iterative error) below 1×10^{-6}. The discretization error, which is the error arising from discretizing the continuous system in space and time, needs to be dominant to use the procedure by Eça & Hoekstra [78], in practice by about two orders of magnitude. The input error results from differences between the numerical simulation and the experimental set-up. The statistical uncertainty is due to the presence of start-up effects within the measured signal.

Discretization error

The discretization error ε_ϕ is estimated using a truncated power series expansion:

$$\varepsilon_\phi \simeq \delta_{\text{RE}} = \phi_i - \phi_o = \alpha_x h_i^{p_x} + \alpha_t \tau_i^{p_t}, \tag{2.107}$$

where ϕ_i is any integral or other functional of a local flow quantity, ϕ_o is the exact solution, α_x and α_t are the constants obtained from the expansion, h_i and τ_i are respectively the typical cell size and typical time step ratios and p_x and p_t denote

the observed order of grid convergence for respectively the space and time discretization. Monotonic convergence is defined by $1.0 \leq p \leq 2.1$, leading to the most accurate estimate of the discretization error. If the convergence is not monotonic, a larger safety factor is applied when calculating the uncertainty. At least five grids and time steps, but in practice more geometrically similar grids and time steps are required to accurately estimate the value of the five unknown parameters: $\alpha_{x,t}$, ϕ_o and $p_{x,t}$. More background on the procedure can be found in [78] and [79].

Statistical uncertainty - Transient-scanning technique

Transient effects are a common issue with CFD simulations looking to obtain stationary values of certain parameter due to the initial flow field and the boundary conditions at start-up. In many cases, a start-up effect is visible in which the flow adjusts itself according to the physical model used. Transient effects should be excluded from the time-averaging procedures of variables to qualitatively assess performance of certain models in predicting flow or geometry parameters. However, the actual uncertainty introduced by these transients is in most cases unknown. To determine this 'aleatory uncertainty' the Transient Scanning Technique (TST) can be used. Usually the selection of data used for the time-averaging is based on experience and guesswork, which would now be taken out of the equation. This allows for an objective statement to be made regarding the period for which the average is statistically converged. The TST was developed by Brouwer [80, 81] and is not limited to CFD, but also has applications for Experimental Fluid Dynamics (EFD). TST calculates the uncertainty of a signal cumulatively from the end (TST-B) or the beginning (TST-A) of the time series. Whether a signal is stationary is apparent from assessing the decay of the uncertainty based on the following hypothesis:

"The realization of a stochastic process, longer than the period corresponding to the lowest frequency component, is stationary if the estimated, random uncertainty of the mean decays with the inverse of the realization length." (80)

The use of the TST in this thesis will be twofold. First, the uncertainty of results can be accurately quantified to clarify the reliability of the obtained results. The second benefit of TST is that it indicates what part of the time-series of results can be used to determine the statistically converged time-averaged value of a parameter, by comparing the slope of the uncertainty with lines parallel to $1/\log(t)$, i.e. the logarithmic decay of the uncertainty in time. The start-up period is easily identified by the hockey-stick (see Figure 2.13) and not used for time-averaging flow variables. Results of DDES and Extra large-eddy simulations (XLES) presented in [80] already demonstrated that SRSs generally require a longer running time to obtain statistically stationary results compared to RANS.
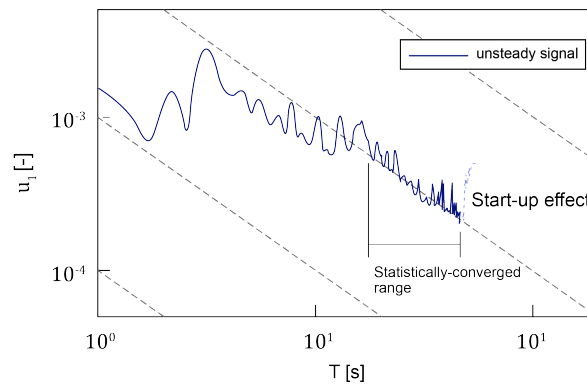
Figure 2.13: Sketch of the TST-B plots with indication of the hockey-stick and logarithmic decay. Image adapted from [81].

Input uncertainty

The input or parameter uncertainty is related to the uncertainties in the fluid properties, the flow geometry and boundary conditions [82]. The uncertainty of the flow properties is for this case mostly attributed to the turbulence quantities that characterize the turbulent flow in a RANS context: the turbulence intensity I and the eddy viscosity ratio ν_t/ν. The turbulence intensity is a measure for the amount of (averaged) fluctuations and is equivalent to specifying the turbulence kinetic energy. In some cases the turbulence intensity is measured, but for this case the quantity was not reported [8]. The uncertainty related to the boundary condition is expected to be of larger importance, as the method of generating a vortex differs with the experimental set-up. In the experiments a fixed-blade swirl generator was mounted in front of the contraction to generate a vortex [8]. CFD simulations of the same case modeled this swirl generator [9]. This was outside of the scope of this thesis due to the added complexity and computation expense. For the present case, a Lamb-Oseen vortex (see Section 2.2.3) is specified at the inlet. The characteristic parameters of the vortex were specified based on the mean velocity angle $\beta = \text{atan}\,(u_\theta/u_x)$ reported by [9]. This was done to obtain a flow field in front of the converging nozzle that was as similar as possible to the

reported one by [9] and to reduce the uncertainty related to the swirl generation process. The procedure is documented in Section 3.4.

2.5.2. Validation procedure

The goal of validating a solution is to estimate the modeling error of a mathematical model (numerical data) in relation to a physical model (experimental data). The validation procedure is based on the work by Eça et al., [82]. The validation uncertainty U_{val} is made up of numerical uncertainty U_ϕ, input uncertainty U_{input} and experimental U_D uncertainty. The validation comparison error $E(\phi)$ is the difference between experimental (D) and simulated result prediction (S / ϕ_i):

$$U_{\text{val}} = \sqrt{U_\phi^2 + U_{\text{input}}^2 + U_D}, \qquad (2.108)$$

$$E(\phi) = S(\phi) - D(\phi). \qquad (2.109)$$

The 95 % confidence interval ($[E(\phi) \pm U_{\text{val}}]$) containing the modeling error δ_{model} needs to be determined. If $|E| \gg U_{\text{val}}$, then the modeling error is dominant and the model must be improved. In case that $|E| < U_{\text{val}}$, δ_{model} is within the numerical uncertainty bounds caused by the numerical, experimental and parameter uncertainties. This either means that the model and the solution are validated with precision U_{val} if E is deemed sufficiently small, or that the quality numerical and/ or experiment should be improved before further conclusions are drawn [82].

Validation procedure using multivariate metrics

When the validation is done for quantities at several points (e.g. a velocity profile), then the method using multivariate metrics is adequate. This method is proposed as a 2016 supplement to the ASME V&V 20-2009 standards [83] and used in the works of Eça et al. [84, 85]. The metric r is introduced, and defined for N evaluations of the comparison error $E(\phi)$ as:

$$r = \sqrt{E^T V_{\text{val}}^{-1} E}, \qquad (2.110)$$

where E is a vector containing the N values of E_ϕ and V_{val} is the covariance matrix given by:

$$V_{\text{val}} = V_S + V_D + V_{\text{input}}. \qquad (2.111)$$

The uncertainties of numerical and experimental results are assumed to be uncorrelated and V_S and V_D are diagonal matrices containing values of U_S^2 (numerical uncertainty) and U_D^2 (experimental uncertainty) respectively. When the uncertainties of the N estimated δ_ϕ are normal distributed, then the expected value of r is obtained from a χ^2 distribution. This yields a reference metric r_{ref}, equal to the expected value plus standard uncertainty, [85]:

$$r_{\text{ref}} = \sqrt{N + \sqrt{2N}}. \qquad (2.112)$$

If the ratio r / r_{ref} is clearly larger than one, the simulations are not consistent with experimental observation. This means that validation uncertainty U_{val} is dominated by modeling errors. If $r / r_{\text{ref}} < 1$, then the differences between the simulation and experimental data are overall within the interval of U_{val}.

2.6. Numerical discretization in ReFRESCO

The open-usage (unsteady) incompressible flow solver ReFRESCO (an acronym for REliable and Fast RANS Equations (solver) for Ships and Constructions Offshore), developed by Marin, was used to obtain the results presented in this thesis. ReFRESCO is optimized for maritime applications and was developed as an unsteady RANS solver and has been validated for a wide array of flow cases [86]. It is able to deal with multiphase flows and moving grids, and contains couplings with structural equations of motion as well as propeller models and wave-generation codes. The turbulence capabilities were extended beyond the unsteady RANS base of the code by including various scale-resolving and EARSM models. A comprehensive description of the code can be found in [87] and [63], which forms the basis for this section covering the linearization and discretization of the Navier-Stokes equations and the solution process in ReFRESCO.

ReFRESCO is a finite-volume code with collocated variables at the cell-center. The principle of the finite volume method can be found in Appendix C.2. The faces of the control volumes are triangulated within ReFRESCO, with no limit to the maximum number of faces per cell. The face-values are calculated using second-order interpolation. The effects of cell non-orthogonality and the eccentricity between neighboring cells, see Figure 2.14, can be and were corrected for in the present simulations.

The non-linearity of the system is contained within the convective term of the momentum equation:

$$\frac{\partial u_i}{\partial t} + \underbrace{u_j \frac{\partial u_i}{\partial x_j}}_{\text{convection}} = -\frac{1}{\rho} \frac{\partial p}{\partial x_i} + \underbrace{\frac{\partial}{\partial x_j}\left(\nu \frac{\partial u_i}{\partial x_j}\right)}_{\text{diffusion}}. \qquad (\text{2.2 revisited})$$
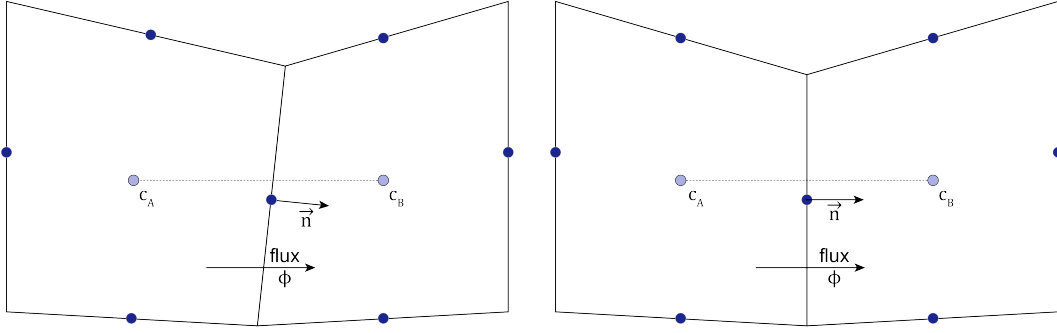
Figure 2.14: Illustration of cell non-orthogonality (left) and eccentricity (both).

The convective term is linearized in REFRESCO using Picard's method, which uses the mass flux from the previous iteration or from an initial condition. The linearization of the convection in the i-th direction in given by:

$$(u_j u_i n_j)^{k+1} \approx (u_j n_j)^k (u_i)^{k+1},$$ (2.113)

where $k+1$ indicates the current iteration number. The effective viscosity $\nu_{\text{eff}} = \nu + \nu_t$ and the second contribution of $\partial u_j / \partial x_i$ (in the diffusion term) are also expected to be known from the previous iteration, so that the momentum and other transport equations can be written as linear advection-diffusion equations. REFRESCO supports first- and second-order accurate advection schemes, whereby second-order κ schemes were chosen for this research to improve accuracy and reduce diffusivity as much as possible. The face value of the convected variable (see Figure C.1 for a sketch) is determined by the cell center values corrected by an anti-diffusive term containing (upwind/ central) weighted gradients of the convected quantity. The distribution between the upwind and central interpolation is controlled by the κ-parameter. The Quadratic Upwind Interpolation for Convective Kinematics (QUICK) scheme, developed by Leonard [88] and for which $\kappa = 1/2$, was used for wetted vortex simulations. This choice was made based on experience at MARIN and generally accurate results as shown in [89, 90]. At MARIN, the model of choice for cavitating simulations is the limited QUICK scheme (T. Lloyd, personal communication, April 2019), developed by Hoekstra [91]. The limited QUICK scheme extends the linear QUICK scheme with a flux-limiter λ that ensures the boundedness of the solution in regions with large gradients. The equations for the face value ϕ_f of both schemes are given in Appendix C.3.

The pressure is calculated from the velocity field using a pressure-correction type method. The system of equations can be written in a simplified form as:

$$\mathbf{A} x = b,$$ (2.114)

where the $\mathbf{A}$ matrix contains the operators of the velocity and pressure terms in x and b contains the force terms. The non-linear iterative method then solves this system of equations as:

$$x^{k+1} = x^k + \gamma \tilde{\mathbf{A}}_k^{-1} \underbrace{(b - A_k x^k)}_{\text{residual}},$$ (2.115)

where γ is the explicit relaxation parameter, and the last term is the residual at time step k. The approximation method of the inverse of the $\mathbf{A}$ matrix; $\tilde{\mathbf{A}}^{-1}$, depends on the solver choice (Semi-Implicit Method for Pressure Linked Equations (SIMPLE) or Fast RANS Equations solver for Ships and Constructions Offshore (FRESCO)). The FRESCO solver is based on the SIMPLE algorithm, but the latter differs from the former in i) the order in which explicit relaxation is applied and ii) the calculation of the residuals.

Relaxation of the iterative solution process can be used to increase the robustness, but slows down the convergence. Two kinds of relaxation can be specified in REFRESCO: i) explicit relaxation of a variable and ii) implicit relaxation of an equation (system). Explicit relaxation (i.e. changing the γ parameter) specifies how much of the solution at the next time step should be used in order to avoid large oscillations of the variable. Implicit relaxation increases the diagonal of the linear system so that it becomes easier to solve. Implicit relaxation can only be added in combination with explicit relaxation.

2.7. Conclusions

The different turbulence models and their respective merits and shortcomings showed that the EARSM and IDDES model are most promising for the accurate representation of the line vortex. The complicated nature of the EARSM made it difficult to estimate the gain with respect to the SST model. The curvature-corrected form of the former is implemented in REFRESCO, but ambiguous results and the ad hoc nature of standard curvature corrections (e.g. Dacles-Mariani) led to the decision not to apply a correction for the SST simulations.

The Lamb-Oseen and Rankine analytical vortex models highlighted the importance of the tangential velocity magnitude and profile inside the vortex core for the value of the minimum pressure on the vortex axis. The Lamb-Oseen vortex will specified as an inflow condition as it is a direct solution of the (laminar) Navier-Stokes equations. The Q-criterion was chosen to identify the vortex as it is readily available within REFRESCO and widely used in literature.

The multiphase flow will be solved using a VOF approach, assuming a homogeneous mixture of vapor and liquid inside the domain. The Schnerr-Sauer model was selected for the cavitating flow cases as it is the most-used for cavitating flow simulations within MARIN. The fact that many dynamic aspects of the cavity behavior are neglected, is commonly accepted, as is the simplification to incompressible flow. It is still unclear within the community as to what the interplay is between cavitation (models) and turbulence (models). The eddy viscosity is known to dampen the shedding of sheet cavities and corrections like the Reboud correction are often applied for RANS models, but no conclusions with respect to vortex cavitation could be found. The self-oscillatory behavior of the cavity, caused by the interplay between centrifugal forces and ambient pressure fluctuations, is probably also dampened by the eddy viscosity. The Reboud correction is therefore applied for the EARSM in the cavitating vortex case. An important hypothesis that was found, is that the VOF method is expected to affect the representation of the cavity more profoundly due to the smearing of the interface. Furthermore, despite the knowledge that pressure fluctuations influence the cavity behavior, they are generally neglected. The square root of the pressure is assumed in literature to be correlated to the turbulent kinetic energy.

The theoretical basis for the spectral analysis of cavity dynamics was provided in this chapter. Modal deformations could be identified in previous research by dispersion lines relating to the inertial (Kelvin) waves on the cavity interface. The analytical dispersion lines were incorporated in the post-processing routine to apply them to the results of the cavitating vortex.

From the theory regarding the V&V procedure, it was established that the discretization uncertainty should be two orders larger than the next-largest uncertainty for the uncertainty estimate to be valid. The statistical uncertainty of the results will be assessed using the TST-B method, which allows an accurate determination of the length of the start-up effect and the use of statistically-converged time-averaged values. The multi-variate metric method was found to be applicable to validate the numerical results using the experimental measurements.

The next chapter will present the numerical set-up, with a strong focus on the determination of the domain as well as the tuning of the inflow condition. The post-processing procedure for the analysis of cavity dynamics is also discussed in detail.

Simulation set-up

This chapter comprises the information regarding the domain and the general settings used in the computations. The discretization of the domain and the generation of the grid are discussed first, as well as the boundary conditions that were applied. The second part of this chapter contains the procedures for data processing (post-processing). Section 3.2 starts off with the way in which variables were extracted from REFRESCO and defines their normalized values which are used throughout Chapters 4 and 5. The spectral analysis of the cavity requires the extraction of isocontour data from REFRESCO at specified intervals. The way in which this data was processed, is outlined in detail in Section 3.2.4. Section 3.3 and Section 3.4 contain the investigation of the domain length and the tuning of the inflow condition respectively.

3.1. Computational domain

First, the validation test case is introduced, including the fluid properties and the uncertainty that was reported. This is followed by the diskretization of the domain in time as well as the grid generation and the used boundary conditions.

3.1.1. Test case

The geometry of the Venturi tube, consisting of a converging nozzle, a parallel section (the throat) and the diverging nozzle, was based on the experimental research by Rudolf et al. [8]. The exact dimensions of the Venturi section, provided in Table 3.1, were obtained in personal correspondence with the main author (P. Rudolf, personal communication, January 25, 2019). A two-dimensional sketch of the entire computational domain can be found in Figure 3.1a.

Table 3.1: Geometrical details of Venturi section of domain. C-nozzle is converging nozzle, D-nozzle is diverging nozzle.

d_{inlet} /m	d_{throat} /m	$l_{C\text{-nozzle}}$ /m	l_{throat} /m	$l_{D\text{-nozzle}}$ /m
0.053	0.030	0.050	0.060	0.090

The experiments in [8] were carried out for wetted and cavitating flow conditions and the axial and tangential velocity profiles were measured in radial direction at a plane in the middle of the Venturi throat. The velocities were measured using an Laser-Doppler Velocimetry (LDV) technique, which could not consistently measure velocities inside the vapor core due to reflections of the laser at the cavity interface. This meant that only the wetted flow measurements could be used for validation purposes of the present simulations. The uncertainty of the velocity measurements was not explicitly given, but were said to be in the order of the velocity fluctuations (P. Rudolf, personal communication, January 25, 2019) and is therefore expected to be small. The flow rate at the inlet was $\dot{Q} = 4.56 \text{ ls}^{-1}$ for the wetted flow conditions, with an uncertainty of $U_{exp} = 5 \times 10^{-5} \text{ ls}^{-1}$. The same geometry was used for cavitating flow simulations at a higher flow rate of $\dot{Q} = 10.00 \text{ ls}^{-1}$. No information was provided regarding measured turbulence intensity inside the flow. For this reason, the standard values of REFRESCO were specified as uniform distributions at the inlet. The turbulence intensity $I = 1\%$ and eddy viscosity ratio $\nu_t / \nu = 1$ correspond to low turbulent conditions.

3.1.2. Domain discretization

A second-order implicit time-discretization scheme using three time levels was selected. This is the highest order time-discretization possible using REFRESCO and is the default option. The interpolation method can be found in Appendix C.1.

The entire control volume can be divided into an inlet section, the converging nozzle, the throat, the diverging nozzle and the outlet section. The influence of the length of the inlet and outlet section was investigated in preliminary simulations, which are discussed in Section 3.3. The geometry, provided in Figure 3.1a, is characterized by sharp edges at the inlet and outlet of the throat. These sharp edges lead to large local pressure and velocity gradients and are potential cavitation sites. In the provided experimental results [8], no mention was made of issues regarding the sharp edges of the geometry. Instead, the choice of making the edges sharp was made deliberately to force boundary layer transition [8].

(a) 2D slice (xy-plane) of the domain.

(b) Perspective view including boundary conditions.
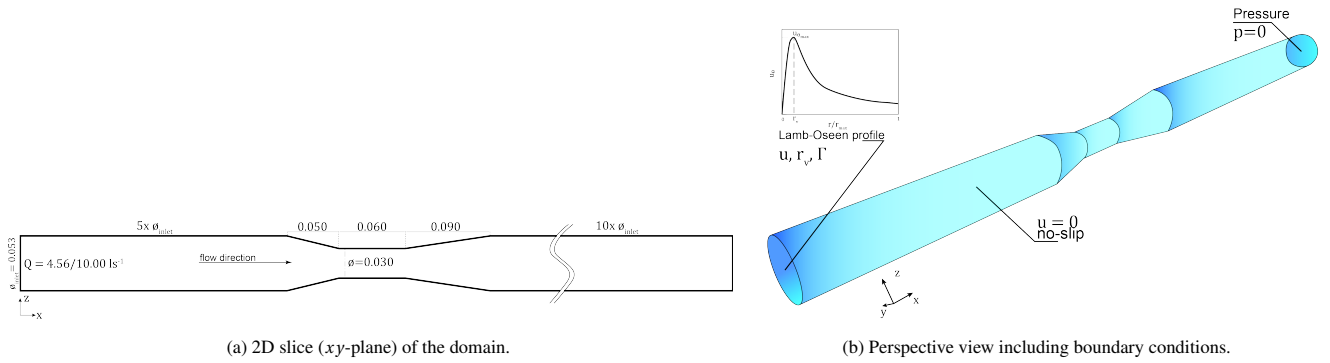
Figure 3.1: Sketches of the computational domain.

3.1.3. Grid generation

A structured grid with OH topology, as seen in Figure 3.2a, was constructed using POINTWISE. The topology was chosen based on a comparison study [92], which highlighted the benefit in accuracy and computational cost compared to O and H-type grids. The same topology was used in the scale-resolved simulation of a turbulent swirling vortex in a suddenly expanding pipe by Javadi & Nilsson [93]. The grid was constructed as a single block so that no hanging nodes were present that might lead to convergence issues.

(a) Cell distribution at section in the middle of Venturi throat.

(b) Cell distribution in streamwise direction, showing clustering of cells in the Venturi.
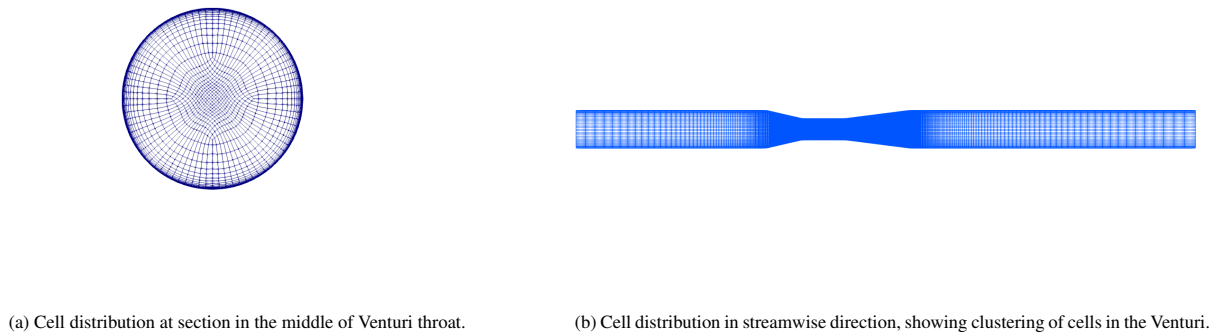
Figure 3.2: Overview of cell distribution for the grid series. Shown images are from coarsest M_1 mesh.

As can be seen in Figure 3.2, the throat and diverging nozzle section were most refined, followed by the converging nozzle. The inlet and outlet sections have relatively large spacing in longitudinal direction. The outlet section is slightly coarser to increase numerical diffusion towards the end of the domain, thereby avoiding numerical issues caused by fixing the pressure at the outlet. This restrictive boundary condition was required to obtain convergence. The walls of the Venturi were resolved up to the viscous sublayer ($y^+ < 1$) and the growth in the first 4 boundary layers was limited to 1.2 in wall-normal direction based on requirements for Large Eddy Simulation (LES) commonly applied in the industry. The level of refinement in streamwise and circumferential direction (measured by x^+ and z^+) was based on staying around the 2 million cell limit on the coarsest mesh to limit the computational expense. The streamwise resolution x^+ was prioritized slightly due to the strongly convective character of the flow and high axial velocities in the throat, as well as the significant cost of increasing the z^+ resolution.

The final grid series M_1, M_2, M_3 and M_4 was created using the findings from the domain length study in Section 3.3, with slightly different settings to improve the quality of the mesh and to reduce the number of cells for the verification study. Results for the prediction of pressure and tangential velocity showed practically no differences between both grids so that the modified version M_1 was refined in three steps to obtain the M_2, M_3 and M_4 grids. The refinement factor in every direction was 1.25, based on common practice at MARIN. The number of cells for the three grids, and characteristic length scales x^+, y^+ and z^+ are given below in Table 3.2 for a flow rate of $\dot{Q} = 10.0$ ls^{-1}; the higher flow rate used for the cavitating flow analyses.

Table 3.2: Characteristics of the meshes used for the verification study of the wetted vortex.

Grid	# cells in millions	x^+	y^+	z^+
M_1	1.89	220	0.65	710
M_2	3.71	176	0.52	568
M_3	7.26	141	0.42	454
M_4	14.37	113	0.34	364

3.1.4. Boundary conditions

The no-slip boundary condition was specified at the wall of the venturi, as can be seen in Figure 3.1b. The pressure was specified at the outlet as $p_{out} = 0$. The reference experimental results by Rudolf et al. [8] were obtained using a swirl generator mounted in front of the converging section. Modeling of this swirl generator was outside the scope of this thesis and the resulting profile had to be replicated using the swirling inflow condition.

In multiple research it was found that the velocity field of the vortex which originates at the tip of a wing can be relatively well-described by the Lamb-Oseen vortex [2, 50]. The Lamb-Oseen vortex was also used as a boundary velocity field in [6, 7] which both numerically studied the development of a line vortex inside a venturi. The Lamb-Oseen vortex is a laminar vortex model, which decays with increasing viscosity and whereby the radial velocity is assumed to be negligible. The definition for a two-dimensional Lamb-Oseen tangential velocity profile $u_\theta(r, t)$ as derived by Bosschers [2] was previously given in Section 2.4.1 but is given below for the reader's convenience:

$$u_\theta(r) = \frac{\Gamma}{2\pi r} \left[1 - \beta_R \exp\left(-\alpha_R \frac{r^2}{r_v^2}\right) \right]. \tag{2.96 revisited}$$

The parameter $\beta_R = 1$ for a non-cavitating vortex. Cavitation is only expected to occur in the contraction, therefore there is no physical reason to use the cavitating version of the Lamb-Oseen vortex specification at the inlet. This equation can be rewritten in a form that is more convenient to apply as a boundary condition, using that the tangential velocity will reach a maximum at the edge of the viscous core radius $r = r_v$:

$$u_{\theta,\max}(r = r_v) = \frac{\Gamma_0}{2\pi r_v} \left(1 - \exp\{-\alpha_R\}\right), \tag{3.1}$$

so that Equation (2.96) can be rewritten as

$$u_\theta(r) = \frac{u_{\theta,\max}}{1 - \exp\{-\alpha_R\}} \frac{r_v}{r} \left[1 - \exp\left(-\alpha_R \frac{r^2}{r_v^2}\right) \right] \quad \text{with } r \in [0, r_{\text{inlet}}] \tag{3.2}$$

The tuning of the inflow conditions to match the experimental flow condition is described in Section 3.4. The boundary conditions are specified in Figure 3.1b.

3.2. Data processing procedure

The extraction of flow variables is treated first, followed by the normalization procedure. The processing needed for assessing the cavity dynamics from a spectral point of view is treated lastly.

3.2.1. Extraction of flow variables from REFRESCO

Various locations of interest where data is saved, called monitors, were defined before the start of the simulations. Two types of monitors were used: line monitors (L), which only write data over a single line and disc monitors (P), which write data in a circular two-dimensional plane and automatically calculate calculate vectors in a polar coordinate system. The disk monitors were used for the analyses in Chapters 4 and 5. The exact locations of all monitor lines/ planes are given in Table 3.3 and sketched in Figure 3.3. Plane A is defined by the measurement location of the velocity angle in experimental measurements and is placed 0.037 m in front of the converging nozzle. Line monitors were normal to the xz-plane (i.e. $z = 0$). For wetted flow, the disk monitors used a first-order nearest cell interpolation without updating the (r, θ) coordinates as this was not possible in REFRESCO. Line monitors used the same interpolation method but with updating the coordinates. The interpolation methods were changed to a second-order nearest cell-gradient interpolation in cavitating vortex simulations, following the observations made during the verification study, see Section 4.2.

3.2.2. Analyzed flow variables

The general flow variables that were analyzed for the wetted flow case were: pressure p, velocity $\mathbf{u}$ and the modeled turbulent kinetic energy k_{mod}. The flow variables were averaged in time following the Transient Scanning Technique (TST)-B method

Table 3.3: Longitudinal position of monitor lines & planes.

Designation	x-position /m	Type
O	0	line
O1	0.053	plane, line
A	0.228	plane
B	0.315	plane, line
B1	0.330	line
C	0.345	plane, line
C1	0.360	line
D	0.375	plane, line
D1	0.390	line
D2	0.405	line
E	0.420	plane, line
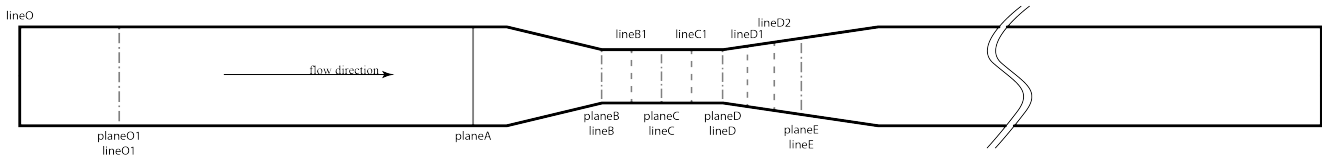
Figure 3.3: Indications of monitor location.

to ensure statistical convergence of the average, see Section 2.5.1, and in tangential direction, implicitly assuming an axisymmetric vortex. The graphs in this work are plotted using non-dimensional forms of the flow parameters. The non-dimensional forms ϕ^* of the flow variables ϕ are given by:

$$u^* = \frac{u_i}{u_\infty} \tag{3.3}$$

$$C_p = \frac{p}{1/2 \rho \, u_\infty} \tag{3.4}$$

$$\Omega_i^* = \frac{\Omega_i \, d_{\text{throat}}}{u_\infty} \tag{3.5}$$

$$k_{\text{mod}}^* = \frac{k_{\text{mod}}}{u_\infty^2}, \tag{3.6}$$

where $d_{\text{throat}} = 0.030$ m and $u_\infty = \dot{Q}/(2\pi r_{\text{throat}})$ is the flow rate divided by the area of the Venturi throat.

3.2.3. Fluctuating variables

The fluctuating components of the pressure p' and velocity components u_i were calculated by subtracting the time-averaged value of the pressure $\bar{p}$ and velocity u_i components. This allowed for the calculation of the resolved Reynolds stresses $\tau_{ij,\,\text{res}} = u_i' u_j'$ and resolved turbulent kinetic energy $k_{\text{res}} = 1/2(\bar{u}_i'^2)$. The resolved turbulent kinetic energy was nondimensionalized in the same way as k_{mod}.

3.2.4. Assessment of cavity dynamics

Data extraction

The data was extracted from PARAVIEW using the *co-processing* capability built into the current version of REFRESCO. Co-processing allows the user to specify a certain (filtered) part of the domain at a frequency specified before the simulation. The goal was to analyze the centerline and diameter variation in space and time, which was accomplished by writing the isocontours of $\alpha_{\text{vap}} = 0.50$ and $\alpha_{\text{vap}} = 0.90$ at a frequency of approximately $f_s = 2500$ Hz. The Nyquist frequency, defined as the largest identifiable frequency by a Fast Fourier Transform (FFT), is therefore equal to $f_N = 1250$ Hz. This is half of the Nyquist frequency used in the work by Bosschers [2], but still significantly larger than the largest dominant frequencies identified in that work. Due to the low-frequency characteristics of tip-vortex cavitation (i.e. 30-100 Hz), it is not expected that a higher frequency should be required. There is no information regarding the expected frequencies in this numerical case, so the value for the sampling (and related Nyquist frequency) are a first estimate only and the obtained results will shed more light on the requirements for further studies into this subject.

The data was extracted using the PARAVIEW-PYTHON coupling and further processed in PYTHON to obtain values for the space- and time dependent diameter d_c and centerline c_{line} location, visualized schematically in Figure 3.4a. The isocontours of $\alpha_{\text{vap}} = 0.50$ and $\alpha_{\text{vap}} = 0.90$ were sliced by two orthogonal planes (y-normal and z-normal) to obtain a similar set-up as in the processing of experimental data by [13] and [2] where two cameras were used. The phase difference between both slices can be assessed in this way. The sharp edges of the geometry lead to significant sheet cavity development as well as cavity shedding in the diverging nozzle. These cavities were filtered out by excluding all points laying outside a $[0.85 \times r_{\text{throat}}]$ interval from the geometry centerline ($y, z = 0$), see Figure 3.4b. The point cloud that is obtained as a result of slicing the isocontours, is not ordered and the spacing is not uniform. Additionally, the diameter and centerline need to be calculated for a set number of (axial) locations, irrespective of the cavity location and extent. The cavity diameter and centerline are therefore interpolated to axial locations x', spaced half a cell-width (as specified in the Venturi throat) apart, spanning a distance of 1.5 throat lengths (from the end of the converging nozzle until half a throat-length after the start of the diverging nozzle). A linear interpolation is performed to obtain a positive y'_+ and negative y'_- spanwise coordinate (z/y value w.r.t. the x-axis) of the cavity, using the closest points for each quadrant. This is shown schematically in Figure 3.4c. This method is not accurate near the end of the cavity due to the inwards folding shape, so that that part of the domain cannot be used in the analysis. Since the extent of the cavity is not known in this part of the process, it has to be removed in the next step. Whenever an interpolation point could not be found for a quadrant within one cell length distance, it is assumed that there is no cavity and diameter and centerline are set to zero. The diameter is then defined by the absolute sum of the y'_+ and y'_- coordinates, whereas the location of the centerline is determined by the half the regular sum of both. The diameter and centerline values are subsequently written for each sampled time step and for both planes.

(a) Workflow for extraction of cavity diameter and centerline data.

(b) Sheet cavity removal.

(c) Interpolation method.
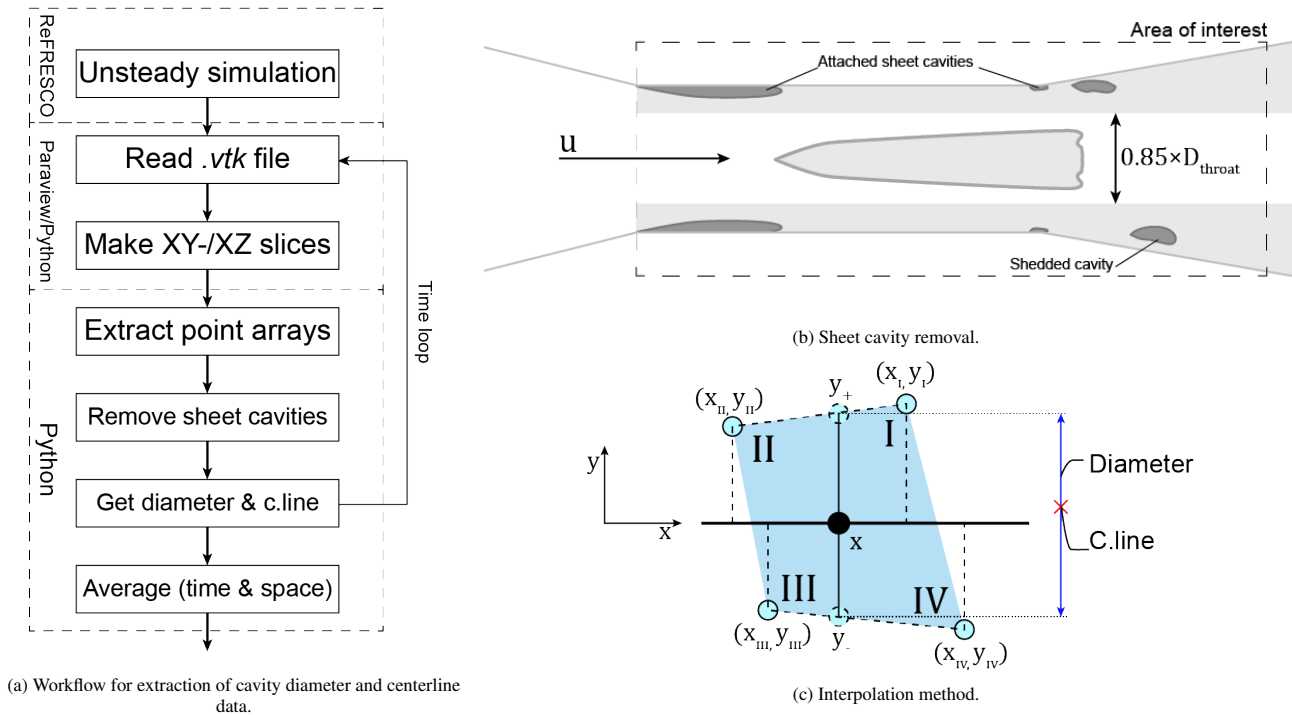
Figure 3.4: Illustrations of the post-processing of the data used in the cavity dynamics assessment for the cavitating vortex. Flow direction is in positive x-direction in b) and c).

Power spectra and transformation to wavenumber-frequency space

Both one-dimensional (time *or* space) and two-dimensional (time *and* space) Power Spectral Density (PSD) analyses were carried out, analogously to the work of Bosschers [2]. All one-dimensional spectra and the two-dimensional phase difference spectra were obtained using a segmented and windowed approach. The entire signal, without applying a window function, was used to determine the Cross-power Spectral Density (CPSD) in wavenumber-frequency space. This was done to increase the resolution of the power spectra.

The time and space sequences were each split into segments half their length. The segment overlap was 75 % as in [2] and a Hann window was used to reduce signal leakage. Zero-padding was applied after windowing the segments to increase the number of points for the FFT to the nearest power of two. This is done to improve the performance of the FFT method. The number of points used for the FFT on each segment differed between the simulations. A two-dimensional Hann window was applied for the two-dimensional FFT, and the overlap was also 75 % in both space and time in that case. The fluctuating

values, obtained by subtracting the time-averaged value from the instantaneous value, were used for the two-dimensional spectra.

The CPSD was calculated from the FFT of the datasets for the z-normal and y-normal plane and will be represented in decibel (dB) values as:

$$\text{CPSD}(k_z, f) = 120 + 10 \log_{10} \left(\frac{G_{\text{top}}(k_z, f) G^*_{\text{side}}(k_z, f)}{d_c^2} \right), \tag{3.7}$$

where $G(k_z, f)$ refers to the two-dimensional FFT of r' and $G^*(k_z, f)$ is the complex conjugate. The dB-valued PSD was obtained in a similar way:

$$\text{PSD}(k_z/f) = 120 + 10 \log_{10} \left(\frac{S(k_z/f) S^*(k_z/f)}{d_c^2} \right), \tag{3.8}$$

where S and is the single-sided spectrum amplitude and its conjugate S^*. The phase difference was calculated from the cross-spectrum $G(k_z, f)_{xy}$ as the angle between the real and imaginary parts of the spectrum.

3.3. Investigation of required domain length

The determination of the inlet and outlet length was the first step in building the grid series. Three different inlet lengths (2.5, 5 and 7.5 $\times D$) were studied, combined with two different lengths for the outlet (7.5 and 10 $\times D$, $D = d_{\text{inlet}} = 0.053$ m). The subscript notation is used for the inlet lengths and the superscript for the outlet lengths when referring to a certain grid; $M_{\text{IN}}^{\text{OUT}}$. The average cell distance was kept the same for all six options, such that an increased length implied a larger number of cells. The simulation parameters were the same for all cases and are given in Table 3.4. An older version of the inflow boundary condition used the swirl number instead of the circulation. Swirl is the ratio of the streamwise transport of angular and axial momentum and is expressed by the swirl number Sn. The swirl number will be elaborated upon in Section 3.4.1 as it is of larger importance there. The swirl number specified for the domain length study was about twice as large as the final value used for the wetted and cavitating vortex simulations.

Table 3.4: Flow variable values for domain length study.

Flow variable	Symbol	Value	Unit
Flow rate	$\dot{Q}$	8.11	ls^{-1}
Velocity in throat	u_∞	11.47	ms^{-1}
Reynolds number	Re_{throat}	605600	-
Swirl number	Sn	0.234	-
Viscous core size	r_v/r_{inlet}	0.2	-
Turbulence intensity	I	1	%
Eddy-viscosity ratio	v_t/v	1	-

The $k-\omega$ Shear Stress Transport (SST) model was used as the turbulence model. Initial simulations indicated that an unsteady approach was required to obtain converged solutions for the wetted vortex case. As this was too expensive for this domain study, a steady simulation was run for the six different grids, where for all grids the largest velocity residual (L_∞) was of $\mathcal{O}(10^{-3})$ after 6000 iterations. This means that the results are not sufficiently converged, however the residuals stagnate around this value. The different grids, along with their respective number of cells, are given below in Table 3.5. Despite this lack of convergence, any large difference between grids still indicates whether respective inlet or outlet length is enough or not. The different grids are shown in Figure 3.5.

Table 3.5: Designation of grids for inlet-/outlet length sensitivity study.

Designation	Inlet length [$\times D$]	Outlet length [$\times D$]	Number of cells [$\times$1M]
$M_{2.5D}^{7.5D}$	2.5	7.5	2.17
$M_{2.5D}^{10D}$	2.5	10.0	2.30
$M_{5D}^{7.5D}$	5.0	7.5	2.25
M_{5D}^{10D}	5.0	10.0	2.39
$M_{7.5D}^{7.5D}$	7.5	7.5	2.33
$M_{7.5D}^{10D}$	7.5	10.0	2.47
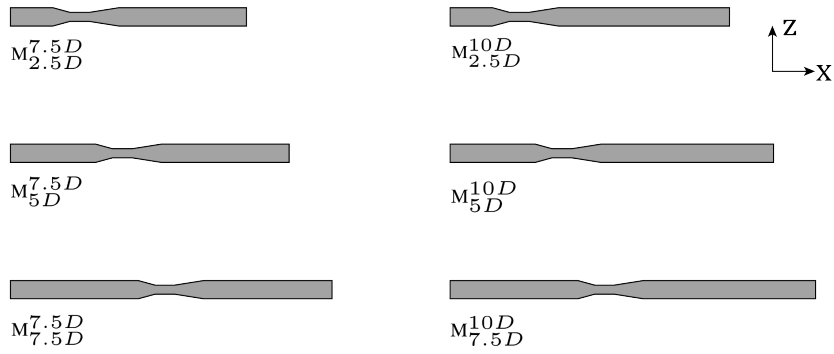
Figure 3.5: Two-dimensional sections of grids used in the domain length study.

3.3.1. Results of length sensitivity study

The results are compared at four locations: at the inlet of the converging nozzle, and at plane B, C and D. All data was obtained from PARAVIEW slices at the final time step and averaged in tangential direction based on the axisymmetric nature of the line vortex.

The spatially-averaged values for the axial velocity are presented in Figure 3.6. Apart from the geometry with the shortest inlet length, there seems to be no influence of the outlet length on the axial velocity. There are significant differences between $M_{2.5D}$ and the other cases. The grids with a longer inflow length (M_{5D} & $M_{7.5D}$) predict a wake-like profile in Figure 3.6a, which is not present for the short inlet. In the middle of the contraction, Figure 3.6c, the shorter inlet length causes a jet-like profile to appear. This increase of axial velocity at the centerline is not visible in the other two cases. This jet-like profile was also not visible in the experimental measurements.
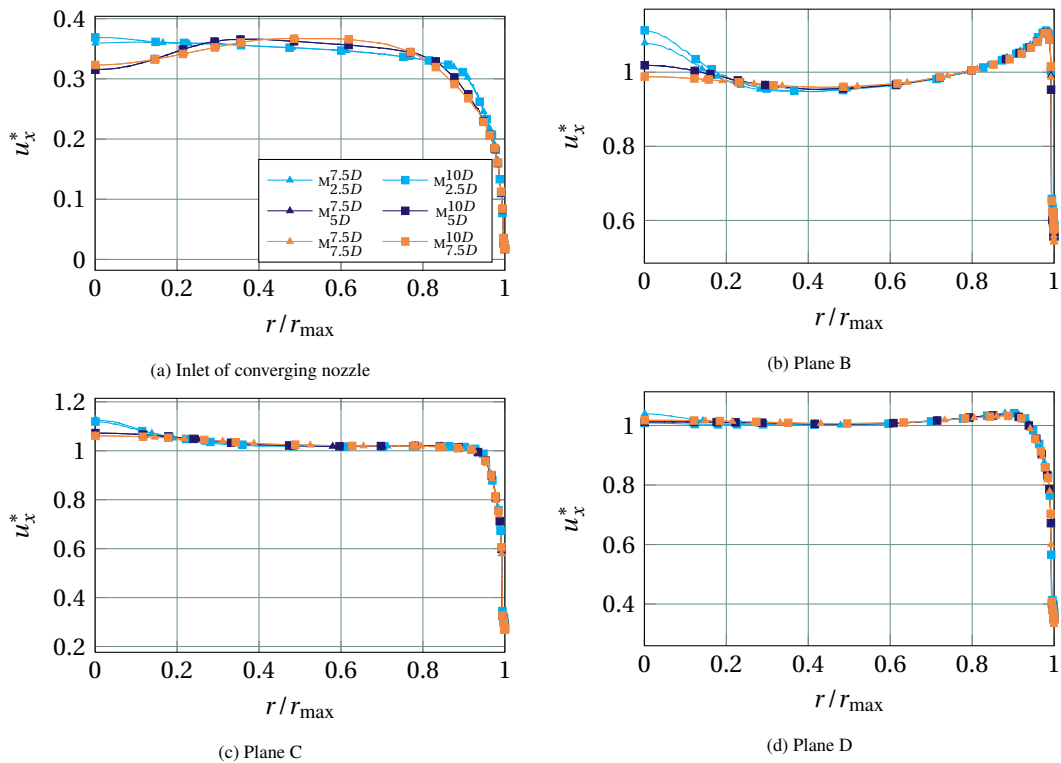
Figure 3.6: Profiles of spatially-averaged normalized axial velocity for the domain length study.

The radial velocity was three to four orders of magnitude smaller than the inflow velocity for all simulated cases. It was therefore correct to neglect the influence of the radial velocity when specifying the Lamb-Oseen vortex as an inflow condition. Again, the outlet length only significantly affects the results for the $M_{2.5D}$ grid. The differences in u_θ are more pronounced at the inlet and outlet of the converging nozzle; Figures 3.7a and 3.7b. The differences between the M_{5D} and $M_{7.5D}$ simulation show the influence of swirl decay between the inlet and the measurement section. This decay is due to viscous diffusion which

reduces the vortex strength and moves the peak of tangential velocity outwards. The velocity distribution also behaves less like the profile of a Lamb-Oseen vortex, indicating a secondary influence from the no-slip condition at the walls on the vortex decay. The spatially-averaged profiles for the pressure coefficient are given in Figure 3.8. Just as for the velocity profiles, the

(a) Inlet of converging nozzle

(b) Plane B

(c) Plane C

(d) Plane D
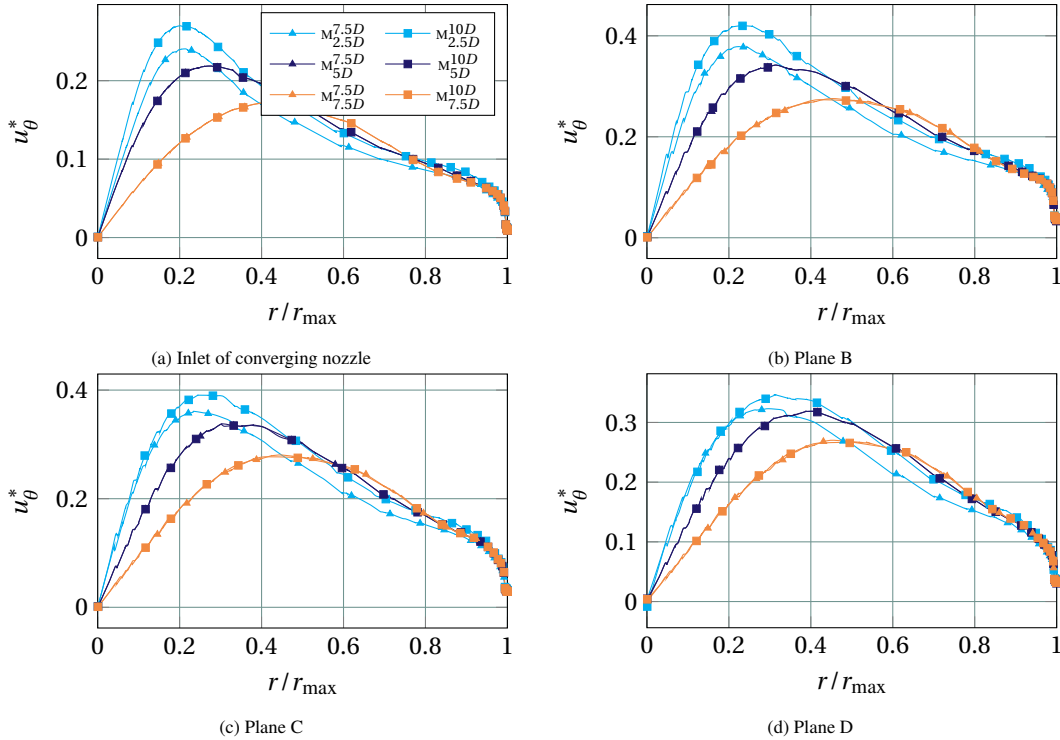
Figure 3.7: Profiles of spatially-averaged normalized tangential velocity for the domain length study.

results obtained for $M_{2.5D}^{7.5D}$ and $M_{2.5D}^{10D}$ display a significant influence of the outlet length. The other two inlet lengths show a very small difference between the pressure for the different outlet lengths. The differences between the M_{5D} and $M_{7.5D}$ cases are again attributed to the swirl decay, which leads to a higher tangential velocity in the center of the core for the M_{5D} case leading to a lower pressure coefficient. The differences between the outlet lengths are very small, and become smaller in the Venturi throat (Figure 3.8c), i.e. the region of interest. Such a small difference might be attributed to the lack of convergence of the simulations, which are of unsteady nature.

The magnitude of the vorticity, Figure 3.9, is predominantly determined by the axial vorticity, Figure 3.10. Again, the shorter inflow length on $M_{2.5D}$ leads to a dependency on the outlet length, which is absent for the other geometries. The decay of swirl for the longest inflow length $M_{7.5D}$ manifests itself also in the vorticity distribution, which is flatter than for the $M_{2.5D}$ and M_{10D} grids. The differences between the three different inlet lengths are less pronounced in the middle of the throat.

The averaged radial distributions of the turbulent kinetic energy are provided in Figure 3.11. The same conclusions can be drawn regarding the dependence of $M_{2.5D}$ on the outflow length. Differences are more pronounced after the converging nozzle (Figures 3.11b and 3.11c) than before (Figure 3.11a). The differences between the M_{5D} and M_{10D} cases are again attributed to the decay of swirl for the latter case, leading to significant differences in the radial turbulent kinetic energy profile. The strain-rate tensor is larger for the M_{5D} case due to the higher tangential velocity, which in return leads to a larger production of turbulent kinetic energy by the SST model following the Boussinesq hypothesis. This explains the larger value of the M_{5D} compared to M_{10D} after the converging nozzle.

3.3.2. Conclusions

The results of the grid with the shorter inflow length $M_{2.5D}$ was the only grid to display significant differences in predicted quantities for the two outlet lengths ($7.5D/10D$). The axial velocity profile, which has a dip in the pressure close to the vortex axis, visible in the M_{5D} and $M_{7.5D}$ simulations, is predicted differently by the $M_{2.5D}$ simulation. These two observations lead to the disqualification of the short inflow length. The differences between the M_{5D} and $M_{7.5D}$ simulations can be explained by the significant difference in the distribution of tangential velocity u_θ, which has significant repercussions for the pressure. The difference in tangential velocity was explained to be a result of swirl decay due to viscous diffusion. Since only the frictional effects of having a longer inflow length are assumed to cause the differences between the M_{5D} and $M_{7.5D}$ simulations, an inlet length of M_{5D} was chosen. No large differences were found between using a shorter or longer outflow section, apart from a small difference in pressure. This difference in pressure is expected to be smaller for time-averaged unsteady simulations
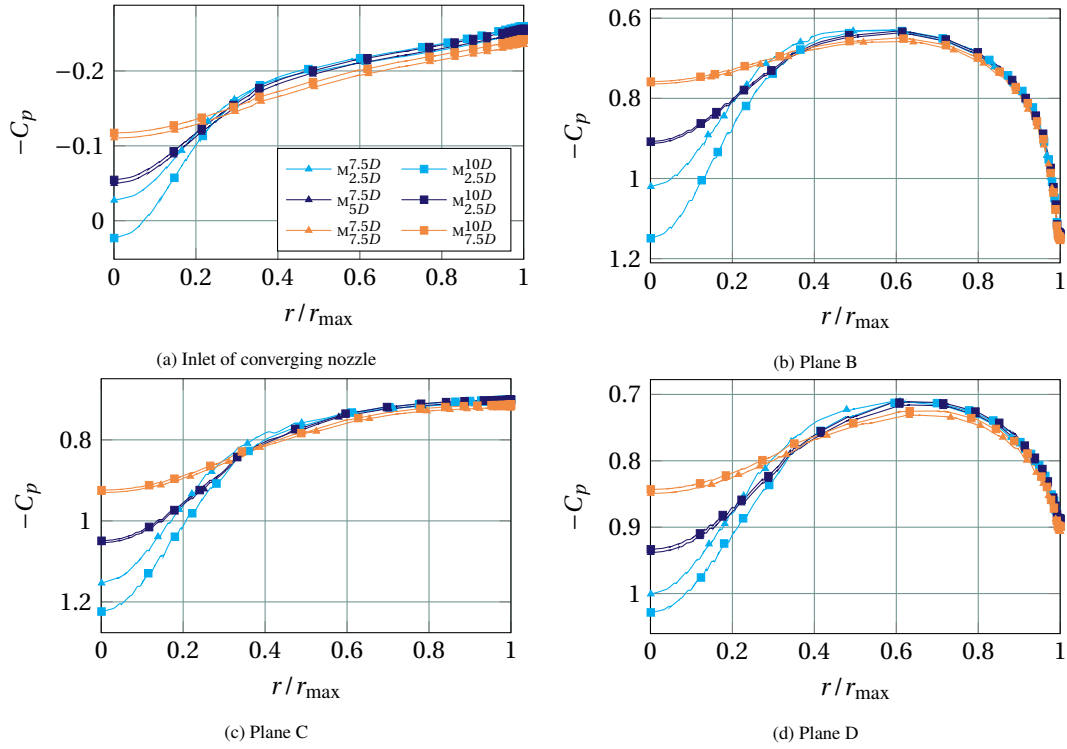
Figure 3.8: Profiles of spatially-averaged pressure coefficient for the domain length study.
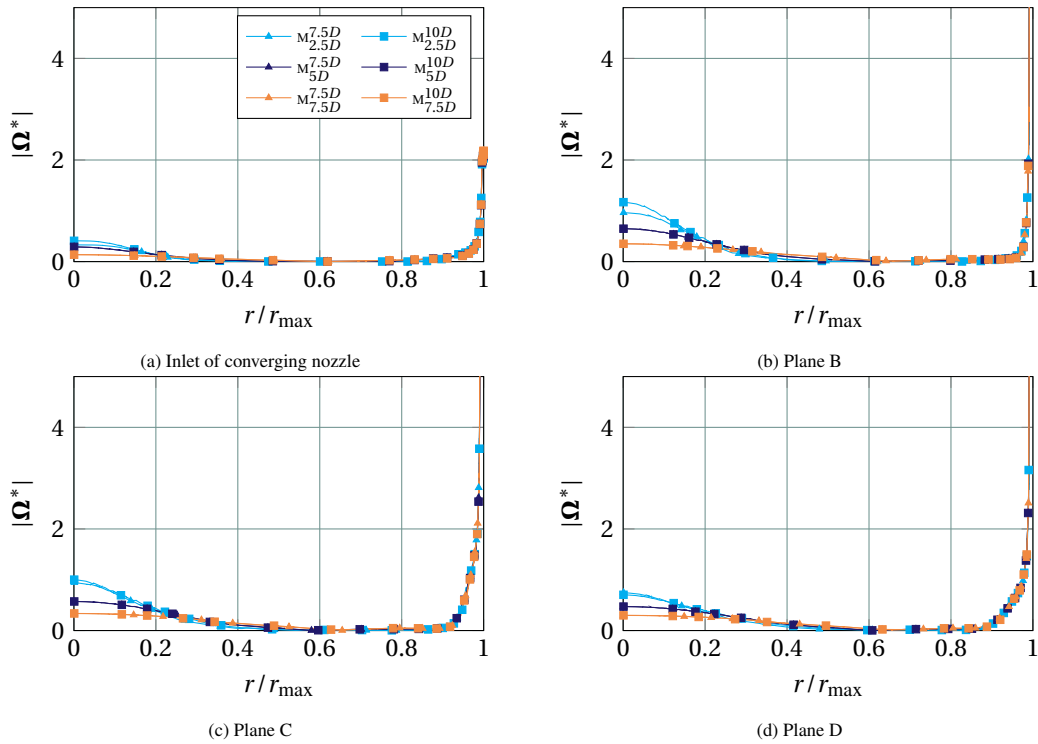
Figure 3.9: Profiles of patially-averaged normalized vorticity magnitude for the domain length study.

and the difference is relatively small compared to the differences between the inflow lengths. The $M_{5D}^{7.5D}$ grid was therefore chosen for the final grid geometry.
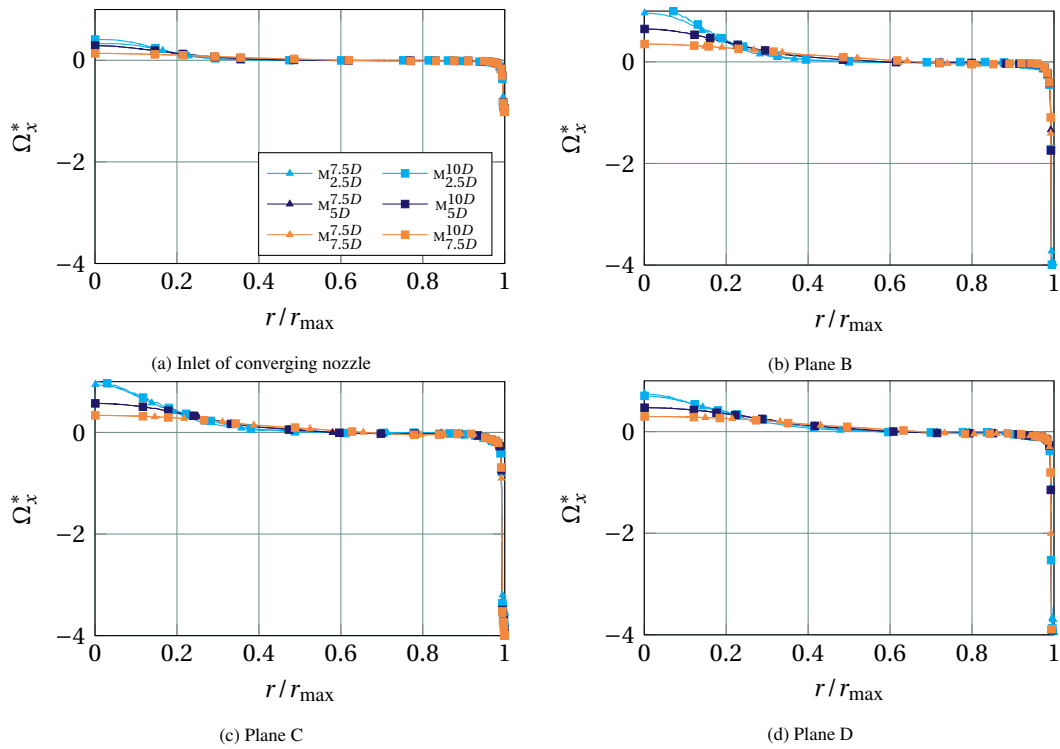
Figure 3.10: Profiles of spatially-averaged normalized axial vorticity for the domain length study.
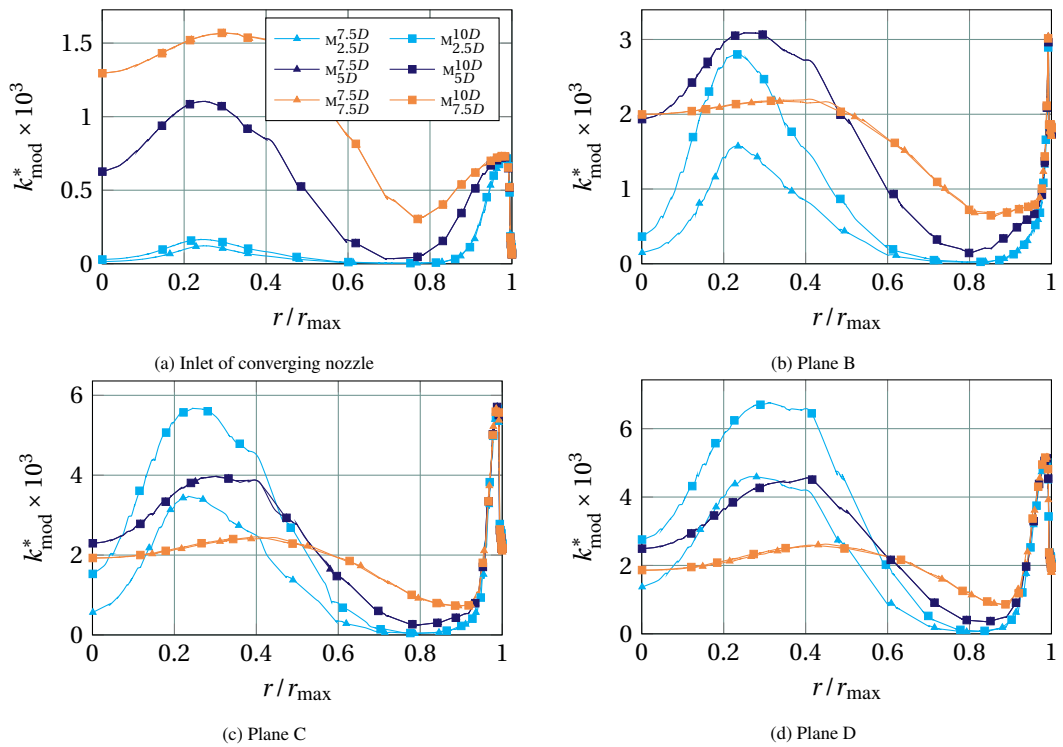
Figure 3.11: Profiles of spatially-averaged normalized turbulent kinetic energy for the domain length study.

3.4. Tuning of the inflow condition

The specified size of the viscous core r_v and the circulation at the inflow boundary Γ_0 were tuned so that the angle of the velocity vector could be matched to the one generated by the swirl generator at the inlet of the converging section.

$$\beta = \text{atan}(u_\theta/u_x) \tag{3.9}$$

The angle β is used only in the case of a radial guide vane swirler. The benefit of using the swirl angle as a reference is that it is independent of the Reynolds number for $Re > 3000$ [94]. This implies that the specified Lamb-Oseen vortex for the higher flow rate $\dot{Q} = 10.0 \text{ ls}^{-1}$ should yield the same distribution of β as for $\dot{Q} = 4.56 \text{ ls}^{-1}$ at the measurement location. This angle is measured most accurately close to the wall according to Steenbergen & Voskamp [95]. The velocity profile in [9] was measured at plane A. It was not possible to achieve the same velocity angles close to the hub of the swirl generator ($0.4 \leq r/r_{\text{inlet}} \leq 0.6$). The numerically obtained velocity angles agree better with the experimental values towards the wall, except close to the wall; i.e. $r/r_{\text{inlet}} \geq 0.92$. The achieved distributions are compared to the experimental measurements in Figure 3.12 for both flow velocities. The tuning parameters in Table 3.6 were obtained by trial and error after assessing the result after 6000 time steps. The data was not time-averaged. Table 3.6.
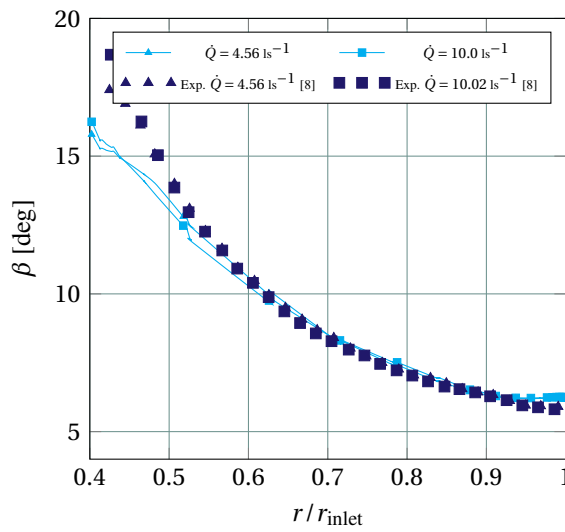
Figure 3.12: Comparison of velocity angles for different values of the circulation Γ_0 and viscous core radius r_v/r_{inlet} at plane A.

Table 3.6: Lamb-Oseen characteristic parameters for flow rates used in wetted and cavitating vortex simulations.

Parameter	$\dot{Q} = 4.56 \text{ ls}^{-1}$	$\dot{Q} = 10.0 \text{ ls}^{-1}$
r_v/r_{inlet}	0.05	0.05
$\Gamma_0/10^{-2} \text{ m}^2\text{s}^{-1}$	3.75	8.22
$u_{x_{\text{inlet}}}/ \text{ms}^{-1}$	2.067	4.533

3.4.1. Swirl decay

Tuning the parameters in Table 3.6 was not straightforward, as the exact amount of decay and the influence of the wall could not be determined. The core radius r_v was more difficult to tune than the circulation Γ_0, which simply increased or decreased the tangential velocity over the entire radius. The decay of swirl from the inlet to the measurement location A was investigated to be able to tune the viscous core radius more accurately. The streamwise decay of swirl is expressed by the Swirl Intensity Decay Rate (SIDR). The swirl number Sn was calculated using the definition by Gupta [96], excluding the pressure terms and turbulent stress terms as they are not commonly included in the consulted literature:

$$Sn = \frac{\int_0^\infty u_x u_\theta r^2 \, \text{d}r}{R \int_0^\infty u_x^2 r \, \text{d}r}. \tag{3.10}$$

Experimental research by Steenbergen & Voskamp [95] and more recent numerical results by Najafi et al. [97] show that the SIDR decreases with an increasing Reynolds number, similar to the friction factor c_f for pipes. This is due to a growing capacity of the transfer of tangential momentum with an increasing Reynolds number, reducing the magnitude of the SIDR

[97]. The Reynolds numbers in this work are of $\mathcal{O}(10^5)$. This is higher than the measurements by both Steenbergen & Voskamp [95] and Najafi et al. [97]. The SIDR is therefore expected to be rather limited. Furthermore, Najafi et al. [97] showed that the the variation in SIDR is more dependent on the swirl intensity than the Reynolds number.

The integral values in Equation (3.10) were calculated at all x-coordinates of the inlet using PARAVIEW. This means that the values are integrated over the entire pipe cross-sectional area instead of the radius. Since the swirl number is a ratio of both integrals, this is not expected to influence the results. The axial evolution of the swirl number is presented in Figure 3.13. There is a negligible difference between the SIDR of the three vortices that are compared in Figure 3.13b. The profiles appear to be parallel and shift upward if the initially specified circulation increases. This behavior was expected, but shows that, for the range of swirl numbers that are of practical interest for this study, there is negligible influence of the initial swirl strength on the SIDR. The Reynolds number is also 1.5 orders of magnitude larger than the numerical results of Najafi et al. [97], which together with the small magnitude of the swirl number explains the similarity of the SIDR across the graphs in Figure 3.13b.

The deviating behavior of the $r_v/r_{max} = 0.05$ vortex close to the inlet of the domain in Figure 3.13a is caused by the relatively low amount of cells around the symmetry axis. This is also expected to cause the lower instead of higher value of swirl at the inlet compared to the $r_v/r_{max} = 0.10$ vortex. In general, the $r_v/r_{max} = 0.05$ and $r_v/r_{max} = 0.10$ simulations show a different behavior than the other two cases, which are parallel. This difference was investigated by looking at the evolution of the vortex core diameter from the inlet towards the converging section. Based on vortex theory, the Lamb-Oseen vortex is expected to decay with the square root of time based on viscous diffusion:

$$r_v(t) = \sqrt{4\alpha_R \nu_t t} \qquad (3.11)$$

This is illustrated in the comparison between the theoretical decay following the relation in Equation (3.11) and the measured viscous core radius in Figure 3.14. The viscous core radius was determined by determining the radial position r at which the maximum tangential u_θ is reached. The results indeed show that the vortex decays purely due to viscous diffusion, but that there is a secondary effect due to blockage from the wall causing a deviation from the theoretical profile.

(a) Constant $\Gamma_0 = 3.75 \times 10^{-3}$

(b) Constant $r_v/r_{max} = 0.12$
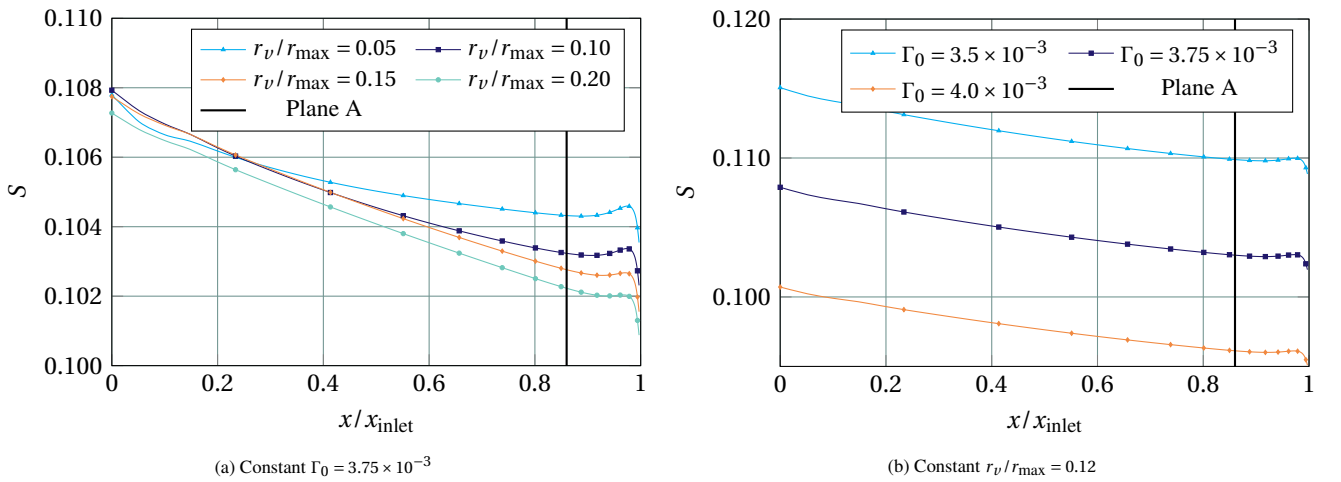
Figure 3.13: Comparison of axial swirl decay at $Re = 340500$.

(a) Constant $\Gamma_0 = 3.75 \times 10^{-3}$

(b) Constant $\Gamma_0 = 3.75 \times 10^{-3}$
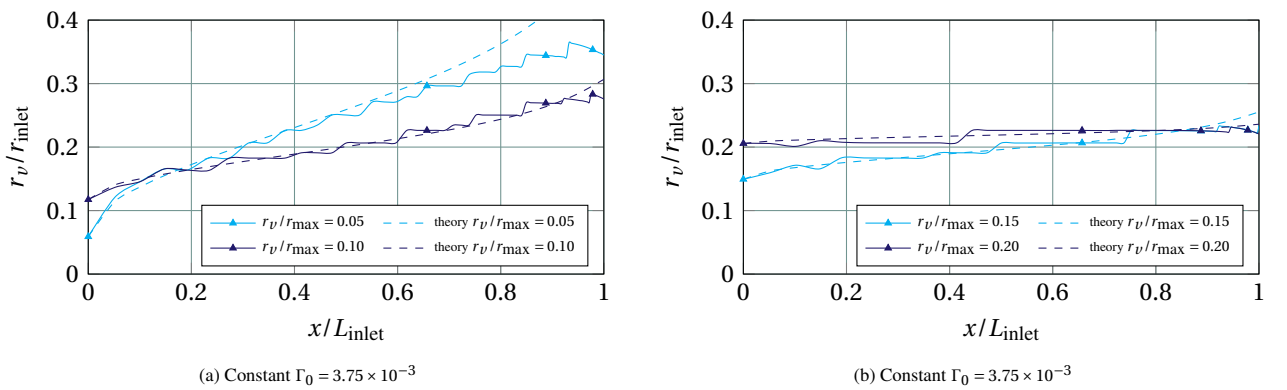
Figure 3.14: Decay of swirl in the inlet section due to viscous diffusion at $Re = 340500$.

3.5. Conclusions

The computational domain was based on the Venturi tube used in experimental measurements by Rudolf et al. [8]. The sharp edges are expected to lead to potential sheet cavitation at the front and back of the parallel section of the venturi. An OH-type grid topology was chosen based on superior results for similar simulations and the grid was constructed from a single block. The non-dimensional resolution in streamwise and spanwise direction (x^+ and z^+) could not be increased to the level of a LES grid due to the constraint of avoiding local grid refinement and computational expenses. Four grids were constructed, whereby the coarsest grid had just under 2 million cells and the finest grid about 14.5 million. The required length of the parallel inlet and outlet sections of the domain was studied in a separate study. Three inlet lengths were assessed of which the middle one was selected and the shortest of the two analyzed outlet lengths was chosen. The inlet boundary condition was determined by a Lamb-Oseen vortex profile. The values of the circulation and the location at which the maximal tangential velocity was reached, were tuned using trial and error to obtain velocity angles as close as possible to experimental values at measurement location A. This study also highlighted the significant decay due to viscosity and identified a secondary influence of the wall on this decay.

Data of the analyzed flow variables was extracted from REFRESCO using monitor disks and lines at multiple locations inside the venturi. Both monitors used first-order nearest-cell interpolation for wetted flow simulations, whereby the disk monitor did not allow for updating coordinates to the cell centers from which the values were interpolated. The interpolation method was changed to a second-order method incorporating the gradient for the cavitating vortex simulations. The isocontours of the vapor pressure, needed for the spectral analysis of the cavity dynamics, were obtained using the co-processing ability of REFRESCO. The link between PYTHON and PARAVIEW was subsequently used to determine the diameter and centerline location at equally-spaced locations in streamwise direction. The procedure from Bosschers [2] was used to determine the parameters of signal segmenting and processing.

Having discussed all relevant literature in Chapter 2 and the numerical set-up in this chapter, all building blocks are present to interpret the results for the wetted and cavitating line vortex simulations in the next two chapters.

<div style="text-align: right; font-size: 3em;">4</div>

Results of wetted vortex simulations

The goal of this chapter is twofold: first, it serves to outline which turbulence model is most suited to solve the flow in a wetted vortex, more particularly in the vortex core. These findings will be compared to the cavitating vortex results in Chapter 5, to determine whether they also hold for a cavitating vortex. The size of the vapor core depends on the pressure on the vortex axis and the shape of the pressure profile in radial direction. The minimum pressure and profile shape were shown in Section 2.2.3 to solely depend on the tangential velocity profile and its maximum value at the viscous core radius. For the test case described in this thesis, the prediction of axial velocity and the gradient in streamwise direction are not as important as in the case of a tip vortex. This is due to the fact that the pressure drop inside the Venturi is controlled mostly by the geometry, which causes an increase of axial velocity.

The second goal of this chapter is to verify the performance of the Explicit Algebraic Reynolds Stress Model (EARSM) by determining whether the solution is independent of the discretization in space and time. This verification is needed to conclude whether or not the EARSM is a suitable model for vortex flows, as i.a. Pereira [10] noted that Reynolds Stress Models (RSMs) have high grid resolution requirements and i.a. Asnaghi [98] also stressed the importance of having enough cells inside the vortex core.

The flow conditions of all wetted vortex simulations are summarized in Table 4.1. The results can be split into two parts, where the first part concerns the comparison in predictions by the Improved Delayed Detached-Eddy Simulation (IDDES), EARSM and $k - \omega$ Shear Stress Transport (SST) turbulence models. The second part deals with the verification study of the results obtained with the EARSM model. The turbulence models were compared on M_1 due to i) the relatively low computational cost, ii) the already known shortcomings of the SST model and iii) the verification study of the EARSM model that is performed on all four grids. An additional simulation of the IDDES model was done on M_2 to determine the improvement when using a finer grid. The verification study was carried out using the EARSM, as the IDDES solutions are inherently grid-dependent. The time step for the simulations was based on the numerical criterion that the maximum Courant number, defined as $Co = u\Delta t/\Delta x$, should be at most equal to one to reduce the temporal discretization error. The maximum Courant number occurred at the sharp edges of the Venturi throat. A higher Courant number ($Co = 10$) was chosen for the verification study to reduce computational cost, after verifying that results were not affected by the time step increase.

Table 4.1: Overview of wetted vortex simulation parameters. Equal color indicates that the same parameter value is shared across simulations.

Simulation	Δt /10^{-5}s	$\dot{Q}$ /ls^{-1}	u_∞ /ms^{-1}	Re_{throat} /10^5	I	ν_t/ν	max (Co)
M_1 SST							
M_1 EARSM	4.0						1.0
M_1 IDDES							
M_2 IDDES	3.2						
M_1 Co10	40.0						
M_2 Co10	32.0	4.56	6.45	3.4	1.0	1.0	
M_3 Co10	25.6						
M_4 Co10	20.5						10.0
M_4 Co12.5	25.6						
M_4 Co15.6	32.0						
M_4 Co19.5	40.0						

4.1. Coarse mesh performance

In this section the results from the SST, IDDES and EARSM turbulence models are compared on the coarsest mesh M_1. The wetted vortex and the surrounding streamlines are visualized in Figure 4.1 and already indicate differences between the

results of the three models regarding the prediction of the vortex size as well as showing the vortex instabilities in IDDES and EARSM simulations. The vortices are visualized using the non-dimensionalized Q-criterion (see Section 2.2.4), so the isocontours only represent connected areas of vorticity and do not give a direct indication of the viscous core size of the wetted vortex.
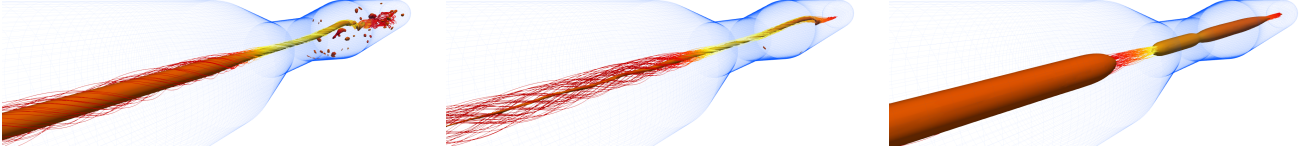
Figure 4.1: Vorticity isocontours ($Q_{\text{crit}} = 5$) and velocity streamlines for the wetted flow vortices on M_1 at $t = 0.694$ s, colored by axial velocity (yellow is higher). From left to right: IDDES, EARSM and SST.

4.1.1. Convergence behavior

The SST simulation converged to the convergence criterion of $L_\infty = 1 \times 10^{-6}$ for all flow variables within the fewest number of iterations, followed by the EARSM and IDDES models. This behavior was expected due to the increased amount of model complexity from SST to EARSM and IDDES as well as the scale-resolving properties of the latter. The iterative convergence plots of the simulations for this coarse mesh comparison study can be found in Appendix D.1.1. A sudden increase of pressure ($\approx 5\%$) occurred in the course of the simulation, without affecting the other flow variables. This effect was caused by the vortex becoming instable in the diverging nozzle. The vortex of which the end (in the diverging nozzle) started to rotate about the vortex axis in the throat led to a considerable start-up effect in the EARSM and IDDES simulations. The SST simulation did not show such unsteady behavior, and the vortex remained axisymmetric throughout the domain. The unsteady periodic phenomenon which occurs, is analyzed more thoroughly in Section 4.1.5 due to its prevalence in all simulations in this thesis (except the SST one). The Transient Scanning Technique (TST)-B plots used to determine the time-averaging period can be found in Appendix D.1.2. The runtime, averaging period and corresponding statistical uncertainty are given in Table 4.2.

Table 4.2: Time-averaging information and statistical uncertainty for the coarse mesh comparative study of the wetted vortex. T_{total} indicates total runtime, T_{avg} indicates period used for time-averaging.

Simulation	T_{total}/s	T_{avg}/s	$U_{\text{stat}}(u_\theta)$/ %	$U_{\text{stat}}(u_x)$/ %	$U_{\text{stat}}(p)$/ %
M_1 SST	0.816	0.616	5×10^{-3}	7×10^{-4}	2×10^{-3}
M_1 EARSM	1.224	0.424	1×10^{-2}	9×10^{-3}	3×10^{-2}
M_1 IDDES	1.224	0.620	2×10^{-2}	4×10^{-3}	2×10^{-1}
M_2 IDDES	0.606	0.192	7×10^{-3}	1×10^{-3}	2×10^{-1}

4.1.2. Flow field results

Velocity angles

The angle of the velocity vector, β, was compared at plane A, which is where the velocity angle was also measured for the reference experimental data [8]. As can be seen in Figure 4.2, the different models agree from a radius of approximately $0.65 r/r_{\text{inlet}}$ onwards, both with each other as with the experimentally measured flow angle. There are differences visible closer towards the centerline, where especially the IDDES model predicts a larger velocity angle and a more narrow vortex core. Even though this could not be avoided by tuning the inflow condition in Section 3.4, the difference (caused by the stronger viscous decay of the vortex in the Reynolds-Averaged Navier-Stokes (RANS) models) is expected to influence the velocity field further downstream. The difference in the growth/ decay of modeled turbulence is apparent from Figure 4.3. This figure shows that turbulent kinetic energy increases from the inflow boundary towards the Venturi section in SST and EARSM simulations, but quickly decreases for the IDDES. The modeled turbulent kinetic energy in the IDDES starts decreasing as soon as the local cell size is small enough to make the model switch to the Large Eddy Simulation (LES) turbulence length scale. Given the similar trend of ω for the three models, the specific dissipation rate remains mostly unaffected by the change in length scale. The effect is further investigated in Section 4.1.3.

Analyzed variables in Venturi throat

The normalized tangential and axial velocity are presented in Figure 4.4a and Figure 4.4b. Regarding the tangential velocity, similar behavior can be noted for the EARSM and SST simulations, which both underpredict the tangential velocity in the viscous core. The velocity gradient in the core is slightly higher for EARSM model, but then decreases and both RANS models predict a similar viscous core size. The IDDES model matches the experimental measurement more closely, but still
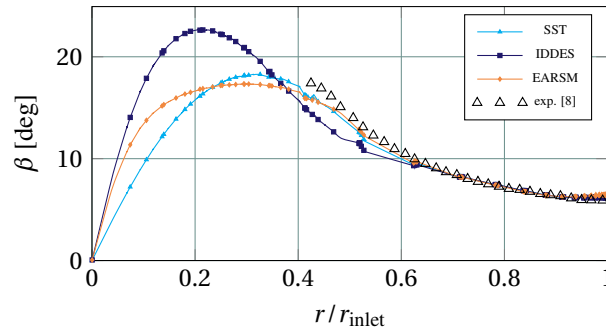
Figure 4.2: Angle of velocity vector measured at plane A for wetted vortex simulations on M_1.
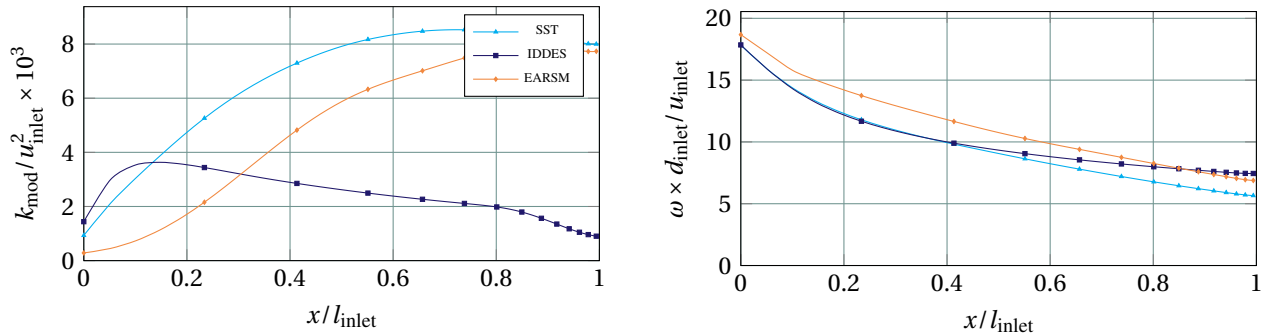
Figure 4.3: Decay of turbulence in the inlet section for wetted vortex simulations on M_1. Data was obtained from PARAVIEW at $t = 0.816$ s. Modeled turbulent kinetic energy (left) and specific dissipation rate (right) are spatially averaged using slices with a radius of $0.57 r_{\text{inlet}}$. Differences at $x = 0$ are due to interpolation in PARAVIEW between the inlet patch and the first cell center in the field.

overpredicts the viscous core size, combined with a too low value of u_θ at the viscous core edge.

Looking at the axial velocity, the IDDES shows a jet-like profile, i.e. an increase of axial velocity at the centerline, which was not measured in the experiments. The EARSM and SST models show identical axial velocity profiles. The pressure coefficient

(a) Normalized tangential velocity

(b) Normalized axial velocity
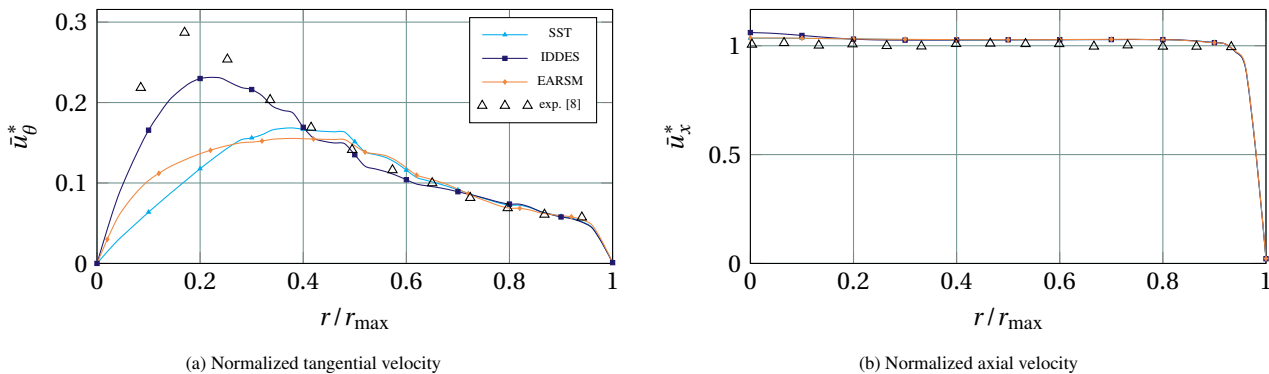
Figure 4.4: Normalized tangential and axial velocity measured at plane C for the comparison study on M_1 of the wetted vortex.

the reference location C is presented for M_1 in Figure 4.5a. As both EARSM and SST models had similar predictions of tangential and axial velocity, their pressure distributions are similar. The larger velocity gradient of the EARSM simulation close to the centerline leads to a larger pressure gradient in the same region, but overall both profiles are almost parallel. The IDDES predicts a stronger radial pressure gradient, as the tangential velocity is less diffuse. The larger velocity gradient and higher maximum of tangential velocity lead to a more defined pressure-dip, with a lower minimum at the centerline. Both EARSM and SST models slightly overpredict the tangential velocity at larger radii due to the diffusion, and the low tangential velocity peak for the EARSM translates into the highest pressure coefficient. From $r/r_{\text{max}} > 0.7$ onwards, the pressure coefficient profiles are parallel for all three models as the velocity profiles (and gradients) also match. The pressure at the wall is clearly determined by a combination of the maximal tangential velocity, defining the minimum pressure, and the velocity gradient, defining the pressure gradient in the radial direction.

The normalized modeled kinetic energy is shown in Figure 4.5b. As expected, the IDDES model hardly predicts any modeled turbulence in the vortex core, whereas the SST model predicts a slightly decreasing but substantial amount of

turbulent kinetic energy throughout the vortex core. The EARSM behaves somewhere in between: a larger turbulent kinetic energy for most of the domain, but a strong reduction (although not to zero) close to the centerline. As highlighted by Liebrand [5], the reduction is linked to the space-dependent value of C_μ, which through the relations in Equations (2.27), (2.29) and (A.25) $C_\mu = f(1/\omega^2)$ instead of $f(1/\omega)$ for the SST model. The increased dissipation ω inside the viscous core therefore leads to a larger reduction of ν_t and modeled turbulent kinetic energy k_{mod}.

(a) Pressure coefficient

(b) Normalized turbulent kinetic energy
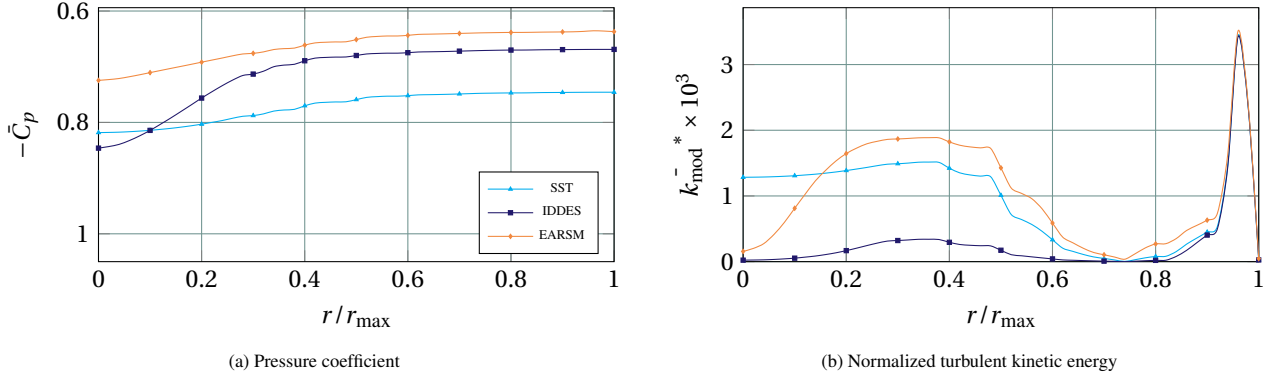
Figure 4.5: Pressure and turbulent kinetic energy measured at plane C for the comparison study on M_1 of the wetted vortex.

The relation between pressure and velocity for a Lamb-Oseen vortex was used to determine an approximate C_p curve for the experimental results (even though they were not measured). A Lamb-Oseen velocity profile was first fitted through the experimental results, and the pressure distribution was subsequently obtained from:

$$\frac{\partial p}{\partial r} = \rho \frac{u_\theta^2}{r},$$

(4.1)

which in itself is derived from the conservation of momentum in the radial direction. The constant that accompanies the integral of the Right-Hand Side (RHS) of Equation (4.1) was determined such that the pressure matches the IDDES value at the wall. The fitted profile is therefore only an indication of the model performance and is only used for qualitative comparison of the predicted pressure dip at the centerline. The fits were obtained by adapting the circulation Γ_0 and the viscous core size r_v of which the respective values are provided in Table 4.3. The corresponding graphs are given in Figure 4.6. The specified circulation for the experimental fit and the IDDES is almost equal, whereas the circulation of the SST simulation was increased to make the profile match a Lamb-Oseen vortex within the core.

The wetted vortex simulated by the IDDES model resembles a Lamb-Oseen vortex at all radial positions, whereas the SST model only does so within the vortex core. The strong velocity gradient of the vortex predicted by the EARSM close to the centerline, followed by the viscous diffusion of the vortex viscous core, leads to a deviation from the Lamb-Oseen profile already close to the centerline.

Outside the viscous core, the IDDES model and the experimentally-fitted C_p distribution show the same pressure gradient. Nevertheless, the minimum pressure coefficient is still overpredicted as a result of the too slight velocity gradient in the viscous core. The increased circulation for the SST, used to fit the theoretical profile to the simulation, is the reason for the higher value of the tangential velocity outside the viscous core and vice versa for the EARSM fit.

The fitted vortices are free vortices; i.e. not confined by a wall, leading to the differences closer to the Venturi wall. The shape of the tangential velocity profile outside the viscous core does not impact the shape of the radial distribution of the pressure coefficient, as the fitted pressure profile and the SST solution almost match each other. The largest difference in this case is expected to be due to the u_θ profile having a smaller gradient and a lower maximum value than the fitted one inside the vortex core.

Table 4.3: Fitting parameters (circulation Γ_0 and viscous core radius r_v) used to obtain Lamb-Oseen tangential velocity and pressure profiles in Figure 4.6

Simulation	r_v/r_{throat}	$\Gamma_0/10^{-2}\text{m}^2\text{s}^{-1}$	u_∞/ms^{-1}
experiment [8]	0.170	4.20	-
M_1 SST	0.400	5.70	6.4511
M_1 EARSM	0.220	3.60	6.4511
M_1 IDDES	0.215	4.25	6.4511
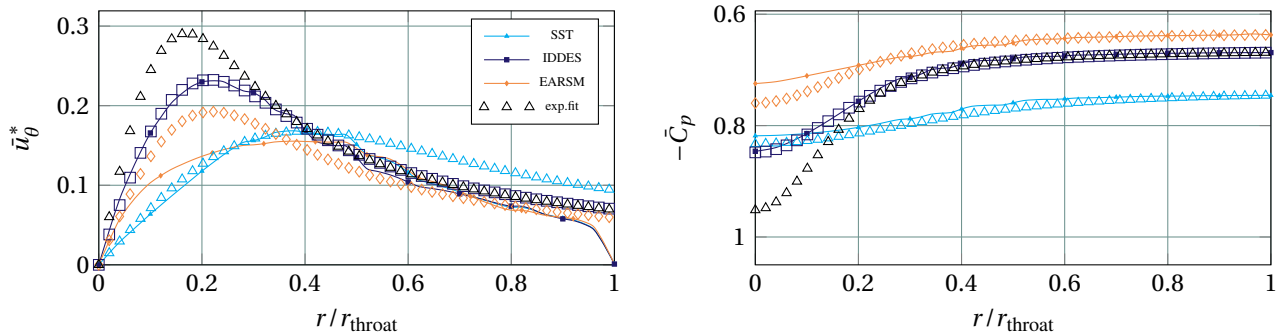
Figure 4.6: Fitting of Lamb-Oseen tangential velocity (left) and pressure profiles (right) to experimental and numerical results for the wetted vortex.

4.1.3. IDDES modeling performance

The IDDES model showed promising performance in the previous section, especially compared to the EARSM which requires similar computational effort. In order to assess the behavior of IDDES on a more refined grid, the model was also run on M_2 and will be compared to the result on the coarser mesh. The LES region of the model should allow for the sustenance of resolved velocity fluctuations and turbulence away from the walls. The LES regions are assessed in the second part of this section, followed by the resolved part of the turbulent kinetic energy and the resolved Reynolds stresses.

Performance comparison between grids

The runtime and averaging period for the M_2 IDDES simulation were shorter than on the M_1 grid. The runtime, averaging period and statistical uncertainty were presented in Table 4.2 and the statistical convergence plots according to the TST-B method can again be found in Appendix D.1.2. The IDDES results in Figure 4.7 show that the model predicts the tangential velocity profile in the core slightly better on the finer M_2 grid. This translates into a pressure minimum which is also lower.

The pressure coefficient outside the core in Figure 4.7c seems to be shifted slightly upwards on the coarser grid. This is due to the increased amplitude of the pressure fluctuations caused by an instability of the vortex. This instability is just occurring on the finer grid as can be seen in Figure 4.8 and the pressure was still lower on average. The parallel shift was also noticed for the EARSM model mentioned in the previous section. The increase in oscillation amplitude occurred suddenly and at different time steps between grids and models. The pressure was already statistically converged and the event could not be captured using the TST technique. Formally one should continue the simulation, but experience with the other simulation learned that the only effect is the upward parallel shift in the C_p graph. As the other flow variables were not affected, the runtime was not increased due to the additional computational expense this would entail. The oscillation frequency will be more closely examined in Section 4.1.5.

Ability to resolve turbulence

The LES and RANS regions are defined by the local turbulence length scale. The LES regions are visualized inside the contraction for M_1 and M_2 in Figure 4.9.

The velocity fluctuations in axial, radial and tangential directions (u'_x, u'_r, and u'_θ) were obtained by subtracting the time-averaged value of each of the velocity components. The Reynolds stress tensor was subsequently calculated as $-\tau_{ij}/\rho = \overline{u'_i u'_j}$. This tensor was time-averaged to determine the time-averaged resolved part of the turbulent kinetic energy, as $\bar{k}_{res} = 1/2\overline{u'^2_i}$. The statistical convergence of the normal components of the Reynolds stress tensor can be found in Appendix D.1.2. According to Pope [16], at least 80% of the turbulence spectrum (i.e. the turbulent kinetic energy) should be resolved in good LES simulations. It is clear from Figure 4.10 that this is not the case for the IDDES simulations on both grids. The normalized resolved turbulent kinetic energy is of $\mathcal{O}(10^{-6}-10^{-7})$, showing that there is virtually no turbulent content present in the flow at plane C. The assessment of the statistical uncertainty showed that the uncertainty of the normal components of the Reynolds Stress lies between 10 and 10000% for the different directions (x, r, θ) for the simulation on M_1, whereas the statistical uncertainty on M_2 is of $\mathcal{O}(10^{-1})$. The differences between both grids therefore fall within the statistical uncertainty. This is expected to be due to the periodicity of the velocity signals following the unsteady behavior of the vortex. While this did not affect the integral quantities (except p), it does influence the calculation of the fluctuations using $u' = u - \bar{u}$. A better method would filter out this periodic variation, but was not implemented given the very small magnitude of the fluctuations, that indicates the absence of resolved turbulence. The negligible amount of resolved turbulence is therefore the main takeaway from the IDDES comparison on M_1 and M_2. The absence of fluctuating quantities is due to the lack of turbulence upstream, which could be sustained in the LES area. The definition of the (global) hybrid RANS-LES models does not allow for communication/ transfer of modeled RANS turbulence into the LES zone as resolved turbulence. Thus, the IDDES model has no turbulence to resolve in the free-stream. The definition of the LES model links the local turbulence length scale to

(a) Normalized tangential velocity

(b) Normalized axial velocity

(c) Pressure coefficient

(d) Normalized turbulent kinetic energy
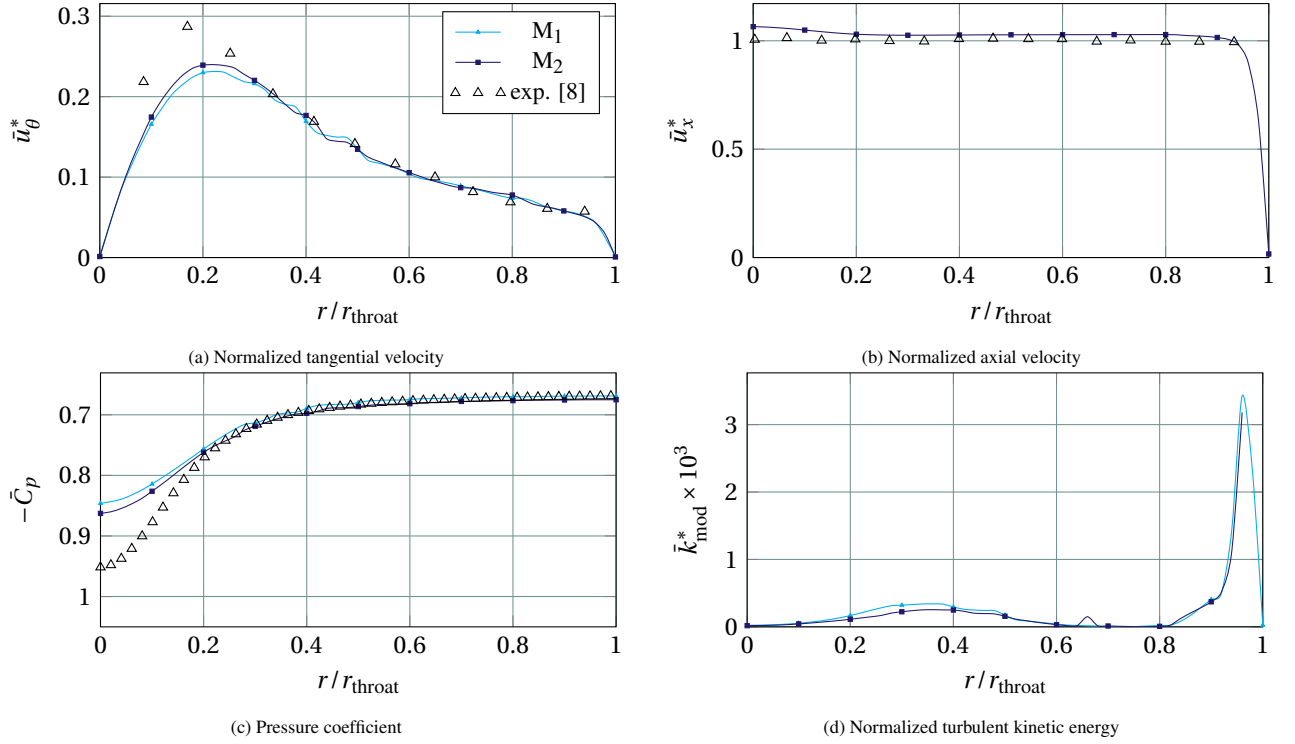
Figure 4.7: IDDES results on M_1 and M_2 measured at plane C for the comparison study on M_1 of the wetted vortex.
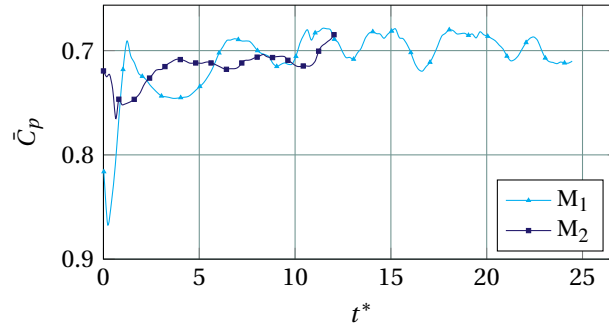
Figure 4.8: Temporal evolution of the pressure signal at $(r, \theta) = (5.4 \times 10^{-3} \, \text{m}, 0.1795 \, \text{rad})$ in plane C.
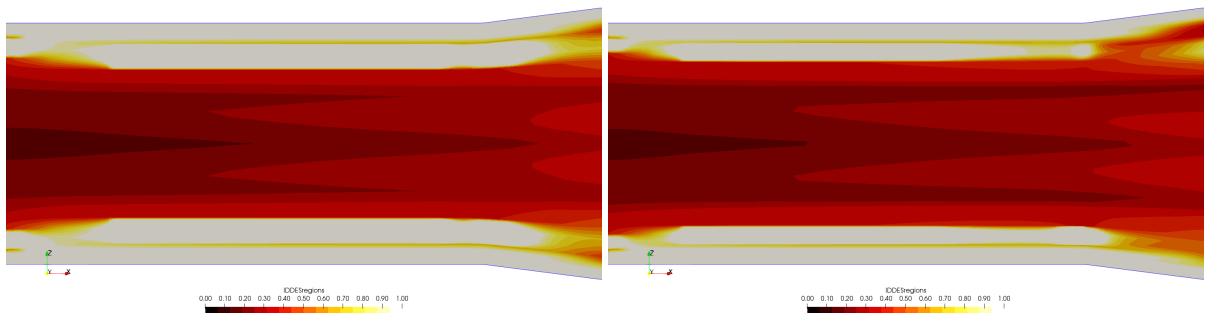
Figure 4.9: LES regions in the contraction on M_1 (left) and M_2 (right) at $t = 0.5712$s, white indicates fully RANS region and red/black indicates LES region.

the maximum cell length Δl (see Equation (2.35)) instead of the ratio $\sqrt{k}/(\beta^* \omega)$. The length scale is incorporated into the dissipation term of the k-equation of the SST model that models the Subgrid-Scale (SGS) turbulence in the LES region. Recalling that the dissipation term is defined as:

$$\mathcal{D}_{\text{SST}}^k = \rho \beta^* k \omega = \rho \frac{k^{3/2}}{l_{k-\omega}}, \tag{2.34 revisited}$$

the amount of modeled turbulent kinetic energy needs to decrease with $\sim 1/l_{k-\omega}$. As previously shown, the specific dissipation rate is not affected by this change in length scale. This reduction of modeled kinetic energy is not balanced by increased production of modeled turbulence, considering the weak contribution of the strain-rate tensor through the Boussinesq hypothesis in the SGSs. Subsequently, the eddy viscosity $\nu_t \sim k/\omega$ also decreases sharply.

In fact, the absence of velocity fluctuations combined with a very low value of the eddy viscosity is similar to solving an almost completely laminar (turbulence-free) vortex. This is in line with the findings of Liebrand [5] for a wetted tip vortex modeled by IDDES and Delayed Detached-Eddy Simulation (DDES). In simulations which use a modeled swirl generator to generate the swirling flow, e.g. [41], the velocity fluctuations originate from the blades of the swirl generator as demonstrated in the results of Saini et al. [41] which are then maintained throughout the LES region, ensuring a turbulent vortex. To generate velocity fluctuations without a geometry, the inflow must already contain turbulent structures. This can be achieved by synthetic turbulence generating methods. The work of Klapwijk [42] is expected to be a valuable contribution for these kinds of cases where turbulence cannot be otherwise generated.
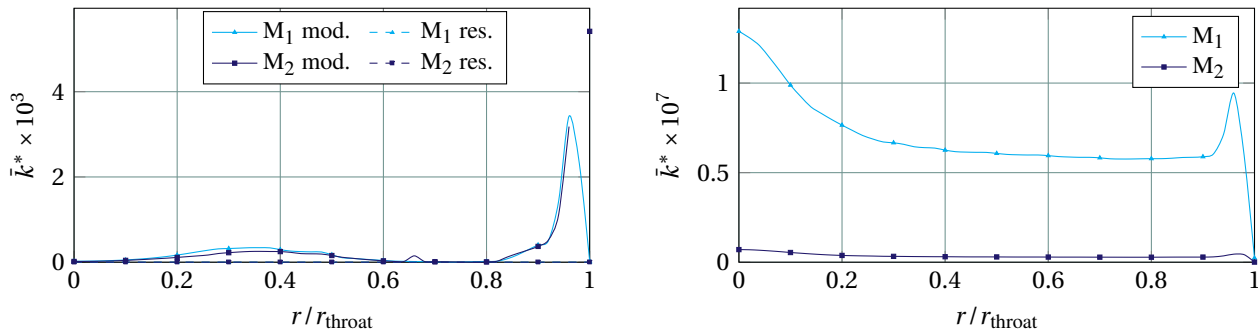
(a) Comparison of resolved and modeled turbulent kinetic energy by the IDDES model on M_1 and M_2 for the wetted vortex.

(b) Comparison of resolved turbulent kinetic energy

Figure 4.10: Comparison of resolved and modeled turbulent kinetic energy at plane C by the IDDES model on M_1 and M_2 for the wetted vortex.

4.1.4. Comparison to previous numerical results from literature

Rudolf et al. presented numerical results for the same experimental test case in [9]. Their results were obtained using a mesh of 5 million cells, clustered around the centerline. The velocity at the non-slip walls of the Venturi tube was treated using a wall-modeled approach. LES (with Smagorinsky SGS model), a RSM and the realizable $k-\varepsilon$ (see [99]) turbulence models were used. Velocity fluctuations for the LES model were generated using a spectral synthesizer. The obtained results did not agree well with the experimental measurements. Both LES and RSM models predicted a vortex core smaller than the one measured in experiments, while the RANS realizable $k-\varepsilon$ model overpredicted the size of the vortex, probably owing to a too large viscous diffusion of the vortex. There was a significant overprediction of the circumferential velocity u_θ in Figure 4.11a for all numerical models at larger radii (i.e. from $r/r_{\text{throat}} > 0.37$). The axial velocity u_x in Figure 4.11b was also overpredicted by all models outside this radius, with significant differences in the vortex core between the two-equation realizable $k-\varepsilon$ model and the more complicated RSM and LES models. The origins of the overprediction were not addressed by the authors. The results from [9] are subsequently compared to the numerical results on M_1 in the present research.

The RANS simulations presented in this thesis show the same shortcoming in predicting u_θ and the viscous core size as the realizable $k-\varepsilon$ of [9]. A noticeable exception is close to the wall, where the current simulations do agree with experimental measurements. The improvement closer to the wall could be due to the wall-resolved approach used for the current simulations instead of the wall-models used in [9]. One hypothesis regarding the overpredicted u_θ is that the excessive production of k and subsequent high ν_t in the core leads to turbulent (numerical) diffusion of the vortex, increasing the tangential velocity outside the core for models based on the Boussinesq hypothesis. This simple explanation is contradicted by the LES and RSM results of Rudolf et al. [9] (RSM not shown, as similar to LES result), which predicted a significantly smaller vortex core, indicating low diffusivity, but overpredicted u_θ just as much at the larger radii. Furthermore, the EARSM results presented in this thesis do not follow the (linear) Boussinesq hypothesis, but show similar behavior as the Boussinesq-based realizable $k-\varepsilon$ and SST simulations.

There are similarities between the IDDES and LES model in the prediction of u_x as they both predict an increase of the axial velocity in the core of the vortex. This increase of u_x is also present for the RSM (not shown), showing a correlation between the narrow viscous core (with a high tangential velocity at the edge) and the axial velocity inside it. Batchelor [100] analyzed an inviscid fluid rotating as a solid body passing through a contraction and noted an increase in the axial velocity close to the vortex axis. This increase is due to a centripetal force induced by the contraction, forcing the vortex lines to move

radially inward, which in turn increases the rotational velocity around the centerline for material elements on the vortex line. The vortex line is also transformed into a spiral which leads to a negative value of $\partial u_x / \partial r$ in the throat. This transformation was assessed qualitatively by investigating the shape of the streamlines in the contraction. There is a clear difference visible in Figure 4.12 between the axial streamline gradient of IDDES and RANS models. The latter are much more stretched in streamwise direction and the streamlines predicted by the IDDES model indeed seem to be more affected by the vortex core, potentially indicating the presence of a larger centripetal force that increases the axial velocity at the centerline .

The experimental measurements show no such increase, but this might be due to the relatively large ($0.4D_{\text{inlet}}$) hub of the swirl generator, which was positioned just in front of the converging nozzle and may have prevented a centripetal effect. The high and much overpredicted tangential velocities and small vortex cores predicted by the RSM and LES simulations by Rudolf et al. [9] may have overcome this, therefore also showing the increase in axial velocity. The realizable $k - \varepsilon$ model in [9] predicted a decrease in axial velocity close to the vortex axis. This behavior was not visible in any of the simulations run for this thesis. Liebrand [5] noticed a similar decrease in axial velocity in EARSM simulations of the tip vortex that was caused by the one-dimensional (i.e. streamwise) character of the turbulence inside the core. The velocity deficit was claimed to be a consequence of the dominance of the shear stress in the streamwise direction. The realizable $k - \varepsilon$ model substitutes the S_{xx} value in the calculation of the x-component of the normal stress by the largest eigenvalue of the strain-rate tensor S_{ij} to satisfy the realizability constraint (positive normal stresses). The usage of the largest eigenvalue of the strain-rate tensor is similar to the approach used in the definition of the Explicit Algebraic Reynolds Stress Model, indicating the possibility that also in the case of the realizable $k - \varepsilon$ model, the one-dimensional dominance of the turbulence in streamwise direction leads to a reduction in axial velocity. Without further information on the Reynolds stresses from Rudoalf et al. [9], this cannot be further assessed.

(a) Normalized tangential velocity

(b) Normalized axial velocity
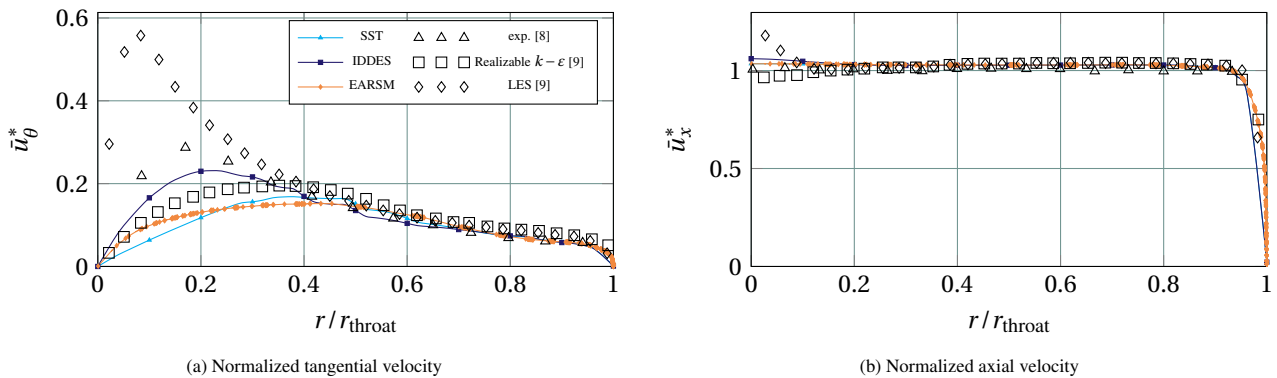
Figure 4.11: Comparison of normalized tangential and axial velocity with numerical results of Rudolf et al. [9] measured at plane C for the comparison study on M_1 of the wetted vortex
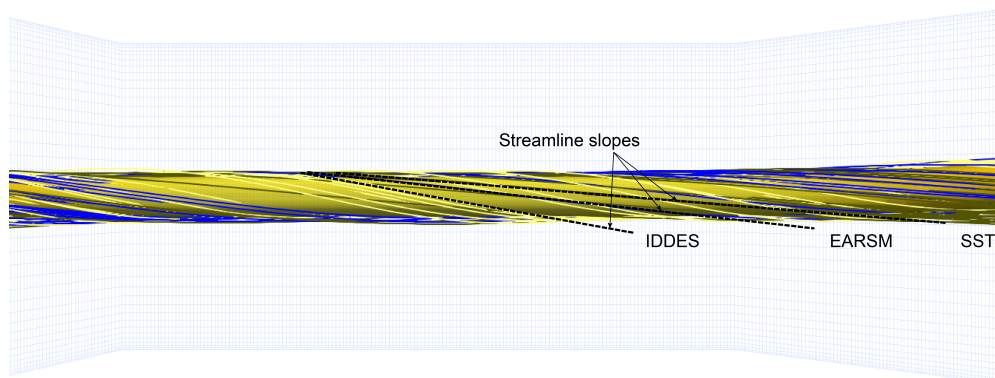
Figure 4.12: Comparison of streamline gradient originating from the inlet between IDDES (yellow), EARSM (blue) and SST (brown). Background is a vortex isocontour of $Q_{\text{crit}} = 5$ from M_1 IDDES.

4.1.5. Vortex instability and breakdown

As mentioned in the previous sections, all wetted flow simulations with the exception of the SST model, experienced a sudden rise in pressure without large effect on the other flow variables. The rise in pressure occurred at different times for the different simulations, although in all cases the initially steady vortex started rotating in the diverging nozzle as can be seen in Figure 4.13.
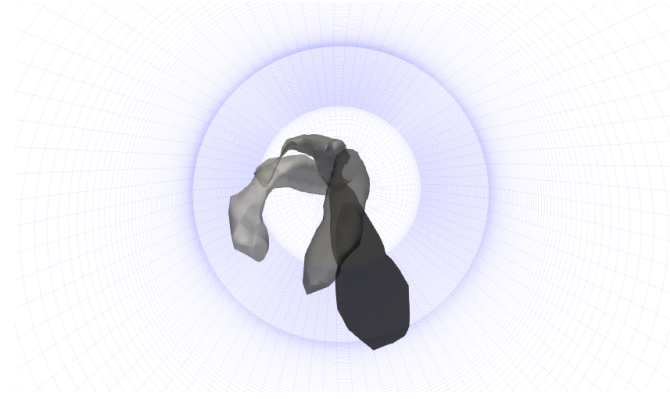
Figure 4.13: Oscillatory behavior of the vortex tail for the M_1 EARSM simulation. Time sequence is indicated by dark to light coloring of vortex identified by $Q_{crit} = 5$. View is from exit of diverging nozzle to the front.
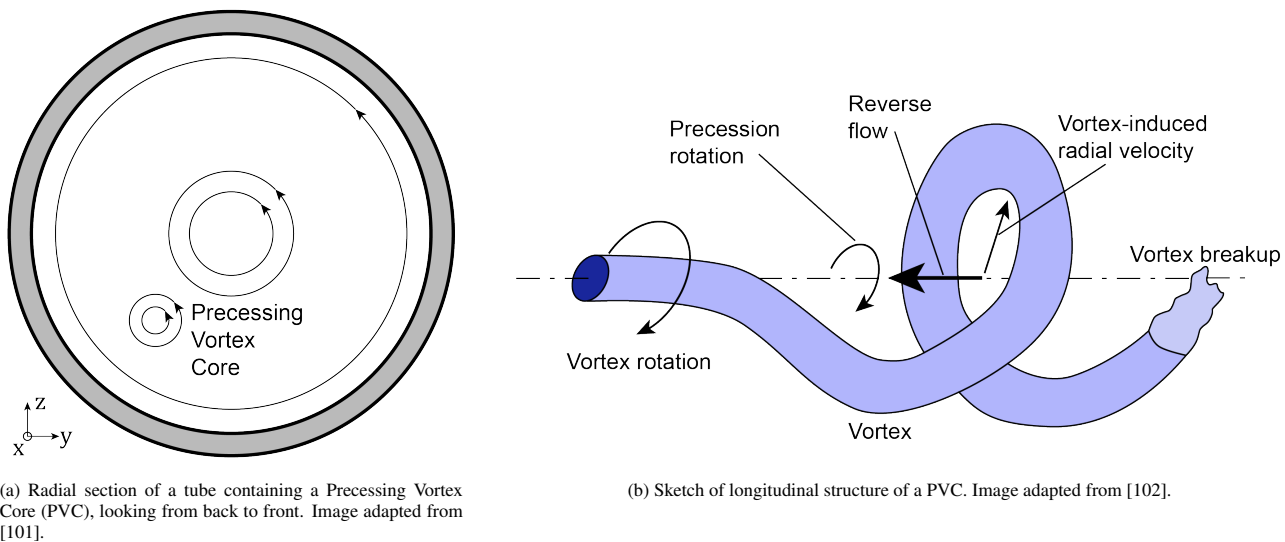
(a) Radial section of a tube containing a Precessing Vortex Core (PVC), looking from back to front. Image adapted from [101].

(b) Sketch of longitudinal structure of a PVC. Image adapted from [102].

Figure 4.14: Sketches of a PVC.

Even though the flow quantities **u** and k did not shift upwards in the same way as the pressure coefficient C_p did, Section 4.1.3 highlighted the periodic character that is also introduced in the velocity signal and influences the estimate of the resolved turbulence. It is therefore important to understand what the cause of this oscillation is, not in the least to minimize its impact on the simulations for used in the verification study.

The geometry used for these simulations was based on a study in the field of hydraulics and fluid dynamics in pumps [8]. Those cases are known for the unstable phenomenon called a Precessing Vortex Core (PVC); the circumferential motion of a vortex around its initial centerline axis. The same breakdown phenomenon is recurrent in combustion dynamics where flame stabilization can be an issue, due to the unstable and highly dynamic character of a PVC. A PVC occurs due to large centrifugal forces, appearing for sufficiently high swirl numbers ($Sn > 0.6 - 0.7$) combined with a central recirculation zone [101]. The vortex breakdown occurring at the end of the PVC leads to pressure pulses and a general pressure drop (draft surge). The precession direction, indicated by the sketches in Figure 4.14, is the same as the rotation of the vortex (i.e. direction of axial vorticity).

When comparing the characteristics of a PVC and what occurs in the present simulation, the following observations can be made regarding the i) central recirculation zone, ii) swirl number, iii) precession direction and iv) pressure drop in the venturi:

i) no zone with reverse flow is present in the current simulations,

ii) the swirl number ($Sn \approx 0.12$) is much lower in the present simulations than typical range of swirl numbers for PVCs,

iii) the precession direction in the current simulations was the same as the direction of axial vorticity and

iv) the unsteadiness in the current simulations increased the pressure instead of lowering it.

The observed unsteadiness of the wetted vortex might be related to, but is not caused by the PVC phenomenon, considering the differences w.r.t. theoretical characteristics of a PVC on three out of four criteria. The frequency corresponding to the instability was assessed by calculating the one-sided Fast Fourier Transform (FFT) of the pressure signal at plane D and E[1]. The signals were detrended by subtracting the mean value before the calculation. The peak in Figure 4.15 occurs at a frequency of 5-6 Hz, but is rather small. The small magnitude indicates that the effect only has a small amplitude and that, apart from the time needed for vortex to start oscillating, no important transient effects need to be accounted for in the verification study discussed in the next section.

(a) Plane D   (b) Plane E
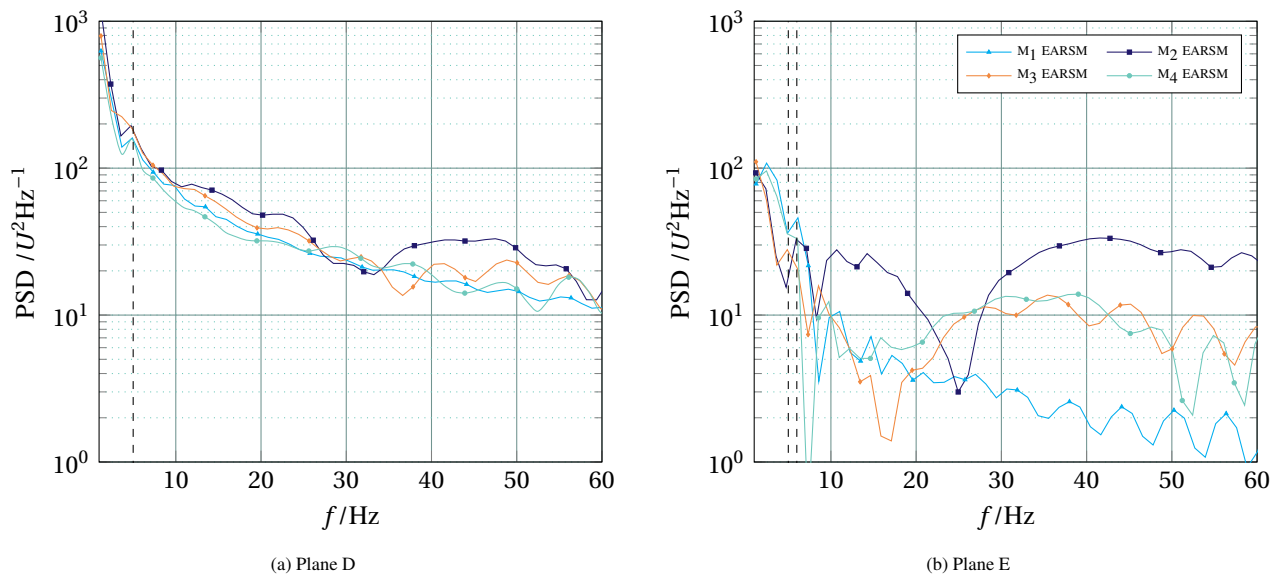
Figure 4.15: Analysis of dominant frequencies in the pressure signal at measurement planes D and E for the wetted vortex simulation.

4.2. EARSM verification study

Simulations were initially run with a time step corresponding to a maximum Courant number of 1. Due to time constraints and the similar performance of the EARSM and SST models, the difference was assessed between a Courant number of 1 and 10. There was a virtually no difference between both time steps, so that the simulations for the verification study were performed using a Courant number of 10. The method used to assess the discretization uncertainty, i.e. to verify the independence of the result on the grid and the time step, requires at least five different grids and time steps, leading to the simulation matrix displayed in Table 4.4. The simulations for the verification study were started from an EARSM simulation on M_1 that had run for about one flow-through time of the entire domain (corresponding to $t = 0.408$ s) to speed up the convergence process.

4.2.1. Flow field results

The velocity in axial and tangential direction is presented in Figure 4.16, showing little difference between the different resolutions. Close to the centerline the coarsest grid (M_1) does deviate from the others, which is expected to be to the limited number of cells in this area combined with the setting of the plane monitor (further addressed in Section 4.2.3). Considering the clustering of M_1 and M_3 as well as M_2 and M_4 results in the rest of the domain, local uncertainties are expected to be higher for those points. The results for the axial velocity are virtually identical for the different grids, and the velocity profile is almost flat throughout the width of the channel.

The pressure coefficient in Figure 4.17a also exhibits much less variation between meshes than the tangential velocity,

---

[1]The data was obtained using from EARSM simulations for the verification study, as the measurement planes D and E were not present in the M_1 comparison simulations.

Table 4.4: Matrix of simulations performed for the verification study of the wetted vortex.

t/t_i \ h/h_i	1.00	1.25	1.56	1.96
1.00	M_4 Co10			
1.25	M_4 Co12.5	M_3 Co10		
1.56	M_4 Co15.6		M_2 Co10	
1.96	M_4 Co19.5			M_1 Co10

albeit slightly more than the axial velocity. The turbulent kinetic energy again displays strong clustering of solutions of the same meshes (i.e. M_1 and M_3, and M_2 and M_4) between 0.5 and 0.65 r/r_{throat} as can be seen in Figure 4.17b. This is a location of strong gradients, enlarging the consequences of interpolation issues. An important conclusion is that an increased number of points in the vortex core and an increased resolution does not change the amount of turbulent kinetic energy inside the vortex core. The eddy viscosity therefore remains large enough to diffuse the vortex, despite the curvature correction which is part of the EARSM model in the REFRESCO implementation. The result also shows that applying the curvature correction does not yield sufficiently accurate results for the flow inside the vortex core. No significant differences were found in the simulations on M_4 with a higher Courant number.

(a) Normalized tangential velocity

(b) Normalized axial velocity
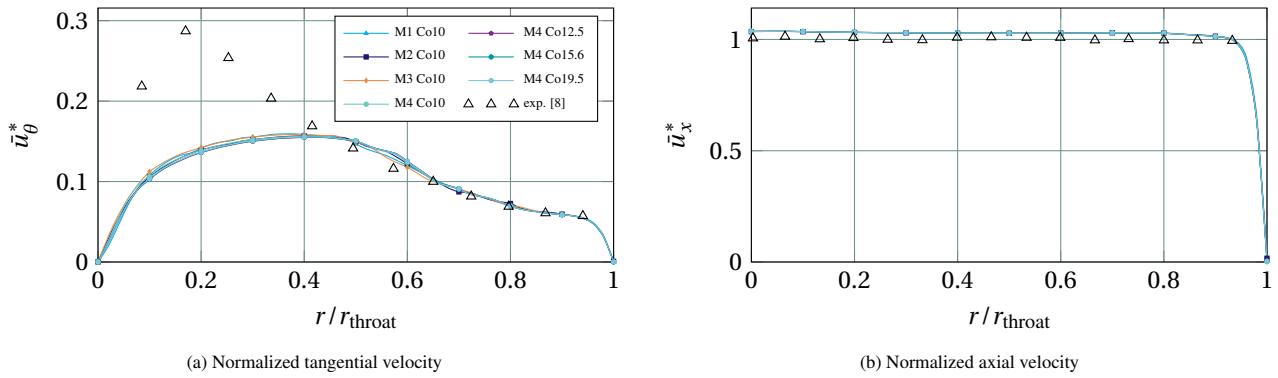
Figure 4.16: Profiles of normalized tangential and axial velocity measured at plane C for the grid convergence study of the wetted vortex simulation using the EARSM.

(a) Pressure coefficient

(b) Normalized turbulent kinetic energy
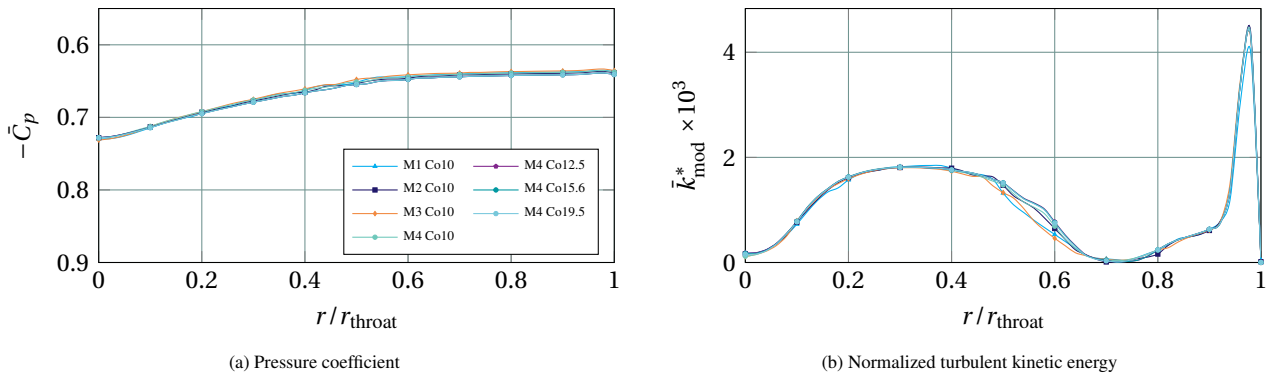
Figure 4.17: Profiles of pressure coefficient and normalized modeled turbulent kinetic energy measured at plane C for the grid convergence study of the wetted vortex simulation using the EARSM.

4.2.2. Iterative & statistical uncertainty

The iterative uncertainty for the different simulations is discussed first, followed by the statistical uncertainty. The value of the statistical uncertainty and the averaging period are provided for the simulations and the convergence behavior is briefly discussed.

Iterative uncertainty

The iterative uncertainty was not calculated explicitly, but all flow variable residuals converged to below 1×10^{-6} in the entire domain (L_∞ norm) for each time step. The iterative uncertainty was not further assessed, but given these residual values is not expected to be significant relative to the other uncertainties. The convergence of the global residual L_∞ is plotted for the simulations on M_3 and M_4 with Courant number 10 in Figure 4.18. The iterative convergence plots for the other simulations, which showed similar behavior as the M_4 Co10 simulation, can be found in Appendix D.2.1. The residual of the entire velocity vector $\mathbf{u} = \sqrt{u_x^2 + u_y^2 + u_z^2}$ was plotted instead of the components to improve the clarity of the graph. The magnitude is slightly larger than 1×10^{-6}, but the individual components are all below this value. The graphs are not intended for detailed inspection of differences in convergence between the different simulations, but to highlight the difference in general behavior of the residuals for the different components. The more unstable behavior of the M_3 simulation is notable however and shows a degree of periodicity in the pressure L_∞ residual. It might be the case that there is a single or a few bad cells that form the issue, however this could not be analyzed further. Additionally, residuals are still sufficiently low, such that the impact of these fluctuations is limited.

(a) Velocity vector (cyan) and pressure (purple)   (b) Turbulent kinetic energy k (cyan) and specific dissipation rate ω (purple)
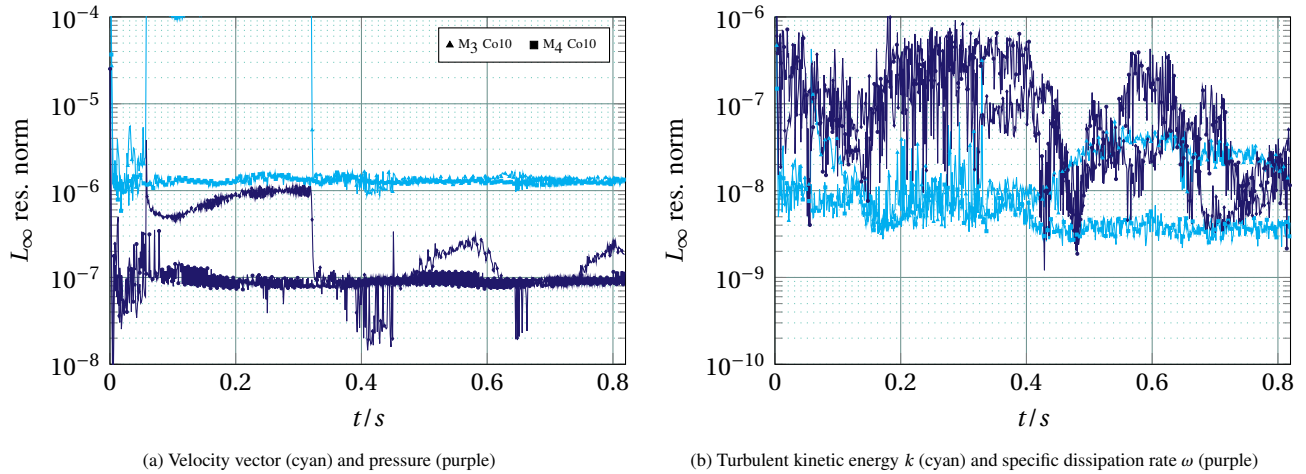
Figure 4.18: L_∞ residual for wetted vortex EARSM verification study. Triangular marks are used for the simulation on M_3 and square marks indicate the M_4 simulation with $Co = 10$.

Statistical uncertainty

The statistical uncertainty for the different simulations was determined using the TST, where the signal was analyzed from the last to the first time step (TST-B). The flow quantities are said to be converged if their uncertainty decays with $1/\log(t)$ in time, i.e. parallel with the dashed gray lines in the graphs. The criterion of statistical convergence was applied only to u_θ, as this is the most critical flow variable in predicting the viscous core of the vortex and as there are measurement data to validate the numerical result. The TST-B plots for the analyzed flow variables u_x, u_θ, and p are provided in Figure 4.19, where the continuous lines indicate the part of the signal used for time-averaging, and the colored dashed lines indicates the discarded 'start-up' part of the signal.

Significant differences are visible in the convergence behavior of M_3 compared to the other grids, as well as in the absolute value of the statistical uncertainty between all grids. The statistical uncertainty was calculated for all meshes on the same monitor point in the plane, hence the difference cannot be due to a difference in interpolation. The M_3 simulation in particular seems to have difficulty converging in the statistical sense. The averaging period for the M_3 grid should in fact be even smaller than what has been chosen to declare the results statistically-converged, but this would mean only using a few dozen samples. Therefore, a longer averaging period was chosen based on the convergence of the pressure. The difference of the M_3 grid was also noted in the residual convergence, but as the settings were the same for all grids, and all grids were constructed in the same way, no explanation has been found for the pronounced unstable behavior. The differences in the duration of the start-up effect between the different grids might be attributed to the instability described in Section 4.1.5. The simulations on M_4 with a higher Courant number all display the same convergence behavior for the tangential velocity, but larger differences are noted for the axial velocity and the pressure. The larger time step does seem to lead to an increase in the statistical
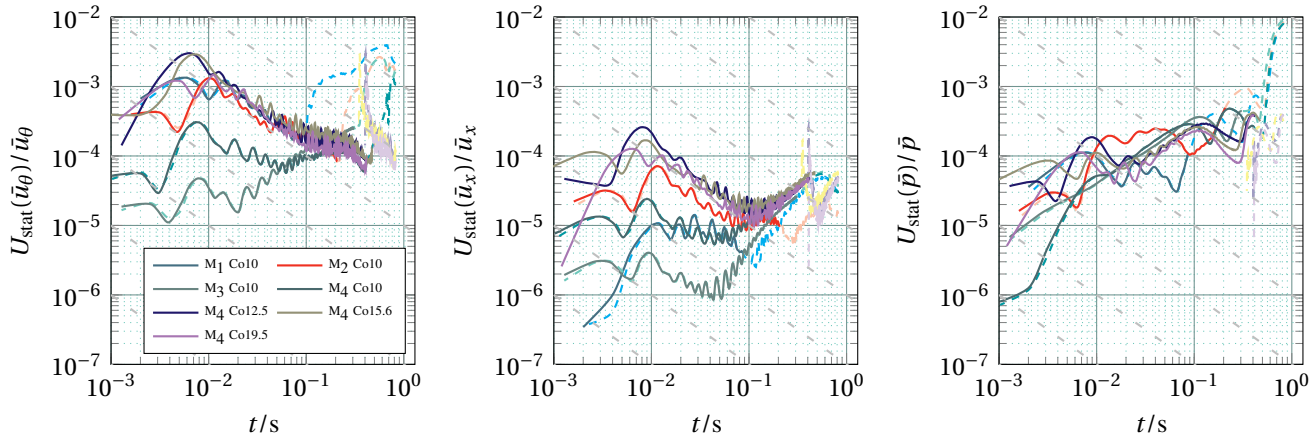
Figure 4.19: Statistical uncertainty plots for u_θ (left), u_x (middle) and p (right) measured at plane C for the EARSM verification study of the wetted vortex, obtained using TST-B. Lighter, dashed versions of the dark solid lines indicate removed start-up effect.

uncertainty when a shorter averaging period is used. The final averaging periods and corresponding statistical uncertainties are given in Table 4.5.

Table 4.5: Time-averaging periods and statistical uncertainty of convergence study simulations of the wetted vortex.

Simulation	$T_{\text{total}}/\text{s}$	T_{avg}/s	$U_{\text{stat}}(u_\theta)/\%$	$U_{\text{stat}}(u_x)/\%$	$U_{\text{stat}}(p)/\%$
M_1 Co10	0.816	0.068	2×10^{-2}	4×10^{-4}	1×10^{-2}
M_2 Co10	0.816	0.208	8×10^{-3}	1×10^{-3}	5×10^{-2}
M_3 Co10	0.816	0.307	3×10^{-2}	3×10^{-3}	5×10^{-2}
M_4 Co10	0.816	0.400	6×10^{-3}	4×10^{-3}	3×10^{-2}
M_4 Co12.5	0.816	0.399	6×10^{-3}	5×10^{-3}	4×10^{-2}
M_4 Co15.6	0.816	0.346	8×10^{-3}	5×10^{-3}	4×10^{-2}
M_4 Co19.5	0.816	0.326	6×10^{-3}	5×10^{-3}	4×10^{-2}

4.2.3. Discretization uncertainty

The discretization uncertainty was determined following the procedure by Eça and Hoekstra, as explained in Section 2.5.2. This method is incorporated in the discretization uncertainty tool developed by MARIN[2], which was used to determine the uncertainty and level of (grid- and time step) convergence for the axial and circumferential velocities as well as the pressure on the four meshes. The discretization uncertainty of the turbulent kinetic energy was not assessed as there were no experimental results that could be used to validate the result. The discretization uncertainty was assessed for 51 points in radial direction. As before, results were circumferentially averaged and time-averages were calculated according to the determination of the statistical uncertainty. The absolute value of the discretization uncertainty for M_4 Co10 (which has the highest resolution) is plotted in Figure 4.20 per point as an error bar on top of the predicted value of u_x, u_θ and C_p.

The uncertainties are smallest for the axial velocity and the largest for the tangential velocity. This is unsurprising as the uncertainties based on the grid discretization should generally be larger for larger gradients. The largest gradients are found in the tangential velocity profile, more specifically in the vortex core, which is indeed where the uncertainties are the largest. This does not take away that there are certain points with much larger uncertainties than the rest. The outliers in the plots of axial velocity and pressure are due to the interpolation method used to determine the discretization uncertainty. For the other locally large uncertainties, the origin can be found in the interpolation method for the disk (circular 2D plane) monitors combined with the OH-topology of the grid, which is subsequently investigated.

Influence of monitor interpolation method

The two first points ($r = 0.02$; $0.04 \times r_{\text{throat}}$) having a very high uncertainty (250 and 77 % respectively) are strongly affected by the circular distribution of monitor points on a square grid in the vortex core. This is combined with the inability of the disk monitor to update the specified monitor coordinates to the coordinates of the (nearest) cell used for interpolation. The effect of this is visualized in Figure 4.21. These illustrations, which are a sketched representation of the actual grid cells

---

[2]Tool can be downloaded here: (http://www.refresco.org/verification-validation/utilitiesvv-tools/).

(a) u_θ

(b) u_x

(c) Pressure coefficient
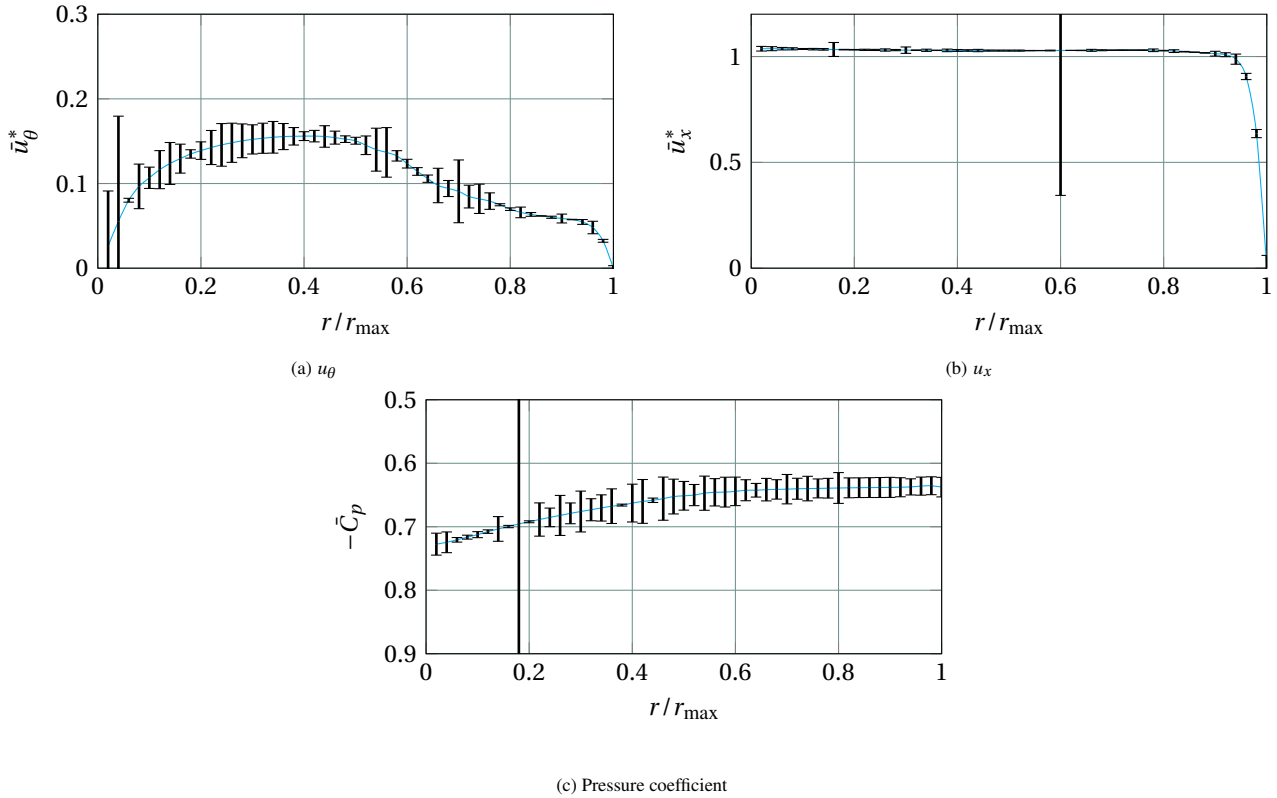
Figure 4.20: Error bars of the uncertainty of the flow variables assessed in the verification study of the wetted vortex. Profiles and uncertainties were obtained on M_4 Co10 and measured at plane C.

inside the vortex core as well as the exact monitor locations, demonstrate two important points. Firstly, the interpolation of the circular distribution of monitor points inside the orthogonal (H-) grid led to significant oversampling in the tangential direction close to the centerline, but not enough circumferential sampling points further outwards. The oversampling was dealt with automatically by the spatial averaging. If the coordinates of the monitor points would be updated to the interpolated cell centers, the accuracy should improve as a result of interpolation between the cell centers in the H-type grid area. The second, more important issue that is highlighted, concerns the significant difference between the grids regarding the selection of the nearest cell centers. The vortex core is the region with the largest gradients for u_θ, which means that a small difference in the location of the selected cell center has large implications for the value of u_θ. The nearest cell centers used for interpolation on the various grids were overlaid to show the relative difference in radial position in Figure 4.22a. The numerical consequences (i.e. the predicted tangential velocity at the monitor points) is quantified in Figures 4.22b and 4.22c, where the horizontal axis is the grid spacing w.r.t. the finest grid so that the grid results are displayed from left to right: M_4, M_3, M_2 and M_1. The difference in the location of the monitor points shown in the sketches and the ones used for the uncertainty assessment is due to the final step in the post-processing, which linearly interpolates the values from the monitor points to the radial positions used to compare values between grids. The significant differences between the u_θ values shown in Figures 4.22b and 4.22c is clearly the main contributor to the large uncertainty at these locations. Similar issues occur also at locations further away from the vortex core (0.68, 0.70, and 0.80 r/r_{throat}). The uncertainties for all points can be found in in Table D.4.

The uncertainty increase linked solely to the coordinates in the disk monitor not being updated, was quantified by comparing the uncertainty at the same location (C) between a disk and a line monitor, which only differ in the updating of the coordinates for the line monitor, and an increase in the number of points in radial direction for the line monitor (50 vs. 40). The simulations with a higher Courant number were not taken into account for this assessment as no line monitors were written for these simulations. The uncertainties for the disk monitor to which the line monitor values are compared, were also obtained without taking the higher Courant number simulations into account. Therefore, these uncertainties are only based on *grid* convergence and do not take into account the time step. The results obtained on the line monitor were averaged over the same period in time and averaged at the same radial position for positive and negative values of y. The difference in uncertainty between the disk and the line monitor for the three assessed flow variables is presented in Figure 4.23a, where a negative value indicates a reduction of uncertainty w.r.t. the disk monitor. A point-by-point comparison of the calculated uncertainties for both monitor types can be found in Table D.4. The line monitor has significantly smaller uncertainties for u_θ at the first two points (−205 and −36 %) and generally lower uncertainties than the disk monitor. The same is true for the other flow variables, although the difference is again smaller. There are still locally large uncertainties present for the tangential velocity,

(a) M_1 (b) M_2 (c) M_3 (d) M_4
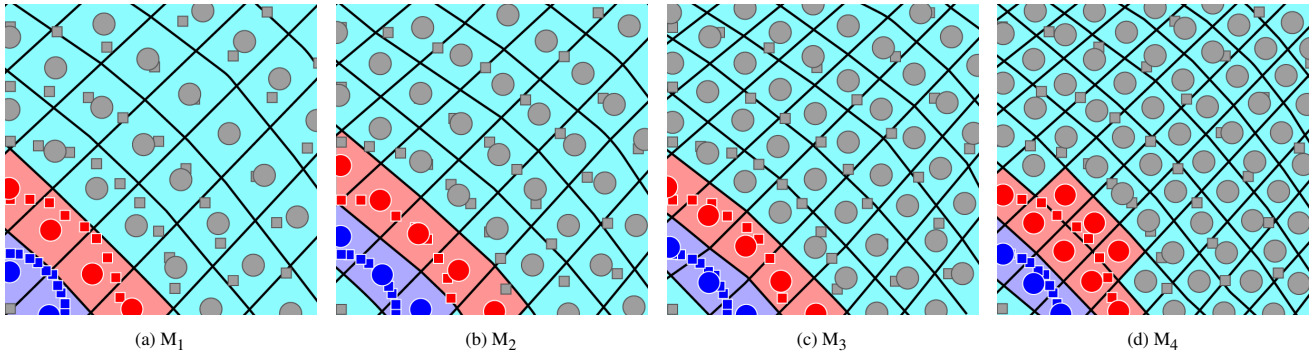
Figure 4.21: Interpolation on disk monitor for monitor points at normalized radial positions r/r_{throat} = 0.026 (blue) and 0.051 (red) for the wetted flow vortex. Cells are colored based on nearest monitor point.

(a) Cell centers interpolated from the different grids overlaid on the grid of M_4.

(b) Point 1 (r/r_{throat} = 0.02)

(c) Point 2 (r/r_{throat} = 0.04)
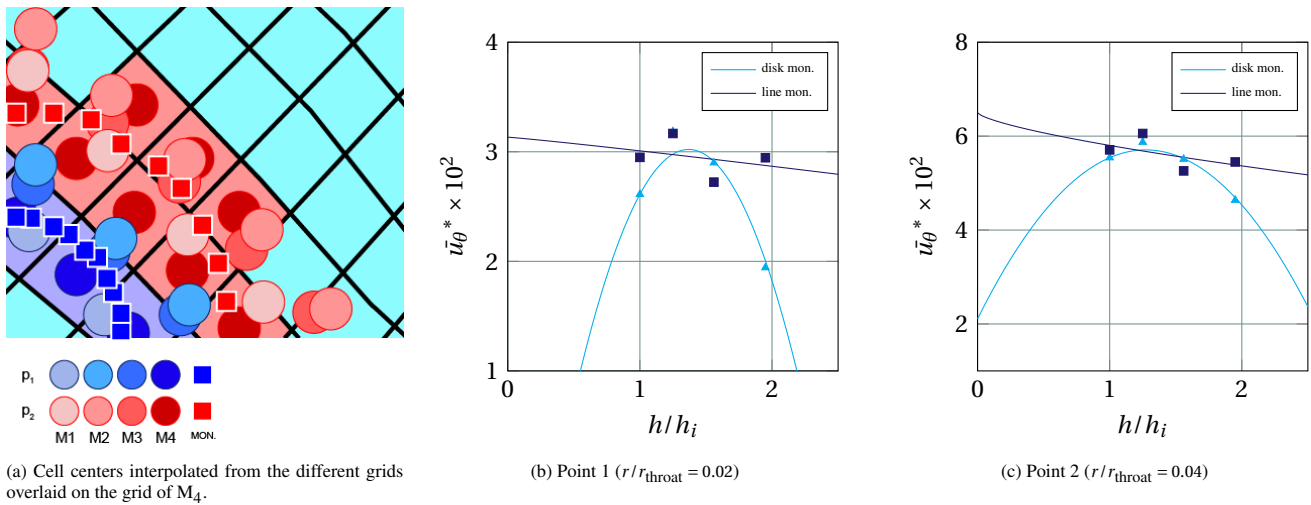
Figure 4.22: Cause and effect of non-updated nearest cell interpolation in the high-gradient vortex core region.

which may be due to the limitation of first-order nearest-cell interpolation. Within the time-frame of this research there was no room to assess the possible uncertainty reduction using higher-order interpolation methods. Considering the implications of not using updated coordinates, higher-order interpolation methods were used for the cavitating vortex simulations.

(a) Difference in calculated uncertainty for M_4 at location C.

(b) Error bars for u_θ for the line monitor at location C.
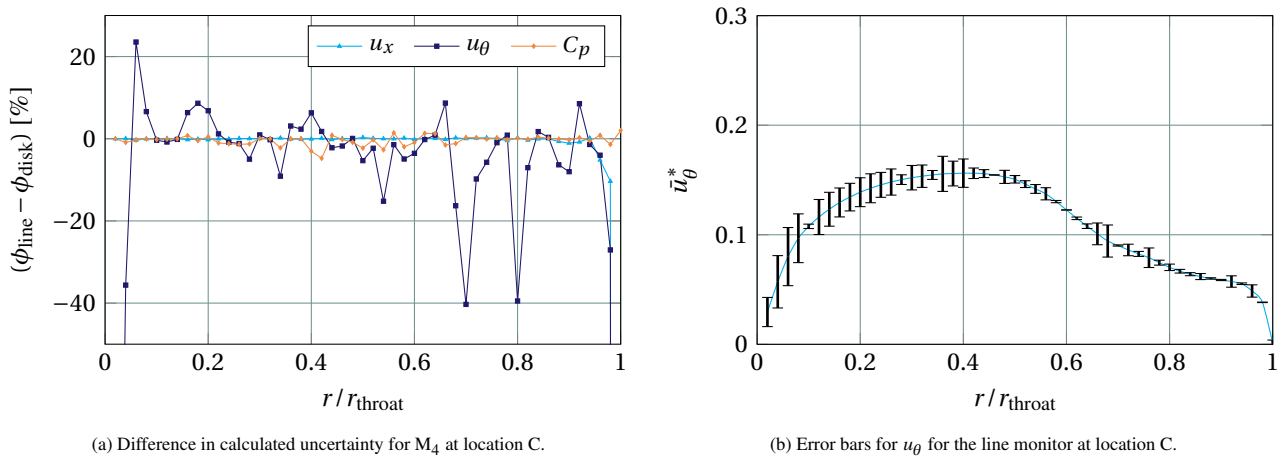
Figure 4.23: Influence of updating monitor locations (line vs. disk monitor) on M_4.

4.2.4. Validation with experimental results

Following the validation procedure by [82], the multivariate metric (see Section 2.5.2) can be used to determine the validation uncertainty for the velocity profile. The large difference between the experimentally measured tangential velocity profile and

the numerical solution already indicates that the result cannot be validated. Furthermore, the velocity profile described by the EARSM simulations is not a valid Lamb-Oseen vortex, whereas a Lamb-Oseen profile could be fitted to the results of the SST and IDDES simulations in Section 4.1.2. If a multivariate metric were to be applied to the entire velocity profile, there might even be a relatively small value of uncertainty due to numerical values being closer to the experimental measurement of the tangential velocity profile for $r/r_{\text{throat}} > 0.5$. This may lead to an incorrect interpolation as the vortex core is the important part of the flow field, which is located in a limited region of the domain.

It was therefore decided to not apply the multivariate metric and conclude that the validation of the data is not possible given the large difference with experimental results.

4.3. Conclusions

All wetted vortex simulations within the present study were characterized by an onset of vortex instability at a certain point, except for the SST model. For the other turbulence models, the vortex started rotating inside the diverging nozzle, which led to an increase of the pressure coefficient but did not affect other flow variables. It did however increase the computational time necessary to obtain a statistically converged average for the flow variables. The vortex instability was shown to be not the same as a PVC as its key features were different. The IDDES model predicted the tangential velocity in the vortex core better than the SST and EARSM models as the viscous diffusion of the vortex was lower, leading to a smaller viscous core radius and higher tangential velocity. Nevertheless, the predicted tangential velocity and pressure drop in the viscous core still fell short of experimental measurements. The reduction of viscous diffusion for the IDDES could be traced back to the absence of resolved turbulence combined with the dissipation of modeled turbulent kinetic energy, making the flow field essentially laminar. The space-dependent coefficient C_μ in the EARSM successfully reduced the eddy viscosity and turbulence kinetic energy close to the centerline, though not enough to prevent excessive diffusion of the vortex.

The results for the EARSM demonstrated a discretization uncertainty for the tangential velocity in most of the domain of less than 10 %. Monotonic convergence was reached for all points, with second-order convergence for 14/51 points. Larger local uncertainties were attributed to the non-updated monitor coordinates of the used disk monitor and shown to decrease for results obtained by a line monitor with updated monitor coordinates. The discretization uncertainties for axial velocity and pressure were respectively one and half an order smaller than for the tangential velocity. The statistical uncertainty was two orders of magnitude smaller and the magnitude of the iterative uncertainty was not determined, but is expected to be even smaller as the local residual $L_\infty \leq 10^{-6}$ for all simulations and flow variables. Considering the above results, the solution obtained with the EARSM model is not expected to improve on finer meshes or with smaller time steps regarding the prediction of the viscous core size and the tangential velocity distribution within the vortex core. Given the large difference between numerical and experimental tangential velocity in the viscous core, the results from the EARSM simulations could not be validated. The convergence of the results for the EARSM does show that there are enough cells inside the viscous core, but that the overprediction of turbulence makes this model unsuitable to simulate a wetted line vortex.

The results on the coarse mesh showed that the flow field of the wetted line vortex is best predicted by the IDDES model. The flow field predicted by this model was almost laminar and the viscous diffusion subsequently lower. The EARSM solution was verified and showed that the model was unable to reduce the production of turbulent kinetic energy inside the vortex core also on the finest grid. Chapter 5 will demonstrate whether these finding also hold for the cavitating vortex simulations and determine differences in the predicted cavity dynamics of both models using a spectral approach.

Results of cavitating vortex simulations

The aim of this chapter is to determine to what extent the conclusions drawn about the turbulence models in the wetted flow case hold ground for cavitation and to what extent cavitation influences the differences between both models. Another important goal of this chapter is to determine whether it is possible to capture the cavity deformations in a similar way as Bosschers [2] did, provided that the cavity in this case also deforms in one or more of the deformation modes. This would mean that Kelvin waves on top of the cavity interface can be identified by the post-processing code using analytical dispersion lines plotted on top of the power density and phase difference spectra (see also Section 2.4.2). Given the identification of deformation modes, the differences in the prediction of cavity dynamics of both Explicit Algebraic Reynolds Stress Model (EARSM) and Improved Delayed Detached-Eddy Simulation (IDDES) turbulence models can be assessed. Fluctuations of the cavity interface occur on small length scales, so that only the finest grids M_3 and M_4 were used. Both grids were used to also get an indication of the grid-dependence of the flow field and the spectral results.

The iterative and statistical convergence behavior is briefly laid out first, followed by the discussion of the averaged flow field at measurement location C for both turbulence models and meshes. The last part of this chapter contains the analysis of cavity dynamics from a spectral point of view, by first identifying possible external sources of periodic excitation and subsequently focusing purely on the cavity inside the vortex.

An overview of the simulation parameters for the cavitating vortex is provided in Table 5.1. The value of the cavitation number was chosen based on another numerical study by Rudolf et al. using similar geometry [103] after consulting with the author (P. Rudolf, personal communication, January 25, 2019), which indicated a cavitation number $\sigma \approx 0.5$ for this flow rate. This was increased to $\sigma = 0.65$ to improve the convergence behavior and reduce the size of the sheet cavities originating from the sharp edges of the Venturi throat. The cavitation number was controlled in the simulations by modifying the vapor pressure of the liquid. The time step follows from a balance of the Courant number criterion $Co \leq 1$ and computational expense. Cavitating simulations used the flow field from a wetted flow solution as an initial condition, that had run at the same flow rate for approximately one flow-through-time of the entire domain, corresponding to 0.186 s. The convergence behavior of the cavitating simulations was improved by limiting the value of the dissipation rate ω (see Appendix A.1.3), as this variable leads to convergence issues in cavitating simulations when the $k-\omega$-based models are used.

An initial impression of the difference in the flow field predicted by both turbulence models is given in Figure 5.1. This figure also shows some of the characteristic features of this case regarding the sheet cavities and the shedding of the attached cavity in the diverging nozzle.

Table 5.1: Overview of cavitating vortex simulation parameters, where SS=Schnerr-Sauer cavitation model. Equal color indicates that the same parameter value is shared across simulations.

Simulation	Δt /10^{-5}s	$\dot{Q}$ /ls^{-1}	u_∞ /ms^{-1}	Re_{throat} /10^5	I	ν_t/ν	σ	$\max(Co)$
M_3 IDDES SS	0.8							
M_3 EARSM SS		10.0	14.147	7.5	1.0	1.0	0.65	1.2
M_4 IDDES SS	0.64							
M_4 EARSM SS								

5.1. Convergence behavior

5.1.1. Iterative convergence

The iterative convergence in the form of the L_∞ and L_2 normalized residuals is provided in Figure 5.2 and Figure 5.3 respectively for the simulations on M_3. Since both models and grids showed the same iterative convergence behavior, the M_4 residual plots can be found in Appendix E.1. The highest residuals belong to the velocity vector $\mathbf{u}$ and the specific dissipation rate ω. The former also showed to be the most difficult to convergence in the wetted flow simulations. The high value of the ω residual is a common issue with $k-\omega$-based models and multiphase flows, caused by the boundary value of ω close
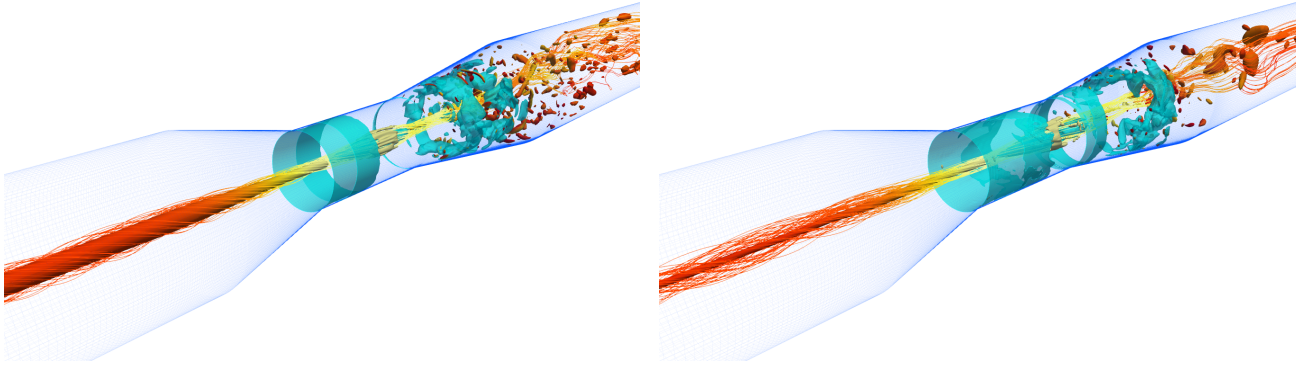
Figure 5.1: Representation of the vortex ($Q_{crit} = 5$) and the vortex cavity, including sheet cavities in the Venturi throat, for IDDES (left) and EARSM (right) simulations in combination with the Schnerr-Sauer model on M_3, at $t = 0.0928$ s. Vortex and streamlines are colored by axial velocity (white/yellow is higher than black/red).

to the vapor interface (acting as a slip wall). The value of the L_∞ residuals could not be reduced further and the residuals stagnated when lower relaxation values were used and diverged when they were increased. The L_∞ norm is a local measure and the largest residual values were found to be concentrated around the end of the cavity. At this location, violent collapse dynamics occur on such a small timescale that an even smaller time step is required to accurately resolve the flow in these cells. This was not feasible due to the increased computational effort this would entail. The root-mean-square residual L_2 is around 1×10^{-4} for the velocity, and slightly larger for the specific dissipation rate.

(a) Velocity vector (cyan) and pressure (purple).

(b) Turbulent kinetic energy k_{mod} (cyan), specific dissipation rate ω (purple) and vapor volume fraction (orange).
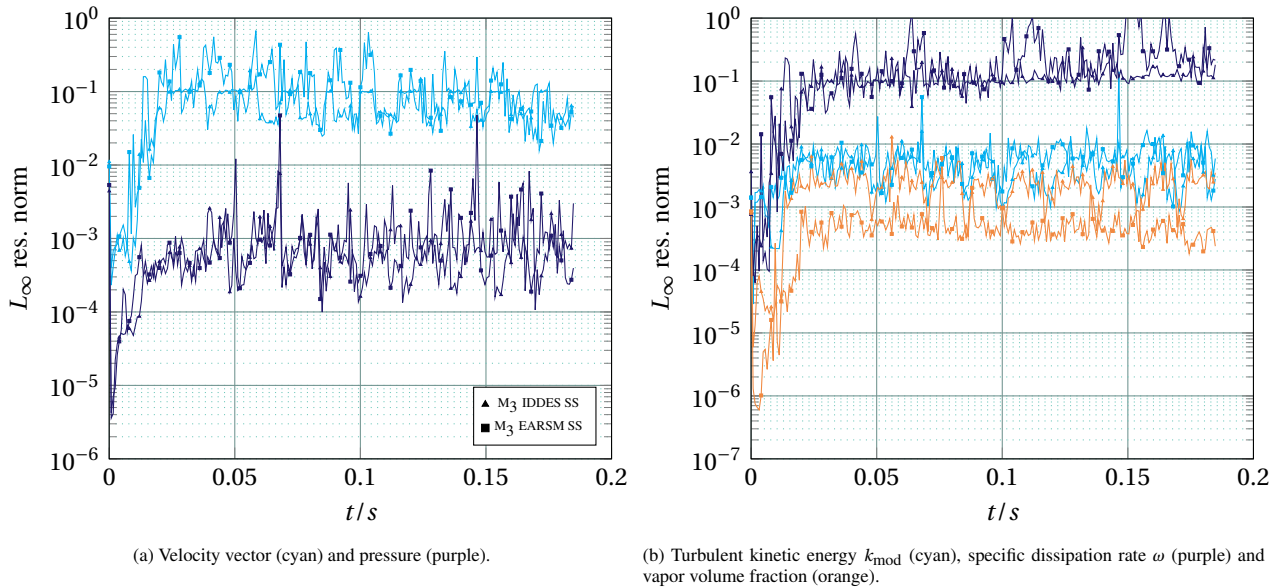
Figure 5.2: L_∞ residual for cavitating vortex simulations on M_3, where triangular marks are used for the IDDES and square marks indicate the EARSM simulation.

5.1.2. Statistical convergence

The statistical convergence for the tangential and axial velocity as well as the pressure is provided in Figure 5.4 for the simulations on M_3 and M_4. The statistical convergence behavior does not differ much between both turbulence models on the same mesh. The finer mesh does display uncertainties that are one order of magnitude smaller. This may indicate that the results are grid-dependent as the flow field behaves differently on both meshes. The averaging periods and corresponding statistical uncertainties for the three flow variables are given in Table 5.2.

(a) Velocity vector (cyan) and pressure (purple).

(b) Turbulent kinetic energy k_{mod} (cyan), specific dissipation rate ω (purple) and vapor volume fraction (orange).
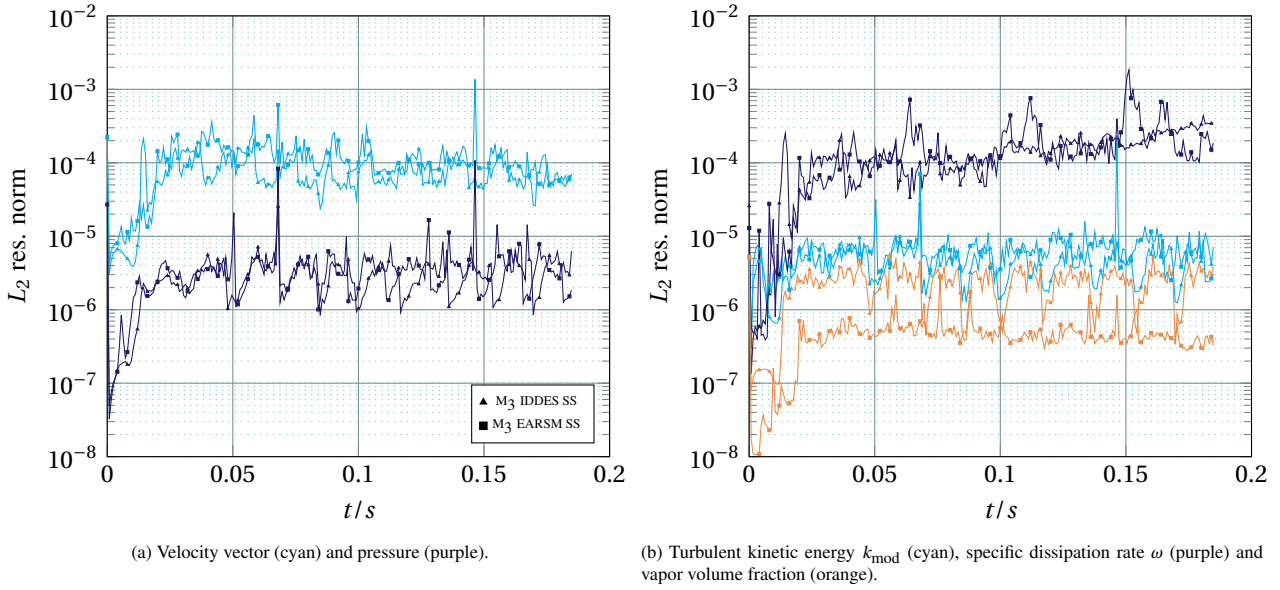
Figure 5.3: L_2 residual for cavitating vortex simulations on M_3, where triangular marks are used for the IDDES and square marks indicate the EARSM simulation.

Table 5.2: Time-averaging periods and statistical uncertainty of cavitating vortex simulations. T_{total} indicates total runtime, T_{avg} indicates period used for time-averaging.

Simulation	T_{total}/s	T_{avg}/s	$U_{stat}(u_\theta)/\%$	$U_{stat}(u_x)/\%$	$U_{stat}(p)/\%$
M_3 IDDES SS	0.186	0.102	3×10^{-2}	1×10^{-2}	5×10^{-2}
M_3 EARSM SS	0.186	0.082	3×10^{-2}	3×10^{-2}	3×10^{-2}
M_4 IDDES SS	0.293	0.141	2×10^{-3}	1×10^{-3}	5×10^{-3}
M_4 EARSM SS	0.262	0.141	3×10^{-3}	7×10^{-4}	3×10^{-3}
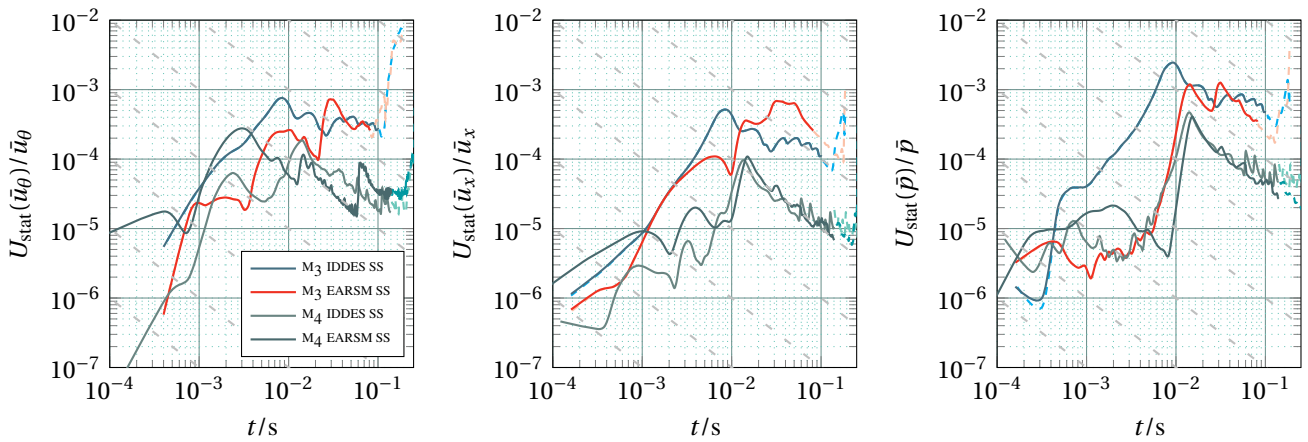
Figure 5.4: Statistical uncertainty plots for u_θ (left), u_x (middle) and p (right) measured at plane C for the simulations of the cavitating vortex using on M_3, obtained using TST-B. Lighter, dashed versions of the dark solid lines indicate removed start-up effect.

5.2. Flow field results

The vapor core size plays an important role in the presented results and was defined as the radius where $\alpha_{vap} = 0.5$. As Figure 5.5a shows, however, the production of vapor starts at the same time for IDDES and EARSM simulations, but the latter has a more diffuse interface characterized by a lower slope in the graph. This leads to a smaller core when defining the core by a certain amount of vapor. The diffusion of the vapor core interface is also linked to the shape of the cavity, as shown in Figure 5.5b, where the cavity of the IDDES model builds up faster, leading to a larger cross section at plane C (in the middle of the Venturi throat) and earlier (i.e. more upstream) formation of the vortex cavity in the Venturi throat. The front end of the vortex cavity additionally seems to be linked to the extent of the sheet cavity, which is shorter for the IDDES simulation. The streamwise location of cavitation inception for the vortex cavity did not change between grids M_3 and M_4.

(b) Comparison of longitudinal shape of the cavity on M_3 between IDDES (blue) and EARSM (green) $\alpha_{vap} = 0.5$, $t = 0.0928$ s. Flow is from left to right.

(a) Vapor fraction comparison on M_3 for the cavitating vortex.

Figure 5.5: Identification of differences between IDDES and EARSM simulations regarding vapor core size.

The velocity in tangential, axial and radial direction is shown in Figure 5.6. All three velocity profiles are affected by the cavitating line vortex in the core of the Venturi; the tangential profile shows an inflection point, the axial velocity is not flat and the radial velocity is significant. The tangential velocity also shows the largest difference between both turbulence models. As there are no reliable experimental measurements for this flow case, the results for the tangential velocity are compared to that of a theoretical cavitating Lamb-Oseen velocity profile. Recalling that the tangential velocity profile u_θ is defined by the viscous and vapor core radii r_v, r_c and the circulation Γ [2]:

$$u_\theta(r) = \frac{\Gamma}{2\pi r} \left[1 - \beta_R \exp\left(-\alpha_R \frac{r^2}{r_v^2} \right) \right], \qquad \text{(2.96 revisited)}$$

and the β_R parameter by

$$\beta_R = \frac{r_v^2}{r_v^2 + \alpha_R r_c^2} \exp\left(\alpha_R \frac{r_c^2}{r_v^2} \right), \qquad \text{(2.97 revisited)}$$

the following fitting parameters were used for the M_4 EARSM and IDDES SS results at plane C; Figure 5.6a:

Table 5.3: Lamb-Oseen fitting parameters for the cavitating vortex simulations

Simulation	r_v / r_{throat}	r_c / r_{throat}	$\Gamma / 10^{-2} \text{m}^2\text{s}^{-1}$	$u_\infty / \text{ms}^{-1}$
M_4 IDDES	0.295	0.21	11.2	14.147
M_4 EARSM	0.412	0.14	12.2	14.147

The theoretical velocity profiles are only plotted for the wetted part of the vortex. As for the wetted vortex, the IDDES model is able to predict larger gradients and a higher tangential velocity. The effect of viscosity is reduced, leading to a smaller viscous core. The vapor core is larger for the EARSM simulation, which suffers from the viscous diffusion of the vortex outward and predicts a larger vortex core size. The tangential velocity profile inside the vapor core strongly resembles that of a Rankine vortex, which subsequently transitions into a Lamb-Oseen-like profile. This is in line with the derivation of the cavitating vortex model in [104], where the vapor core rotates like a solid body. The comparison with the theoretical cavitating Lamb-Oseen velocity profile in Figure 5.6a, demonstrates that the magnitude of the tangential velocity in the vapor core is underpredicted by the IDDES model and that the EARSM matches better with the theoretical profile inside the viscous core. The IDDES model does not match the fitted profile except at the edge of the viscous core (which is how the fit was obtained). The EARSM matches the fitted Lamb-Oseen profile until just after the viscous core, after which the blockage due to the proximity to the wall causes the deviation from the fitted profile of the free vortex.

The axial velocity profiles of both models seem to contradict each other. For the EARSM simulation, the axial velocity

decreases slightly towards the center, whereas IDDES predicts an increase towards the vapor core, followed by a decrease towards the centerline. The axial velocity for the EARSM is also larger. Both differences are caused by the presence of the sheet cavity at the measurement location C, making the effective area through which liquid can flow smaller for the EARSM. The radial gradient of axial velocity violates an assumption made by Bosschers [2] in deriving the theoretical form of a cavitating Lamb-Oseen vortex. Furthermore, it is clear that the presence of a vapor core has made the radial velocity significant and of the same order of magnitude as the tangential velocity. This also contradicts the assumption made in the derivation of the analytical vortex model of Bosschers [104], as the flow inside the vapor core now cannot rotate like a solid body. The distribution of the radial velocity looks quite similar to that of a Rankine vortex' tangential velocity, with a linear increase of velocity towards the edge. No velocity measurements inside a vortex core were performed due to limitations of Laser-Doppler Velocimetry (LDV) and Particle-Image Velocimetry (PIV) techniques, so there is no information regarding the radial velocity distribution inside a cavitating tip vortex. The current distribution could, however, follow from the formation of the vapor core, which directs all liquid outwards outwards until it finds an equilibrium based on the local pressure and the cavity diameter oscillates around this equilibrium. The fact that the cavity is still developing, would lead to a radial acceleration towards the edge of the vortex core. The distribution after the peak looks remarkably similar to the tangential velocity distribution of a free inviscid vortex.

(a) Normalized tangential velocity (b) Normalized axial velocity (c) Normalized radial velocity
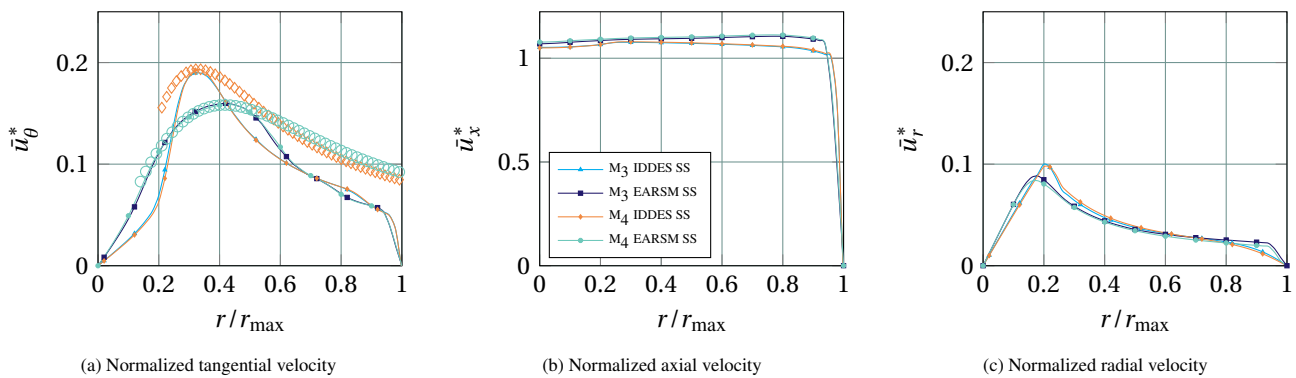
Figure 5.6: Profiles of normalized velocity components measured at plane C for cavitating vortex simulations.

The pressure coefficient, as well as the modeled and resolved turbulent kinetic energy are presented in Figure 5.8.

Even though the pressure profiles in radial direction are radically different for both turbulence models, the minimum pressure remains the same and is slightly below the vapor pressure. The actual pressure is slightly lower than the vapor pressure but cannot decrease further until the core contains pure vapor ($\alpha_{\text{vap}} = 1$) as it is balanced by cavity growth. Until then, the pressure difference $p - p_{\text{vap}} < 0$ leads to a production of vapor and growth of the cavity until the local pressure exceeds the vapor pressure; $p - p_{\text{vap}} \geq 0$. The maximum vapor volume fraction is 10 % higher for the IDDES model, but remains below 90 %, as can be seen in Figure 5.5a. The larger vapor fraction indicates a more developed cavity with a larger vapor core for the IDDES model.

Despite the differences in the vapor core size apparent from the results of the velocity vector, the pressure coefficients as predicted by both models match until $r/r_{\text{throat}} \approx 0.2$, which is the defined size of the vapor core in the IDDES result. The pressure at the wall is equal to the vapor pressure for the EARSM simulation, contrary to the IDDES result which shows a positive radial pressure gradient. The low pressure for the EARSM simulation is caused by the longer extension of the sheet cavities originating from the hard edge at the entrance of the Venturi throat. This strongly influences the rest of the radial pressure profile.

The modeled turbulent kinetic energy k_{mod} is, as in the case of the wetted vortex, close to zero for the IDDES due to the extent of the Large Eddy Simulation (LES) region, given in Figure 5.7, which reduces the amount of k_{mod}. The bumps around $r/r_{\text{throat}} = 0.25$ and 0.45 are due to the increased local length scale ($l \approx l_{\text{RANS}}$) as part of cavity interface is seen as a slip wall and the liquid flow around it is identified as an attached shear layer. Although the effect seems more pronounced on M$_3$, Figure 5.7 only provides a snapshot in time and the Reynolds-Averaged Navier-Stokes (RANS) area on the cavity interface also occurs on M$_4$. This observation might represent a possible shortcoming of applying the IDDES model to such a case, as the repeated transition from one mode into the other increases the non-physical gray area in between the formulations. Another important observation is the LES area inside the stable attached sheet cavity at the front (see Section 5.3.1), which possibly contributes to the shorter extent of the sheet cavity compared to the EARSM simulation. The EARSM predicts a zero k_{mod}^* right at the center of the vortex, which may be the reason for the higher value of the tangential velocity in the vapor core compared to the IDDES simulations.

The resolved turbulent kinetic energy k_{res} is still more than two orders of magnitude smaller than the modeled k, again indicating that the flow field as simulated by the IDDES model is almost laminar. The statistical convergence and uncertainty of the normal components of the Reynolds stress tensor can be found in Appendix E.2. Uncertainties for the M$_3$ IDDES are
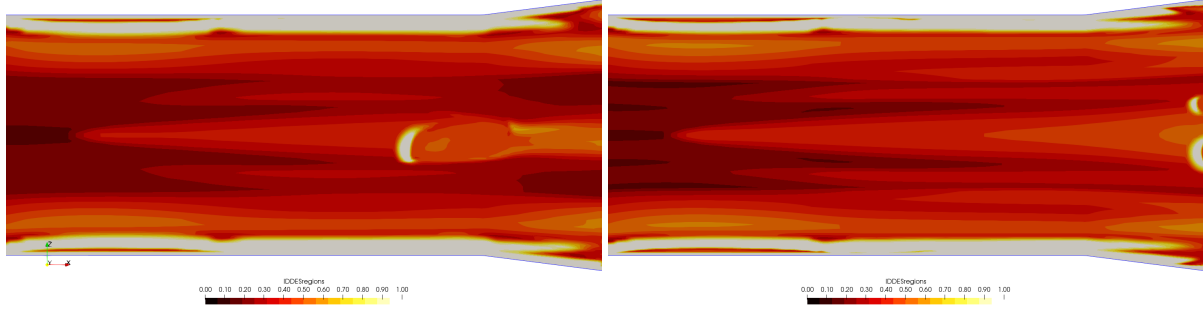
Figure 5.7: LES regions in the contraction on M_3 (left) and M_4 (right) for the cavitating vortex at $t = 0.0928$s, white indicates fully RANS region and red/black indicates LES region.

of $\mathcal{O}(10^1)$, whereas they are of $\mathcal{O}(10^{-1})$ on M_4. The large uncertainties are, as in the wetted vortex simulations, expected to be due to periodic non-turbulent fluctuations of the velocity signal. Ideally, a high-pass filter would be applied to these signals to remove the low-frequency fluctuations and thereby hopefully improve convergence as the presented value of the resolved kinetic energy is currently inaccurate (especially on M_3). However, the main point of Figure 5.8c is to show that the resolved kinetic energy is negligible compared to the modeled value and that statement is not affected by applying a high-pass filter or not.

(a) Pressure coefficient

(b) Normalized modeled turbulent kinetic energy

(c) Normalized resolved turbulent kinetic energy
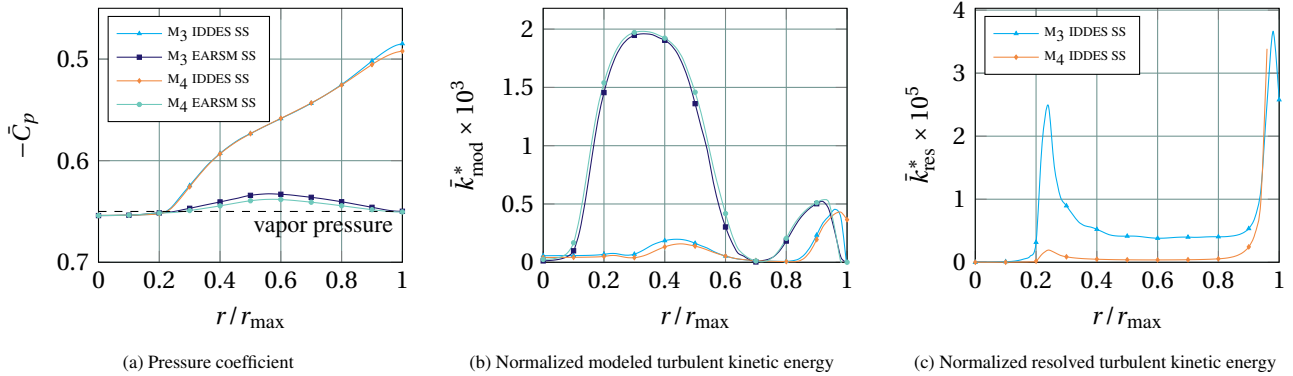
Figure 5.8: Profiles of normalized pressure and modeled and resolved turbulent kinetic energy measured at plane C for cavitating vortex simulations.

5.3. Analysis of cavity dynamics

This section will discuss the performance of the EARSM and IDDES turbulence models from a cavity dynamics point of view. The previously identified sheet cavities seem to influence the flow field and the streamwise inception of the vortex in a static way, but their dynamics are also expected to have an effect of the unsteady behavior of the cavitating vortex. The influence of the shedding of the sheet cavities originating at location B and D is therefore assessed first, followed by the spectral analysis of the isolated cavitating line vortex.

5.3.1. Influence of sheet cavity shedding

The sharp edges of the Venturi geometry lead to local low pressure regions at the beginning and at the end of the Venturi throat. Unsurprisingly these low pressure regions lead to cavitation inception and the formation of attached sheet cavities. The sheet cavity forming at the front of the Venturi throat is stable and does not show shedding behavior. The cavity formed at the end of the Venturi throat does display periodic shedding of vapor clouds that collapse due to the increase of pressure above the vapor pressure. Cavity collapse mechanisms will not be treated in detail in this thesis. The numerical prediction of sheet cavity shedding in a Venturi with axial flow was the topic of the MSc thesis of Cointe [69], who used an inviscid approach to determine the shedding frequencies and characteristics of the re-entrant jet and the bubbly-shock mechanisms.

First a short outline of both mechanisms will be given, followed by the assessment of the dominant frequencies of the cavity shedding to be taken into account when analyzing the cavity dynamics inside the venturi. The behavior of the sheet cavity at the end of the throat and the vortex cavity is shown in a sequence of instantaneous isocontours of the vapor fraction $\alpha_{\text{vap}} = 0.5$ in Figure 5.10. This chronological series of images shows the impact of the collapse mechanism on the vortex cavity dynamics upstream. Possible cavity collapse mechanisms are discussed next.

Cavity collapse mechanisms

The re-entrant jet can be understood by considering the local velocity field at the location of the sheet cavity. The re-entrant jet is a characterized by a reverse flow which wraps around and underneath the vapor cavity that is being advected by the flow. Franc & Michel [44] explained that this jet is caused by the inward directed curvature of the low-pressure region that is the cavity, leading the free streamlines to wrap around the cavity and join again at the front. The re-entrant jet is sketched in Figure 5.9a. It is the least violent of the two mechanisms, occurring at larger values of the cavitation number σ and is characterized by a higher shedding frequency as demonstrated by Cointe [69] and experimental investigations by Hogendoorn [105].

(a) Sketch of the re-entrant jet phenomenon.

(b) Sketch of the bubbly shock phenomenon.
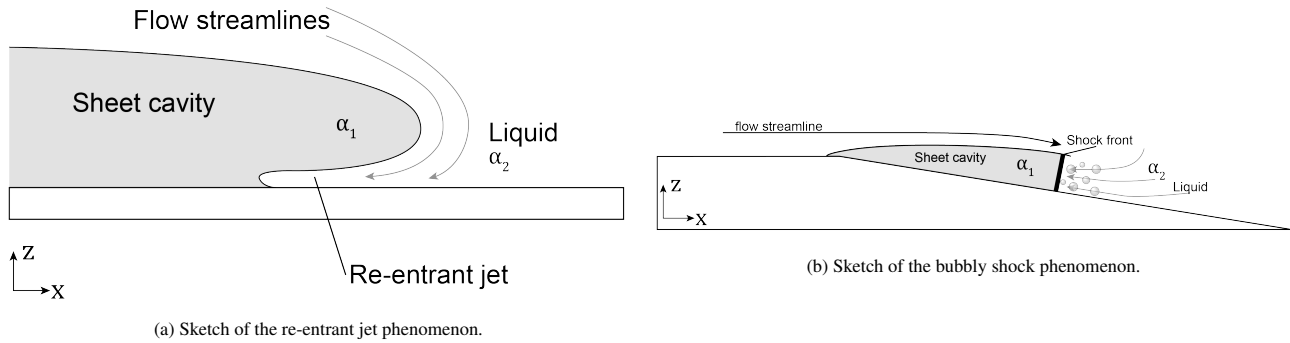
Figure 5.9: Attached cavity shedding mechanisms

The bubbly-shock mechanism, sketched in Figure 5.9b is a result of collapsing bubbles inside cloud cavitation. The cloud of bubbles originates from the attached sheet cavity and is convected by the mean flow until the increased pressure leads to the collapse of the bubbles. As the collapse of individual bubbles leads to very high pressures, an omnidirectional shock wave is formed. In the incompressible approach a shock wave (characterized by a pressure discontinuity) cannot exist. A pressure wave, however, which is not characterized by a discontinuity, can exist and travel upstream. There it leads to the detachment of the sheet cavity as it reaches the attachment point. In incompressible single-phase flows, this pressure wave occurs instantaneously in the domain. Cointe [69] showed that in a multi-phase flow the propagation velocity of the pressure wave can be calculated from the shape of the volume fraction plotted in a two-dimensional T-s (time-space) diagram, further elaborated upon later in this section. The bubbly-shock mechanism is thus characterized by an discontinuity of the vapor fraction traveling upstream that spans the entire height of the cavity [69, 106].

Assessment of dominant frequencies

The frequencies associated with the cavity shedding are analyzed using four different methods; by i) analyzing the frequency spectrum (using Fast Fourier Transform (FFT)) of pressure oscillations at planes B and C for the shedding at the throat entrance, and C and D for the throat exit, ii) inspecting the behavior of the total vapor volume in the domain, iii) assessing the dominant frequency in the FFT of the cavity diameter and finally iv) qualitative comparison with spatio-temporal plots of liquid fraction from [69].

The frequency analysis using the monitor lines at locations B, C and D is presented in Figure 5.11. Only the EARSM simulations show a significant power density at location B, which is linked to the shorter sheet cavities in the case of IDDES. Peaks in the detrended spectra are visible at all measurement locations around the fundamental frequency of 60 Hz and its harmonics at integer multiples of this frequency, except for the M_3 EARSM simulation which shows the fundamental frequency peak at 50 Hz. The origin of the discrepancy between the M_3 EARSM simulation and the others was not found.

The temporal evolution of the total volume of vapor in the domain and the corresponding frequency spectrum are presented in Figure 5.12. The total vapor volume is characterized by two different periodic motions; i) a low frequency periodic oscillation of the vapor volume fraction in the entire domain with a frequency of 10/15 Hz and ii) the earlier identified periodic phenomenon occurring at $f = 50/60$ Hz. The presence of the same frequency in the vapor fraction frequency spectrum as in Figure 5.11 indicates that the periodic phenomenon is related to cavitation. The low frequency component might be the same kind of unsteady behavior identified for the wetted vortex simulations in Section 4.1.5, since the oscillation frequency of a Precessing Vortex Core (PVC) increases with an increase in velocity [101].

The spatially-averaged variation and the frequency spectrum of the cavity diameter (z-normal observation plane) are presented in Figure 5.13. The periodic motion with a frequency of approximately 60 Hz can be recognized in Figure 5.13a and strongly affects the time-averaged diameter of the cavity. Figure 5.13a also shows that the contraction of the cavity is irregular and does not occur simultaneously across different simulations. Peaks at integer multiples of the fundamental frequency are
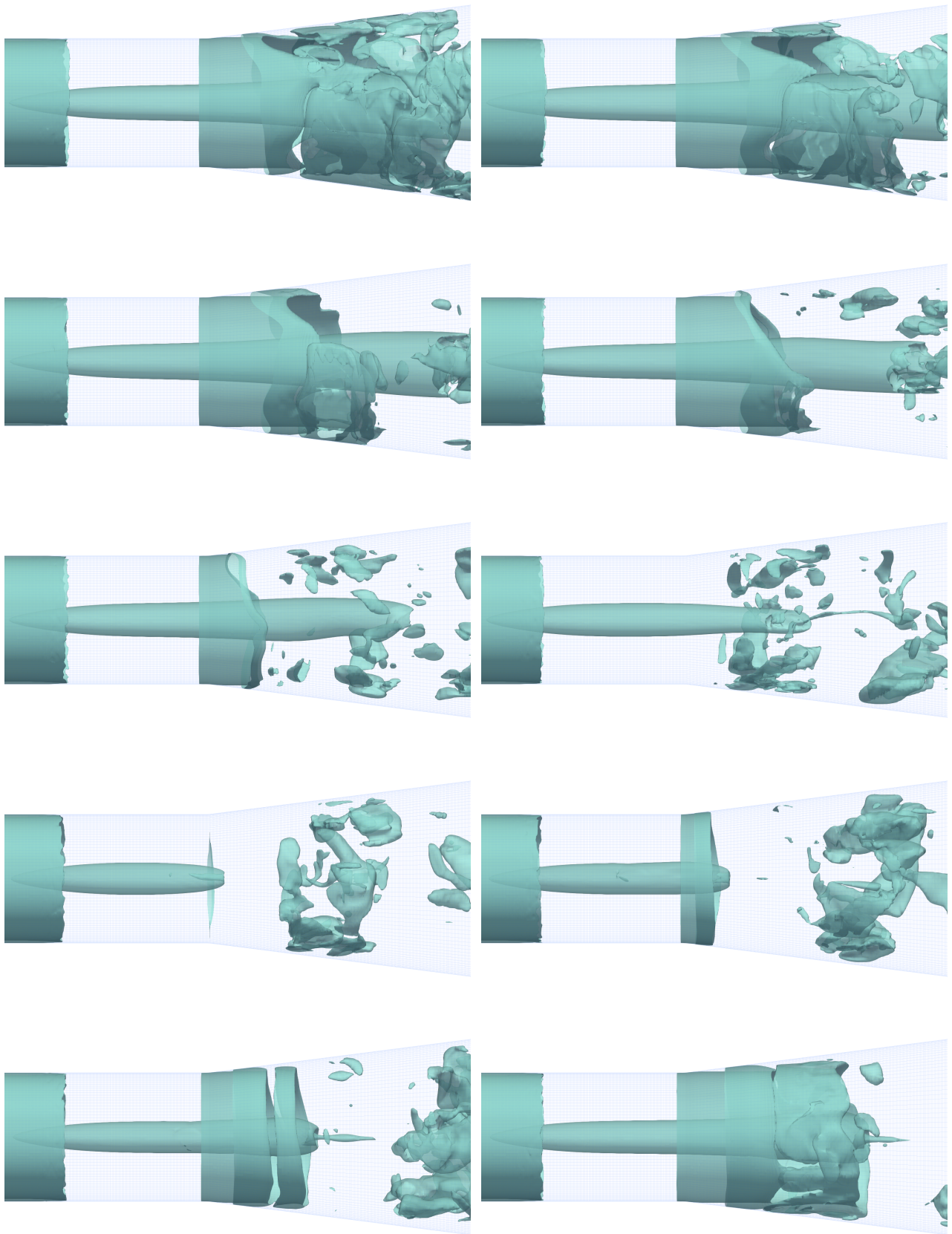
Figure 5.10: Shedding sequence of the sheet cavity at the end of the Venturi throat, showing the contraction of the vortex cavity as the attached sheet cavity collapses. Images obtained on M_3 using the IDDES model in combination with the Schnerr-Sauer cavitation model, with $\alpha_{vap} = 0.5$ isocontours. Sequence is chronological from left to right and top to bottom, with 1.98×10^{-3} s between presented events. Flow direction is from left to right.

(a) Line B (solid) & C (dashed)

(b) Line C (solid) & D (dashed)
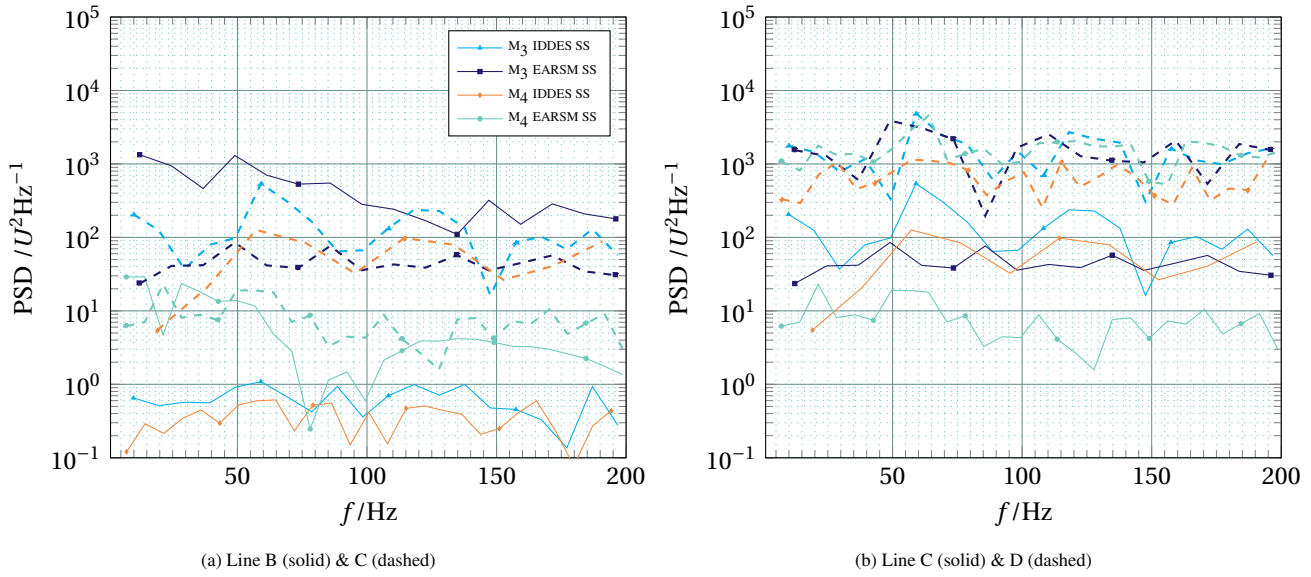
Figure 5.11: Assessment of dominant frequencies using the line monitors. Frequency spectra were calculated for each point from the detrended pressure signal using the FFT algorithm in MATLAB and subsequently averaged.

(a) Time-series

(b) Frequency spectrum
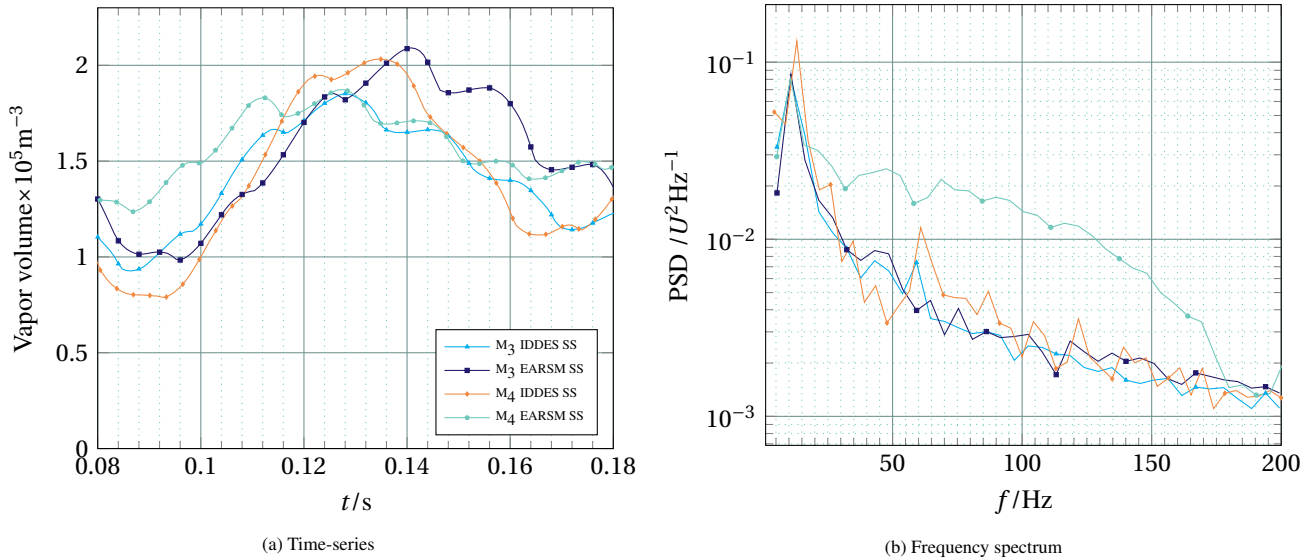
Figure 5.12: Assessment of dominant frequencies using the time-series and corresponding frequency spectra of the vapor fraction. Frequency spectra were obtained with the FFT algorithm in MATLAB from the detrended vapor volume signal.

distinguishable in Figure 5.13b.

The following conclusions can be made based on results for the above three criteria showing a periodic phenomenon occurring with a fundamental frequency of 50/60 Hz:

i) Given that the pressure exhibits a periodic motion at various measurement locations, the phenomenon causes a periodic global rise in pressure. The amplitude of the pressure oscillation also becomes larger towards the end of the Venturi throat (location D).

ii) Considering the peaks in the total amount of vapor inside the domain, the global rise in pressure is accompanied by a reduction of vapor volume as the vapor pressure is periodically exceeded. This again confirms that the effects of the phenomenon are acting globally.

iii) Taking into account that the cavity diameter is significantly affected by the phenomenon, the effect cannot simply be discarded on the grounds that only the cavity dynamics are of interest. Furthermore, the time-series of the cavity diameter is characterized by rather flat peaks and sharp troughs, indicating that the phenomenon acts on a short timescale.

These separate conclusions hint towards the periodic occurrence of a pressure wave, which (as mentioned before) is instantaneous for a single-phase incompressible flow but can be identified in incompressible multiphase flows as demonstrated by

Cointe [69]. Such a pressure wave could be the result of the violent collapse of a cloud of bubbles shed from the sharp edge at the end of the parallel section, referred to commonly as the bubbly-shock mechanism. The qualitative comparison between the spatio-temporal evolution of the cavity diameter and the liquid volume fraction for the bubbly-shock mechanism obtained from [69] is presented in Figure 5.14. The clean triangular shapes (normally plotted in a pressure diagram) were found to be typical for the bubbly-shock mechanism [105]. The pressure was not measured in such a way that similar diagrams could be made for the present simulations, but the cavity diameter in the present simulation is directly dependent on the vapor/liquid volume fraction, which in turn depends on the pressure. Hence, it is expected that in the present simulation, the bubbly-shock mechanism is responsible for the shedding of the cavity at the end of the Venturi throats. The velocity of the pressure wave was not calculated as it does not contribute to the research regarding the cavitating line vortex dynamics and deeper analysis of the dynamics of sheet cavity shedding is outside of the scope of this work.

(a) Time series of the spatially-averaged cavity diameter.

(b) Frequency spectrum of the spatially-averaged cavity diameter
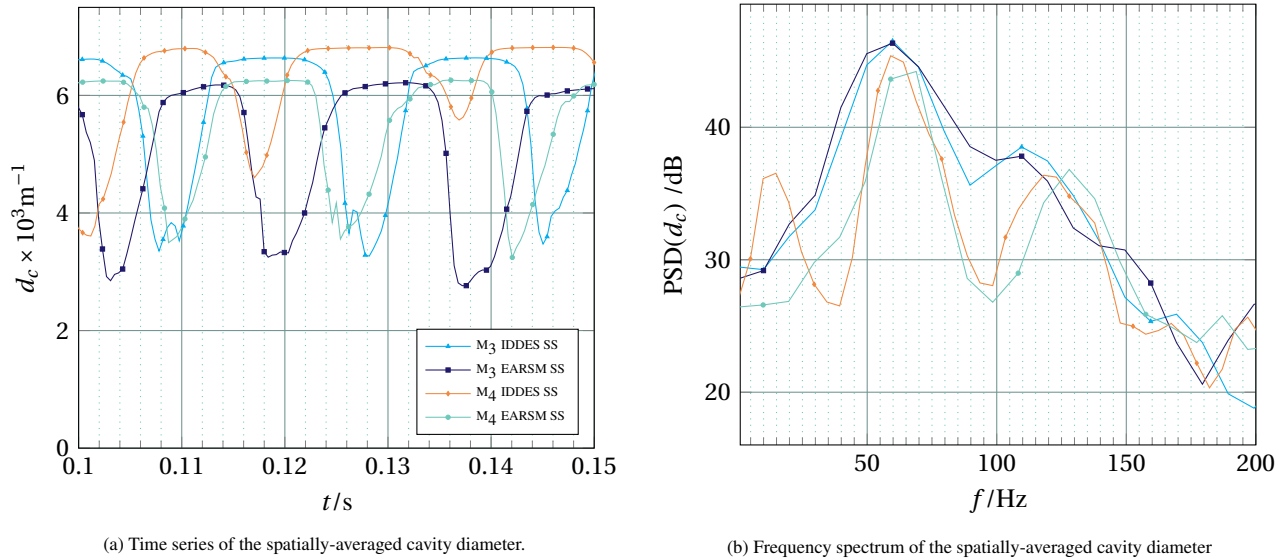
Figure 5.13: Assessment of dominant frequencies in cavity diameter using the co-processing capability of PARAVIEW and the written PYTHON script. Results for the z-normal observation plane.

(a) T-s diagram of cavity diameter from z-normal observation plane, M_3 IDDES simulation.

(b) T-s diagram of liquid fraction, reproduced with permission from [69].
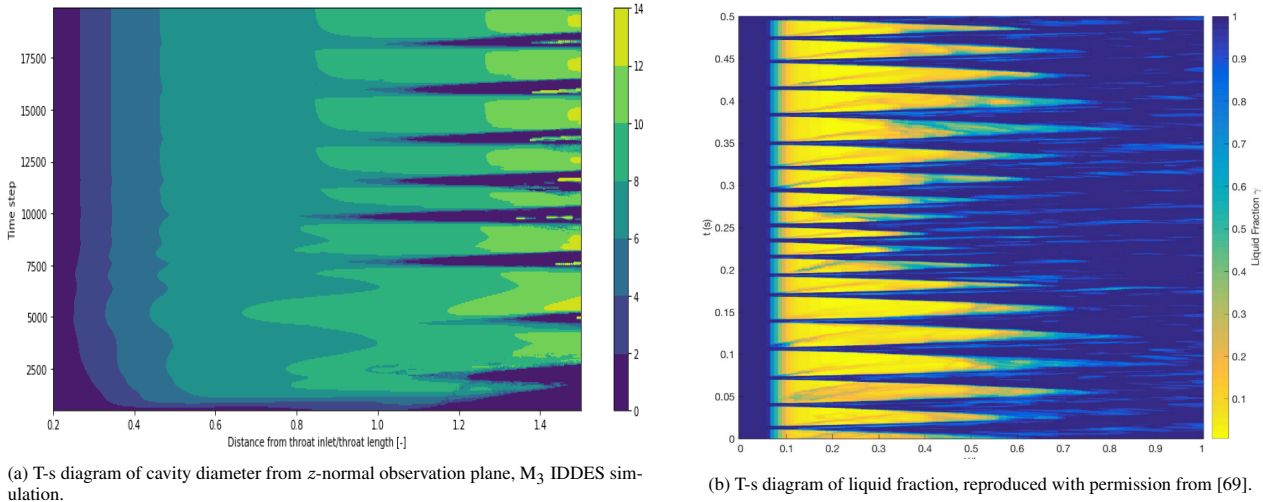
Figure 5.14: Side-by-side qualitative comparison of spatio-temporal evolution of cavity diameter in present research and liquid volume fraction from [69].

5.3.2. Spectral analysis of the cavitating vortex

The spectral methods described in Sections 2.4.2 and 3.2.4 were applied to the vortex cavity in order to assess whether the different oscillatory modes visible in the experiments of [15, 77] could also be reproduced numerically and to quantify the differences between the IDDES and EARSM turbulence models. The spatio-temporal evolution of the cavity diameter and cavitating vortex centerline are considered first, followed by the two-dimensional Cross-power Spectral Density (CPSD) and phase difference results.

Spatio-temporal evolution and one-dimensional spectra

The analyzed length of the signal in space and time was determined based on the development length of the vortex cavity and how long it took for the cavity to stabilize. The signal lengths and spectral resolutions are provided in Table 5.4. The table shows that the analyzed length of the cavity for the EARSM simulations is 33 % shorter than for the IDDES cases due to the larger diffusion of the cavity interface in the former. The resolution of the wavenumber and frequency is defined as the sampling frequency divided by the number of samples; $f_{s,\ time/space}/N_{samples}$. The resolution is a measure for the size of the wavenumber and frequency bins, so that the lower the value, the more accurate the estimate of both parameters. The simulations on M_4 were run for a longer period[1] to get the lowest value for the resolution of wavenumber and frequency. The M_3 EARSM SS simulation has the least accurate estimate. It is noticeable that the analyzable length of the cavity grew with a decreasing cell size, showing that a grid-/time step converged solution has not yet been reached. When compared to the resolutions in Bosschers' work [2], with resolutions of 0.15 s^{-1} and 31.6 m^{-1}, it is apparent that the resolution of both parameters in the present numerical simulations is lower. Bosschers highlighted that his frequency resolution was more than required, whereas the wavenumber resolution was still insufficient (J. Bosschers, personal communication, June 2019).

Table 5.4: Spatio-temporal domains and resolutions of cavitating vortex simulations. Time t^* is nondimensionalized as $t u_\infty / L_{throat}$ and the location x^* is measured as x'/L_{throat}, where x' is measured from the front of the throat of the venturi.

Simulation	t^*_{start}	t^*_{end}	x^*_{start}	t^*_{end}	res. frequency /Hz	res. wavenumber / m^{-1}
M_3 IDDES SS	13.31	43.72	0.6	0.9	7.33	55.80
M_3 EARSM SS	15.16	43.72	0.7	0.9	8.23	84.32
M_4 IDDES SS	15.16	68.95	0.6	1.05	4.37	36.96
M_4 EARSM SS	16.65	61.66	0.75	1.05	5.23	55.25

The calculation of the dB-valued spectra is repeated below for convenience:

$$\text{CPSD}(k_z, f) = 120 + 10\log_{10}\left(\frac{G_{top}(k_z,f)G^*_{side}(k_z,f)}{d_c^2}\right), \qquad (3.7\ \text{revisited})$$

where $G(k_z, f)$ refers to the two-dimensional FFT of r' and $G^*(k_z, f)$ is the complex conjugate. The dB-valued Power Spectral Density (PSD) was obtained similarly:

$$\text{PSD}(k_z/f) = 120 + 10\log_{10}\left(\frac{S(k_z/f)S^*(k_z/f)}{d_c^2}\right), \qquad (3.8\ \text{revisited})$$

where S and is the single-sided spectrum amplitude and its conjugate S^*. The phase difference was calculated from the cross-spectrum $G(k_z, f)_{xy}$ as the angle between the real and imaginary parts of the spectrum. Figure 5.15 contains the time-averaged signals and one-dimensional spectra of the cavity diameter d_c and centerline location c_{line}. Even though a significant part of the domain is not taken into account for the analysis, Figure 5.15a shows that the cavity isocontours are not yet parallel when averaged in time. This is caused by the conical shape of the vapor core as mentioned earlier. Part of the cavity development length therefore had to be included in the analysis. The analytical model by Bosschers [2] is based on an infinitely long, parallel cavitating vortex; an assumption violated by incorporating part of the cavity development length into the solution. The effect on the spectral results was limited by removing a linearly increasing trend from the solution (i.e. linear detrending). The wavenumber spectrum in Figure 5.15c identified no non-zero wavenumber component that was above the noise level, and the time-averaged diameter of the cavity is smooth. It can therefore be concluded that there are no standing waves present on the cavity interface. The simulations on the finer mesh demonstrate that the cavity size grows further in the radial direction with increasing grid resolution, hence the solution is grid dependent.

Assessing the time-averaged centerline location in the normalized form presented in Figure 5.15b, it appears that the cavity centerline deviates significantly from the geometrical centerline. These static deviations and all measured fluctuations are of $\mathcal{O}(10^{-5})$ m, which is one order smaller than the cell size. PARAVIEW interpolates cell-centered values to point-values with a point spacing of approximately half the cell spacing, which is still larger than the static and dynamic deviations of the centerline. The grid size yields an estimate for the uncertainty of the measurements, which therefore is of $\mathcal{O}(10^{-4})$ m. Considering that the uncertainty of the measurements exceeds the measured centerline positions, the one- and two-dimensional spectra of centerline (fluctuations) are only given for completeness and the graphs should be interpreted with caution. The power spectra of both measurement planes are more spread-out and are not as similar as for the cavity diameter measurement, probably resulting from the measurement noise and the large uncertainty.

The spatially-averaged evolution of cavity and centerline along with their respective frequency spectra are provided in Figure 5.16. The spatially-averaged cavity diameter in Figure 5.16a and its corresponding frequency spectrum in Figure 5.16c

---

[1]The computational cost for each simulation on M_4 is over 300000 CPUhours

(a) Normalized cavity diameter.

(b) Normalized cavity centerline location. Negative values indicate a position in the negative y-/z-plane.

(c) One-sided wavenumber diagram of the cavity diameter.

(d) One-sided wavenumber diagram of the cavity centerline.
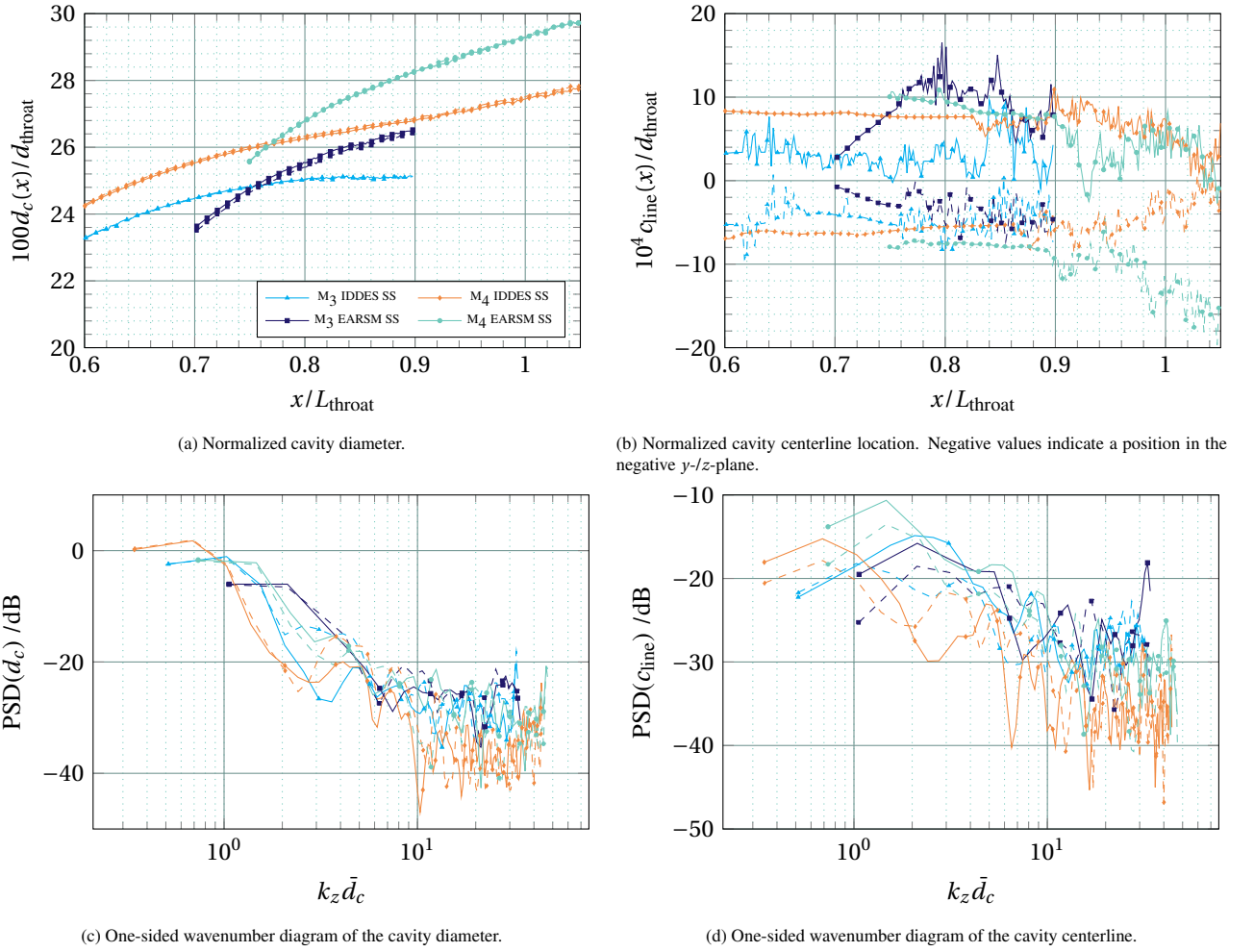
Figure 5.15: Time-averaged evolution and one-sided spectra of the vortex cavity diameter and cavitating vortex centerline. Solid lines indicate z-normal plane, dashed lines indicate y-normal plane.

were previously presented in dimensional form in Section 5.3.1 to highlight the periodic oscillation of the cavity diameter in time. The fundamental frequency of shedding and its higher harmonics can be distinguished in Figure 5.16c. The peaks do not align exactly as they did in Figure 5.13, which is due to the normalization with the spatially-averaged cavity diameter d_c which differs slightly between and simulations. Nevertheless, peaks are clustered together for the same mesh, indicating that the cavity response is almost the same for both turbulence models.

The average centerline position in Figure 5.16b is close to zero, with large peaks occurring when the sheet cavity at the end of the Venturi collapses and the cavity contracts. The peaks of the centerline oscillation are more narrow, pointing out that the deviation is more instantaneous than the contraction of the cavity. The larger power density at low wavenumbers in Figure 5.16d suggests that the centerline variation occurs over the entire length of the cavity. The deviation is about as large as the measurement uncertainty, however, so that this statement is made with caution. Just as for the time-averaged centerline spectrum in Figure 5.15d, the spectra of both measurement planes are further apart than for cavity diameter.
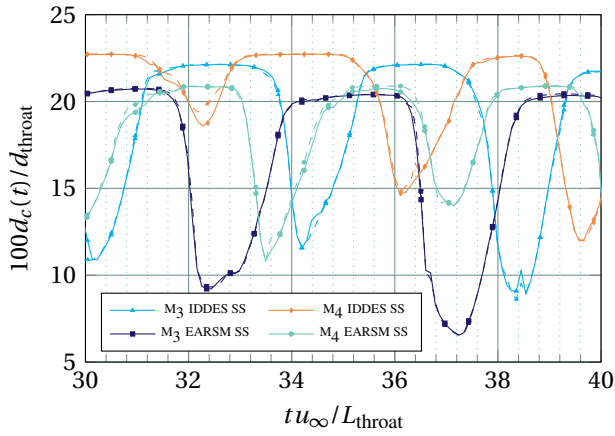
(a) Normalized cavity diameter (excerpt of analyzed result).
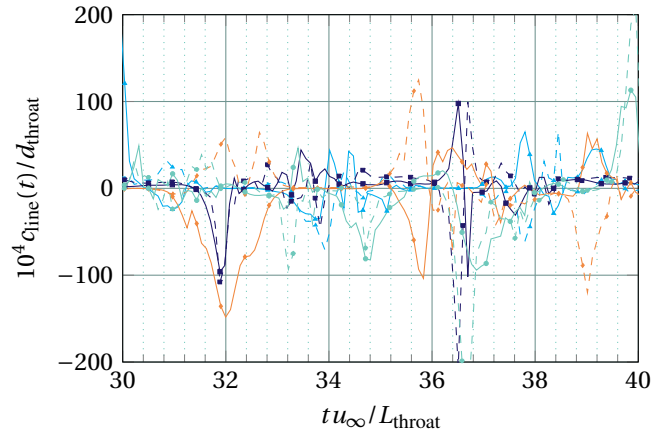
(b) Normalized cavity centerline location (excerpt of analyzed results). Negative values indicate a position in the negative y-/z-plane.
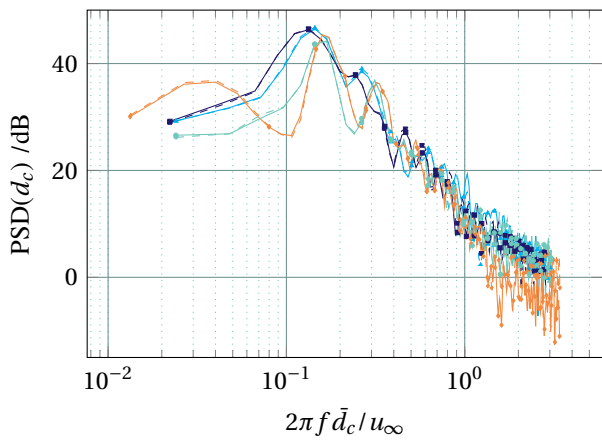
(c) One-sided wavenumber diagram of the cavity diameter.
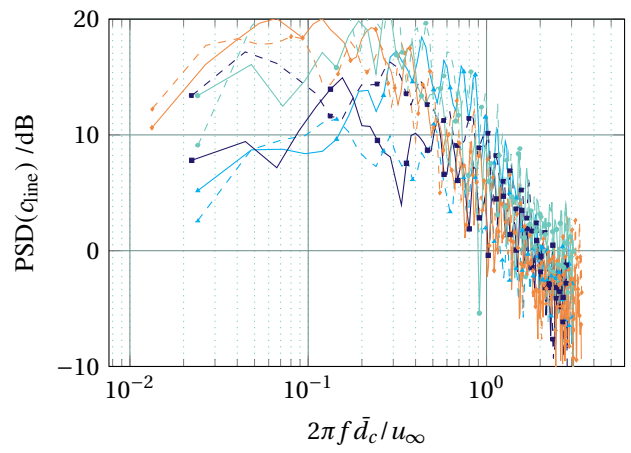
(d) One-sided wavenumber diagram of the cavity centerline.

Figure 5.16: Space-averaged evolution and one-sided spectra of the vortex cavity diameter and cavitating vortex centerline. Solid lines indicate z-normal plane, dashed lines indicate y-normal plane.

Cross-spectra and phase differences

The two-dimensional wavenumber-frequency diagrams, using the results of both measurement planes, are given for the diameter and centerline fluctuations in Figure 5.17 and Figure 5.18 respectively. The result of two-dimensional Fourier-transforms is divided over four quadrants; for both positive and negative wavenumbers and frequencies. The deformations of the cavity are real (i.e. do not contain imaginary components), making the resulting full spectrum symmetrical, thus only two quadrants are needed to represent the solution in wavenumber-frequency space. The waves are assumed to be only traveling forwards in time and in both directions in space, hence only positive frequencies and both positive and negative wavenumbers are plotted, following the reasoning of Bosschers [2]. The results for the phase difference are only displayed if the coherence of the data between both measurement planes is larger than 0.2. Bosschers [2] only plotted results for coherence> 0.4, which was too restrictive for the results presented in this work. The coherence is a measure of the amount of noise between two measurements, whereby a coherence equal to 1 indicates no noise. Bosschers chose the value of 0.4 by determining the highest value at which the dispersion lines were still visible (J. Bosschers, personal communication, September 5, 2019). Hence, the amount of numerical noise is larger for the present simulations than for the experimental measurements by Pennings et al. [13].

As expected from the one-dimensional spatially-averaged diameter spectrum, the two-dimensional CPSD shows clear horizontal lines at the fundamental shedding/ collapse frequency and higher harmonics of the sheet cavity at the end of the throat. This is the case for both turbulence models and on M_3 and M_4. The energy of the spectrum is concentrated around the zero-wavenumber, indicating that the diameter variation occurs simultaneously over the length of the vortex cavity. When increasing the mesh resolution, a longer part of the cavity can be analyzed and the runtime was increased to improve the frequency resolution. Consequently, the M_4 spectra show a clearer separation between peaks in the frequency domain. There are no diagonal lines visible in the spectrum, indicating that there is no identifiable group velocity of waves and that no wave-like structures can be identified on the cavity interface.

Looking at the CPSD of the centerline oscillations, the number of oscillations is clearly lower than for the diameter (which was already highlighted by the one-dimensional spectral analysis). Most of the energy is found around the zero wave-number, but the fundamental shedding frequency and harmonics are less visible than for the diameter. The absence of diagonal lines indicates that wave-like deformations of the cavity centerline, demonstrating the presence of a $n = 1$ mode, are not found. As mentioned previously, the spatial resolution is be too low to capture oscillations of the cavity centerline accurately. For this test case there was no any out-of-plane disturbance of the vortex, i.e. the vortex remains centered around the geometrical centerline. Subsequently, a 'serpentine mode' ($n = 1$) deformation of the cavity is not likely to occur for this flow case. The tip vortex originating from a wing tip is generated by a lifting surface (which already introduces more unsteadiness), and follows a certain trajectory, therefore increasing the likelihood of finding such a modal deformation for those cases.

The absolute values of the phase differences are plotted in Figure 5.18. The results show that for the diameter, a phase difference of 30 to 60 degrees accompanies the contraction of the cavity at the shedding frequency and the harmonics thereof. This indicates that the cavity did periodically deform into an noncircular shape as a result of the contraction. However, this amount of phase difference does not correspond to the phase difference required for the 'double-helix mode' ($n = 2$) deformation, which is the only other mode where the cross-section becomes noncircular. The M_3 EARSM SS spectrum does not display the same features as the other simulations due to a coarser wavenumber distribution (i.e. a resolution of 84 m^{-1} vs. 55 m^{-1} on M_4, see Table 5.4). The coarser grid possibly also influences the lack of phase angles that are identified.

The lack of reliable (coherence> 0.2) data in the phase difference spectrum for the centerline oscillations complicates the analysis of results for the coarser M_3 mesh simulations. The IDDES results show a lower coherence, which is likely caused by an increased amount of small-scale fluctuations that are not resolved by the EARSM model. Comparing results between meshes shows that the higher mesh resolution generally increases coherence. This confirms the hypothesis that part of the numerical noise can be attributed to the coarse mesh resolution. The phase difference of 30 to 50 degrees might indicate an out-of-plane movement of the cavity, but given the large uncertainty this is unlikely.

(a) M_3 IDDES SS, diameter oscillations

(b) M_3 IDDES SS, centerline oscillations

(c) M_3 EARSM SS, diameter oscillations

(d) M_3 EARSM SS, centerline oscillations

(e) M_4 IDDES SS, diameter oscillations

(f) M_4 IDDES SS, centerline oscillations

(g) M_4 EARSM SS, diameter oscillations

(h) M_4 EARSM SS, centerline oscillations
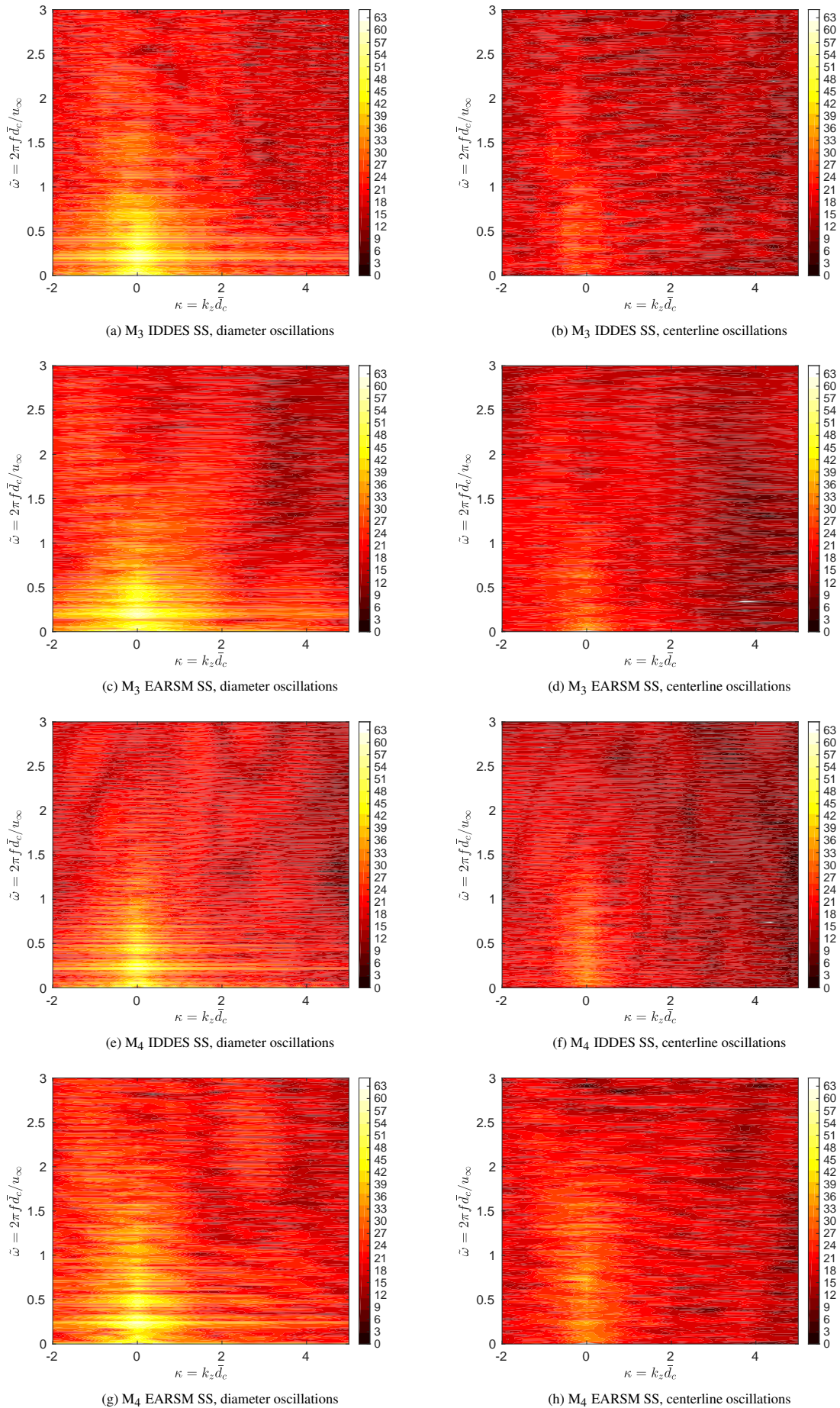
Figure 5.17: Cross-power spectral densities of cavity diameter fluctuations and fluctuations of the cavity centerline position.

(a) M_3 IDDES SS, diameter oscillations

(b) M_3 IDDES SS, centerline oscillations

(c) M_3 EARSM SS, diameter oscillations

(d) M_3 EARSM SS, centerline oscillations

(e) M_4 IDDES SS, diameter oscillations

(f) M_4 IDDES SS, centerline oscillations

(g) M_4 EARSM SS, diameter oscillations

(h) M_4 EARSM SS, centerline oscillations
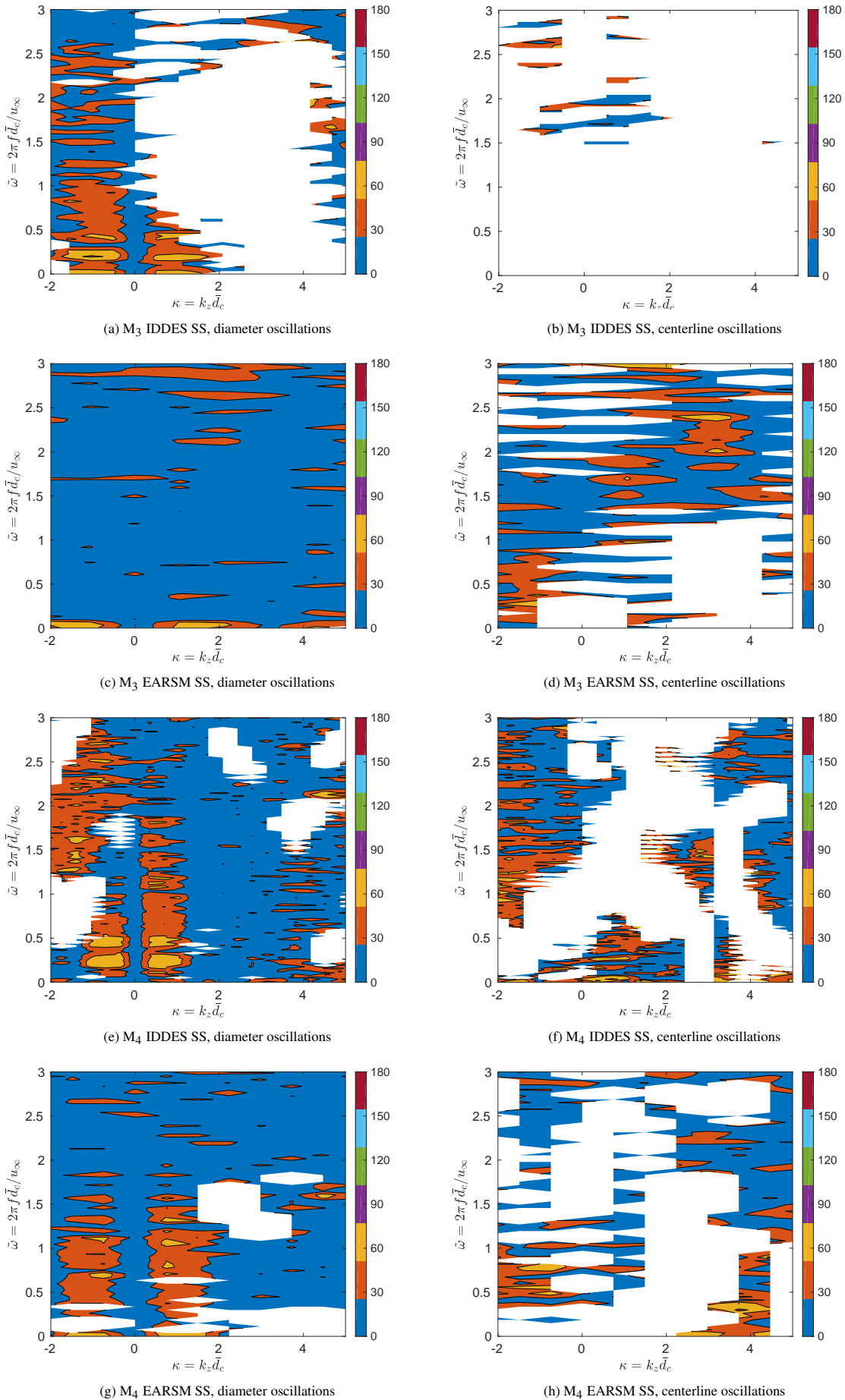
Figure 5.18: phase difference between measurement planes of cavity diameter fluctuations and fluctuations of the cavity centerline position, coherence > 0.2.

5.4. Conclusions

The simulations of the cavitating vortex were characterized by troublesome convergence, caused by high local residuals $L_\infty = \mathcal{O}(10^{-1})$ for the axial velocity and specific turbulent dissipation rate at the end of the cavity. The largest RMS residual $L_2 = \mathcal{O}(10^{-4})$ was acceptable. A further reduction in time step and increased refinement of the grid are expected to improve convergence, but were not feasible due to the already large computational cost.

The flow field for the cavitating vortex differed from the wetted case in all three velocity components. The tangential velocity profile within the vapor core was linearly increasing and followed a Lamb-Oseen-like profile in the rest of the vortex. The axial velocity profile was no longer flat. The radial velocity increased linearly towards the edge of the vapor core and was no longer negligible. The sheet cavity extending from the front of the Venturi throat was still present at the measurement location in the EARSM simulations on both grids. Furthermore, the EARSM demonstrated a more diffuse vapor core interface. The diffusive interface and presence of the sheet cavity influenced the flow field at the measurement location as well as the development length of the cavity.

The shedding of the cavity originating from the end of the Venturi caused a periodic contraction of the vortex cavity in streamwise and radial direction. A noncircular deformation of the cavity was found to accompany the contraction, but the phase of the deformation did not correspond to the double-helix ($n = 2$) mode identified by Bosschers [2]. Both temporal and spatial resolutions were lower than the ones reported by Bosschers [2], owing to the high runtime required and the short length of the cavity that could be analyzed given the geometry. The fundamental collapse frequency of the sheet cavity at the end of the Venturi throat and its higher harmonics were dominant features in the two-dimensional spectral analysis of cavity diameter oscillations and the one-dimensional frequency spectrum of the spatially-averaged cavity diameter. The centerline fluctuations were in the most part smaller than the grid spacing (i.e. the measurement uncertainty), making the results unreliable. The coherence between measurement planes was, particularly for the centerline phase difference, considerably lower than from the experimental measurements by Pennings et al. [13]. Furthermore, the average cavity diameter increased on finer grids, indicating strong grid dependency. The grid resolution in the region of interest was therefore concluded to be still too coarse to accurately determine the cavity dynamics.

No traveling or standing waves were captured using the spectral analysis method and the cavity deformations did not correspond to any of the modal shapes characterizing a cavitating tip vortex. Despite the aforementioned issues regarding the resolution and measurement noise, the conical shape of the vortex cavity may also have influenced the absence of identifiable surface waves. The dispersion relation was derived by Bosschers [14] for an infinitely long parallel cavity and described by (a cavitating formulation of) a Lamb-Oseen vortex. Both these assumptions are violated in the present simulations, therefore it is not unthinkable that the simulated line vortex does not experience the same kinds of modal deformations as a cavitating tip vortex

The next chapter will provide the overall conclusions and additional recommendations for this work. This will include both answers to the research questions from the introduction in Chapter 1 as well as a discussion on the applicability of this geometry for the simulation of a cavitating line vortex.

6

Conclusions & recommendations

This thesis has discussed the numerical modeling of a wetted and cavitating line vortex in a converging-diverging nozzle in detail. Chapter 2 provided a broad overview of the theory and numerical concepts used for this research. The simulation set-up, including the studies of the domain length and the inflow boundary condition, was discussed in Chapter 3. This was followed by the results obtained for the wetted vortex case in Chapter 4. This chapter discussed both the time-averaged flow field as well as the Verification and Validation (V&V) study performed with the EARSM model. Cavitating vortex results were presented in Chapter 5, where both the flow field and the vortex cavity dynamics were analyzed in detail.

The conclusions in this chapter are formed around answering the research questions formulated in the introduction. More detailed information regarding conclusions about the wetted and cavitating flow cases can be found in Chapter 4 and Chapter 5 respectively. The first section will start off with the research question, followed by the conclusions from the simulations answering the particular question. The second section contains the conclusions with respect to the flow case; i.e. whether simulating a cavitating line vortex in this geometry is a useful abstraction of the cavitating tip vortex. The final section contains recommendations for further research.

6.1. Conclusions with respect to the research questions

6.1.1. Inflow conditions
The first research questions concerns both the selection of a suitable inflow condition as well as a discussion of its validity as a representation of the vortex generated by a swirl generator in [8].

The Lamb-Oseen vortex model was used as an inlet condition based on previous studies [6, 7] and since it represented the flow field in the reference measurements [8]. After the tuning of the inflow condition in Chapter 3, the velocity angles at measurement plane A, obtained using the Shear Stress Transport (SST) model matched the reference angles at radial positions $0.6 \leq r/r_{max} \leq 0.92$, whereby no experimental data was available for $r/r_{max} < 0.4$ due to the presence of the hub of the swirl generator. The SST and EARSM showed the same angles at these radial positions, whereas the IDDES model matched the reference angles from $r/r_{max} = 0.6$ until the wall. The reason for the deviation close to the wall was not found. Large differences were found in the area $r/r_{max} < 0.4$, where the vortices predicted by the RANS models experienced larger viscous diffusion (i.e. lower peak tangential velocity and larger viscous core radius) from the inlet towards the measurement section. The lower of diffusion of the IDDES model is due to the lack of modeled *and* resolved turbulence in the regions solved using the LES form of the equations, i.e. using a smaller turbulence length scale. As the region of interest is in the middle of Venturi throat, upstream differences in the flow field could be interpreted as having different inflow conditions for the three turbulence models and is an unwanted consequence of specifying the vortex at the inlet.

6.1.2. SRS performance in wetted line vortex prediction
The results of all models were compared to experimental measurements [8] in the middle of the Venturi throat (measurement plane C). As in the inlet section, most of the domain for the IDDES was solved in LES mode, reducing the modeled turbulence to almost zero. The lack of velocity fluctuations also led to negligible amounts of resolved turbulence. The result from the IDDES model is therefore an almost laminar flow field, whereas the solutions for the RANS models $k - \omega$ SST and EARSM are characterized by increased viscous diffusion due to the high eddy viscosity predicted by both models. The computationally more expensive EARSM was not able to predict a tangential velocity profile that fit the experiments better than the SST model, both simulating an excessively large viscous core size and too low tangential velocity. The IDDES predicted the experimentally measured Lamb-Oseen more closely, but still underpredicted the peak tangential velocity and pressure decrease in the core and slightly overpredicted the viscous core size. The simulated vortex of the IDDES model was the only one to correspond to an actual Lamb-Oseen vortex, which can be explained by the almost entirely laminar flow field for this model and the laminar nature of the Lamb-Oseen vortex. The results of the EARSM were verified to be grid- and time step independent, making this particular EARSM (the Hellsten model for this thesis) unsuitable for the prediction of a wetted line vortex in this geometry. Results of the IDDES model improved slightly on the finer M_2 grid due to a further decrease in

modeled turbulence, but the lack of resolved turbulence makes the comparison with the (modeled) turbulent flow fields of the RANS models somewhat biased.

6.1.3. Influence of turbulence models on cavitating line vortex structure

The cavitating results were characterized by two sheet cavities originating from the sharp edges at the front and end of the Venturi throat. The front sheet cavity was shown to influence the development of the vortex cavity, which developed more downstream for the EARSM simulations due to a longer sheet cavity. All data was compared by defining the vapor core as the region in the vortex defined by a vapor volume fraction greater than 0.5. Viscous diffusion of the cavity interface, combined with the less developed vapor core and the presence of sheet cavities at the measurement plane C for the EARSM simulations led to pronounced differences in the radial profiles of axial velocity and pressure coefficient. Both EARSM and IDDES models predicted a solid-body rotation for the vapor core, followed by a tangetial velocity distribution similar to that of a Lamb-Oseen vortex outside the vortex, which is in line with the theory for cavitating vortices. The radial velocity was in all simulations of the same order of magnitude as the tangential velocity, and resulted in a conical shape of the vapor core inside the cavitating vortex. This means that the cavitating line vortex simulated in this Venturi geometry using the current simulation set-up was not representative for the cavitating tip vortex originating from a propeller or foil, since those vortices are characterized by a (cavitating form of the) Lamb-Oseen velocity distribution (where the radial velocity is negligible).

6.1.4. Influence of turbulence models on line vortex cavity dynamics

The IDDES model showed more noise between measurement signals leading to a lower coherence between the diameter measurements of both planes. The increased amount of noise is attributed to the partial resolution of turbulence by IDDES, which is modeled in EARSM simulations. The coherence was significantly lower than for the experimental results by [13], whereby especially M_3 demonstrated large amounts of numerical noise. Additionally considering that most measurements of centerline deviations were smaller than the uncertainty, the phase difference spectra did not allow for a reliable analysis. As coherence improved when increasing grid resolution, a finer mesh than M_4 is required to increase the accuracy of the analysis, also for the diameter oscillations. The grid-dependence of the solution was also demonstrated by the larger cavity diameter on the finer M_4 grid.

The dominant feature visible in the one- and two-dimensional spectra was the contraction of the vortex cavity following the shedding of the sheet cavity at the end of the venturi. This contraction was, based on the analysis, accompanied by an oval-shaped cavity cross-section not corresponding to any of the deformation modes identified by Bosschers [2]. this cross-sectional deformation is still unclear and might be measurement noise given the previously mentioned low coherence.

No wave-like disturbances of the cavity interface could be found, which may have various origins: i) the violation of the assumption of a cavitating tip vortex due to the high radial velocity, ii) the periodic contraction of the cavity is so large in amplitude that it possibly prohibits the vapor core to evolve to a 'quasi-steady' self-oscillatory state before it is contracted again, iii) the lack of resolution even on the finest M_4 grid and iv) the diffusivity of the interface caused either by the Volume-of-Fluid (VOF) method or eddy viscosity (for the EARSM simulations). Based on the results it seems as if the IDDES model would be better suited to assess cavity dynamics of a cavitating tip vortex using the spectral approach as the interface diffusivity is lower and the length of the cavity that could be analyzed was larger than for the EARSM model. Nonetheless, it needs to be taken into account that the solution from the IDDES model was again almost laminar, so that only IDDES with added velocity fluctuations to compensate the lack of resolved wall-generated turbulence and inflow turbulence would yield an unbiased comparison to the EARSM simulations for this flow case.

The answers to the sub-questions above can be combined to answer the general research question:

Which turbulence model is most suitable to be used for the accurate simulation of an isolated cavitating tip vortex in a converging-diverging nozzle?

Considering the above results, the IDDES model, combined with the stable Schnerr-Sauer model is a more suitable candidate than the RANS models to which it was compared. It needs to be taken into account, however, that the IDDES model predicts an almost fully laminar flow field. No turbulence that would normally be generated by the shear at the wall or be present at the inlet, was resolved in the LES region which contained the wetted and cavitating vortices. Generally speaking, it was shown that the vortex simulated in this work was not representative of a cavitating tip vortex originating from a wing or propeller tip. This leads to the following conclusions regarding the use of this geometry of a converging-diverging nozzle and simulation parameters to simulate an isolated cavitating tip vortex.

6.2. Conclusions with respect to the flow case

The wetted flow simulations were more expensive than expected due to a vortex instability which increased the required runtime to obtain statistically-converged results. Furthermore, the upstream differences at measurement plane A between

turbulence models are due to viscous diffusion of the vortex specified at the inlet. This difference in the flow field before the actual converging-diverging nozzle is unwanted as it could be interpreted as a difference in inflow condition for all models. Thirdly, it is unclear to what extent this flow case benefits from resolving the flow up to the wall, as walls are modeled in RANS mode for the IDDES model and turbulent fluctuations would have to be specified as resolved inflow turbulence for this model. The loss in accuracy given the usage of wall models is not expected to significantly affect the generation of modeled turbulence inside the vortex core for the RANS models, as this is predominantly caused by the magnitude of the strain-rate tensor at the edge of the viscous core (where the tangential velocity is largest).

The sharp edges at the front and end of the Venturi throat led to the development of sheet cavities with a dominating effect on the flow field at measurement plane C and the cavity development and dynamics, possibly suppressing the development of smaller wave-like deformations of the cavity. It can therefore be concluded that the chosen geometry is not suitable for the simulation of an isolated cavitating tip vortex and to assess its dynamics. Possible improvements and recommendations regarding the flow case and simulation set-up will be provided in the next section.

6.3. Recommendations for further research

In order to make sure that the velocity field upstream of the converging nozzle is as similar as possible for all simulations, the swirl generator could be modeled. If a rotating swirl generator would be modeled, the computational expense would increase, but then velocity fluctuations leading to resolved turbulence for the IDDES model would be introduced into the flow field, similar as in simulations by Saini et al. [41]. This would help to confirm or reject the conclusions regarding the performance of the IDDES model.

Secondly, the specification of the Lamb-Oseen vortex at the inflow did not take into account that the profiles of eddy viscosity and turbulence intensity are not uniform due to the presence of the vortex. In future research that specifies a vortex at the inflow in combination with RANS models, more attention may be devoted to assessing the influence of specifying non-uniform turbulent inflow parameters.

Furthermore, a different geometry with rounded edges and a longer parallel section would decrease or remove the external (sheet cavity) influence on the flow field and cavity dynamics as well as improve the spatial resolution. The parallel section should be made as long as possible based on the decay of the vortex and computational power. Adaptive grid refinement could be used to further improve the grid resolution in the analyzed section without incurring unnecessary computational costs. Additionally, the increase in cavity size when increasing grid resolution showed that the result was not yet grid-independent, requiring further investigation. Given that the required spatial and temporal sampling frequency are linked to the cavity size and axial and tangential velocity at the vapor core interface, it would be useful to determine clearer criteria to select the appropriate sampling frequency.

For research into the numerical assessment of cavity dynamics using a spectral approach, the post-processing script could be improved by using the entire available three-dimensional geometry instead of just two measurement planes. It would also be interesting to apply the script to a tip vortex generated by a wing, which is sure to display more dynamics, as the vortex roll-up process from the wing tip into the tip vortex is then preserved, in contrast to the present flow case.

Simulations with another cavitation model (the Ahuja model) were attempted within the time frame for this work. The simulations did not converge, despite numerous attempts. This highlights the difficulty in setting appropriate values, both for model constants (i.e. the mass transfer terms) as for the solver (i.e. the relaxation and discretization). The influence of cavitation models and the interplay with turbulence (models) remains an open issue, requiring further studies with multiple cavitation models. Furthermore, the setting of cavitation model limiters and constants should be addressed in future work, as e.g. the maximal bubble size and number of nuclei for the Schnerr-Sauer model may influence cavity dynamics.

Bibliography

[1] J. Bosschers. Broadband hull pressure fluctuations and cavitating vortices. In *The Ship Noise and Vibration Conference*, pages 1–9, London, September 2007.

[2] J. Bosschers. *Propeller tip-vortex cavitation and its broadband noise*. PhD thesis, Technische Universiteit Twente, 2018.

[3] R. Arndt and B. Maines. Viscous effects in tip vortex cavitation and nucleation. In *20th Symposium on Naval Hydro-dynamics*, Santa Barbara, 1994. NRC, Naval Studies Board.

[4] B. Maines and R. Arndt. Tip vortex formation and cavitation. *Journal of Fluids Engineering*, 119(2):413–419, 1997.

[5] R. Liebrand. *Tip vortex modelling for cavitation noise applications: A verification and validation study in ReFRESCO*. MSc thesis, Delft University of Technology, 2019.

[6] A. Janssen. *A numerical and semi-analytical study of the structure of stationary vortices*. MSc thesis, University of Twente, 2008.

[7] A. de Montgolfier. *Simulation of line vortex cavitation*. MSc thesis, ENSTA Bretagne, 2011.

[8] P. Rudolf, M. Hudec, and P. Zubík. Experimental study of straight cavitating vortex tube. In *9th IASME/WSEAS International Conference on Fluid Mechanics & Aerodynamics*, pages 373–378, 2011.

[9] P. Rudolf, M. Hudec, P. Zubík, and D. Štefan. Experimental measurement and numerical modeling of cavitating flow in converging-diverging nozzle. *EPJ Web of Conferences*, 2012.

[10] F. Pereira. *Towards predictive scale-Resolving simulations of turbulent external flows*. PhD thesis, Instituto Superior Técnico, 2018.

[11] R. Liebrand, M. Klapwijk, T. Lloyd, G. Vaz, and R. Lopes. A sensitivity analysis of CFD transition modelling in the context of vortex roll-up prediction. In *8th International Conference on Computational Methods in Marine Engineering*, Gothenburg, Sweden, 2019.

[12] J. Bosschers. Analysis of inertial waves on inviscid cavitating vortices in relation to low-frequency radiated noise. *Proceedings of the Warwick Innovative Manufacturing Research Centre (WIMRC) Cavitation: Turbo-machinery and Medical Applications Forum*, 2(July), 2008.

[13] P. Pennings, J. Bosschers, J. Westerweel, and T.J.C. Van Terwisga. Dynamics of isolated vortex cavitation. *Journal of Fluid Mechanics*, 778:288–313, 2015.

[14] J. Bosschers. On the dispersion relation of a vortex cavity. In *10th International Symposium on Cavitation (CAV2018)*, number May, Baltimore, MD, 2018.

[15] P. Pennings. *Dynamics of vortex cavitation*. PhD thesis, 2016.

[16] S. Pope. *Turbulent flows*, volume 1. 2000.

[17] P. Sagaut, S. Deck, and M. Terracol. *Multiscale and multiresolution approaches in turbulence*. 2013.

[18] O. Reynolds. On the dynamical theory of incompressible viscous fluids and the determination of the criterion (reprinted from papers on mechanical and physical subjects, vol 2, pg 535-577, 1901). In *Proceedings of the Royal Society-Mathematical and Physical Sciences*, volume 451, pages 5–47, 1995.

[19] A. Hellsten. *New two-equation turbulence model for aerodynamic applications*. PhD thesis, Helsinki University of Technology, 2004.

[20] D. Wilcox. *Turbulence modeling for CFD*, volume 1. Birmingham Press, San Diego, 2006.

[21] F. Schmitt. About Boussinesq's turbulent viscosity hypothesis: historical remarks and a direct evaluation of its validity. *Comptes Rendus Mécanique, Elsevier Masson*, 335(9-10):617–627, 2007.

[22] F. Menter. Two-equation eddy-viscosity turbulence models for engineering applications. *AIAA journal*, 32(8):1598–1605, 1994.

[23] F. Menter, M. Kuntz, and R. Langtry. Ten years of industrial experience with the SST turbulence model. In K. Hanjalic, Y. Nagano, and M. Tummers, editors, *Turbulence, Heat and Mass Transfer*, volume 4. Begell House, Inc., 2003.

[24] P. Smirnov and F. Menter. Sensitization of the SST turbulence model to rotation and curvature by applying the Spalart-Shur correction term. *Journal of Turbomachinery*, 131(October 2009):2305–2314, 2009.

[25] J. Dacles-Mariani, G. Zilliac, J. Chow, and P. Bradshaw. Numerical/experimental study of a wingtip vortex in the near field. *AIAA journal*, 33(9):1561–1568, 1995.

[26] N. Kamphuis. *Analysis of Refresco Computations Applied To a Tip Vortex of a Wing*. Internship report, University of Twente, 2012.

[27] J. Schot, P. Pennings, M. Pourquie, J. Tom, and T. van Terwisga. Modelling of tip vortex cavitation for engineering applications in OpenFOAM. *11th World Congress on Computational Mechanics (WCCM XI)*, (11):4753–4764, 2014.

[28] J. Schot. *Numerical study of vortex cavitation on the elliptical Arndt foil*. MSc thesis, Delft University of Technology, 2014.

[29] T. Frank, C. Lifante, S. Jebauer, M. Kuntz, and K. Rieck. CFD simulation of cloud and tip vortex cavitation on hydrofoils. In *6th International Conference on Multiphase Flow*, pages 134–147, Leipzig, 2007.

[30] H. Yu Cheng, X. Ping Long, Y. Zhi Liang, Y. Long, and B. Ji. URANS simulations of the tip-leakage cavitating flow with verification and validation procedures. *Journal of Hydrodynamics*, 30(3):531–534, 2018.

[31] J. Rotta. Statistische Theorie nichthomogener Turbulenz. *Zeitschrift für Physik*, 129:547–572, 1951.

[32] S. Wallin and A. Johansson. An explicit algebraic Reynolds stress model for incompressible and compressible turbulent flows. *Journal of Fluid Mechanics*, 403:89–132, 2000.

[33] S. Wallin and A. Johansson. Modelling streamline curvature effects in explicit algebraic reynolds stress turbulence models. *International Journal of Heat and Fluid Flow*, 23(5):721–730, 2002.

[34] P. Spalart, W-H. Jou, M. Strelets, and S. Allmaras. Comments on the feasibility of LES for wings and on a hybrid RANS/LES approach. In *Proceedings of the First AFOSR International Conference on DNS/LES*, Ruston, Louisiana, USA, 1997. Greyden Press.

[35] A. Travin, M. Shur, M. Strelets, and P. Spalart. Detached-eddy simulations past a circular cylinder. *Flow Turbulence and Combustion*, 63(1-4):293–313, 2000.

[36] M. Kh. Strelets. Detached eddy simulation of massively separated flows. In *39th Aerospace Sciences Meeting and Exhibit*, number 0879, Reno, 2001. American Institute of Aeronautics and Astronautics.

[37] P. R. Spalart, S. Deck, M. L. Shur, K. D. Squires, M. Kh. Strelets, and A. Travin. A new version of detached-eddy simulation, resistant to ambiguous grid densities. *Theoretical and Computational Fluid Dynamics*, 20(3):181–195, 2006.

[38] M. Gritskevich, A. Garbaruk, J. Schütze, and F. Menter. Development of ddes and iddes formulations for the k-ω shear stress transport model. *Flow, turbulence and combustion*, 88(3):431–449, 2012.

[39] M. Shur, P. Spalart, M. Strelets, and A. Travin. A hybrid RANS-LES approach with delayed-DES and wall-modelled LES capabilities. *International Journal of Heat and Fluid Flow*, 29:1638–1649, 2008.

[40] J. Larsson, S. Kawai, J. Bodart, and I. Bermejo-Moreno. Large eddy simulation with modeled wall-stress: recent progress and future directions. *Mechanical Engineering Reviews*, 3(1):15–00418–15–00418, 2015.

[41] R. Saini, N. Karimi, A. Sadiki, and A. Mehdizadeh. Effects of near wall modeling in the Improved Delayed Detached-Eddy Simulation (IDDES) methodology. *Entropy*, 20(10), 2018.

[42] M. Klapwijk, T. Lloyd, and G. Vaz. On the accuracy of Partially Averaged Navier-Stokes resolution estimates. *Elsevier - TBD*, 2019.

[43] G. Kuiper. Vortex cavitation. In *Reader for the course on Cavitation in Ship Propulsion*, chapter 9. Delft University of Technology, Delft, 2012.

[44] J-P. Franc and J-M. Michel. *Fundamentals of cavitation*, volume 76. Kluwer Academic Publishers, Dordrecht, 2004.

[45] P. Kundu and I. Cohen. *Fluid mechanics*. Elsevier Inc., Oxford, fourth edition, 2008.

[46] R. Taghavi and S. Farokhi. Turbulent swirling jets with excitation. Technical report, The University of Kansas Center for Research, Inc., Lawrence, Kansas, 1998.

[47] V. Mudkavy. The phenomenon of vortex breakdown. *Computational and Fluid Dynamics Division*, Bangalor,(National Aerospace Laboratories):123–135, 1993.

[48] M. Vanierschot, M. Percin, and B. Van Oudheusden. Double helix vortex breakdown in a turbulent swirling annular jet flow. *Physical Review Fluids*, 3(3), 2018.

[49] T. Sarpkaya. On stationary and travelling vortex breakdowns. *Journal of Fluid Mechanics*, 45(3):545–559, 1971.

[50] D. Fruman, C. Dugué, A. Pauchet, P. Cerruti, and L. Briançon-Marjolet. Tip vortex roll-up and cavitation. In *19th Symposium on Naval Hydrodynamics*, pages 633–654, Washington, D.C., 1994. National Academy Press.

[51] W. Devenport, M. Rife, S. Liapis, and G. Follin. The structure and development of a wing-tip vortex. *Journal of Fluid Mechanics*, 312:67–106, 1996.

[52] S. Robinson, S. Kline, and P. Spalart. A review of quasi-coherent structures in a numerically simulated turbulent boundary layer. 1989.

[53] A. Oprea. *Prediction of tip vortex cavitation for ship propellers*. PhD thesis, University of Twente, 2013.

[54] V. Holmén. *Methods for vortex identification*. MSc thesis, Lund University, 2012.

[55] C. Brennen. *Cavitation and bubble dynamics*. Oxford University Press, New York, 1995.

[56] L. Briggs. Limiting negative pressure of water. *Journal of Applied Physics*, 21(7):721–722, 1950.

[57] M. van Rijsbergen and T. van Terwisga. High-speed micro-scale observations of nuclei-induced sheet cavitation. In *WIMRC 3rd International Cavitation Forum 2011*, Warwick, 2011.

[58] C. Brennen. *Fundamentals of multiphase flows*. Cambridge University Press, Cambridge, 2008.

[59] G. Schnerr and J. Sauer. Physical and numerical modeling of unsteady cavitation dynamics. In *4th International Conference on Multiphase Flow*, number March, New Orleans, 2001.

[60] C. Hirt and B. Nichols. Volume of Fluid (VOF) method for the dynamics of free boundaries. *Journal of Computational Physics*, 39:201–225, 1981.

[61] A. Singhal, M. Athavale, H. Li, and Y. Jiang. Mathematical basis and validation of the full cavitation model. *Journal of Fluids Engineering*, 124(3):617, 2002.

[62] E. Ghahramani, M. H. Arabnejad, and R. E. Bensow. A comparative study between numerical methods in simulation of cavitating bubbles. *International Journal of Multiphase Flow*, 2018.

[63] G. Vaz and M. Hoekstra. Refresco theory manual. Technical report, Maritime Research Institute Netherlands (MARIN), Wageningen, Netherlands, 2017.

[64] M. van der Eijk. *Numerical modelling of homogeneous aerated-water wave impacts*. MSc thesis, Delft University of Technology, 2018.

[65] O. Coutier-Delgosha, R. Fortes Patella, and J-L. Reboud. Simulation of unsteady cavitation with a two-equation turbulence model including compressibility effects. *Journal of Turbulence*, 3(58), 2002.

[66] E. Goncalvès da Silva, M. Champagnac, and R. Fortes Patella. Comparison of numerical solvers for cavitating Flows. *International Journal of Computational Fluid Dynamics*, 24(6):201–216, 2010.

[67] B. Ji, X. Luo, Y. Wu, X. Peng, and Y. Duan. Numerical analysis of unsteady cavitating turbulent flow and shedding horse-shoe vortex structure around a twisted hydrofoil. *International Journal of Multiphase Flow*, 51:33–43, 2013.

[68] A. Asnaghi, A. Feymark, and R. Bensow. Effect of Turbulence Closure on the Simulation of the Cavitating Flow on the Delft Twist11 Foil. 2013.

[69] B. Cointe. *CFD analysis of cavitation dynamics in a converging-diverging nozzle*. MSc thesis, Delft University of Technology, 2018.

[70] J-L. Reboud, B. Stutz, and O. Coutier. Two phase flow structure of cavitation: experiment and modeling of unsteady effects. In *3rd International Symposium on Cavitation CAV1998, Grenoble, France*, volume 26, 1998.

[71] O. Coutier-Delgosha, R. Fortes-Patella, and J-L. Reboud. Evaluation of the turbulence model influence on the numerical simulations of unsteady cavitation. *Journal of Fluids Engineering*, 125(1):38, 2003.

[72] G. Vaz and N. Hoekstra. Cavitation modelling in FReSCo. Technical report, 2008.

[73] P. Genoux and G. Chahine. Équilibre statique et dynamique d'un tore de vapeur tourbillonnaire. *Journal de Mecanique theorique et Appliquee*, 2(5):829–857, 1983.

[74] P. Ligneul. Theoretical tip vortex cavitation inception threshold. *European journal of mechanics. B, Fluids*, 8(6):495–521, 1989.

[75] G. Vaz, T. Lloyd, and A. Gnanasundaram. Improved modelling of sheet cavitation dynamics on Delft TWIST11 hydrofoil. *7th International Conference on Computational Methods in Marine Engineering, MARINE 2017*, 2017-May(May):143–156, 2017.

[76] J. Bosschers. Investigation of hull pressure fluctuations generated by cavitating vortices. In *Proc. First Symposium on Marine Propulsors*, 2009.

[77] P. Pennings, J. Westerweel, and T. J.C. van Terwisga. Flow field measurement around vortex cavitation. *Experiments in Fluids*, 56(11):1–13, 2015.

[78] L. Eça and M. Hoekstra. A procedure for the estimation of the numerical uncertainty of CFD calculations based on grid refinement studies. *Journal of Computational Physics*, 262:104–130, 2014.

[79] G. Rosetti, G. Vaz, and A. Fujarra. URANS calculations for smooth circular cylinder flow in a wide range of Reynolds numbers: Solution Verification and Validation. *Proceedings of the International Conference on Offshore Mechanics and Arctic Engineering - OMAE*, 5(December):549–571, 2012.

[80] J. Brouwer, J. Tukker, and M. van Rijsbergen. Uncertainty analysis and stationarity test of finite length time series signals. *4th International Conference on Advanced Model Measurement Technology for the Maritime Industry*, September 2015.

[81] J. Brouwer, J. Tukker, and M. van Rijsbergen. Uncertainty analysis of finite length measurement signals. *3rd International Conference on Advanced Model Measurement Technology for the Maritime Industry*, September 2013.

[82] L. Eça, G. Vaz, and M. Hoekstra. A verification and validation exercise for the flow over a backward facing step. (June):14–17, 2010.

[83] ASME. Standard for verification and validation in computational fluid dynamics and heat transfer. Technical report, The American Society of Mechanical Engineers, New York, 2009.

[84] L. Eça, G. Vaz, A. Koop, F. Pereira, and H. Abreu. Validation: what, why and how. In *ASME 35th International Conference on Ocean, Offshore and Arctic Engineering*, number June, pages 1–13, 2016.

[85] L. Eça, R. Lopes, G. Vaz, J. Baltazar, and D. Rijpkema. Validation exercises of mathematical models for the prediction of transitional flows. *31st Symposium on Naval Hydrodynamics*, (September):11–16, 2016.

[86] G. Vaz, F. Jaouen, and M. Hoekstra. Free-surface viscous flow computations: Validation of URANS code. In *ASME 28th International Conference on Ocean, Offshore and Arctic Engineering*, number September 2014, pages 425–437, 2010.

[87] G. Vaz and M. Hoekstra. Theoretical and numerical formulation of FreSCo. Technical Report Report No. 18572-WP4-2, Maritime Research Institute Netherlands (MARIN), Wageningen, Netherlands, 2008.

[88] B. Leonard. The QUICK algorithm-A uniformly third-order finite-difference method for highly convective flows. *Computer methods in fluids*, pages 159–195, 1980.

[89] N. Waterson and H. Deconinck. Design principles for bounded higher-order convection schemes - a unified approach. *Journal of Computational Physics*, 224(1):182–207, 2007.

[90] F. Moukalled, L. Mangani, and M. Darwish. *The finite volume method in Computational Fluid Dynamics*, volume 113. Springer International Publishing Switzerland 2016, Switzerland, 2016.

[91] A. Hoekstra, J. Derksen, and H. Van Akker. An experimental and numerical study of turbulent swirling flow in gas cyclones. *Chemical Engineering Science*, 54(13-14):2055–2065, 1999.

[92] V. Hernandez-Perez, M. Abdulkadir, and B. Azzopardi. Grid generation issues in the CFD modelling of two-phase flow in a pipe. *The Journal of Computational Multiphase Flows*, 3(1):13–26, 2011.

[93] A. Javadi and H. Nilsson. LES and DES of strongly swirling turbulent flow through a suddenly expanding circular pipe. *Computers and Fluids*, 107:301–313, 2015.

[94] H. Sheen, W. Chen, and T. Jeng, S.and Huang. Correlation of swirl number for a radial-type swirl generator. *Experimental thermal and fluid science*, 12(4):444–451, 1996.

[95] W. Steenbergen and J. Voskamp. The rate of decay of swirl in turbulent pipe flow. *Flow Measurement and Instrumentation*, 9(2):67–78, 1998.

[96] A. Gupta, D. Lilley, and N. Syred. *Swirl flows*. Abacus Press, Kent, first edition, 1984.

[97] A. Najafi, S. Mousavian, and K. Amini. Numerical investigations on swirl intensity decay rate for turbulent swirling flow in a fixed pipe. *International Journal of Mechanical Sciences*, 53(10):801–811, 2011.

[98] A. Asnaghi, A. Feymark, and R.E. Bensow. Numerical analysis of tip vortex flow. *Proceedings of 19th Numerical Towing Tank Symposium*, (October):5–10, 2016.

[99] T-H. Shih, W. Liou, A. Shabbir, Z. Yang, and J. Zhu. A new k-ϵ eddy viscosity model for high Reynolds number turbulent flows - model development and validation. *NASA Technical Memorandum*, 106721, 1994.

[100] G. Batchelor. *An introduction to fluid dynamics*. Cambridge University Press, Cambridge, 2000.

[101] N. Syred. A review of oscillation mechanisms and the role of the precessing vortex core (PVC) in swirl combustion systems. *Progress in Energy and Combustion Science*, 32(2):93–161, 2006.

[102] R. C. Chanaud. Observations of oscillatory motion in certain swirling flows. *Journal of Fluid Mechanics*, 21(1):111–127, 1965.

[103] P. Rudolf, M. Hudec, M. Gríger, and D. Štefan. Characterization of the cavitating flow in converging-diverging nozzle based on experimental investigations. *EPJ Web of Conferences*, 67, 2014.

[104] J. Bosschers. Modeling and analysis of a cavitating vortex in 2D unsteady viscous flow. In *7th International Symposium on Cavitation (CAV2009)*, Ann Arbor, MI, 2009.

[105] W. Hogendoorn. *Cavitation: Experimental investigation of cavitation regimes in a converging-diverging nozzle*. MSc thesis, Delft University of Technology, 2017.

[106] H. Ganesh, S. Makiharju, and S. Ceccio. Bubbly shock propagation as a mechanism for sheet-to-cloud transition of partial cavities. *Journal of Fluid Mechanics*, 802:37–78, 2016.

[107] X. Zheng, C. Liu, F. Liu, and C.-I. Yang. Turbulent transition simulation using the k–ω model. *International Journal for Numerical Methods in Engineering*, 42(5):907–926, 1998.

[108] M. Howe. *Theory of vortex sound*, volume 33. Cambridge University Press, 2003.

A
Turbulence modeling

This appendix provides additional equations, definitions and values of the constants used in the turbulence models.

A.1. k-omega SST 2003

A.1.1. Blending functions

The blending function F_1 is defined by Equation (A.1)

$$F_1 = \tanh\left\{\left\{\min\left[\max\left(\frac{\sqrt{k}}{\beta^*\omega y}, \frac{500\nu}{y^2\omega}\right), \frac{4\rho\sigma_{w2}k}{CD_{k\omega}y^2}\right]\right\}^4\right\},$$

$$CD_{k\omega} = \max\left(2\rho\sigma_{w2}\frac{1}{\omega}\frac{\partial k}{\partial x_i}\frac{\partial\omega}{\partial x_i}, 10^{-10}\right). \tag{A.1}$$

F_2 is a second blending function defined by:

$$F_2 = \tanh\left[\left[\max\left(\frac{2\sqrt{k}}{\beta^*\omega y}, \frac{500\nu}{y^2\omega}\right)\right]^2\right]. \tag{A.2}$$

A.1.2. Production limiter

The definition of the production term $\mathcal{P}_k$ is derived from the Boussinesq hypothesis, and is given by:

$$\mathcal{P}_k = \tau_{ij}\frac{\partial U_i}{\partial x_j} = \left\{\mu_t\left[\left(\frac{\partial U_i}{\partial x_j} + \frac{\partial U_j}{\partial x_i}\right) - \frac{2}{3}\delta_{ij}\frac{\partial U_k}{\partial x_k}\right] - \frac{2}{3}\rho k\delta_{ij}\right\}\frac{\partial U_i}{\partial x_j}, \tag{A.3}$$

$$= \mu_t\left[\left(\frac{\partial U_i}{\partial x_j} + \frac{\partial U_j}{\partial x_i}\right)\right]\frac{\partial U_i}{\partial x_j} - \mu_t\frac{2}{3}\delta_{ij}\frac{\partial U_k}{\partial x_k}\frac{\partial U_i}{\partial x_j} - \frac{2}{3}\rho k\delta_{ij}\frac{\partial U_i}{\partial x_j}, \tag{A.4}$$

$$= \mu_t\boldsymbol{S}^2 - \mu_t\frac{1}{3}\left(\frac{\partial U_k}{\partial x_k}\right)^2 - \frac{2}{3}\rho k\left(\frac{\partial U_k}{\partial x_k}\right)^2. \tag{A.5}$$

For incompressible flows, the velocity field is divergence-free: $\nabla\cdot\mathbf{u} = 0 \iff \left(\frac{\partial U_k}{\partial x_k}\right) = 0$, therefore reducing the expression for $\mathcal{P}_k$ to the usual formulation of $\mathcal{P}_k = \mu_t\boldsymbol{S}^2$. For cavitating flows, which are not divergence free and $\left(\frac{\partial U_k}{\partial x_k}\right) = S_{\text{vap}}$, the additional terms should be incorporated.

A.1.3. Omega limiter

The limiter for ω used in the cavitating flow simulations was originally proposed by Zheng & Liu in 1995 (as cited in [107]) to reduce the dependency on far-field values of ω and to account for transport effects of the total turbulent shear-stress. An upper bound was introduced for the sum of the Reynolds stresses [107]:

$$\sqrt{\sum\tau_{ij}} \leq 2\rho k. \tag{A.6}$$

This limit is essentially a limit on the fraction of deviant turbulent stress and can be rewritten into the form that is implemented in REFRESCO:

$$\omega \geq \phi\alpha_0^*\sqrt{2\left(S_{ij} - \frac{1}{3}\frac{\partial u_k}{\partial x_k}\delta_{ij}\right)\frac{\partial u_i}{\partial x_j}}, \tag{A.7}$$

$$\omega = \max\left(\omega_0, \phi\alpha^*\sqrt{P_d}\right), \tag{A.8}$$

where: \hfill (A.9)

$$\alpha^* = \frac{\alpha_0^* + Re_T/R_\omega}{1 + Re_T/R_\omega}. \tag{A.10}$$

The constant values are $\alpha_0^* = \beta/3$, $\beta = 3/40$, $\phi = \sqrt{3}/2$, $Re_T = \rho k/\omega\mu$, $R_\omega = 2.7$. The value for ϕ represents the least requirement from the turbulence model realizability [107].

A.1.4. Model constants

The Shear Stress Transport (SST) model constants are obtained by blending the $k-\varepsilon$ and $k-\omega$ constants; $\alpha = \alpha_1 F + \alpha_2(1-F)$, etc.

$$\sigma_{k_1} = 0.85 \qquad\qquad\qquad\qquad \beta^* = 0.09$$
$$\sigma_{k_2} = 1.0 \qquad\qquad\qquad\qquad \alpha_1 = 5/9$$
$$\sigma_{\omega_1} = 0.5 \qquad\qquad\qquad\qquad \alpha_2 = 0.44$$
$$\sigma_{\omega_2} = 0.856 \qquad\qquad\qquad\qquad a_1 = 0.31$$
$$\beta_1 = 0.075 \qquad\qquad\qquad\qquad b_1 = 1.0$$
$$\beta_2 = 0.0828 \qquad\qquad\qquad\qquad c_1 = 10.0$$

A.2. Reynolds Stress Modeling

This section adds additional background regarding the modeling of the redistributive, dissipative and turbulent transport terms in the transport equation. Secondly, it provides the basis for Algebraic Reynolds Stress Model (ARSM).

A.2.1. Reynolds Stress transport equation

Modeling the redistributive and dissipative terms

The approach by Hellsten [19] lumps all anisotropic elements together by subtracting the deviatoric part of the dissipation tensor:

$$\Pi_{ij} = \Phi_{ij} - \underbrace{\left(\varepsilon_{ij} - \varepsilon\delta_{ij}\right)}_{\text{dissipation anisotropy}}. \tag{A.11}$$

The ε is introduced here, and therefore requires modeling similar to standard two-equation models also involving k and ε. Except close to the walls, the dissipation anisotropy is generally relatively small, so that $\Pi_{ij} = \Phi_{ij}$ is a common assumption also present in the constitutive model used for the simulations discussed in this thesis [32].

The redistribution tensor Φ_{ij} is a traceless and symmetrical tensor function $\mathcal{F}_{ij}$ of the anisotropy tensor a_{ij} (i.e. the deviatoric part of the Reynolds stresses), the mean-velocity gradient and k and ε Equation (A.12). The velocity-gradient tensor can be split in a symmetric and skew-symmetric part using respectively the strain-rate and the vorticity tensor S_{ij} and Ω_{ij}. This is mainly a numerical step to make the involved tensors less more sparse and thereby easier to solve. All tensors are non-dimensionalized using a timescale defined by $\tau = k/\varepsilon$.

$$\Pi_{ij} = \varepsilon\mathcal{F}_{ij}\left(a_{ij},\ S_{ij},\ \Omega_{ij}, \delta_{ij}\right), \tag{A.12}$$

where

$$a_{ij} = \frac{\overline{u_i' u_j'}}{k} - \frac{2}{3}\delta_{ij}, \tag{A.13}$$

$$S_{ij} = \frac{1}{2}\tau\left(\frac{\partial U_i}{\partial x_i} + \frac{\partial U_j}{\partial x_j}\right), \tag{A.14}$$

$$\Omega_{ij} = \frac{1}{2}\tau\left(\frac{\partial U_i}{\partial x_i} - \frac{\partial U_j}{\partial x_j}\right). \tag{A.15}$$

The Poisson equation for fluctuating pressure is used to model the pressure-strain relation:

$$\nabla^2 p' = -2\rho\frac{\partial U_k}{\partial x_l}\frac{\partial u_l'}{\partial x_k} - \rho\frac{\partial^2}{\partial x_k \partial x_l}(u_k' u_l' - \overline{u_k' u_l'}). \tag{A.16}$$

There are three solutions to this equation: a *harmonic* one satisfying the Laplace equation $\Delta p' = 0$ and two particular solutions; called *slow* and *rapid*. The correlation between the velocity and the pressure gradient is therefore also split into these three parts. The harmonic part is zero for homogeneous turbulence and negligible for inhomogeneous turbulence except very close to the wall. The slow part does not depend on the mean velocity gradient and is the cause of the return-to-isotropy process when the mean-velocity gradient is zero for initially anisotropic turbulence. The absence of a velocity gradient means that there is no directional forcing of turbulence in that situation. The slow term $\Phi^{(s)}$ is modeled using the Rotta model, and only

a function of the anisotropy a_{ij}. The rapid term $\Phi^{(r)}$ is more complex, and a quasi-linear model (regarding the dependence of the coefficients on the anisotropy tensor) is used based on the curvature-corrected model by Wallin & Johansson [33].

$$\Phi_{ij}^{(s)} = -C_1 a_{ij}\varepsilon \tag{A.17}$$

$$\Phi_{ij}^{(r)} = C_2 k S_{ij} + \frac{C_3}{2} k \left(a_{ik} S_{kj} + S_{ik} a_{kj} - \frac{2}{3} a_{kl} S_{lk} \delta_{ij} \right) - \frac{C_4}{2} k \left(a_{ik} \Omega_{kj} - \Omega_{ik} a_{kj} \right) \tag{A.18}$$

The values of the coefficients C_1 through C_4 depend on the parameter A_0, which is typical only for the algebraic modeling approach that is introduced in Section 2.1.4. In the derivation of the rapid term $\Phi^{(r)}$ the assumption of homogeneous turbulence was made, limiting the application of these quasi-homogeneous models to flows in which the turbulent quantities only vary slowly in space. Generally speaking, this causes no issues away from walls.

Modeling of the turbulent fluxes
The fluctuating velocity field is random, leading to the reasoning that turbulent transport can be modeled as diffusion. A *gradient-diffusion* model is therefore used for the turbulent transport and pressure diffusion terms. The model used for the simulations discussed in this thesis applies a very simple scalar diffusion model equaling the eddy viscosity concept:

$$T_{ijk} \approx \sigma_K \nu_t \frac{\partial \overline{u_i' u_j'}}{\partial x_k}, \tag{A.19}$$

where σ_k is the model constant present in the transport equation for the kinetic energy in the SST model.

A.2.2. Algebraic Reynolds Stress Models
The quasi-linear transport equation for the anisotropy tensor a_{ij} is defined as:

$$\tau \left(\frac{\mathrm{D} a_{ij}}{\mathrm{D} t} - \Phi_{ij} \right) = A_0 \Bigg[\left(A_3 + A_4 \frac{\mathcal{P}}{\varepsilon} \right) a_{ij} + A_1 S_{ij} - (a_{ik}\Omega_{kj} - \Omega_{ik} a_{kj})$$
$$+ A_2 \left(a_{ik} S_{kj} + S_{ik} a_{kj} - \frac{2}{3} a_{kl} S_{lk} \delta_{ij} \right) \Bigg]. \tag{A.20}$$

The A coefficients stem from the original Reynolds Stress Model (RSM) coefficients. The integrity basis for a_{ij} is given by:

$$\begin{aligned}
a_{ij} = & \beta_1 S_{ij} \\
& + \beta_2 (S_{ik} S_{kj} - \mathrm{II}\delta_{ij}/3) + \beta_3 (\Omega_{ik}\Omega_{kj} - \mathrm{II}_\Omega \delta_{ij}/3) + \beta_4 (S_{ik}\Omega_{kj} - \Omega_{ik} S_{kj}) \\
& + \beta_5 (S_{ik} S_{kl}\Omega_{lj} - \Omega_{ik} S_{kl} S_{lj}) + \beta_6 (S_{ik}\Omega_{kl}\Omega_{lj} + \Omega_{ik}\Omega_{kl} S_{lj} - \mathrm{IV}\delta_{ij}/3) \\
& + \beta_7 (S_{ik} S_{kl}\Omega_{lp}\Omega_{pj} + \Omega_{ik}\Omega_{kl} S_{lp} S_{pj} - 2\mathrm{V}\delta_{ij}/3) \\
& + \beta_8 (S_{ik}\Omega_{kl} S_{lp} S_{pj} - S_{ik} S_{kl}\Omega_{lp} S_{pj}) + \beta_9 (\Omega_{ik} S_{kl}\Omega l p\Omega_{pj} - \Omega_{ik}\Omega kl S_{lp}\Omega_{pj}) \\
& + \beta_{10} (\Omega_{ik} S_{kl} S_{lp}\Omega_{pq}\Omega_{qj} - \Omega_{ik}\Omega_{kl} S_{lp} S_{pq}\Omega_{qj}). \tag{A.21}
\end{aligned}$$

A linear system can be written to solve for the β coefficients. The five independent scalar invariants are defined as

$$\begin{aligned}
& \mathrm{II}_S = S_{kl} S_{lk}, && \mathrm{II}_\Omega = \Omega_{kl}\Omega_{lk}, \\
& \mathrm{III}_S = S_{kl} S_{lm} S_{mk}, && \mathrm{IV} = S_{kl}\Omega_{lm}\Omega_{mk}, && \mathrm{V} = S_{kl} S_{lm}\Omega_{mn}\Omega_{nk}. \tag{A.22}
\end{aligned}$$

A.3. Hellsten's Explicit Algebraic Stress Model
The following definitions are specific for the Hellsten Explicit Algebraic Reynolds Stress Model (EARSM) used for the simulations in this thesis.

A.3.1. Constitutive model
The curvature correction for the vorticity tensor is given by:

$$\Omega_{ij}^* = \frac{1}{2} \left(\frac{\partial U_i}{\partial x_i} - \frac{\partial U_j}{\partial x_j} \right) - \frac{\tau}{A_0}\Omega_{ij}^{(r)}, \tag{A.23}$$

where:

$$\Omega_{ij}^{(r)} = \epsilon_{ijk} \frac{\mathrm{II}_S^2 \delta_{km} + 12\mathrm{III}_S S_{km} + 6\mathrm{II}_S S_{kl} S_{lm}}{2\mathrm{II}_S^3 - 12\mathrm{III}_S^2} S_{pr}\dot{S}_{rq}\epsilon_{pqm}, \tag{A.24}$$

in which ϵ_{ijk} is the third-order permutation tensor. Its component values are 1 if their indices form a positive permutation of (1,2,3) and −1 in case of a negative permutation. Components with repeated indices are zero [19]. The same applies for ϵ_{pqm}. The β functions are redefined using the modified timescale

$$\tau = \max\left(\frac{1}{\beta^*\omega};\ C_\tau\sqrt{\frac{\nu}{\beta^* k\omega}}\right) \tag{A.25}$$

, and Equation (A.23):

$$\beta_1 = -\frac{N(2N^2 - 7\text{II}_\Omega)}{Q}, \qquad \beta_3 = -\frac{12\text{IV}}{NQ},$$

$$\beta_4 = -\frac{2(N^2 - \text{II}_\Omega)}{Q}, \qquad \beta_6 = -\frac{6N}{Q}, \qquad \beta_9 = \frac{6}{Q}. \tag{A.26}$$

$$\text{II}_S = S_{kl}S_{lk} \qquad \text{II}_\Omega = \Omega^*_{kl}\Omega^*_{lk}$$
$$\text{III}_S = S_{kl}S_{lm}S_{mk} \qquad \text{IV} = S_{kl}\Omega^*_{lm}\Omega^*_{mk} \tag{A.27}$$

The value of the denominator Q is determined by:

$$Q = \frac{5}{6}(N^2 - 2\text{II}_\Omega)(2N^2 - \text{II}_\Omega). \tag{A.28}$$

The solution for the N function only has an explicit solution in two-dimensional flows. In three-dimensional flows, the approach from [32] is used. This method uses the explicit solution of the cubic equation for the two-dimensional case, N_c, and adds a correcting term which is zero when the flow is two-dimensional. The solution for the cubic equation is:

$$N_c = \begin{cases} A'_3/3 + \left(P_1 + \sqrt{P_2}\right)^{1/3} + \text{sign}\left(P_1 - \sqrt{P_2}\right)\left|P_1 - \sqrt{P_2}\right|^{1/3} & \text{for } P_2 \geq 0, \\ A'_3/3 + 2(P_1^2 - P_2)^{1/6}\cos\left(\frac{1}{3}\arccos\left(\frac{P_1}{\sqrt{P_1^2 - P_2}}\right)\right) & \text{for } P_2 < 0, \end{cases} \tag{A.29}$$

where

$$P_1 = \left(\frac{A'^2_3}{27} + \frac{9}{20}\text{II}_S - \frac{2}{3}\text{II}_\Omega\right)A'_3, \tag{A.30}$$

$$P_2 = P_1^2 - \left(\frac{A^{2'}_3}{9} + \frac{9}{10}\text{II}_S + \frac{2}{3}\text{II}_\Omega\right)^3. \tag{A.31}$$

The approximation for N then becomes:

$$N \approx N_c + \frac{162\left[\text{IV}^2 + \left(V - \frac{1}{2}\text{II}_S\text{II}_\Omega\right)N_c^2\right]}{20N_c^4\left(N_c - \frac{1}{2}A'_3\right) - \text{II}_\Omega(10N_c^3 + 15A'_3 N_c^2) + 10A'_3\text{II}_\Omega^2}. \tag{A.32}$$

The A'_3 function is required to model the ignored diffusion of the anisotropy by choosing the algebraic approximation and is defined as:

$$A'_3 = \frac{9}{5} + \frac{5}{4}C_{\text{Diff}}\max\left(1 + \beta_1^{(eq)}\text{II}_S;\ 0\right). \tag{A.33}$$

$\frac{9}{5}$ is the original value of the A_3 coefficient. A new parameter $\beta_1^{(eq)}$ was introduced, which has the value of:

$$\beta_1^{(eq)} = -\frac{6}{5}\frac{N^{(eq)}}{(N^{(eq)})^2 - 2\text{II}_\Omega}, \tag{A.34}$$

where the coefficients $N^{(eq)}$ and C_{Diff} are given by

$$N^{(eq)} = A_3 + A_4 = \frac{81}{20} \qquad \text{and} \qquad C_{\text{Diff}} = 2.2. \tag{A.35}$$

The A-coefficients for the quasi-linear transport equation for a_{ij} in Equation (A.20) are defined as:

$$
\begin{aligned}
A_0 &= \frac{C_4}{2} - 1, \\
A_1 &= \frac{3C_2 - 4}{3A_0}, \\
A_2 &= \frac{C_3 - 2}{2A_0}, \\
A_3 &= -\frac{C_1^{(0)} - 2}{2A_0}, \\
A_4 &= -\frac{C_1^{(1)} + 2}{2A_0}.
\end{aligned}
\tag{A.36}
$$

Constitutive model coefficients and the values of the A-coefficients for the standard model (as based on the Launder-Reece-Rodi RSM model) are given in Tables A.1 and A.2. The coefficients for the curvature-corrected model after recalibration of $A_0 = -0.72$ are provided in Table A.3.

Table A.1: Redistribution model coefficients for the Hellsten EARSM.

C_0^1	C_1^1	C_2	C_3	C_4
3.6	0	0.8	2	1.11

Table A.2: A-coefficients for the standard version of the Hellsten EARSM.

A_0	A_1	A_2	A_3	A_4
-0.44	1.20	0	1.80	2.25

Table A.3: Redistribution model coefficients for the curvature-corrected version of the Hellsten EARSM.

C_1^0	C_1^1	C_2	C_3	C_4
4.6	1.24	0.47	2	0.56

A.3.2. Scale-determining model

The coefficients in the k and ω transport equations of the EARSM are defined using the modified blending function f_{mix} as:

$$
\begin{pmatrix} \gamma \\ \beta \\ \sigma_k \\ \sigma_\omega \\ \sigma_d \end{pmatrix} = f_{\mathrm{mix}} \begin{pmatrix} \gamma_1 \\ \beta_1 \\ \sigma_{k1} \\ \sigma_{\omega 1} \\ \sigma_{d1} \end{pmatrix} + (1 - f_{\mathrm{mix}}) \begin{pmatrix} \gamma_2 \\ \beta_2 \\ \sigma_{k2} \\ \sigma_{\omega 2} \\ \sigma_{d2} \end{pmatrix}.
\tag{A.37}
$$

The new blending function is made up out of a variety of indicators, including the turbulent length scale, distance to the wall d_w (Γ_1), viscosity (Γ_2) and the local solutions for the turbulent quantities k and ω(Γ_3).

The three measures Γ_1 through Γ_3 are defined as:

$$
\Gamma_1 = \frac{\sqrt{k}}{\beta^* \omega d_w},
\tag{A.38}
$$

$$
\Gamma_2 = \frac{500\nu}{\omega d_w},
\tag{A.39}
$$

$$
\Gamma_3 = \frac{20k}{\max\left[d_w^2 (\nabla k \cdot \nabla \omega)/\omega, \ 200k_\infty\right]},
\tag{A.40}
$$

where k_∞ is a free-stream value of k to be specified by the user, not of importance for internal flows. The mixing is designed to occur closer to the edge of the boundary layer compared to the SST model. The blending function f_{mix} is then defined by:

$$f_{\mathrm{mix}} = \tanh\left(C_{\mathrm{mix}}\Gamma^4\right) \qquad \text{with} \qquad \Gamma = \min\left[\max\left(\Gamma_1, \Gamma_2\right), \Gamma_3\right]. \tag{A.41}$$

The coefficient $C_{\mathrm{mix}} = 1.5$ to maintain $f_{\mathrm{mix}} = 1$ almost up to the boundary layer edge. The coefficient values for the SST formulation used in [19] are listed in Table A.4.

Table A.4: Coefficient values for the SST model as implemented in the Hellsten EARSM.

	γ	β	σ_k	σ_ω	σ_d
Set 1	0.518	0.0747	1.1	0.53	0.4
Set 2	0.440	0.0828	1.1	1.00	0.4

There is a relation between the coefficients γ_1, β_1 and $\sigma_{\omega 1}$ through the log-layer relation:

$$\gamma_1 = \frac{\beta_1}{\beta^*} - \frac{\kappa^2 \sigma_{\omega 1}}{\sqrt{\beta^*}}, \tag{A.42}$$

where β^* assumes its standard value of 0.09 and the von Karman constant $\kappa = 0.42$.

A.4. Detached-Eddy Simulation

The SST-based Detached-Eddy Simulation (DES) model blends between $k-\varepsilon$ and $k-\omega$ formulations, each with their own C_{DES} constant. For the $k-\varepsilon$ and $k-\omega$ model they are respectively $C_{\mathrm{DES}}^{k-\varepsilon} = 0.61$ and $C_{\mathrm{DES}}^{k-\omega} = 0.78$. The blended coefficient is defined as:

$$C_{\mathrm{DES}}^{\mathrm{SST}} = F_1 C_{\mathrm{DES}}^{k-\omega} + (1 - F_1) C_{\mathrm{DES}}^{k-\varepsilon}. \tag{A.43}$$

The $k-\varepsilon$ branch is active in most of the region where the Large Eddy Simulation (LES) mode is activated so that the importance of the $k-\omega$ coefficient of the SST-DES is limited.

A.5. Delayed Detached-Eddy Simulation

The constants $C_{d1} = 20$ en $C_{d2} = 3$ are tuned specifically for the SST model, see [38]. The shielding function involves a new parameter r_d, which is defined as [38]:

$$r_d = \frac{\nu + \nu_t}{\kappa^2 d_w^2 \sqrt{0.5(S^2 + \Omega^2)}}. \tag{A.44}$$

where ν_t and ν are respectively the eddy and molecular viscosity. Ω and S are the vorticity and strain-rate tensor invariants, and $\kappa = 0.41$ is the Von Karman constant. The quantity r_d identifies a wall region ($r_d = 1$ in the log-layer and $r_d = 0$ in free-shear flows). The inclusion of the strain-rate and vorticity tensors in the definition of the length scale l_{DDES} means that the length scale is both grid and solution dependent [38].

A.6. Improved Delayed Detached-Eddy Simulation

A.6.1. Modification of the subgrid length scale

If no explicit filter width for the subgrid scales is defined in the LES model, as is the case for these hybrid models, the relation between the grid-spacing and the subgrid length scale is rather turbid. This becomes even more of an issue when the grid is refined significantly more in a single (usually the wall-normal) direction. In Wall-modeled Large Eddy Simulation (WMLES) the principle of subgrid eddies close to the wall extracting energy from the larger scales further away from the wall is violated since spacing parallel to the wall (non-dimensionally expressed by x^+ and z^+) exceeds the distance to the wall. Larsson et al. [40] also point out that there is only a limited exchange of information between both regions/models: i) the Reynolds-Averaged Navier-Stokes (RANS) model receives velocity data from the LES model at the edge of the inner layer ($y = h_{\mathrm{wm}}$ and ii) the wall shear stress τ_w is fed to the LES model at $y = 0$. The filter/subgrid length scale was changed from the previously common cube root of the cell volume towards a maximum of the cell dimensions in the development of DES [34]. The issue of using a correct value for the Smagorinsky constant in the LES sub-grid model still remains, however, as the value differs significantly between wall-bounded and free turbulent flows. An alternative that does not require switching between two different constants is therefore required for Improved Delayed Detached-Eddy Simulation (IDDES). The subgrid length scale Δ now includes the proximity to the wall d_w and is defined as:

$$\Delta = f(h_x, h_y, h_z, d_w), \tag{A.45}$$

where Δ is the subgrid length scale, h_x, h_y and h_z are local cell sizes in streamwise, wall-normal and lateral direction ans d_w is the distance to the wall.

In the free-stream, small eddies behave in a statistically isotropic way, so that the subgrid length scale is set equal to the maximum local grid spacing:

$$\Delta_\infty = h_{\max} \equiv \max\{h_x, h_y, h_z\}. \tag{A.46}$$

Close to the wall, it should depend only on the wall-parallel grid dimensions to reduce the sensitivity introduced by the drastic decrease of the wall-normal step and mitigating the violation of the energy cascade principle for the smaller eddies:

$$\Delta_{\text{wall}} = \Delta(h_x, h_z). \tag{A.47}$$

To blend both formulations into a single function Δ, it is assumed that Δ is linearly dependent on d_w and that it varies within the range $h_{\min} \le \Delta \le h_{\max}$, at any distance from the wall.

The additional model constants for the SST-based IDDES model are given in Table A.5.

Table A.5: Additional model constants for the SST-based IDDES model.

C_w	C_{dt1}	C_{dt2}	C_l	C_t
0.15	20	3	5.0	1.87

$\huge\mathsf{B}$

Cavity dynamics

This appendix contains the derivation of the analytical dispersion relation as originally derived by Bosschers [2]. The notations from [13] are used.

B.1. Analytical dispersion relation

Assuming an irrotational disturbance $\phi'(\mathbf{x}, t)$ to the velocity potential $\phi_0(\mathbf{x})$, with (bounded) mean velocity vector $\mathbf{u} = \nabla\phi_o$:

$$\varphi(\mathbf{x}, t) = \varphi_0(\mathbf{x}) + \tilde{\varphi}(\mathbf{x}, t). \tag{B.1}$$

The general non-linear equation that is satisfied by φ is then given by Equation (B.2) [108].

$$\frac{1}{c^2}\frac{\partial^2\varphi}{\partial t^2} + \frac{1}{c^2}\frac{\mathrm{D}}{\mathrm{D}t}\left(\frac{1}{2}(\nabla\varphi)^2\right) + \frac{1}{c^2}\frac{\partial}{\partial t}\left(\frac{1}{2}(\nabla\varphi^2)\right) - \nabla^2\varphi = 0. \tag{B.2}$$

This equation can be linearized to describe the propagation of small amplitude sound waves determined by $\tilde{\varphi}(\mathbf{x}, t)$. If the mean flow is assumed to be steady, the perturbation potential ϕ' can be used instead of $\dot{\phi}$ so that Equation (B.3) can be derived as the vortex sound equation, based on rewriting the Lighthill equation to a vortex sound equation, see [108] for more details.

$$\left\{\left(\frac{\partial}{\partial t} + \mathbf{u}\cdot\nabla\right)\left[\frac{1}{c^2}\left(\frac{\partial}{\partial t} + \mathbf{u}\cdot\nabla\right)\right] - \frac{1}{\rho}\cdot(\rho\nabla)\right\}\tilde{\varphi} = 0, \tag{B.3}$$

where $c = c(\mathbf{x})$ and $\rho = \rho(\mathbf{x})$ are the local sound speed and density. For incompressible and homogeneous flows, the density term in Equation (B.3) drops out, and the following form is obtained:

$$\nabla^2\tilde{\varphi} - \frac{1}{c^2}\left(\frac{\partial}{\partial t} + \mathbf{u}\cdot\nabla\right)^2\tilde{\varphi} = 0. \tag{B.4}$$

A harmonic variation of the disturbance is defined in cylindrical coordinates as

$$\tilde{\varphi} = \phi(r)e^{i(k_x x + n\theta - \omega t)}, \tag{B.5}$$

where $\phi(r)$ is a potential that only depends on the radial position, k_x is the axial wave number, n is the azimuthal wave number and ω is the angular frequency. Considering only the axial component u_x of the velocity $\mathbf{u}$ allows writing Equation (B.4) as

$$\phi'' + \frac{\phi'}{r} + \left[-k_x^2 - \frac{n^2}{r^2} + \frac{1}{c^2}(\omega - u_x k_x)^2\right]\phi = 0, \tag{B.6}$$

where $'$ indicates a derivative with respect to r. The acoustic wave number is projected on the radial direction and the radial wavenumber is subsequently defined as

$$k_r^2 = \frac{1}{c^2}(\omega - u_x k_x)^2 - k_x^2. \tag{B.7}$$

Furthermore, sound is radiated away from the vortex core, so that the solution for the disturbance potential is given by a Hankel function of the first kind:

$$\tilde{\varphi} = \hat{\phi}H_n^1(k_r)e^{i(k_x x + n\theta - \omega t)}, \tag{B.8}$$

where $\hat{\phi}$ is the amplitude of the disturbance potential. Modes $n = 1, 2$ require the addition of the azimuthal velocity. This complicates the solution procedure and for low frequencies and typical vortex strengths the additional terms can be neglected, given that $|\mathbf{u}| \ll c$. Mode $n = 0$ does not require additional terms. The distortion $\tilde{r}$ of the cavity with average radius r_c can then be described by a number of modes, each with k_x, n, ω and amplitude $\hat{r}$.

$$\eta = r_c + \tilde{r} = r_c + \hat{r}e^{i(k_x x + n\theta - \omega t)}, \tag{B.9}$$

where η is the local cavity radius. The dispersion relation is subsequently obtained after determining the kinematic and dynamic boundary conditions using a small-perturbation analysis [2]. Both boundary conditions yield a relation between the perturbation amplitude $\hat{\phi}$ and the cavity radius variation amplitude $\hat{r}$. Combining the kinematic and dynamic boundary condition then yields an expression of the frequency as a function of the wavenumber. The derivation of both boundary conditions is described in [2]. The kinematic and dynamic boundary conditions are given by:

$$\frac{\hat{\phi}}{\hat{r}} = \frac{i\left(W_c k_z + V_c \frac{n}{r_c} - \omega\right)}{k_r H_n^{(1)'}(k_r r_c)}, \tag{B.10}$$

$$\frac{\hat{\phi}}{\hat{r}} = \frac{\frac{T}{r_c}(n^2 + k_z^2 r_c^2 + 1) + 2(p_\infty - p_{\text{vap}})^*}{i\rho r_c \left(u_{x,c} k_z + u_{\theta,c} \frac{n}{r_c} - \omega\right) H_n^{(1)}(k_r r_c)}, \tag{B.11}$$

where $u_{x,c}c$ and $u_{\theta,c}$ are respectively the axial and azimuthal velocity at the cavity interface.

Discretization methods in ReFRESCO

This appendix chapter contains additional definitions and background for the discretization methods applied in REFRESCO.

C.1. Time discretization

The time-derivative for a control volume that remains unchanged in time, is defined by

$$\frac{\partial}{\partial t} \int_V (\rho\phi) \mathrm{d}V, \tag{C.1}$$

and discretized by an implicit backward Euler scheme using three time levels n, $n-1$ and $n-2$:

$$\frac{\partial}{\partial t} \int_V (\rho\phi) \mathrm{d}V \approx \frac{c_1(\rho\phi_c\Delta V)^n + c_2(\rho\phi_c\Delta V)^{n-1} + c_3(\rho\phi_c\Delta V)^{n-2}}{\Delta t}, \tag{C.2}$$

where n indicates the time level and Δt the time step. For the second-order three-time level scheme used for the present simulations, the coefficients are defined as:

$$c_1 = 1.5; \; c_2 = -2.0; \; c_3 = 0.5. \tag{C.3}$$

C.2. Finite-volume discretization

In finite volume codes the domain is divided into a finite number of non-overlapping control volumes where the integral forms of the governing equations are solved for each cell. The discretization process will be outlined using a simple transport equation for an arbitrary flow parameter ϕ, given below in differential conservative form:

$$\frac{\partial\phi}{\partial t} + \nabla\cdot(\phi\mathbf{u}) = \nabla\cdot(\mathrm{D}\nabla\phi) + Q_\phi, \tag{C.4}$$

where D represents the diffusivity of ϕ and Q_ϕ is a source term. In the finite volume method this transport equation would be solved in its integral form:

$$\int_V \frac{\partial\phi}{\partial t}\mathrm{d}V + \int_S \phi(\nabla\phi\cdot\mathbf{n})\mathrm{d}S = \int_S \mathrm{D}(\nabla\phi\cdot\mathbf{n})\mathrm{d}S + \int_V Q_\phi\mathrm{d}V, \tag{C.5}$$

using the Gauss divergence theorem and with V, S denoting respectively the volume and surface area of the control volume.

C.3. Convective term discretization

The description of the Quadratic Upwind Interpolation for Convective Kinematics (QUICK) scheme below was based on [89]. The downwind face value ϕ_f for the QUICK scheme ($\kappa = 1/2$) is given by:

$$\phi_f = \phi_C + \frac{\Delta x_C}{2}\left[\frac{1+\kappa}{2}\left(\frac{\partial\phi}{\partial x}\right)_f + \frac{1-\kappa}{2}\left(\frac{\partial\phi}{\partial x}\right)_u\right], \tag{C.6}$$

where

$$\Delta x_C = x_f - x_u, \qquad \left(\frac{\partial\phi}{\partial x}\right)_f = \frac{\phi_D - \phi_C}{x_D - x_C}, \qquad \left(\frac{\partial\phi}{\partial x}\right)_u = \frac{\phi_C - \phi_U}{x_C - x_U}. \tag{C.7}$$

Figure C.1 provides an illustration of the faces and gradients used in the interpolation. The formulation for the face value ϕ_f using the limited QUICK scheme converted to flux-limited form is given by:

$$\phi_f = \phi_C + \frac{\Delta x}{2}\lambda\left[(1+\kappa)\left(\frac{\partial\phi}{\partial x}\right)_f - 2\kappa\left(\frac{\partial\phi}{\partial x}\right)_u\right], \tag{C.8}$$
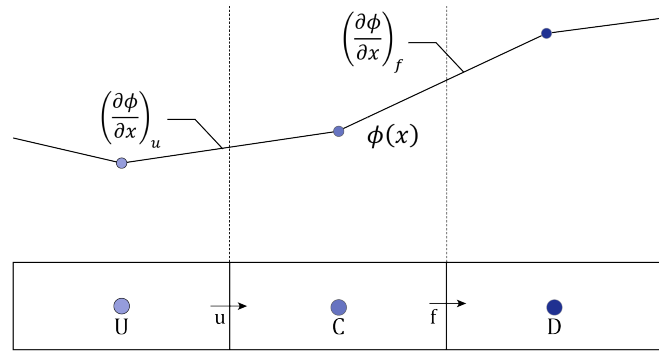
Figure C.1: Sketch indicating fluxes, cells and face values. Image adapted from [89].

where

$$\lambda = \max\left[0,\ \bar{\phi}_C(1 - \bar{\phi}_C)\right]. \tag{C.9}$$

The normalized variable $\bar{\phi}_C$ is defined as [89]:

$$\bar{\phi}_C = \frac{\phi_C - \phi_U}{\phi_D - \phi_U} = \frac{1}{r+1}. \tag{C.10}$$

D

Wetted line vortex simulations

This appendix chapter contains additional plots of the iterative and statistical convergence for the wetted line vortex simulations on M_1 and for the verification study. Furthermore, in contains the point-wise values of the discretization uncertainties

D.1. Comparison of turbulence models on M1

D.1.1. Iterative convergence

The plots of the residual convergence of the coarse mesh simulations of the wetted vortex are given in Figures D.1 and D.2.

(a) Velocity vector (cyan) and pressure (purple).

(b) Modeled turbulent kinetic energy k_{mod} (cyan) and specific dissipation rate ω (purple).
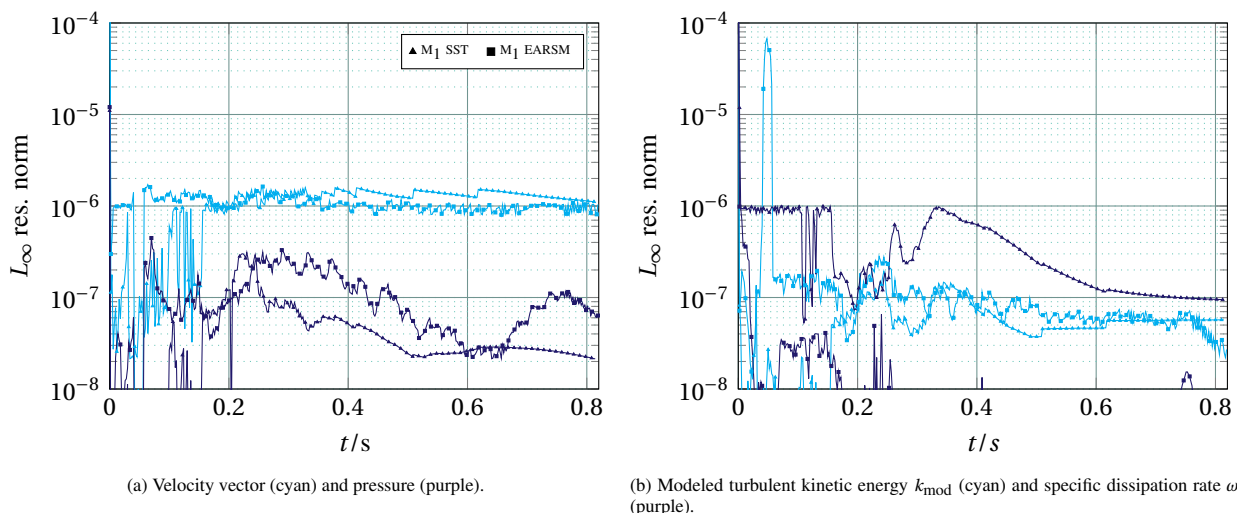
Figure D.1: L_∞ residual for wetted vortex simulations on M_1, where triangular marks are used for the SST and square marks indicate the EARSM simulation.

(a) Velocity vector (cyan) and pressure (purple).

(b) Turbulent kinetic energy k_{mod} (cyan) and specific dissipation rate ω (purple).
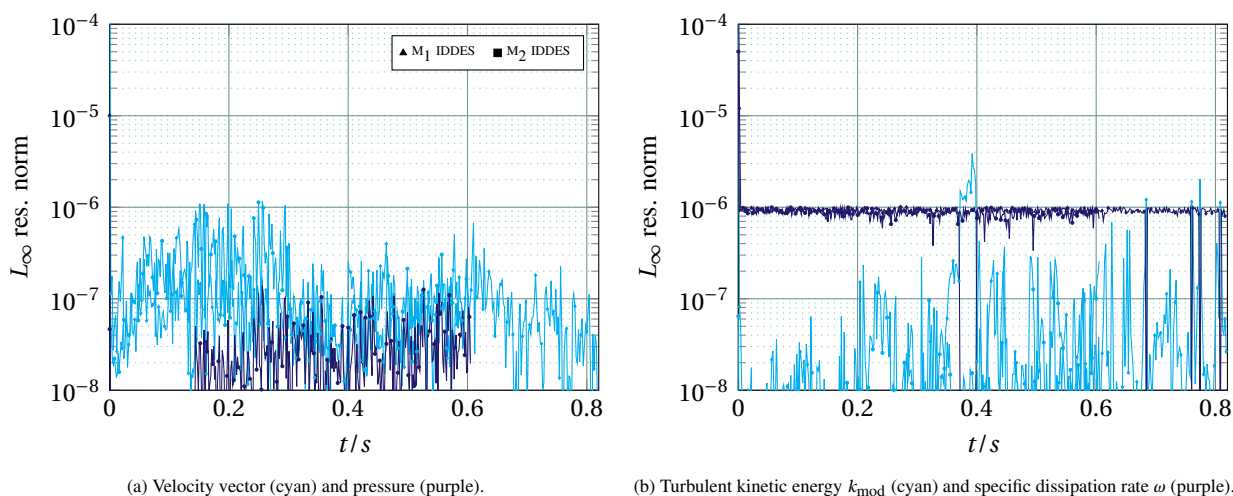
Figure D.2: L_∞ residual for wetted vortex simulations using the IDDES model, where triangular marks are used for the simulation on M_1 and square marks for M_2.

D.1.2. Statistical uncertainty

The statistical uncertainty plots for the coarse mesh simulations of the wetted vortex are given in Figure D.3. The statistical
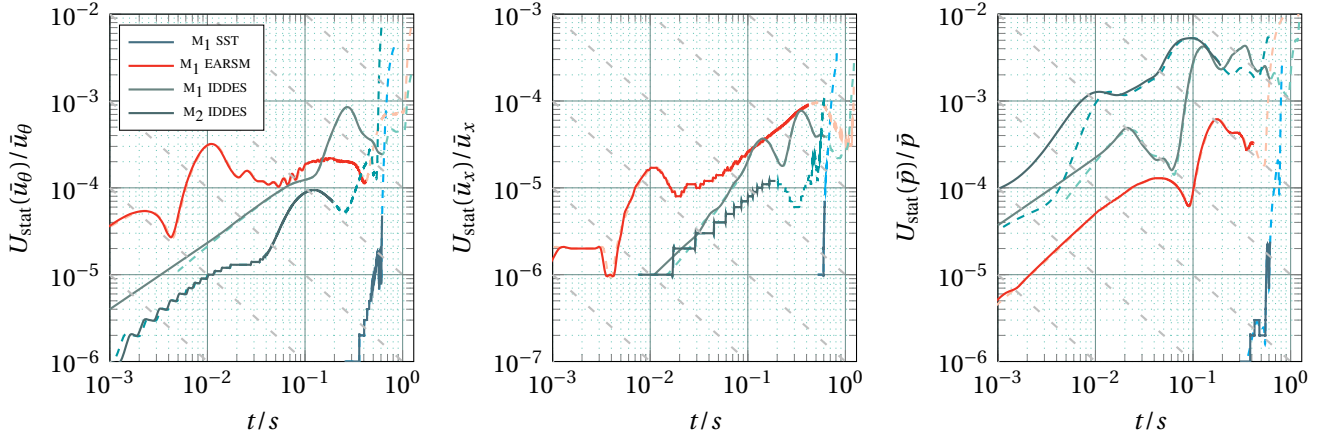
Figure D.3: Statistical uncertainty plots for u_θ (left), u_x (middle) and p (right) measured at plane C for the turbulence model comparison in the wetted vortex case, obtained using TST-B. Lighter, dashed versions of the dark solid lines indicate removed start-up effect.

convergence and uncertainty of the Reynolds stresses in normal direction $u_i' u_i'$ are shown for the IDDES on M_1 and M_2 in Figure D.4.
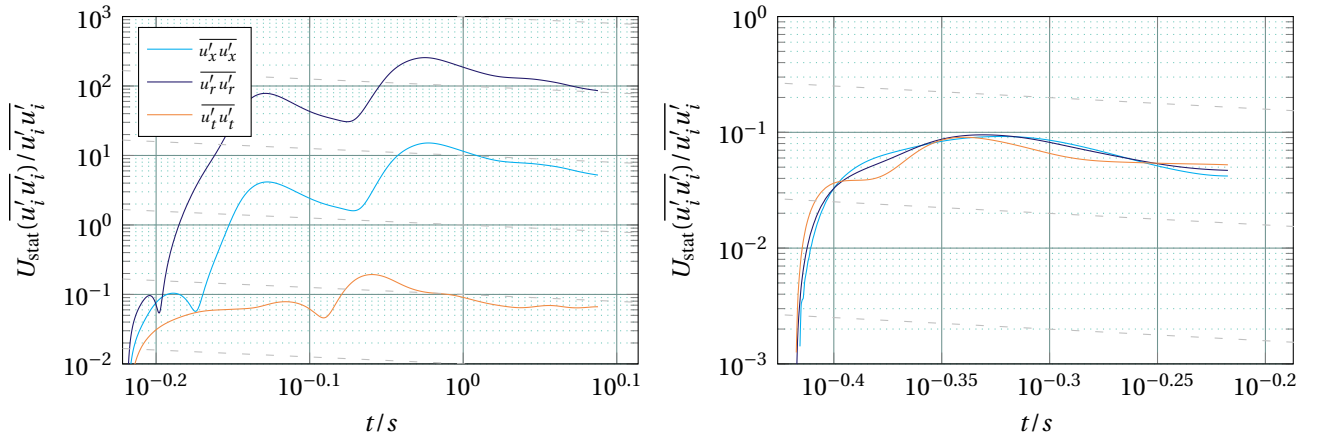
Figure D.4: Statistical uncertainty plots for normal Reynolds stresses resolved by the IDDES model in axial, radial and tangential direction, measured at plane C on M_1 (left) and M_2 (right). Results are for the wetted vortex case, obtained using TST-B.

D.2. Verification study

D.2.1. Iterative convergence

The residual plots for the simulations in the verification study are given in Figure D.5 for M_1 and M_2 and in Figure D.6 for the high Courant simulations on M_4.

(a) Velocity vector (cyan) and pressure (purple).

(b) Turbulent kinetic energy k_{mod} (cyan) and specific dissipation rate ω (purple).
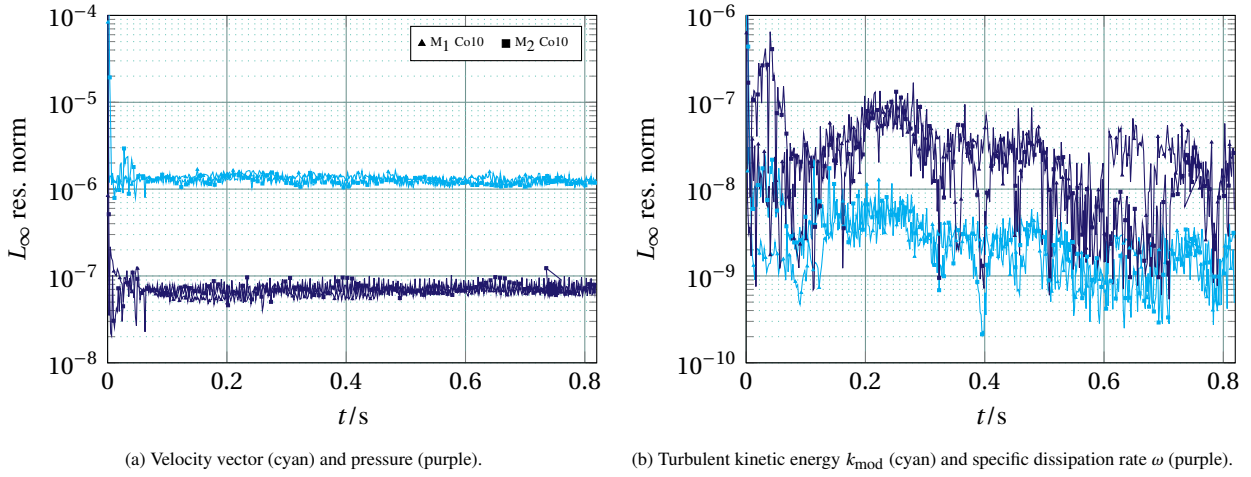
Figure D.5: L_∞ residual for wetted vortex EARSM verification study. Triangular marks are used for the simulation on M_1 and square marks indicate the M_2 simulation.

(a) Velocity vector (cyan) and pressure (purple).

(b) Turbulent kinetic energy k_{mod} (cyan) and specific dissipation rate ω (purple)
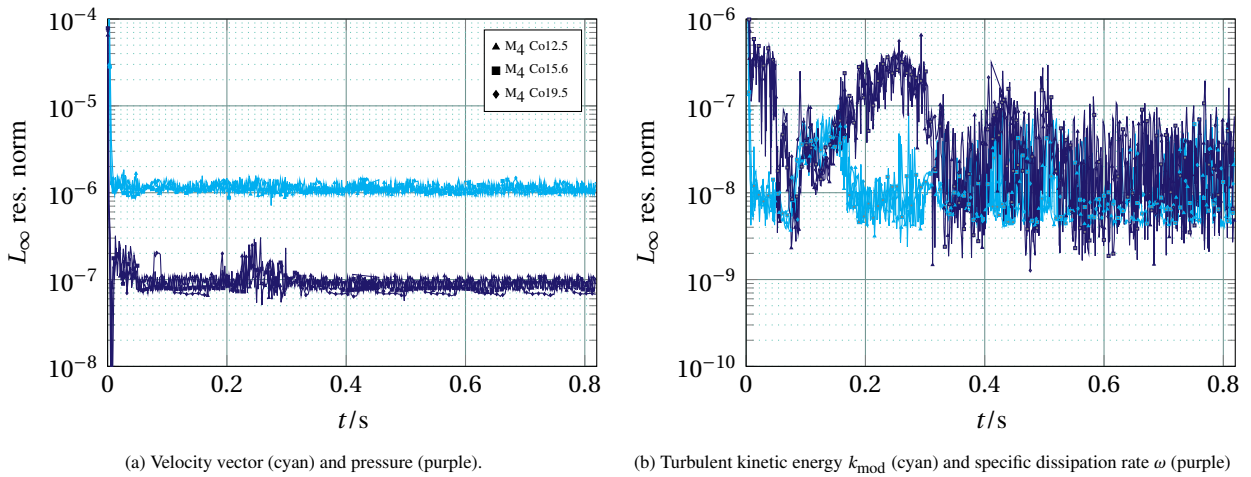
Figure D.6: L_∞ residual for wetted vortex simulations on M_4 using higher Courant numbers. Triangular marks are used for M_4 Co12.5, square marks indicate the M_4 Co15.6 simulation and diamond-shaped marks the M_4 Co19.5 simulation.

D.2.2. Discretization uncertainty

Disk monitor uncertainty values

The uncertainty and fitting parameter data (p and q) for the grid- and time step convergence study are given for the axial and tangential velocity and the pressure coefficient in respectively Tables D.1 to D.3.

Table D.1: Discretization uncertainty values for the axial velocity at plane C, obtained with the disk monitor in the grid- and time step convergence study. Last column is the result of M_4 EARSM Co10, the 1,2 in p and q columns indicates the use of both first- and second-order exponents in the fitting process.

r/r_{throat}	$U_{\mathrm{disc,abs}}(u_x^*)$	$U_{\mathrm{disc,rel}}(u_x^*)$ /%	p	q	$\phi_{\mathrm{num,M_4}}$
0.02	0.01	1.06	1,2	1,2	1.04
0.04	0.01	0.92	1,2	1,2	1.04
0.06	0.01	0.57	2	1,2	1.04
0.08	0.01	0.49	2	1,2	1.04
0.10	0.00	0.21	2	1,2	1.04
0.12	0.00	0.35	2	1,2	1.03
0.14	0.00	0.37	1,2	1,2	1.03
0.16	0.03	3.19	1,2	1,2	1.03
0.18	0.00	0.11	2	1,2	1.03
0.20	0.00	0.12	2	1,2	1.03
0.22	0.00	0.28	1	1,2	1.03
0.24	0.00	0.26	1	1,2	1.03
0.26	0.01	0.52	2	1,2	1.03
0.28	0.00	0.28	1,2	1,2	1.03
0.30	0.02	1.47	1,2	1,2	1.03
0.32	0.00	0.11	2	1	1.03
0.34	0.01	0.51	1	1,2	1.03
0.36	0.00	0.07	2	2	1.03
0.38	0.01	0.59	1,2	1,2	1.03
0.40	0.00	0.44	1	1,2	1.03
0.42	0.00	0.36	2	1,2	1.03
0.44	0.01	0.53	1,2	1,2	1.03
0.46	0.00	0.27	1	1,2	1.03
0.48	0.00	0.25	2	1,2	1.03
0.50	0.00	0.25	2	1,2	1.03
0.52	0.00	0.26	2	1,2	1.03
0.54	0.00	0.09	1,2	1,2	1.03
0.56	0.00	0.05	2	1,2	1.03
0.58	0.00	0.18	1,2	1,2	1.03
0.60	0.68	66.57	1,2	1,2	1.03
0.62	0.00	0.02	2	1,2	1.03
0.64	0.00	0.08	1,2	1,2	1.03
0.66	0.00	0.45	1,2	1,2	1.03
0.68	0.00	0.23	1,2	1,2	1.03
0.70	0.00	0.08	1,2	1,2	1.03
0.72	0.00	0.12	1,2	1,2	1.03
0.74	0.00	0.05	2	1,2	1.03
0.76	0.00	0.10	2	2	1.03
0.78	0.01	0.60	1,2	1,2	1.03
0.80	0.00	0.12	1	1,2	1.03
0.82	0.01	0.63	1,2	1,2	1.03
0.84	0.00	0.13	2	2	1.02
0.86	0.00	0.04	1	1,2	1.02
0.88	0.00	0.10	1	1,2	1.02
0.90	0.01	1.12	1,2	1,2	1.01
0.92	0.01	0.92	1,2	1,2	1.01
0.94	0.02	2.43	1,2	1,2	0.99
0.96	0.01	1.62	2	1,2	0.91
0.98	0.02	3.02	2	1,2	0.64
1.00	0.06	2713.76	1,2	1,2	0.00

Table D.2: Discretization uncertainty values for the tangential velocity at plane C, obtained with the disk monitor in the grid- and time step convergence study of the EARSM for the wetted vortex case. Last column is the result of M_4 EARSM Co10, the $1,2$ in p and q columns indicates the use of both first- and second-order exponents in the fitting process.

r/r_{throat}	$U_{\text{disc,abs}}(u_\theta^*)$	$U_{\text{disc,rel}}(u_\theta^*)$ /%	p	q	$\phi_{\text{num,M}_4}$
0.02	0.07	249.16	1,2	1,2	0.03
0.04	0.12	224.06	1,2	1,2	0.06
0.06	0.00	2.83	2	1,2	0.08
0.08	0.03	27.25	1,2	1,2	0.10
0.10	0.01	11.78	1,2	1,2	0.11
0.12	0.02	19.32	1,2	1,2	0.12
0.14	0.02	20.03	1,2	1,2	0.12
0.16	0.02	13.22	1,2	1,2	0.13
0.18	0.00	3.67	1,2	1,2	0.13
0.20	0.01	7.46	1,2	1,2	0.14
0.22	0.02	14.13	1	1,2	0.14
0.24	0.03	17.28	2	1,2	0.15
0.26	0.02	15.61	2	1,2	0.15
0.28	0.02	13.25	1,2	1,2	0.15
0.30	0.02	11.33	1	1,2	0.15
0.32	0.02	11.58	2	1,2	0.15
0.34	0.02	12.09	2	1,2	0.15
0.36	0.02	9.92	2	1,2	0.16
0.38	0.01	6.63	1,2	1,2	0.16
0.40	0.01	3.34	1,2	1,2	0.16
0.42	0.01	4.36	1,2	1,2	0.16
0.44	0.01	8.16	1,2	1,2	0.16
0.46	0.01	4.97	1,2	1,2	0.15
0.48	0.00	2.56	2	2	0.15
0.50	0.00	2.70	2	2	0.15
0.52	0.01	7.56	1,2	1,2	0.15
0.54	0.03	18.12	1,2	1,2	0.14
0.56	0.03	21.40	1,2	1,2	0.14
0.58	0.01	4.62	1	1,2	0.13
0.60	0.01	4.17	1,2	1,2	0.12
0.62	0.00	3.97	1,2	1,2	0.11
0.64	0.00	4.08	1,2	1,2	0.11
0.66	0.02	20.84	1	1,2	0.10
0.68	0.01	10.08	2	1,2	0.09
0.70	0.04	40.85	1,2	1,2	0.09
0.72	0.01	15.89	1,2	1,2	0.08
0.74	0.02	21.12	1,2	1,2	0.08
0.76	0.01	12.27	1,2	1,2	0.08
0.78	0.00	1.62	2	2	0.07
0.80	0.00	2.20	2	1,2	0.07
0.82	0.01	9.54	1,2	1,2	0.07
0.84	0.00	3.48	1,2	1,2	0.06
0.86	0.00	0.14	2	1,2	0.06
0.88	0.00	2.09	1.5	1.5	0.06
0.90	0.01	8.93	1,2	1,2	0.06
0.92	0.00	0.43	2	2	0.06
0.94	0.00	5.22	1,2	1,2	0.05
0.96	0.01	15.36	1,2	1,2	0.05
0.98	0.00	5.23	1	1,2	0.03
1.00	0.00	2 657.44	1,2	1,2	0.00

Quantification of uncertainty due to non-updated monitor coordinates

Table D.4 shows the point-wise difference in estimated discretization uncertainty between both monitors at measurement plane C. This data was obtained without taking into account the time step refinement as line monitors were not used in higher Courant number simulations on M_4.

Table D.3: Discretization uncertainty values for the pressure coefficient at plane C, obtained with the disk monitor in the grid- and time step convergence study of the EARSM for the wetted vortex case. Last column is the result of M_4 EARSM Co10, the 1,2 in p and q columns indicates the use of both first- and second-order exponents in the fitting process.

r/r_{throat}	$U_{\text{disc,abs}}(Cp)$	$U_{\text{disc,rel}}(Cp)$ /%	p	q	$\phi_{\text{num,M}_4}$
0.02	0.02	2.38	1,2	1,2	−0.73
0.04	0.02	2.25	1,2	1	−0.72
0.06	0.00	0.50	2	2	−0.72
0.08	0.00	0.43	1,2	1,2	−0.72
0.10	0.00	0.66	1,2	1,2	−0.71
0.12	0.00	0.39	2	1,2	−0.71
0.14	0.02	2.76	1	1,2	−0.70
0.16	0.00	0.26	2	2	−0.70
0.18	0.53	76.90	1,2	1,2	−0.70
0.20	0.00	0.22	1,2	1,2	−0.69
0.22	0.03	3.80	1	1,2	−0.69
0.24	0.01	2.14	1,2	1,2	−0.69
0.26	0.03	4.62	1,2	1,2	−0.68
0.28	0.02	2.41	2	1,2	−0.68
0.30	0.03	4.76	1	1,2	−0.68
0.32	0.02	2.58	1,2	1,2	−0.67
0.34	0.02	3.08	1,2	1,2	−0.67
0.36	0.03	4.08	1,2	1,2	−0.67
0.38	0.00	0.23	2	2	−0.67
0.40	0.03	4.49	1	1,2	−0.66
0.42	0.03	5.23	2	1,2	−0.66
0.44	0.00	0.53	1,2	1,2	−0.66
0.46	0.03	5.19	1	1,2	−0.66
0.48	0.03	4.20	1,2	1,2	−0.65
0.50	0.02	3.47	1,2	1,2	−0.65
0.52	0.02	2.57	1,2	1,2	−0.65
0.54	0.03	4.16	1	1,2	−0.65
0.56	0.02	3.33	1,2	1,2	−0.65
0.58	0.02	3.64	1,2	1,2	−0.65
0.60	0.02	3.48	1,2	1,2	−0.64
0.62	0.02	2.58	1,2	1,2	−0.64
0.64	0.01	1.67	1,2	1,2	−0.64
0.66	0.02	2.76	1,2	1,2	−0.64
0.68	0.02	2.38	1,2	1,2	−0.64
0.70	0.02	3.61	1,2	1,2	−0.64
0.72	0.02	2.58	1,2	1,2	−0.64
0.74	0.02	3.02	1,2	1,2	−0.64
0.76	0.01	2.33	1,2	1,2	−0.64
0.78	0.02	2.43	1,2	1,2	−0.64
0.80	0.02	3.80	1,2	1,2	−0.64
0.82	0.02	2.45	1,2	1,2	−0.64
0.84	0.02	2.43	1,2	1,2	−0.64
0.86	0.02	2.44	1,2	1,2	−0.64
0.88	0.02	2.47	1,2	1,2	−0.64
0.90	0.02	2.48	1,2	1,2	−0.64
0.92	0.01	2.35	1,2	1,2	−0.64
0.94	0.01	2.00	1,2	1,2	−0.64
0.96	0.01	2.24	1,2	1,2	−0.64
0.98	0.01	2.22	1,2	1,2	−0.64
1.00	0.02	2.42	1,2	1,2	−0.64

Table D.4: Comparison of calculated discretization uncertainties at plane C, obtained only from the grid-convergence study of the EARSM for the wetted vortex case. All uncertainties and differences (diff.) are relative to the mean value.

$r/r_{\max}$	$U_{\text{disk}}(u_x^*)$/%	$U_{\text{line}}(u_x^*)$/%	diff. /%	$U_{\text{disk}}(u_\theta^*)$/%	$U_{\text{line}}(u_\theta^*)$/%	diff. /%	$U_{\text{disk}}(C_p)$/%	$U_{\text{line}}(C_p)$/%	diff. /%
0.02	1.05	1.03	−0.02	250.46	45.15	−205.31	1.20	1.21	0.01
0.04	0.91	0.94	0.03	77.47	41.85	−35.62	1.25	0.36	−0.89
0.06	0.71	0.38	−0.33	9.60	33.14	23.54	1.22	0.90	−0.32
0.08	0.30	0.26	−0.04	16.38	22.98	6.60	0.45	0.39	−0.06
0.10	0.58	0.51	−0.07	2.23	1.87	−0.36	0.38	0.17	−0.21
0.12	0.42	0.47	0.05	14.55	13.76	−0.79	0.40	0.30	−0.10
0.14	0.37	0.37	0.00	12.70	12.54	−0.16	0.27	0.27	0.00
0.16	0.43	0.20	−0.23	3.84	10.20	6.36	0.19	0.95	0.76
0.18	0.55	0.46	−0.09	0.73	9.37	8.64	0.68	0.23	−0.45
0.20	0.48	0.22	−0.26	2.68	9.50	6.82	0.37	0.86	0.49
0.22	0.34	0.31	−0.03	8.09	9.27	1.18	1.27	0.24	−1.03
0.24	0.26	0.19	−0.07	8.64	7.80	−0.84	2.26	1.05	−1.21
0.26	0.26	0.33	0.07	9.23	8.06	−1.17	1.57	0.22	−1.35
0.28	0.28	0.30	0.02	7.90	2.94	−4.96	2.34	1.07	−1.27
0.30	0.32	0.36	0.04	6.40	7.34	0.94	1.03	1.09	0.06
0.32	0.27	0.29	0.02	6.89	6.65	−0.24	1.29	1.28	−0.01
0.34	0.22	0.41	0.19	11.75	2.64	−9.11	3.33	1.12	−2.21
0.36	0.30	0.24	−0.06	7.19	10.29	3.10	1.41	1.39	−0.02
0.38	0.44	0.34	−0.10	4.91	7.25	2.34	0.22	0.24	0.02
0.40	0.20	0.14	−0.06	1.98	8.28	6.30	4.37	1.34	−3.03
0.42	0.16	0.28	0.12	1.31	3.08	1.77	5.09	0.33	−4.76
0.44	0.36	0.15	−0.21	4.51	2.32	−2.19	0.52	1.36	0.84
0.46	0.26	0.31	0.05	1.77	0.00	−1.77	1.89	1.73	−0.16
0.48	0.15	0.15	0.00	3.84	3.92	0.08	2.37	1.50	−0.87
0.50	0.16	0.46	0.30	7.61	2.28	−5.33	2.66	0.38	−2.28
0.52	0.17	0.27	0.10	4.44	2.13	−2.31	0.65	0.41	−0.24
0.54	0.02	0.03	0.01	18.03	2.83	−15.20	4.03	1.34	−2.69
0.56	0.04	0.01	−0.03	5.48	4.04	−1.44	1.71	3.15	1.44
0.58	0.14	0.31	0.17	5.71	0.78	−4.93	2.27	0.31	−1.96
0.60	0.18	0.01	−0.17	3.61	0.06	−3.55	2.19	1.27	−0.92
0.62	0.03	0.13	0.10	1.21	1.01	−0.20	1.58	2.89	1.31
0.64	0.01	0.07	0.06	1.05	1.94	0.89	0.25	1.48	1.23
0.66	0.45	0.30	−0.15	1.16	9.84	8.68	1.74	0.22	−1.52
0.68	0.22	0.44	0.22	31.83	15.52	−16.31	1.42	0.26	−1.16
0.70	0.05	0.08	0.03	40.91	0.60	−40.31	1.22	1.51	0.29
0.72	0.05	0.22	0.17	15.90	6.11	−9.79	1.58	1.83	0.25
0.74	0.24	0.48	0.24	8.48	2.76	−5.72	1.42	1.36	−0.06
0.76	0.10	0.06	−0.04	12.24	11.28	−0.96	1.45	1.70	0.25
0.78	0.62	0.16	−0.46	2.14	3.02	0.88	1.55	1.28	−0.27
0.80	0.11	0.35	0.24	43.67	4.18	−39.49	1.60	1.69	0.09
0.82	0.63	0.30	−0.33	9.57	2.53	−7.04	1.47	1.35	−0.12
0.84	0.13	0.08	−0.05	0.41	2.16	1.75	1.47	1.86	0.39
0.86	0.14	0.10	−0.04	4.13	4.48	0.35	1.51	1.64	0.13
0.88	0.70	0.04	−0.66	7.41	1.06	−6.35	1.54	1.46	−0.08
0.90	1.12	0.05	−1.07	8.93	0.91	−8.02	1.52	1.25	−0.27
0.92	0.92	0.13	−0.79	0.55	9.08	8.53	1.50	1.76	0.26
0.94	1.30	1.47	0.17	2.71	1.31	−1.40	1.55	1.07	−0.48
0.96	11.61	6.44	−5.17	15.53	11.53	−4.00	1.54	2.37	0.83
0.98	22.61	12.26	−10.35	27.68	0.62	−27.06	1.49	0.10	−1.39
1.00	3 007.37	310.45	−2 696.92	2 957.34	296.01	−2 661.33	1.52	3.53	2.01

Cavitating line vortex simulations

This chapter contains additional plots of the iterative and statistical convergence of cavitating line vortex simulations.

E.1. Iterative convergence

The local L_∞ and root-mean-square L_2 residual plots for the cavitating vortex simulations on M_4 are given in Figures E.1 and E.2 respectively. Monitor data for both M_4 simulations was accidentally deleted for a period of 0.078s in the beginning of the simulation and is therefore omitted in the graphs. The larger peaks in the residuals are due to restarts of the simulation.

(a) Velocity vector (cyan) and pressure (purple).

(b) Turbulent kinetic energy k_{mod} (cyan), specific dissipation rate ω (purple) and volume vapor fraction (orange).
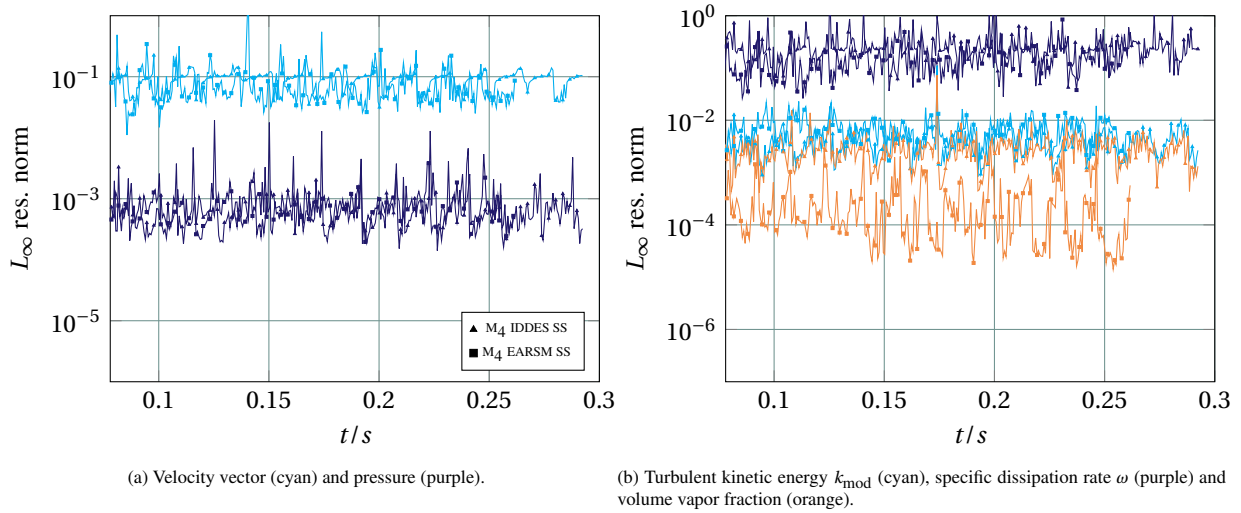
Figure E.1: L_∞ residual for cavitating vortex simulations on M_4, where triangular marks are used for the IDDES and square marks indicate the EARSM simulation.

(a) Velocity vector (cyan) and pressure (purple).

(b) Turbulent kinetic energy k_{mod} (cyan), specific dissipation rate ω (purple) and volume vapor fraction (orange).
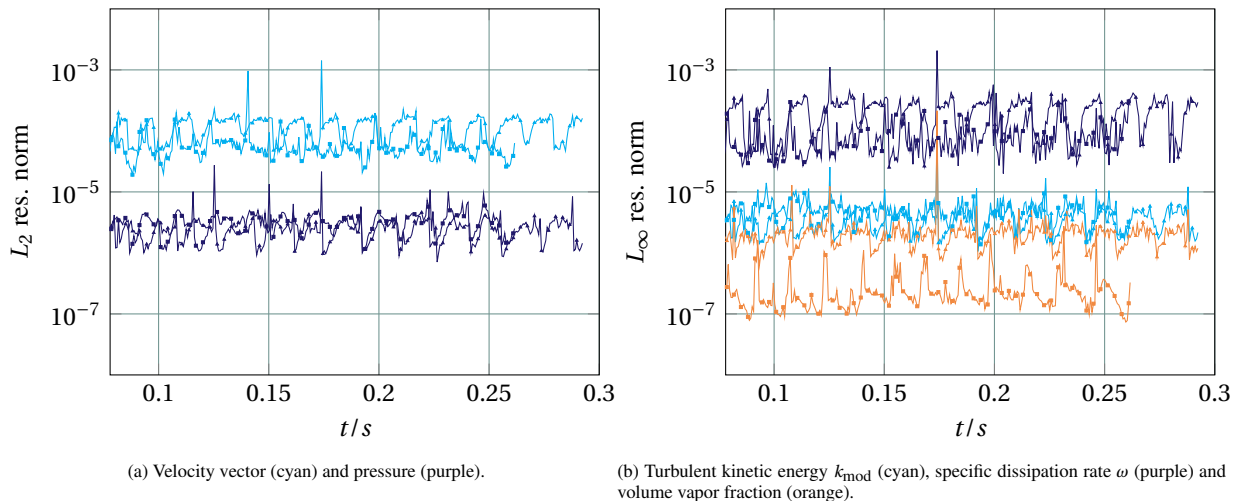
Figure E.2: L_2 residual for cavitating vortex simulations on M_4, where triangular marks are used for the IDDES and square marks indicate the EARSM simulation.

E.2. Statistical convergence

The statistical convergence and uncertainty of the Reynolds stresses in normal directions $u_i' u_i'$ are shown for the IDDES in combination with the Schnerr-Sauer cavitation model on M_3 and M_4 in Figure E.3.
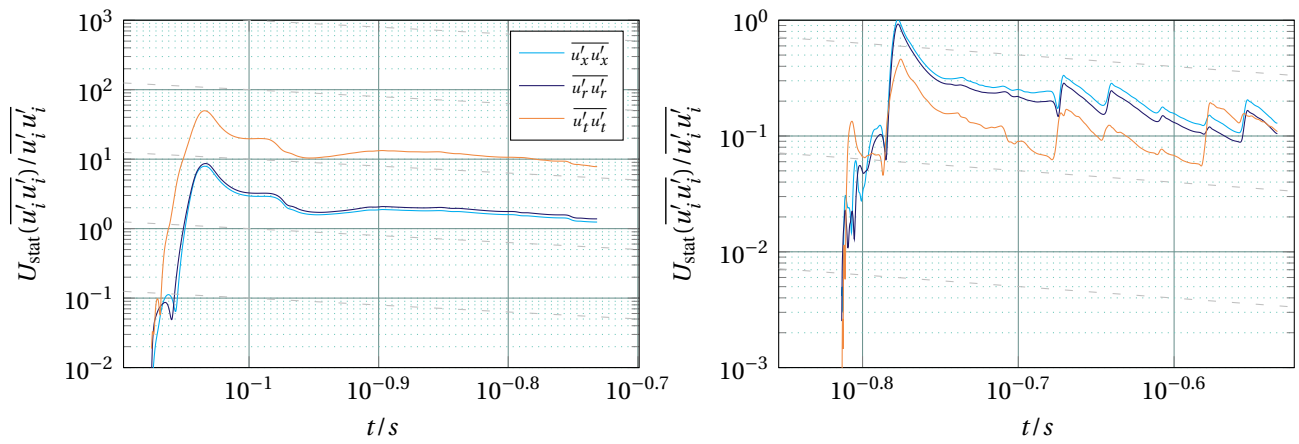
Figure E.3: Statistical uncertainty plots for normal Reynolds stresses resolved by the IDDES model in axial, radial and tangential direction, measured at plane C on M_3 (left) and M_4 (right). Results are for the cavitating vortex case, obtained using TST-B.